Universidad Rey Juan Carlos

TESIS DOCTORAL

UV LED TECHNOLOGY FOR WATER DISINFECTION: A SPECTRUM OF POSSIBILITIES

ADITHYA PAI UPPINAKUDRU

DIRECTORES:
JAVIER MARUGÁN AGUADO
CRISTINA PABLOS CARRO
KEN REYNOLDS

Programa de Doctorado en Tecnologías Industriales: Química, Ambiental, Energética, Electrónica, Mecánica y de los Materiales

Escuela Internacional de Doctorado

2023

Universidad Rey Juan Carlos

TESIS DOCTORAL

UV LED TECHNOLOGY FOR WATER DISINFECTION: A SPECTRUM OF POSSIBILITIES

Autor:

Adithya Pai Uppinakudru

Directores:

Javier Marugán Aguado
Cristina Pablos Carro
Ken Reynolds

Programa de Doctorado en Tecnologías Industriales: Química, Ambiental, Energética, Electrónica, Mecánica y de los Materiales

Escuela Internacional de Doctorado

2023

El Dr. D. Javier Marugán Aguado, Catedrático de Universidad, la Dra. Dña. Cristina Pablos Carro, Profesora Titular de Universidad ambos del área de Ingeniería Química del Departamento de Tecnología Química y Ambiental de la Universidad Rey Juan Carlos, y El Dr. D. Ken Reynolds, investigador de ProPhotonix IRL LTD., Irlanda.

CERTIFICAN:

Que el presente trabajo de investigación titulado "UV LED TECHNOLOGY FOR WATER DISINFECTION: A SPECTRUM OF POSSIBILITIES" constituye la memoria que presenta D. Adithya Pai Uppinakudru, para aspirar al grado de Doctor y ha sido realizada en los laboratorios del Grupo de Ingeniería Química y Ambiental del Departamento de Tecnología Química y Ambiental de la Universidad Rey Juan Carlos y en los laboratorios de ProPhotonix (Cork, Irlanda) bajo nuestra dirección.

.

Y para que así conste, firmamos el presente certificado en Móstoles, 02 de junio de 2023.

Fdo. Javier Marugán Aguado Fdo. Cristina Pablos Carro Fdo. Ken Reynolds

To my family and mentors

"We do not need magic to transform our world.
We carry all of the power we need inside ourselves already".
J. K. Rowling

Acknowledgements

"We will get there Adithya!" said my colleague, Conor, back in 2019 and here I am writing my heartfelt thank you to everyone who was part of this journey. First and foremost, to Dr. Javier Marugán Aguado, Dr. Cristina Pablos, Dr. Ken Reynolds, and Mr. Simon Stanley, my supervisors and mentors, through this entire doctoral journey. It was not easy and feels like just yesterday when I walked in to ProPhotonix, my industrial placement company, on my first day and Ken introduced me to the team. Every time I went with an idea, Ken and Simon always listened and gave me great insights and input on my work. They made a nervous boy feel just like a part of the team from day 1. All those coffee break conversations always gave me a story to enjoy or ponder. Javier and Cristina, moving to a new country where English was not commonly used, I was overwhelmed, but your guidance and support is something I cannot thank you enough for. From having a chat nearly every week to responding to my doubts at any time in the day, I do not think this PhD would have been complete without you two. During one of the toughest times in this journey, Javier said, "It might look slow, but the light is there at the end of the tunnel" and here we are! It has been a pleasure working alongside you two and grateful to have you as my supervisors. I think the toughest time in a PhD is when you hit a roadblock and have no answers, Cristina was one of the first ones to ask me questions and pushed me to approach it from other ends. Their valuable advices, encouragement, scientific guidance, and constructive discussions made this a successful PhD dissertation. I would also like to thank my mentors in India, Dr. K Rama Narasimha sir and Dr. M Umashankar sir for their guidance and help.

I don't think starting this PhD could have been any easier for me because of this man. They say you don't need to look for inspiration, it is always around you. In Ireland, every time I felt homesick or felt too lazy to cook or demotivated with work, my flat mate and a great friend Amarjit (Ammo!) came to my rescue. His sheer presence helped me get through tough days and motivated me. He was, is, and will always be one of my biggest cheer leaders through these years. I also met Suyash in Cork who always said "ಏನು ಆಗಲ್ಲ macha, ಟೈಮ್ ಆದಂಗೆ ಎಲ್ಲ ಸರಿ ಹೋಗತ್ತೆ" meaning "Nothing is going to happen, with time it will be fine again" and kept me on my heels every time. From cooking food to going on a run to clear my head and motivating me to get better, he never said "No".

To Karol, Maggie, Jean, Kieran, Diarmuid, Aideen, and the entire ProPhotonix team – Thank you! I could not have asked for a better group of colleagues and friends. My time at ProPhotonix was exceptionally smooth due to every one of them. “It’s Mondays problem Adithya” - Karol would say on a late Friday evening if I jumped on him with a question and followed it with “We can talk about it on the way home”. Thank you for driving me home, constantly keeping me engaged and always answering my questions. From having a chat about work to discussing football, I have had the pleasure of learning so much from them. From work to home, I made another great set of friends – “The Rutland Street gang”. During the pandemic, they are what kept me going. Every Friday evening, we would sit on the balcony and enjoy a cup of coffee, talk about work/football/music and just enjoy. It almost never ended early ;). I am very thankful to Ed, Dan, John, Chelsea, Aoife, Yoshita and Chris, for always being around to have a chat and take my mind off work. I think I would have missed home a lot more if not for my little family in Cork.

To Conor, what would this PhD be without you? He was a great friend, researcher and an amazing person. From having a conversation over lunch to chatting about Tottenham/United (and watching) while plating the experiments, I don’t think I can ask for more. He said, “It might not look like much progress but small steps Adithya!”. To Maria, thank you for teaching me microbiology, analysis and working without making too many mistakes. A student is only as good as his teacher ;) She gave me the confidence to start speaking in whatever broken Spanish I knew.

To the entire REWATERGY team, this project would never have taken place if not for you all. To Cristina, Carlos, Rohit, Fran, and the entire Photoners team, thank you for supporting me and guiding me during my time at URJC. Coming from a background of mechanical engineering, this thesis would not have been possible without their motivation and teachings. To Cristina Adan, thank you for being there through the stress of visas and moving to a new country. This PhD would not be complete without your assistance and guidance.

To Carmen, I am grateful for your help and support during the final stages of my work. She never said no to a coffee break or help me with organizing my thoughts. She listened and let me work my way out of a slump. Thank you for having such a keen eye to detail and teaching me so much. “Step by step but we will get there” ;)

To Nikki, Ritika, Ankush, Aditya and Shrawan – you know what you mean to me, and I will forever be grateful for your monologues and motivation over the past three years. These five people have picked my call at any time (even with the 5-h time difference) and would say “You can do this adi, I know you can” no matter how demotivated I sounded.

Finally, and most importantly, to my family back home. Aanu, Amma, Akka, Bhavaji, and Aarav – I can say a million things about how much your support has meant to me throughout and I will forever be grateful. Aanu, amma thank you for the values you have given me and akka since our childhood and always standing with us through our decisions. From calming me down, calling me every day, to making sure I eat a lot of food when I went home, I can’t put into words how much you all mean to me. To my little ones, Aarav and Anika, I love you.

I have been lucky to go through this doctoral journey making so many friends and family that I cannot put my gratitude to words. It would not have been possible without you! This thesis is for you, and I hope I make you all proud in whatever comes next.

Adi

Index

Summary / Resumen 1

Chapter 1. Introduction 21

1.1. Light Spectrum 23

1.2. Ultraviolet (UV) Light 26

1.2.1. Properties and Applications of Ultraviolet Light 27

1.2.2. UV Sources 28

1.2.2.1. Mercury Lamps 29

1.2.2.2. Light Emitting Diodes (LEDs) 30

1.3. Water 34

1.3.1. Availability 35

1.3.2. Contamination 35

1.3.3. Treatment 37

1.3.4. Improvement of Water Quality 38

1.4. UV Disinfection 39

1.4.1. Mechanism of Action 39

1.4.2. Factors Affecting the Efficiency of UV LED Disinfection 41

1.4.3. Developments in UV LED Disinfection 41

1.5. Challenges in UV LED Disinfection Process 43

1.5.1. Objectives of the PhD Thesis 44

Chapter 2. LED Characterization 49

2.1. Introduction 51

2.2. Methodology 53

2.2.1. LED Selection 53

2.2.2. Testing Equipment 54

2.2.3. Rollover Test 56

2.2.4. Balancing and Burn–In 57

2.2.5. Spectral Measurement 58

2.2.6. Uniformity Characterization 58

2.2.7. Lifetime Set–up and Measurements 59

2.3. Results and Discussions 61

2.3.1. LED Selection 61

2.3.2. COBRA FX–1 Device 63

2.3.3. Rollover Test 66
2.3.4. Emission Spectrum 68
2.3.5. Effect of Current on Intensity 70
2.3.6. Device Light Output 73
2.3.7. Effect of Working Distance on Intensity and Dose 76
2.3.8. Device Lifetime 78
2.4. Conclusions 82
2.5. Appendix Chapter 2 83
2.A. LED Product Library 83
2.B. Lifetime Measurements 85
Chapter 3. UV Sensors 87
3.1. Introduction 89
3.2. Methodology 92
3.2.1. Sensors 92
3.2.2. Sources – Light Emitting Diodes 93
3.2.3. Set–up for Experiments 94
3.2.3.1. Angle of Acceptance 94
3.2.3.2. Ambient and Stray Light 96
3.2.3.3. Integration Time 96
3.2.3.4. Sensor Temperature 96
3.2.3.5. Measurement of the Intensity 97
3.3. Results and Discussions 98
3.3.1. Angle of Acceptance 98
3.3.2. Effect of Ambient Light 103
3.3.3. Effect of Integration Time on Readings 105
3.3.4. Effect of Temperature of the Sensor 107
3.3.5. Differences in Intensity Measurements between Sensors 109
3.3.6. Recommendations 110
3.4. Conclusions 111
3.5. Appendix Chapter 3 112
3.A. Experimental Set–up 112
3.B. Ambient Light Measurements 115

Chapter 4. Radiation Modeling **117**
4.1. Introduction 119
4.2. Methodology 122
4.2.1. LED Source, Fixture Design, and Spectral Characterization 122
4.2.1.1. Set–up to Quantify the Effect of the Quartz Tube 123
4.2.2. Optical Modeling of the Devices with Ray Tracing 124
4.2.3. Characterization using Chemical Actinometry 128
4.2.4. Discrete Ordinate Method (DOM) Modeling 129
4.2.5. Modeling of a 4–Wavelength Germicidal System 132
4.3. Results and Discussions 133
4.3.1. Ray Tracing and Radiometry 133
4.3.1.1. Effect of Quartz Tube 136
4.3.2. Discrete Ordinate Method 139
4.3.3. Characterization using Actinometry 142
4.3.4. Analysis of a 4–Wavelength Germicidal System 146
4.4. Conclusions 149
4.5. Appendix Chapter 4 150
4.A. UV Fixture Design 150
4.B. ZeMax Optic Studio Design Layout 152
4.C. Mesh Sensitivity Analysis on DOM 152
4.D. Other Wavelengths 154
4.D.1. Optical Model *vs* Experimental Data 154
4.D.2. ZeMax and Radiometry 155
4.D.3. Effect of Quartz Tube 156
4.E. Quartz Tube Transmission Curve (FAB027469, GE214) 157
4.F. ZeMax *vs* DOM (other wavelengths) 158
4.G. Data on Ferrioxalate Actinometry 159
Chapter 5. UV Disinfection **161**
5.1. Introduction 163
5.2. Methodology 165
5.2.1. Test Water 165
5.2.2. Microorganism Propagation and Enumeration 165
5.2.3. UV Irradiation 167

5.2.4. Experimental Set–up 167
5.2.4.1. Combinations of UV Sources 168
5.2.4.2. Flow Rates 169
5.2.5. Residence Time and Kinetic Constants 171
5.2.6. Synergy of Inactivation 171
5.2.7. Statistical Analysis 171
5.2.7.1. Student's *t*–Distribution Analysis 171
5.2.7.2. Codified Analysis of Variance (ANOVA) 172
5.2.8. Error Propagation 174
5.2.9. Dark Control Experiments 175
5.2.10. Electrical Energy Consumption 175
5.3. Results and Discussions 175
5.3.1. Inactivation Mechanism 175
5.3.2. Recirculating Batch Reactor 177
5.3.3. Kinetic Order and Effect of Dose 182
5.3.4. UV Inactivation by Individual Wavelengths 183
5.3.5. UV Inactivation by Combination of Wavelengths 184
5.3.5.1. Sequential Mode (SE) 184
5.3.5.2. Simultaneous Mode (SI) 185
5.3.5.3. Sequential + Simultaneous Mode (SS) 185
5.3.6. Effect of Arrangement 187
5.3.7. Effect of Flow Rate 191
5.3.8. Synergy of Inactivation 192
5.3.8.1. Dual Wavelength Combinations 194
5.3.8.2. Three Wavelength Combinations 197
5.3.8.3. Synergistic Damage Mechanism 198
5.3.9. Electrical Energy Consumption 202
5.4. Conclusions 205
5.5. Appendix Chapter 5 207
5.A. FX–1 310 Disinfection 207
5.B. Inactivation Rate Constants 207
5.C. Synergy of Inactivation (in terms of kinetic constants) 208
5.D. *t*–Student Analysis (in terms of kinetic constants) 209

5.E. Codified ANOVA Results 210
5.E.1. Dual Wavelength Combinations 210
5.E.2. Three Wavelength Combinations 217
Chapter 6. Wastewater Disinfection 221
6.1. Introduction 223
6.2. Methodology 225
6.2.1. Test Wastewater 225
6.2.2. Microorganism Propagation and Enumeration 227
6.2.3. UV Combinations 227
6.2.4. Water Quality Characterization 228
6.2.5. Statistical Analysis 229
6.3. Results and Discussions 230
6.3.1. Water Quality 230
6.3.2. UV Inactivation by Individual Wavelengths in Wastewater 231
6.3.3. UV Inactivation by Combination of Wavelengths in Wastewater 233
6.3.4. Synergy of Inactivation 234
6.3.5. Electrical Energy Consumption 239
6.4. Conclusions 242
6.5. Appendix Chapter 6 244
6.A. FX–1 310 Disinfection 244
6.B. Synergy of Inactivation (in terms of kinetic constants (k_c)) 244
6.C. *t*–Student Analysis (in terms of kinetic constants) 245
6.D. Codified ANOVA Results 246
6.D.1. Dual Wavelength Combinations 246
6.D.2. Three Wavelength Combination 251
Chapter 7. Conclusions 253
7.1. Future Work 257
References 259
List of Figures 285
List of Tables 291

SUMMARY

RESUMEN

Summary

➢ Background

Access to clean and safe drinking water is a basic human right, as declared by United Nations General Assembly in 2010 (Resolution 64/292). Maintaining and achieving safe water quality is a crucial factor in promoting public health and economic development. Despite technological progress in certain areas, in the 21st century, approximately 29% of the world's population (2.1 billion people) lack access to drinking water at home. There exist multiple challenges of water scarcity, pollution, and inadequate infrastructure that require a concerted effort from governments and communities to aid the progress of providing safe drinking water worldwide. Climate change is expected to exacerbate water scarcity in many parts of the world, with some regions facing a 50% reduction in available water by 2050. By investing in water infrastructure, promoting water conservation and implementing effective water treatment methods, we can ensure that everyone has access to this essential resource. Traditionally, various methods have been employed for treating water, such as chlorination, sedimentation, filtration, and coagulation. Since the early 1950s, Ultraviolet (UV) light sources have been used by local and national bodies for water disinfection in the final stages to eliminate pathogenic microorganisms. The use of UV light has been found to reduce the growth of microorganisms by inhibiting their reproduction when the DNA/RNA within the microorganism absorbs radiation. Sunlight is the most commonly available natural source of UV. However, it doesn't provide enough UV radiation for quick and effective disinfection. For this reason, artificial UV sources like mercury lamps, light emitting diodes (LEDs), or plasma lamps have been explored for generating UV wavelengths of interest. It is worth noting that sunlight has been used in disinfection processes in low– and medium– income countries using a process called solar water disinfection (SODIS). The technology of UV LEDs is relatively new, with the first commercial UV LED being available in 2003, and has evolved significantly since its discovery with applications in multiple fields like catalysis, air, and surface disinfection etc. Nevertheless, there are still significant challenges associated with the technology and disinfection process that need to be investigated and resolved. Treatment of drinking water and wastewater using UV sources can be energy–intensive and requires optimization to minimize energy consumption. While it may seem that more input radiation to the water matrix can result in faster and higher disinfection rates, it is essential to balance treatment effectiveness, cost, and energy efficiency. In a UV disinfection process, the type and kind of light source used, such as the wavelength of emission and whether it is

a mercury lamp or UV LED, mainly determine the effectiveness of the process. As mentioned earlier, UV LED technology is relatively new, and the output efficiency of these light sources is low (the maximum reported efficiency is 13% as of 2023). Due to this fact, obtaining a sufficient UV dose on the target is challenging for researchers and companies. Additionally, due to their low output efficiency, there is a need to evaluate the lifetime of these devices and understand critical parameters that affect the degradation of the LEDs used. Also, it has been observed in the literature that certain microorganisms of interest are more susceptible to the irradiation of specific wavelengths than others, and therefore, selecting the right wavelength of irradiation is crucial for an effective disinfection process. In conclusion, a complete understanding of the light source being used is necessary before its application in a water disinfection system. One of the significant challenges faced by researchers in the field of UV sources is obtaining valid and accurate readings of the amount of light irradiated. Ensuring accurate measurements is crucial as it directly impacts the analysis of the effectiveness of the process. However, measuring UV radiation requires specialized instrumentation that may not be readily available and requires an understanding of various parameters that could affect the measurements directly or indirectly. Alternatively, these measurements could be conducted in a simulated environment using software tools. However, even in this area, there exist complex challenges, such as programming the multi–peaked nature of light output and the water medium of radiation transport. Moreover, a significant gap exists in modeling sources in complex environments where multiple interactions are in play. In this context, the main objective of this PhD thesis is to evaluate UV–C LED technology and its application to water disinfection processes by establishing a comprehensive understanding of the light source, light output, and investigating the potential synergistic effect between multiple wavelengths.

➢ Objectives

To achieve this, the work was divided into several parts in an attempt to solve the challenges discussed above. The work has been carried out in the framework of REWATERGY project (H2020-MSCA-ITN-2018, Project No.: 812574).

- To select LED sources centered at different wavelengths from the market and characterize the sources using multiple techniques such as rollover, uniformity, and current behavior. This will help build an understanding of light emission and the device controlling the emission.

- To validate the measurement of UV sources by comparing multiple sensors measuring in the same region and investigating parameters like the angle of acceptance and ambient conditions that may affect the obtained measurements.
- To model UV radiation using the ray tracing technique, initially in an air medium, and compare it with other techniques used in the literature. Furthermore, a model will be built to simulate radiation transport in a water medium in a complex system of four wavelengths.
- Apply the built UV sources to disinfect buffered water spiked with the model bacterium *Escherichia coli* (*E. coli*), in order to determine their effectiveness in the disinfection process and investigate the potential synergistic effect of using multiple wavelengths.
- To evaluate the disinfection efficiency of the UV sources on a real wastewater matrix obtained from the secondary effluent of a wastewater treatment plant (WWTP), in order to assess the practical utility of the technology and compare its performance to the results obtained from the previous objectives.

➢ Methodology and Results

The UV LED selection process involved listing different products and creating a decision criterion based on LED size, emission profile, light output efficiency, and device operation. Four LEDs centered in the 260 – 320 nm region (UV–C, UV–B) were selected from three manufacturers (Klaran- Crystal IS, Luminus, and EpiGap) and built onto a COBRA FX–1 device by ProPhotonix IRL. The devices were then characterized to evaluate optimum input current, spectral output, uniformity, and lifetime (minimum of 5000 h). The optimum input current was determined as the point of non–linearity of the device power output with increase in current supplied. This was found to be 300, 120, 450, and 420 mA for 265, 275, 285, and 310 nm LED devices, respectively and was set as the programmed drive current of the devices. The light output was linear with the increase in input current for all devices tested. Further spectral tests found that there was a shift in the peak wavelength of the devices with an increase in current supplied. The devices were then tested for uniformity, and it was found that the side chains of the device emitted higher intensity due to the relative position of the sensor to the light source. The characterization of the source output with increase in distance between the source and sensor, also called working distance, showed that the intensity loss followed an exponential trend, while dose loss was more gradual (Fig. 1). Finally, the overall comparison results showed that the 285 nm LEDs emitted the highest

light intensity but were not reliable due to a 15% intensity loss after 3000 h and observed spectral shifts at high currents.

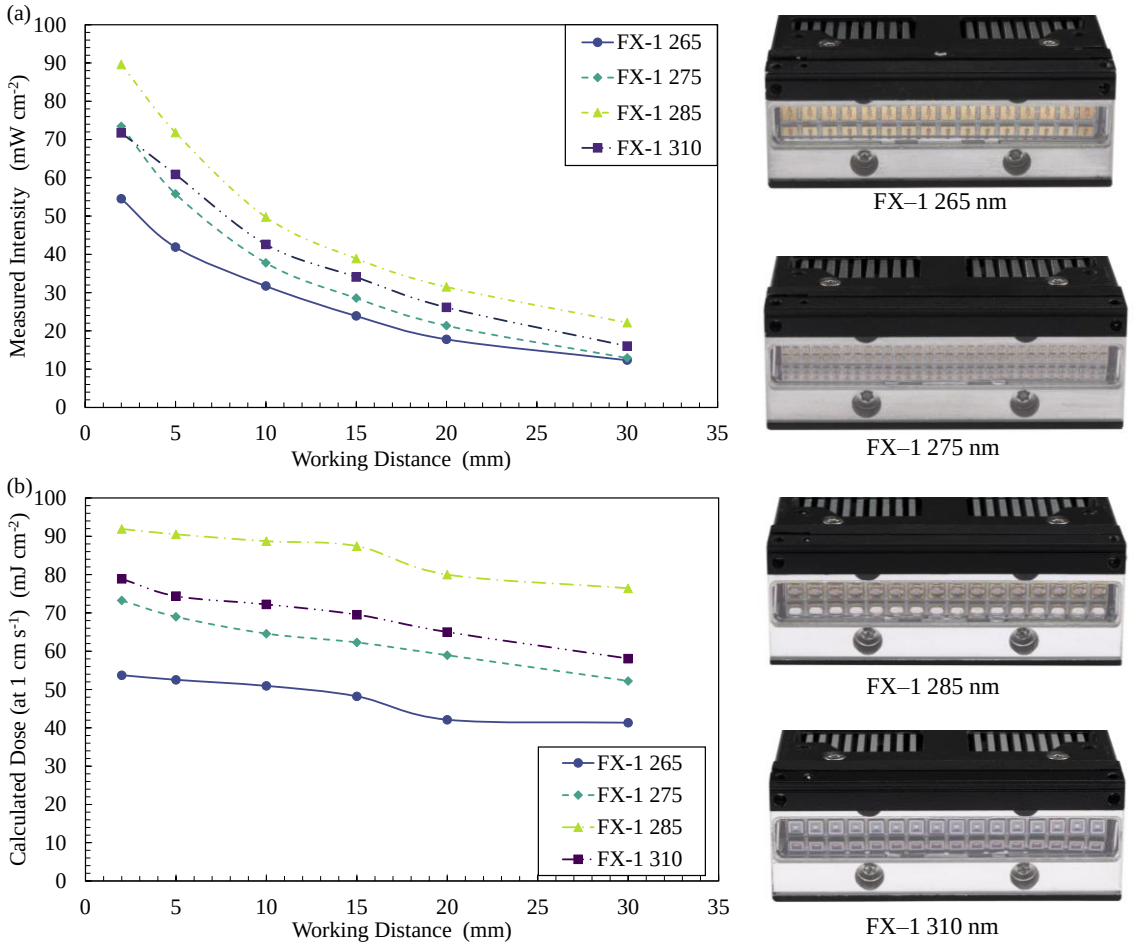

Figure 1: (L) – (a) Measured intensity *vs* working distance and (b) Calculated dose *vs* working distance. (R) COBRA Clean FX–1.

To validate the measurements conducted in the earlier objective, the ILT RAA4 sensor and ILT 950UV spectroradiometer were compared to 5 UV light sensors, from different manufacturers (Ophir, Loctite, ILT, Thorlabs), operating in the same region of measurements. The effect of 4 parameters i.e., angle of acceptance, ambient light, integration time, and temperature were evaluated for each of the systems studied. To do this, three UV LEDs (centered at 265, 310, and 395 nm) were mounted onto a heatsink and used to compare the performance of UV light measurement sensors. It was found that there existed significant differences between them. The angular responses of the sensors were evaluated and correlated to an ideal cosine response and the sensor's mechanical designs (Fig. 2). It was further seen that certain sensors (ILT W optic and Thorlabs S120VC) showed different angle of acceptances depending on the wavelength studied. This could be due to

possible Brillouin scattering occurring in the set–up. The study further highlighted the effect of ambient light on readings by providing guide figures on ambient light present in a lab environment and observed that even sensors with the same wavelength range of measurement can have different output readings for the same light source. For the ILT–based sensors, the effect of integration time on measurements was studied and it was found that low integration times resulted in loss of data while high integration times resulted in sensor saturation. Hence it was seen that choosing the right integration time was important to obtain reliable data for further use. It was also concluded that measurement results are application–specific and need to be evaluated on a case–by–case basis. For extended light sources (where the light source is larger than the measuring sensor), the angle of acceptance of the detectors and distance, between source and sensor, should be considered to ensure accurate data capture. The study also emphasized the importance of correctly interpreting the recorded data and ensuring the compatibility of the sensor to the specific application.

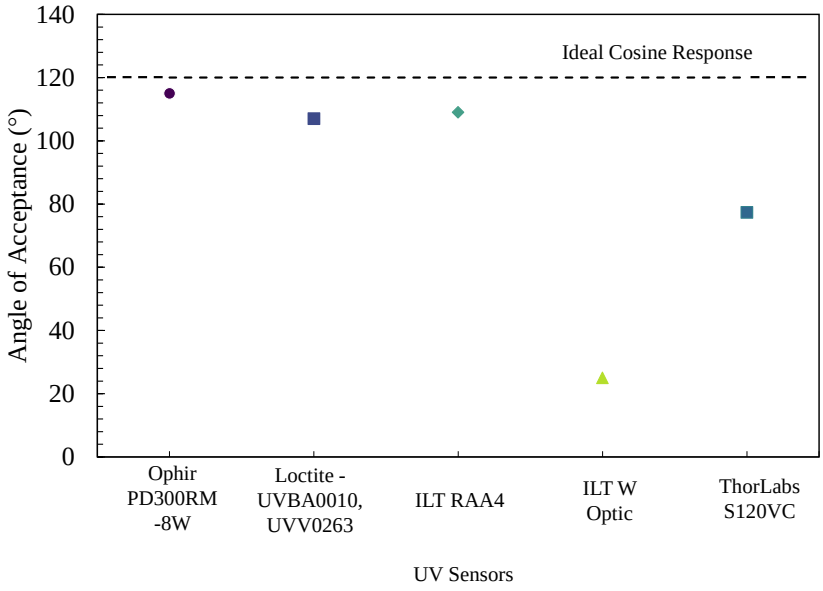

Figure 2: Angle of acceptances of multiple UV sensors compared to an ideal cosine response.

To answer the third objective in this thesis, first, an investigation of different techniques used in the literature was conducted. The study found that Discrete Ordinate Method (DOM) was commonly used in radiation modeling and ferrioxalate actinometry for calculating the cumulative radiation received. This thesis used an optical ray tracing method for predicting irradiation within a germicidal system in a water medium and compared the results with radiometry, DOM, and chemical actinometry. The method was found to be in

close agreement (± 6%) with the other techniques, indicating that it can overcome challenges in measuring and simulating irradiation in water. The study also quantified the effect of quartz material on irradiation and found that the loss of light intensity was different at each wavelength studied. For instance, a loss of 11 % was observed for FX–1 265 nm source, whereas only 8% loss was found for the FX–1 310 nm source. Further, a model was built for water media and validated using results from actinometry. Both the methods were in close agreement and hence the method was applied to a 4–wavelength complex system to use it in providing a better understanding of the system design and individual wavelength contributions. Although the predictions of radiant intensities were higher than experimental and other simulation methods, the differences were within the error range. The study concluded that the method provides valuable insights into light propagation (Fig. 3) and optimization of light irradiation in water–based systems.

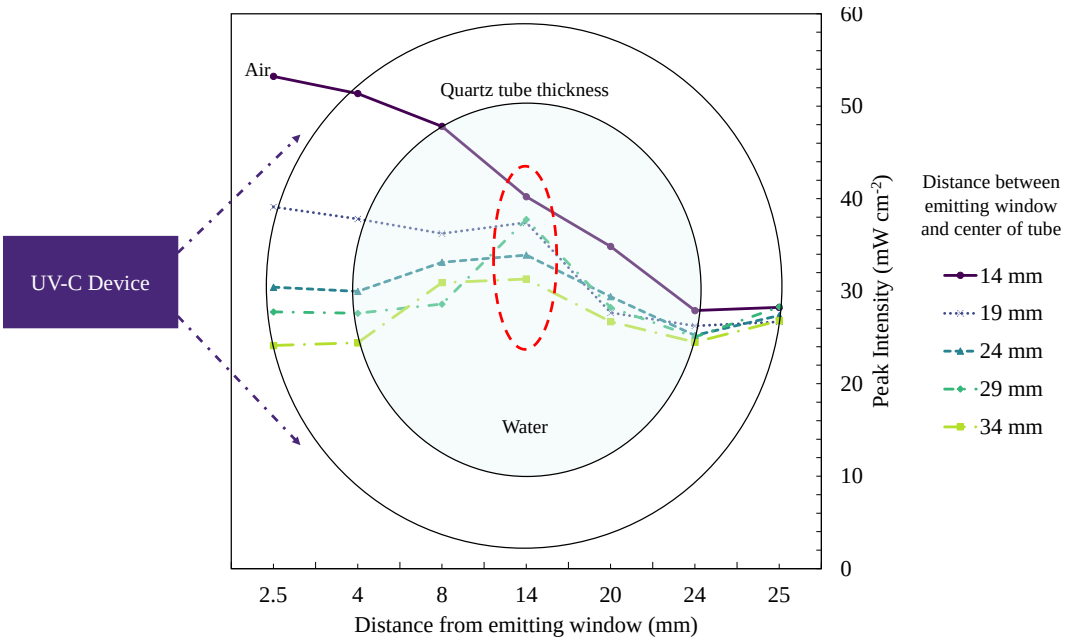

Figure 3: Light propagation in a germicidal system at multiple working distances away from the center of the tube.

Using a comprehensive understanding of the light sources from the earlier objectives, they were applied to the inactivation of *E. coli* K12 to evaluate their disinfection efficiencies. The model bacterium was spiked to buffered water and circulated through the system in a single pass type set–up. It was seen that at ~25 mJ cm^{-2} UV dose, the 265 nm source was the most effective (2.8 ± 0.2 log units of reduction) compared to the other wavelengths used while the 310 nm source was the least effective (0.0004 ± 0.0002 log units of reduction). Further, different combinations of wavelengths were tested (Fig. 4), and it was seen that dual

wavelength combinations of 310 nm with 265 nm or 275 nm devices, sequentially irradiated, presented a significant synergistic effect at both radiant intensities tested (maximum possible intensity and half of the maximum). This was confirmed by a robust statistical analysis (*t*–Student and Codified ANOVA) and the observed synergistic effect was correlated to the emission spectra of the respective UV LEDs to elucidate the possible mechanisms of inactivation. The study also calculated the electrical energy per order of inactivation and found that the combination of 265 nm and 275 nm sources presented an energy efficient process. All four possible combinations of 3 wavelengths (sequential and simultaneous irradiation) showed significant synergistic effect and their electrical energy consumption per unit order of removal exhibited the lowest rates of 0.40 ± 0.02 kWh m^{-3} and 0.30 ± 0.01 kWh m^{-3}, at 50% and 100% intensity respectively, in comparison with other combinations that yielded synergy. Combinations of 310 nm with 265 nm device resulted in an electrical energy consumption of 0.47 ± 0.08 kWh m^{-3} and 0.41 ± 0.06 kWh m^{-3}, at 50% and 100% intensity, respectively, while combinations of 310 nm with 275 nm device resulted in an electrical energy consumption of 0.66 ± 0.07 kWh m^{-3} and 0.46 ± 0.06 kWh m^{-3}, at 50% and 100% intensity, respectively. The results provided a perspective on the application of designed LED sources in a buffered water matrix and provided the inputs to be able to select only some combinations for the next objective.

To assess the efficiency of these devices in real wastewater matrixes, the UV sources were irradiated to a secondary effluent obtained from the wastewater treatment plant (WWTP) at URJC facilities. The wastewater matrix was spiked with wild *E. coli*. Similar to the findings in buffered water, at ~25 mJ cm^{-2} UV dose, the 265 nm source was the most effective (2.2 ± 0.2 log units of reduction) followed by the 275 nm source (1.3 ± 0.1 log units of reduction) and the 310 nm source (0.0002 ± 7.03×10^{-5} log units of reduction) (Fig. 4). The same combinations resulted in synergistic effect; however the damage mechanism could be due to multiple reasons. The electrical energy consumption per unit order in wastewater was seen to be higher than the buffered water experiments as the microorganism might be much more UV resistant compared to the model bacterium used in the earlier study and the presence of other competing aerobic bacteria and species in wastewater, such as ions meant that more photons were required to achieve the same level of inactivation. This was evident when the 265 nm source was compared between the two matrixes. At 100% radiant intensity, the electrical energy consumption was seen to be 0.40 ± 0.02 kWh m^{-3} in wastewater whereas it was 0.30 ± 0.03 kWh m^{-3} in the buffered water matrix. While the

overall results were similar, in a wastewater matrix – further investigation is necessary considering if chemical composition of wastewater (ions, turbidity, organic matter, suspended solids) could affect or enhance the synergistic effect obtained.

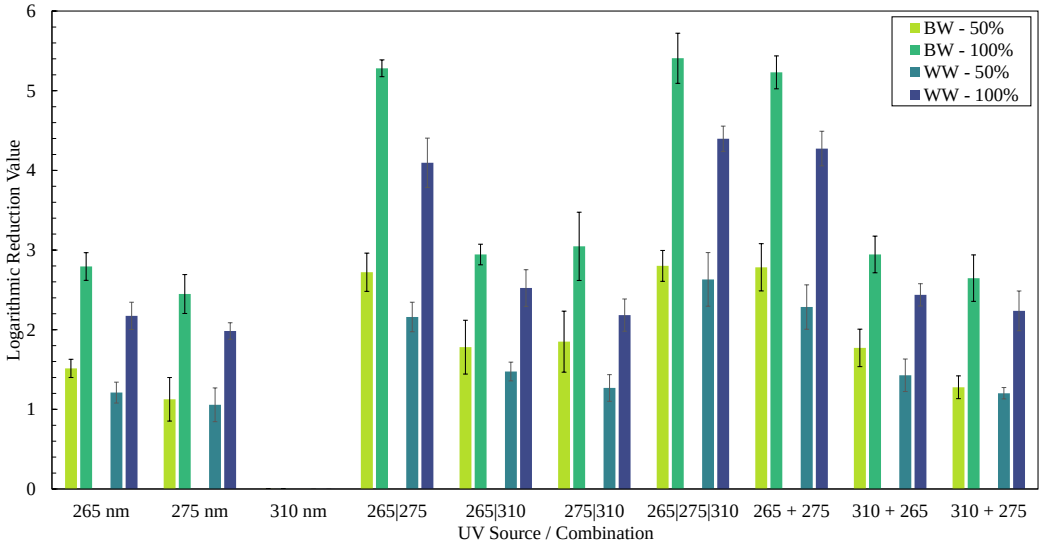

Figure 4: Logarithmic reduction values (LRV) for UV sources and combinations in two matrixes. (Legend – BW is Buffered Water and WW is Wastewater)

➢ Conclusions

It is possible that as our knowledge of UV light expands, we will find more uses for this adaptable type of radiation. The results of this thesis can be applied to the design and execution of effective UV LED disinfection systems. The use of multiple wavelengths in UV disinfection processes was shown to have a synergistic effect, that results in improved effectiveness. This was because different wavelengths have varying levels of effectiveness in disinfection, with some being more effective against certain microorganisms than others or certain components within the microorganism being more susceptible to one wavelength. By combining multiple wavelengths, a broader region within the microorganisms could be targeted and eliminated, leading to more thorough disinfection. Additionally, synergistic effects can result in a lower overall dose requirement for disinfection, which can reduce energy consumption and operating costs. Furthermore, the use of multiple wavelengths can reduce the risk of microorganisms developing resistance to a single wavelength over time, ensuring continued effectiveness of the disinfection process. Overall, this work highlights the need for research into the potential synergistic effects between several wavelengths by careful source selection, adding to the expanding body of knowledge on UV–C LED technology and its potential for disinfection applications.

Resumen

➢ Antecedentes

El acceso a agua potable es un derecho humano esencial, reconocido explícitamente por la Asamblea General de las Naciones Unidas a través de la Resolución 64/292 en 2010. La adopción de medidas para lograr y mantener agua de calidad es una condición indispensable tanto para garantizar la salud pública como para impulsar el desarrollo socioeconómico. A pesar del progreso tecnológico, todavía en el siglo XXI, el 29% de la población mundial (2.100 millones de personas) carece de acceso a agua potable en su vivienda. Los servicios básicos de agua segura en todo el mundo se enfrentan a múltiples desafíos como la escasez de agua, la contaminación de los ecosistemas de agua dulce y la inexistencia de infraestructura apropiada, por lo que requieren el esfuerzo conjunto de gobiernos y organizaciones internacionales. En cuanto a la escasez de agua, se espera que el cambio climático empeore la situación en muchas partes del mundo (se estima que, en 2050, los recursos hídricos de algunas regiones experimentarán una reducción de hasta el 50%). Por ende, para conseguir una cobertura universal de agua potable es necesario establecer estrategias orientadas a conservar el medio ambiente, implementar métodos efectivos de tratamiento del agua e invertir en infraestructura de suministro. Tradicionalmente, se han empleado métodos para tratar el agua como la cloración, sedimentación, filtración y coagulación. Desde principios de la década de 1950, las fuentes de luz ultravioleta (UV) han sido utilizadas por organismos locales y nacionales en la etapa final de desinfección del agua, con el objetivo de eliminar microorganismos patógenos. Esto se debe a que la radiación UV reduce el crecimiento de los microorganismos al inhibir su reproducción cuando es absorbida por el ADN/RNA del microorganismo. La luz solar es una fuente natural de radiación UV. Sin embargo, no proporciona la suficiente para llevar a cabo una desinfección rápida y efectiva. Por dicho motivo, se ha investigado el uso de diferentes fuentes artificiales de radiación UV como las lámparas de mercurio, los diodos emisores de luz (LED, siglas del inglés *Light Emitting Diodes*) o las lámparas de plasma para generar la longitud de onda de irradiación UV deseada. Cabe destacar que, en países con escasos recursos económicos, la luz solar se utiliza en la desinfección de agua mediante una técnica conocida como SODIS (del inglés *Solar Disinfection*). Desde que el primer LED UV salió al mercado en 2003, esta tecnología se encuentra en auge con interesantes aplicaciones en campos como la catálisis, la desinfección del aire y superficies, etc. No obstante, todavía existen grandes desafíos asociados a dicha tecnología y al proceso de

desinfección que necesitan ser investigados y resueltos. Tanto el tratamiento del agua potable como de las aguas residuales, a partir de fuentes UV artificiales, puede ser energéticamente costoso y requiere ser optimizado para minimizar el consumo de energía. Si bien cabe esperar que un incremento en la dosis de radiación recibida por el agua se traduzca en una tasa de desinfección rápida y alta, es necesario alcanzar un compromiso razonable entre la eficacia y el coste del tratamiento y la eficiencia energética. La eficacia de un proceso de desinfección UV viene determinada principalmente por la fuente de iluminación utilizada (por ejemplo, lámpara de mercurio o LED UV) y por la longitud de onda de emisión. Puesto que la tecnología LED UV es muy reciente, todavía, su eficiencia de salida de luz es baja (la eficiencia máxima reportada hasta ahora es del 13 %). Por ello, la obtención de la dosis de radiación UV precisa es un gran reto al que se enfrentan los investigadores y las empresas. Además, debido a su baja eficiencia de salida, es necesario evaluar la vida útil de estos dispositivos y comprender los parámetros críticos que afectan a la degradación de los LED utilizados. Por otro lado, se ha observado en la literatura que la inactivación de los microorganismos es sensible a la longitud de onda a la que son irradiados, por lo que una correcta selección de esta es crucial para un proceso de desinfección eficaz. Atendiendo a todo lo anterior, se concluye la importancia de conocer plenamente la fuente de luz antes de su aplicación en un sistema de desinfección de agua. Uno de los desafíos más significativos al que se enfrentan los investigadores en el campo de las fuentes de iluminación UV es la obtención de medidas fiables y precisas de la cantidad de luz irradiada, ya que afecta directamente al análisis de la eficacia del proceso. La toma de estas medidas requiere instrumentación especializada, la cual podría no estar fácilmente disponible, y la comprensión de diversos parámetros que podrían afectar a las mismas directa o indirectamente. Alternativamente, estas medidas pueden simularse con la ayuda de programas informáticos. Sin embargo, incluso en este campo, existen desafíos complejos como la programación de la naturaleza policromática de la radiación emitida y del medio acuático por el cual se transmite la radiación. Además, existe un vacío de conocimiento en la modelización de fuentes de iluminación en entornos complejos donde se dan múltiples interacciones. En este contexto, el objetivo principal de la presente Tesis Doctoral es la evaluación de la tecnología LED UV–C para su aplicación en procesos de desinfección de agua mediante un estudio en profundidad de las fuentes de iluminación LED UV–C y de la radiación emitida, a la vez que se investiga el posible efecto sinérgico entre múltiples longitudes de onda.

➢ Objetivos

Para su consecución, este se ha desglosado en las siguientes partes con la intención de dilucidar los retos mencionados anteriormente. El trabajo se ha llevado a cabo en el marco del proyecto REWATERGY (H2020-MSCA-ITN-2018, Proyecto nº: 812574).

- Selección y caracterización de fuentes de iluminación LED comerciales centradas en diferentes longitudes de onda. Para la caracterización, se han utilizado técnicas como la curva de voltaje, la uniformidad y el comportamiento de la corriente. Dicho estudio ayudará a comprender la emisión de luz y el dispositivo que controla la emisión.
- Validación de un método de medida de las fuentes UV mediante la comparación de diferentes sensores que miden en la misma región y la investigación de parámetros como el ángulo de aceptación y las condiciones ambientales que pueden afectar a la obtención de las medidas obtenidas.
- Modelado de la radiación UV utilizando la técnica de trazado de rayos, inicialmente en aire, y su comparación con otras técnicas comúnmente utilizadas en la literatura. Además, se ha construido un modelo para simular el transporte de radiación en agua en un sistema complejo de cuatro longitudes de onda.
- Utilización de las fuentes UV seleccionadas en la desinfección de agua tamponada con la bacteria modelo *Escherichia coli (E. coli)*, con el fin de determinar su eficacia en el proceso de desinfección e investigar el posible efecto sinérgico del uso de múltiples longitudes de onda.
- Evaluación de la eficiencia de desinfección de las fuentes UV en una matriz de aguas residuales reales obtenida del efluente secundario de una planta de depuración de aguas residuales, con el fin de evaluar la utilidad práctica de la tecnología y comparar su rendimiento con los resultados obtenidos en los objetivos anteriores.

➢ Metodología y Resultados

El proceso de selección de los LED UV se basó en el tamaño, el perfil de emisión, la eficiencia de salida de luz y el funcionamiento del dispositivo. Siguiendo el criterio establecido, se eligieron cuatro modelos de LED, centrados en la región del ultravioleta correspondiente a 260 – 320 nm (UV–C, UV–B), de tres fabricantes (Klaran, Luminus y EpiGap) y se dispusieron en un dispositivo COBRA FX–1 (ProPhotonix IRL). Para cada uno de ellos, se evaluó la corriente de entrada óptima, el espectro de emisión, la uniformidad en la radiación emitida y la vida útil (mínimo de 5000 h). Para todos los dispositivos LED estudiados, la potencia de salida aumentó linealmente con la corriente suministrada a los

mismos hasta alcanzar un valor de corriente máxima para la cual la potencia de salida se mantuvo constante en su valor máximo. Por lo tanto, se decidió fijar dicha corriente máxima como la óptima de entrada para el accionamiento de los dispositivos. Los dispositivos LED evaluados, centrados en 265, 275, 285 y 310 nm, presentaron corrientes máximas de 300, 120, 450 y 420 mA, respectivamente. Paralelamente, el análisis de los espectros de emisión de los LED reveló un desplazamiento de la longitud de onda de pico con el aumento de la corriente suministrada. La evaluación de la uniformidad en la emisión reveló que los dispositivos emitían una mayor intensidad de radiación en las partes exteriores debido a la posición relativa del sensor con respecto a la fuente de luz. Por último, se estudió la relación entre la intensidad de radiación emitida por los LED y el aumento de la distancia entre la fuente de iluminación y el sensor (definida como distancia de trabajo). Los resultados demostraron que la pérdida de intensidad siguió una tendencia exponencial, mientras que la pérdida de dosis fue más gradual (Fig. 1). Tras un análisis comparativo de todos los resultados generados, se concluye que los LED centrados en 285 nm emitieron la mayor intensidad luminosa. Sin embargo, no eran fiables debido a que experimentaron una pérdida de intensidad del 15% tras 3000 h de funcionamiento y un desplazamiento de la longitud de onda de emisión con el incremento de la corriente de alimentación.

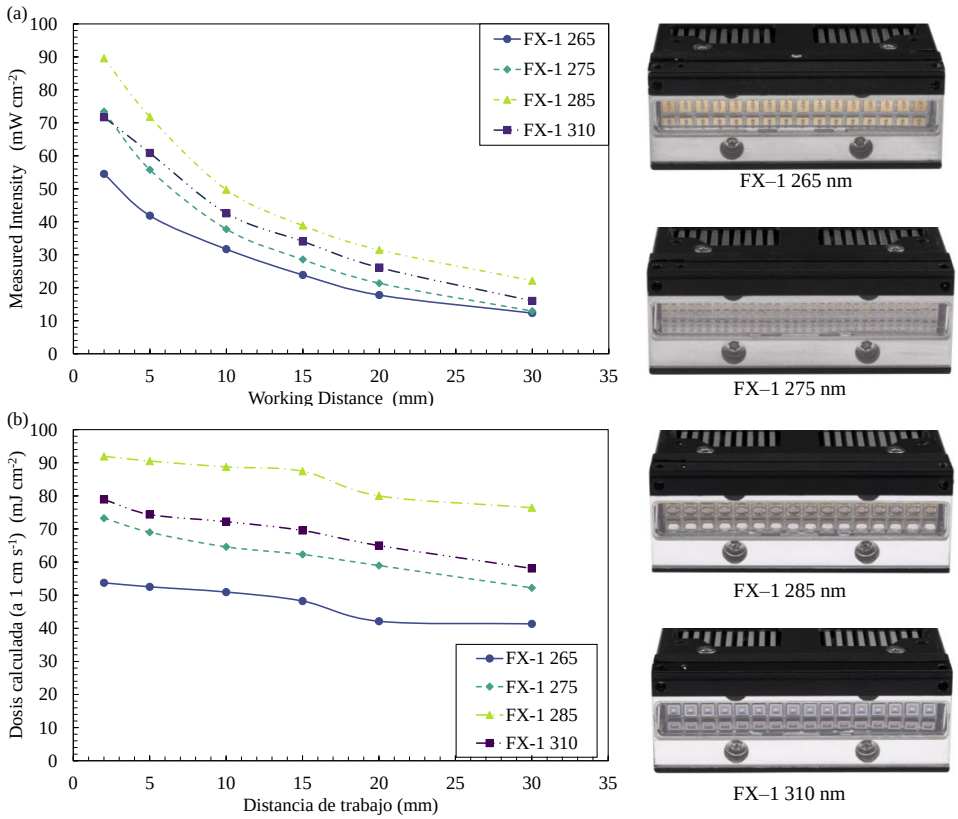

Figura 1: (Izq.) (a) Intensidad de radiación medida en función de la distancia de trabajo y (b) Dosis calculada en función de la distancia de trabajo. (D) COBRA Clean FX–1.

Con el fin de validar las medidas realizadas, tanto el sensor ILT RAA4 como el radiómetro ILT 950UV se compararon con cinco sensores de luz UV que operan en la misma región de medición de diferentes fabricantes (Ophir, Loctite, ILT, ThorLabs). Para cada uno de ellos, se evaluaron los efectos de cuatro parámetros: ángulo de aceptación, luz ambiental, tiempo de integración y temperatura. Con el fin de comparar el rendimiento de los sensores de luz, tres LED UV (centrados en 265, 310 y 395 nm) se montaron en un disipador de calor y se encontró que existían diferencias significativas entre ellos. Se evaluaron las respuestas angulares de los sensores y se correlacionaron con una respuesta coseno ideal y los diseños mecánicos de los sensores (Fig. 2). También se observó que ciertos sensores (ILT W óptico y ThorLabs S120VC) mostraron diferentes ángulos de aceptación en función de la longitud de onda estudiada. Esto podría deberse a la posible dispersión de Brillouin producida en el montaje. El estudio también manifestó el efecto de la luz ambiental en las lecturas, proporcionando cifras orientativas sobre la luz ambiental presente en un entorno de laboratorio, y observó que incluso los sensores con el mismo rango de longitud de onda de medición proporcionan lecturas de salida diferentes para una misma fuente de luz. Para los sensores ILT, se estudió el efecto del tiempo de integración en las mediciones y se observó que bajos tiempos de integración provocaban una pérdida de datos, mientras que altos dan lugar a una saturación del sensor. Por lo tanto, una adecuada elección del tiempo de integración es importante para una obtención de datos fiables para un uso posterior de los mismos. Asimismo, se concluyó que los resultados de las mediciones son específicos para cada aplicación y que deben evaluarse caso por caso. En el caso de las fuentes de luz extendidas (cuando la fuente de luz es mayor que el sensor de medición), hay que tener en cuenta el ángulo de aceptación de los detectores y la distancia de trabajo para garantizar una captura de datos precisa. El estudio también destacó la importancia de interpretar correctamente los datos registrados y garantizar la compatibilidad del sensor con la aplicación específica.

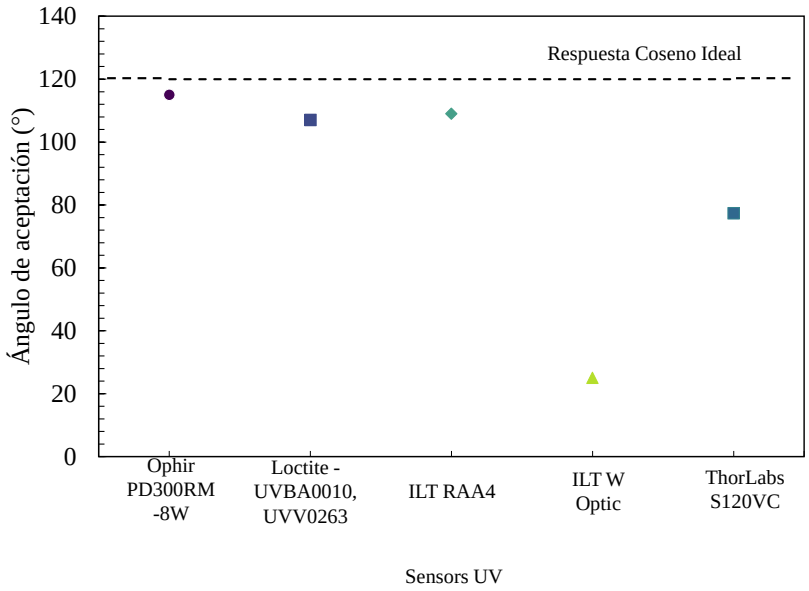

Figura 2: Ángulo de aceptación de múltiples sensores UV comparados con una respuesta de coseno ideal.

Para responder al tercer objetivo de esta tesis, en primer lugar, se llevó a cabo una revisión de las técnicas más comúnmente utilizadas en la literatura. Este estudio reveló que el Método de Ordenadas Discretas (DOM, siglas del inglés *Discrete Ordinate Method*) es ampliamente empleado en la modelización de la radiación y la actinometría de ferri oxalato en el cálculo de la radiación acumulada recibida. En esta tesis, se utilizó un método de trazado de rayos ópticos para predecir la irradiación en un sistema germicida en medio acuoso y los resultados se compararon con la radiometría, el DOM y la actinometría. Se observó que el método de trazado de rayos proporcionó resultados dentro del rango de error (± 6%) de las otras técnicas frente a las que se comparó, lo cual indica que puede superar los desafíos existentes en la medición y simulación de la irradiación en agua. También se cuantificó el efecto del material de cuarzo en la irradiación y se observó que la pérdida de intensidad luminosa fue diferente para cada longitud de onda estudiada. Por ejemplo, mientras que la fuente FX–1 de 265 nm experimentó una pérdida del 11 %, la fuente FX–1 de 310 nm tan solo una del 8%. Además, se construyó un modelo para un medio acuoso y se validó utilizando los resultados de la actinometría. Ambos métodos presentaron resultados similares, por lo tanto, el método de trazado de rayos se aplicó a un sistema complejo de 4 longitudes de onda para proporcionar una mejor comprensión del diseño del sistema y de las contribuciones individuales de cada longitud de onda. Aunque las intensidades predichas fueron superiores a las observadas con los métodos experimentales y de simulación, las diferencias se encontraban dentro del rango de error.

El estudio concluyó que el método proporciona valiosos conocimientos sobre la propagación de la luz (Fig. 3) y la optimización de la irradiación luminosa en sistemas basados en agua.

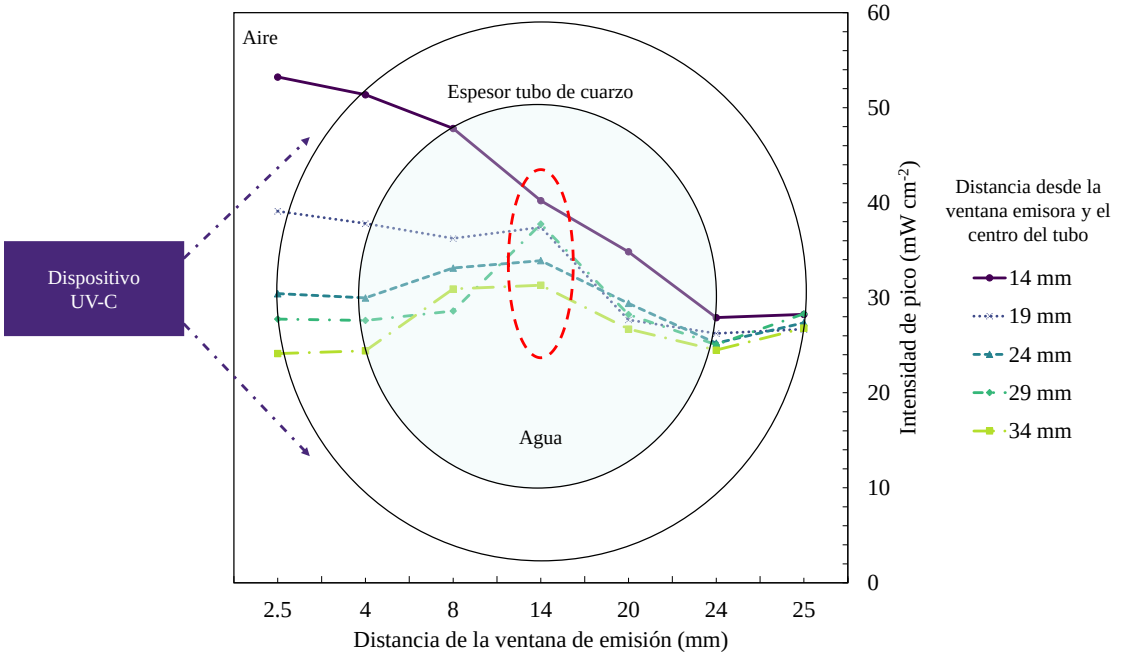

Figura 3: Propagación de la luz en un sistema germicida a múltiples distancias de trabajo desde el centro.

Una vez que se adquirió un conocimiento completo de las fuentes de luz, estas se emplearon para lograr la inactivación de *E. coli* K12 y se evaluó su eficiencia de desinfección. La bacteria modelo fue inoculada al agua tamponada y circulada a través del sistema en una configuración de paso único. Se observó que con una dosis de UV de ~25 mJ cm^{-2}, la fuente de 265 nm fue la más efectiva (2,793 ± 0,173 unidades logarítmicas reducidas) en comparación con las demás longitudes de onda utilizadas, mientras que la fuente de 310 nm fue la menos efectiva (0,0004 ± 0,000145 unidades logarítmicas reducidas). Además, se probaron diferentes combinaciones de longitudes de onda (Fig. 4) y se observó que las combinaciones de dos longitudes de onda, 310 nm con dispositivos de 265 nm o 275 nm, irradiados secuencialmente, presentaron un efecto sinérgico significativo en ambas intensidades radiantes evaluadas (máxima intensidad posible y la mitad de la máxima). Esto fue confirmado por un análisis estadístico robusto (*t*–Student y ANOVA codificado) y el efecto sinérgico observado se correlacionó con los espectros de emisión de los respectivos LED UV para dilucidar los posibles mecanismos de inactivación. El estudio también calculó la energía eléctrica por orden de inactivación y encontró que la combinación de fuentes de 265 nm y 275 nm presentaba un proceso eficiente en términos energéticos. Las cuatro

posibles combinaciones de tres longitudes de onda (irradiación secuencial y simultánea) mostraron un efecto sinérgico significativo y su consumo de energía eléctrica por orden de eliminación exhibió las tasas más bajas de 0,368 ± 0,023 kWh m^{-3} y 0,293 ± 0,014 kWh m^{-3}, a 50% y 100% de intensidad, respectivamente, en comparación con otras combinaciones que produjeron sinergia. Las combinaciones de 310 nm con un dispositivo de 265 nm dieron como resultado un consumo de energía eléctrica de 0,469 ± 0,083 kWh m^{-3} y 0,404 ± 0,054 kWh m^{-3}, al 50% y al 100% de intensidad, respectivamente, mientras que las combinaciones de 310 nm con un dispositivo de 275 nm dieron como resultado un consumo de energía eléctrica de 0,662 ± 0,077 kWh m^{-3} y 0,460 ± 0,060 kWh m^{-3}, al 50% y al 100% de intensidad, respectivamente. Los resultados ofrecieron una perspectiva sobre la aplicación de fuentes LED diseñadas en una matriz de agua tamponada y brindaron los elementos necesarios para poder seleccionar únicamente algunas combinaciones para el próximo objetivo.

Para evaluar la eficiencia de estos dispositivos en matrices reales de aguas residuales, las fuentes de UV se irradiaron en un efluente secundario obtenido de la planta de tratamiento de aguas residuales en las instalaciones de la URJC. Al igual que en los hallazgos en agua tamponada, a una dosis de UV de ~25 mJ cm^{-2}, la fuente de 265 nm fue la más efectiva (2,174 ± 0,171 unidades logarítmicas reducidas), seguida por la fuente de 275 nm (1,342 ± 0,103 unidades logarítmicas reducidas) y la fuente de 310 nm (0,00022 ± 7,03 × 10^{-5} unidades logarítmicas reducidas) (Fig. 4). Las mismas combinaciones resultaron en un efecto sinérgico, sin embargo, el mecanismo de daño podría deberse a múltiples razones. El consumo de energía eléctrica por unidad de orden en aguas residuales se vio más alto que en los experimentos de agua tamponada, ya que el microorganismo podría ser más resistente a la UV en comparación con la bacteria modelo utilizada en el estudio anterior y la presencia de otras bacterias aerobias competidoras y presencia de compuestos en el agua como iones significaba que se requerían más fotones para lograr el mismo nivel de inactivación. Esto fue evidente cuando se comparó la fuente de 265 nm entre las dos matrices. A una intensidad radiante del 100%, el consumo de energía eléctrica se vio de 0,388 ± 0,019 kWh m^{-3} en aguas residuales, mientras que en la matriz de agua tamponada fue de 0,301 ± 0,025 kWh m^{-3}. Si bien los resultados generales fueron similares, en una matriz de aguas residuales, se requiere una investigación adicional para considerar si la composición química de las aguas residuales (iones, turbidez, materia orgánica, sólidos suspendidos) podría afectar o mejorar el efecto sinérgico obtenido.

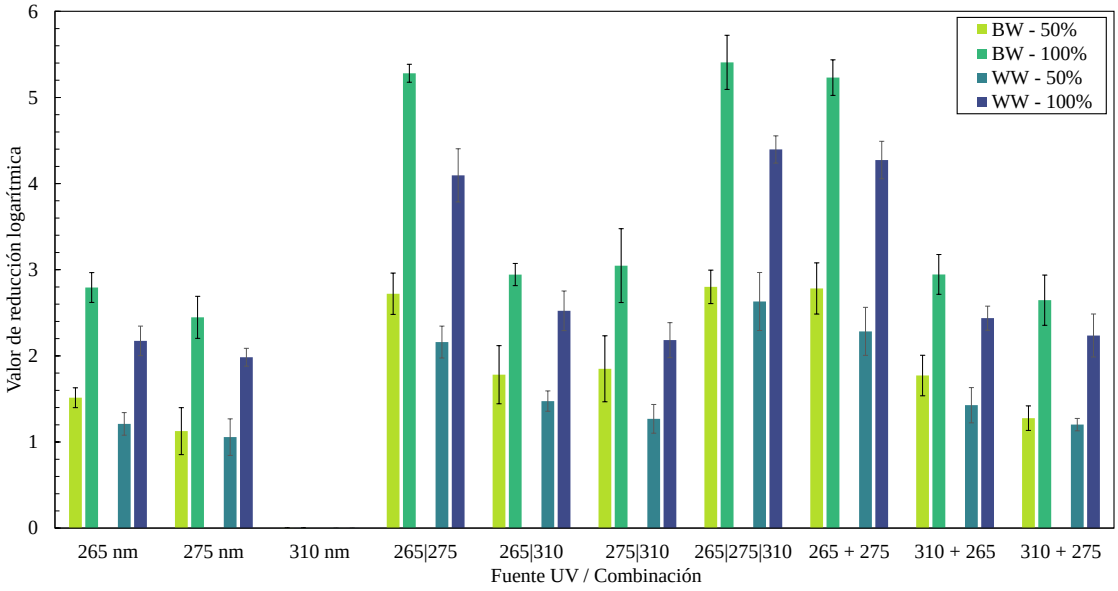

Figura 4: Valores de reducción logarítmica para fuentes y combinaciones de UV en dos matrices. (Leyenda: BW es agua tamponada y WW es aguas residuales).

➢ Conclusiones

Es posible que a medida que nuestro conocimiento sobre la luz UV aumente, aparezcan más usos para este tipo de radiación tan versátil. Los resultados de esta tesis pueden aplicarse al diseño y ejecución de sistemas efectivos de desinfección con LED UV en el agua. Se demostró que el uso de múltiples longitudes de onda en los procesos de desinfección UV tiene un efecto sinérgico que mejora la efectividad. Esto se debe a que diferentes longitudes de onda tienen niveles variables de efectividad en la desinfección, siendo algunas más efectivas frente a ciertos microorganismos que otras, o ciertos componentes dentro del microorganismo siendo más susceptibles a una longitud de onda específica. Al combinar múltiples longitudes de onda, se puede eliminar un mayor rango de tipos de microorganismos patógenos activando diferentes mecanismos de inactivación, lo que lleva a una desinfección más completa. Además, los efectos sinérgicos pueden resultar en un requisito de dosis general más bajo para la desinfección, lo que puede reducir el consumo de energía y los costes operativos. Además, el uso de múltiples longitudes de onda puede reducir el riesgo de que los microorganismos desarrollen resistencia a una sola longitud de onda con el tiempo, asegurando la efectividad continua del proceso de desinfección. En general, este trabajo destaca la necesidad de investigar los posibles efectos sinérgicos entre varias longitudes de onda mediante una cuidadosa selección de la fuente, lo que contribuye al aumento de conocimientos sobre la tecnología LED UV–C y su potencial para aplicaciones de desinfección en agua.

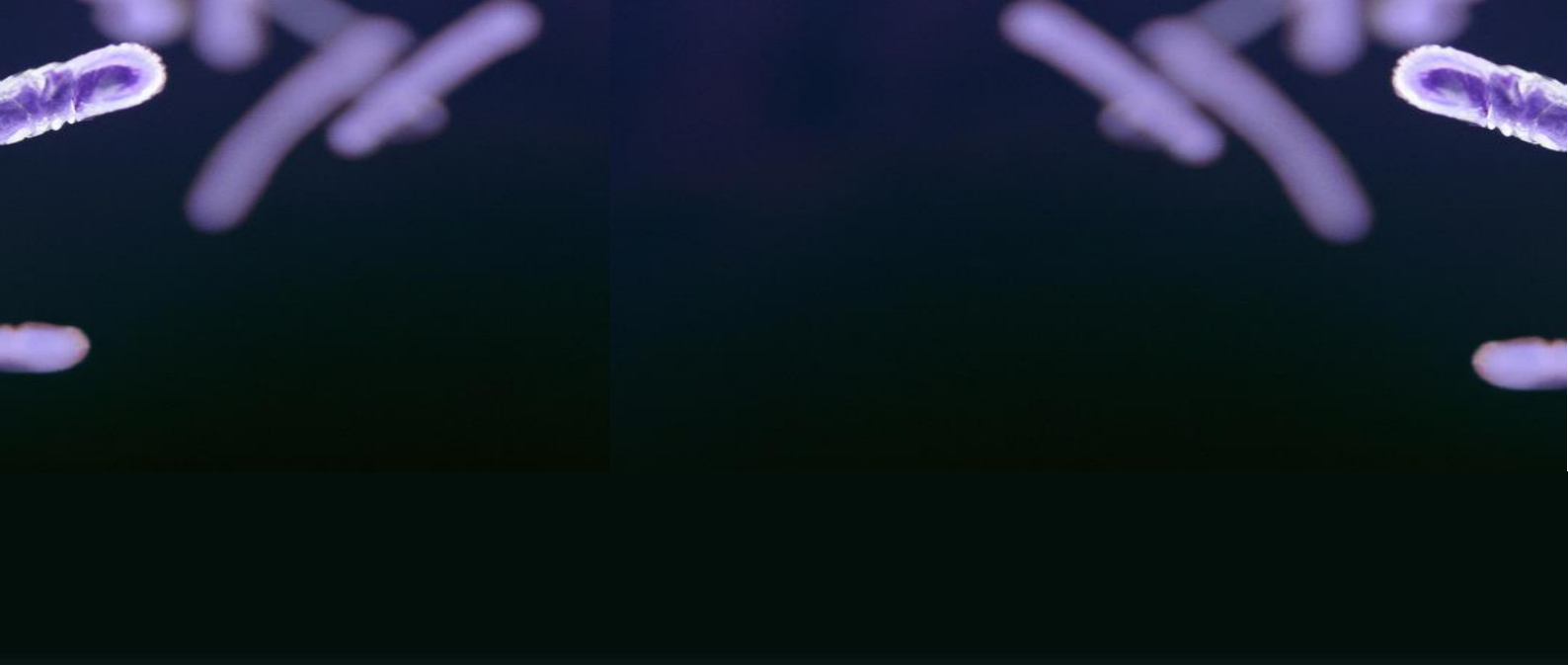

CHAPTER 1

INTRODUCTION

1.1. Light Spectrum

The history of light and its usage spans thousands of years and is closely tied to the development of human civilization [1]. One of the earliest uses of light was by ancient civilizations, who used fire for warmth and light at night. The Egyptians and Greeks were also known to use mirrors to reflect sunlight and start fires [2]. They also were known to be one of the first humans to use sunlight for drinking water and as quoted beautifully by Mcguigan et al. (2012) "placed drinking water outside in open trays to be "blessed" by the sun" [3]. Fascinatingly, the earliest known contribution to the concept of light and light spectrum comes from the Greeks. They noticed that as light passes through a glass prism, it separated into different colors – creating what we know today as a "rainbow" (Fig. 1.1, [4]). However, they had little to no understanding of what caused this phenomenon.

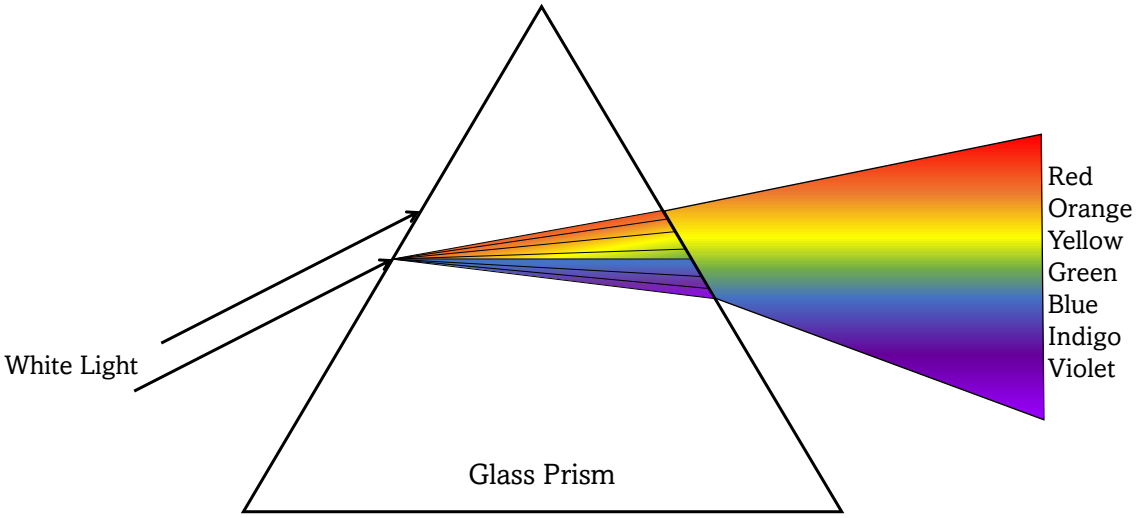

Figure 1.1: White light splitting as it passes through a prism (Source: [4]).

As early as the 17th century, Sir Isaac Newton conducted a series of experiments with glass prisms that allowed the discovery that white light is, in its core, made up of a "spectrum of colors from red to violet". He observed that each color has a different refractive index and laid the foundation for our present understanding of the light spectrum (Fig. 1.2, [5]). This was followed by the invention of the telescope and microscope by Galileo Galilei and Antonie van Leeuwenhoek respectively, opening up new avenues for the study of light and optics [5]. While the study was relatively new, it attracted attention due to the curiosity of "what is light" [4,5].

At the start, light was only a concept – something humans saw outdoors and the occasional "splitting of light through the prism" magic. It was in the 19th century, when the development

of gas and electric lighting revolutionized indoor lighting and made it possible for people to work and socialize after dark [5]. It was during this era of curiosity that Thomas Edison invented the incandescent light bulb in 1879. This was a major milestone in the entire field [7]. In the 20th century, light found new applications in fields like telecommunications, with the invention of the laser by Theodore Maiman in 1960 [8], and in medicine, with the development of phototherapy and laser surgery [9-11]. For instance, the development of the laser made it possible to create extremely pure and precise light sources, which have been used in a range of applications [7-9]. Through decades of research, light has now been used in multiple fields like household lighting, cinema and heating on a daily use basis whereas in solar simulation, medicine, catalysis, disinfection etc., in the world of science [5].

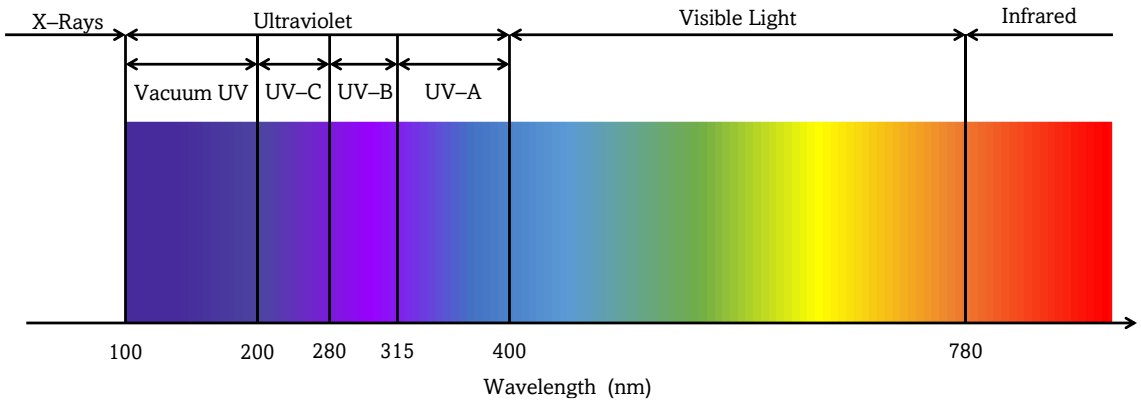

Figure 1.2: Light spectrum as defined by Sir Isaac Newton (Representation drawn from [5]).

Also, in the early 19th century, German physicist, Joseph von Fraunhofer studied the spectrum of the sun and noticed that there were dark lines present, which were not accounted for by Newton's work [12]. He discovered that these lines corresponded to specific wavelengths of light that were being absorbed by different elements in the sun's atmosphere. These lines are now called Fraunhofer lines [12]. Research by Fraunhofer paved the way for studies on spectroscopy [12]. Spectroscopy is the study of the interaction between light and matter, and it has become an important tool in many different fields of science [13]. In the mid–19th century, scientists began using spectroscopy to study the spectra of different elements, which allowed them to identify new elements and study their properties. Following the extensive interest in the field of light and its applications in the late 19th century, in the early 20th century, the field of quantum mechanics revolutionized the understanding of the behavior of light and matter [14-16]. Scientists found that the energy of light is “quantized”, meaning that it can only exist in certain discrete levels. In recent decades, advances in technology have allowed scientists to study the spectrum of light in

greater detail. To summarize, the light spectrum is a range of electromagnetic waves of varying wavelengths and frequencies. The different parts of the light spectrum, in order of increasing wavelength, are:

- Gamma rays: These have the shortest wavelengths and highest frequencies in the spectrum (Ranging between 10^{-6} nm to 0.01 nm). They are produced by radioactive decay and nuclear explosions [17].
- X–rays: These have slightly longer wavelengths than gamma rays but are still short (0.01 nm to 10 nm). They are used in medical imaging and scientific research [18].
- Ultraviolet (UV) radiation: This part of the spectrum includes wavelengths that are just shorter than those of visible light ranging between 100 to 400 nm. UV radiation is responsible for sunburn and can cause skin cancer with overexposure [19].
- Visible light: This is the part of the spectrum that we can see, with wavelengths ranging from about 400 to 700 nm. The colors of the rainbow – violet, indigo, blue, green, yellow, orange, and red – are all part of the visible spectrum [20].
- Infrared (IR) radiation: This includes wavelengths that are longer than those of visible light (in the range of 800 nm to 1 mm) and are responsible for heat radiation. Infrared radiation is used in thermal imaging and remote sensing applications [21].
- Microwaves: These have longer wavelengths than infrared radiation and are used in microwave ovens and telecommunications (Ranging between 1 mm to 0.1 m) [22].
- Radio waves: These have the longest wavelengths (between 0.1 m to 106 m) in the spectrum and are used in radio and television broadcasting, as well as in other telecommunication applications [23].

The different parts of the light spectrum were defined by scientists and researchers over time, as they discovered and studied the properties of different types of electromagnetic waves. Notable contributors to our understanding of the light spectrum include James Clerk Maxwell, Heinrich Hertz, Max Planck, and Albert Einstein, among others [17-23]. Among the different parts of the light spectrum, this thesis is focused on the ultraviolet region of the spectrum. The following sections of this chapter focus on the history, state–of–art, and applications of this range of light spectrum.

1.2. Ultraviolet (UV) Light

UV light discovery dates back to the early 19th century when Johann Wilhelm Ritter found certain substances like silver chloride (AgCl) turned black when exposed to sunlight through a prism, following on footsteps of principles and experiments set by Sir Isaac Newton. He explained that this change was due to certain radiation and coined them to be a new form of radiation – "chemical rays" [24-26]. Emerging from the discovery of chemical rays, in 1804, an English scientist Thomas Young discovered that beyond the violet end of the visible spectrum (< 400 nm, Fig. 1.2), there was no visible light, which he called "invisible rays" [26]. Later experiments showed that these invisible rays had the ability to cause chemical reactions and were responsible for the darkening of silver chloride observed by Ritter [27]. These rays were eventually renamed "ultraviolet rays". In 1877, Arthur Downes, in his work titled "*The action of sunlight on micro-organisms*", used UV rays and showed that they inhibited growth in bacteria and micro–fungi by inducing certain chemical changes [28, 29]. This was a turning point for future research and application of UV radiations (Fig. 1.3).

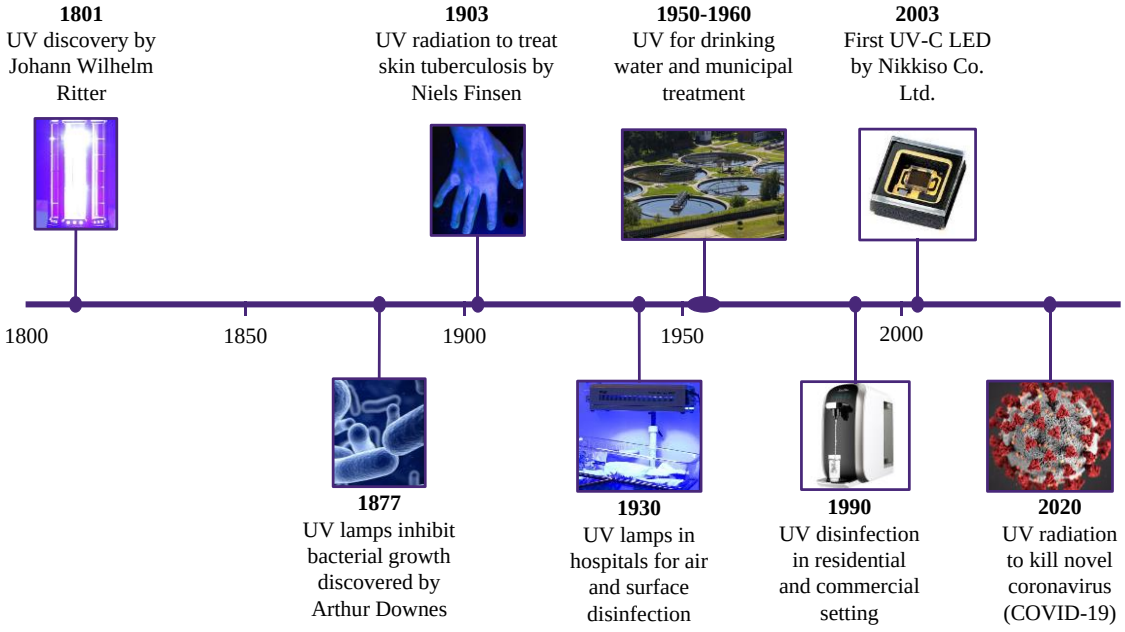

Figure 1.3: Timeline of significant research on UV light (Source: [23-26]).

Early 1900s began century–long research on UV region of the light spectrum. Researchers began to investigate the effect of UV on living organisms. One of most notable studies in this era was by Niels Finsen, in 1903, who used UV light in the treatment of tuberculosis and found that it could kill the bacteria responsible (*Mycobacterium tuberculosis*) [24,30]. He further developed a device called a Finsen lamp that would, in its later stages, be used to

treat patients. This work won Niels Finsen a Nobel Prize in Medicine [30,31]. In the years following this discovery, the interest in UV light and its effect rose exponentially. It was found that UV light could cause skin damage and sunburns to human beings, and that it causes mutations in cells and DNA [31]. In the 1930s and 1940s, studies began investigating, in more detail, the germicidal properties of UV light for disinfecting air, water, and surfaces. One of the most prominent studies was by Wells et al. (1936) which investigated the effect of UV for airborne contagions and found it to be effective in killing bacteria and viruses present in air [32]. The results generated great attention from local public and government and saw the installation of UV lamps in hospital for air and surface treatment. Between 1950 – 1960, researchers continued to explore various applications in medical and dental settings [33,34], this decade also saw the installation of UV lamps for drinking water and municipal treatment.

In the 1990s and 2000s, studies explored the use of UV light from a point–of–use perspective with notable studies by Drescher et al. (2001) [35] which found that low–pressure UV light was effective in inactivating *Cryptosporidium parvum*, a dangerous waterborne parasite [33-35]. UV radiation was also divided into three categories based on their wavelength: UV–A (400–315 nm), UV–B (315–280 nm), and UV–C (280–100 nm) [32-35]. Finally, more recently, UV light was proven to be effective in disinfection of the novel COVID–19 virus and widely used during the pandemic for disinfection of air and surfaces [36].

1.2.1. Properties and Applications of Ultraviolet Light

UV light possesses a number of unique properties that make it effective and useful in a variety of applications. One of the most well–known properties is its ability to cause chemical reactions [29,32,34]. This property has been efficiently used in a number of industrial processes like the production of plastics, coatings, and adhesives [37]. Another important property of UV light, as mentioned earlier, is its ability to kill bacteria and other microorganisms. This property has been used in the development of water purification systems and the sterilization of medical equipment [28, 29]. UV light has also been known to cause fluorescence, which is the emission of light by substances when exposed to UV radiation [38, 39]. This property has been widely used in applications such as the detection of counterfeit money and the analysis of DNA in forensic investigations [40].

In terms of application of UV light, it has been tested in various fields, including medicine, industry, and science. Some of the most common applications of UV light have been discussed below.

- *Medical Applications* – UV light is used in the treatment of skin conditions, such as psoriasis, and eczema. This is also called UV light therapy, which involves exposing the affected skin to UV radiation in a controlled environment. This therapy can help to reduce inflammation and improve the appearance of the skin. UV light is used in the sterilization of medical equipment and surfaces. UV light is also commonly used in hospitals and other healthcare settings to reduce the spread of infectious diseases [19, 24, 28, 31, 35].
- *Industrial Applications* – UV light has a number of applications in the industrial sector. UV radiation, in this case, is used to initiate a chemical reaction that causes these materials to harden and form a strong bond for application in the curing of plastics, coatings, and adhesives. UV light is also used in the process of photolithography which involves using UV radiation to etch patterns onto a substrate, which is then used to create electronic circuits and other components [41-43].
- *Scientific Applications* – Using the property of fluorescence, UV radiation is used in the analysis of DNA and other biological molecules, and in the study of genetic disorders. UV light has been used in astronomy to study the properties of celestial objects. UV radiation can provide valuable information about the temperature, composition, and other properties of stars and other astronomical objects [15, 18, 39].

1.2.2. UV Sources

Naturally occurring UV radiation comes from the sun, with the UV–A and a portion of the UV–B radiation reaching the surface of the Earth, while the UV–C part of radiation is nearly completely absorbed by the atmosphere [12]. Given its energetic, damaging, and beneficial properties, researchers and industrialists have searched for artificial UV radiation sources. Artificial UV lamps, plasma lamps, electrical arcs, fluorescent lamps are some of the artificial radiation sources discovered so far (an example of one such source can be seen in Fig. 1.4) [33]. The most prominent artificial sources are mercury lamps and light emitting diodes (LEDs). The following section discusses the operation and advantages/disadvantages of these sources.

(a) (b)

Figure 1.4: (a) A high pressure mercury vapor lamp (Source: [44]) and (b) Mercury lamp emitting bright blue light (Source: [45]).

1.2.2.1. Mercury Lamps

Mercury lamps are a type of gas discharge lamp that uses mercury vapor as the primary light source (Fig. 1.4). These lamps were first developed, by Peter Cooper Hewitt, in the early 1900s. Hewitt found that a tube filled with mercury (Hg) vapor emitted a bright blue light when an electric current was passed through it [46]. This invention was patented in 1901 and consequently, was launched into the public domain in 1902. In the decades following this invention, multiple improvements were made to its design such as the addition of electrodes and the use of different pressures of mercury vapor. These improvements led to the development of high–intensity discharge (HID) lamps, which are widely used for lighting and other applications today [47].

A typical mercury lamp (Fig. 1.4 (a)) consists of a sealed glass tube that contains a small amount of vapor mercury, as well as electrodes at either end. When an electric current is applied to the electrodes, the mercury ionizes and emits light (Fig. 1.4 (b)). In fluorescent lamps, the glass tube is coated with a phosphor layer that converts some of the UV light emitted by the mercury into visible light [46, 47]. The pressure of the mercury vapor inside the tube can vary depending on the design of the lamp. Three types of mercury lamps are available in the present day [48-50]. First, low/medium–pressure (LP/MP) mercury vapor lamps that contain a small amount of mercury and operate at a pressure of around 1–10 Pascals (Pa). These lamps produce a wavelength peak of 254 nm and were commonly used

in water treatment plants [48]. Second, high–pressure (HP) mercury vapor lamps which contain a larger amount of mercury and operate at a pressure of around 2000 Pa. They produce a broad spectrum of radiation, including visible light and UV radiation, and are used for lighting applications [49]. Lastly, mercury–xenon lamps which contain both mercury and xenon gas and produce a broad spectrum of radiation for use in microscopy and lithography [50]. In operation, mercury lamps operate by creating an arc of electric current through the mercury vapor inside the glass tube. When the current flows through the vapor, it ionizes the gas, which emits ultraviolet light. The voltage required to start a mercury lamp varies depending on its design and operating pressure. Low–pressure mercury lamps typically require a starting voltage of around 300 – 600 volts, while high–pressure mercury lamps may require starting voltages of several kilovolts [47, 48].

Despite the range of applications for mercury lamps, multiple environmental concerns have been raised by researchers through the years [51]. The mercury used inside these lamps is toxic and can cause significant environmental damage if not disposed of properly. The lamp, in itself, is fragile and if broken, the mercury inside could release into the environment causing contamination of soil and other water sources in its proximity [52]. While some of these issues could be mitigated, the main concern of toxic mercury usage, in applications, has caused these lamps to become redundant. To add to this, ruling governments of major countries have implemented regulations that restrict the use and disposal of mercury lamps. For instance, the European Union (EU) has banned the sale of most types of mercury lamps and has implemented regulations for the safe disposal of used lamps [53]. The United States Environmental Protection Agency (EPA) has also established guidelines for the proper handling and disposal of mercury lamps [54]. As a result of regulations and growing public concern, there has been a push towards using alternative light sources, such as LEDs and plasma lamps, that are energy–efficient and environmentally friendly [52-54].

1.2.2.2. Light Emitting Diodes (LEDs)

In the early 1960s, Nick Holonyak (General Electric) first invented LEDs that emitted low intensity infrared light. This was followed by the invention of the first red LED capable of producing invisible light [55]. From then on, research and development in this area began growing with studies on different materials such as gallium arsenide (GaAs) and aluminum–gallium–arsenide ((Al, Ga) As), for the development of brighter and more efficient LEDs [56]. Since then, the technology has continuously evolved, with advances in efficiency, color

ranges, and lifetime. At present, LEDs are used in a large variety of applications including, but not limited to, lighting, displays, and indicators. While visible light LEDs are common and have been used for nearly 5 decades, UV LED technology is a relatively recent development.

The need for UV LEDs began to gain momentum as early as the beginning of the century and, more specifically, when the use of mercury lamps gained widespread attention for the wrong reasons [51, 52]. The first commercial UV LED was developed by Nikkiso Co. Ltd. in 2003 [57]. However, it must be noted that early UV LEDs were not efficient enough for practical use, and their output was limited to a few milliwatts. Since 2003, significant advancements have been made in UV LED technology, resulting in LEDs that are more efficient, reliable, and have higher output power [56]. UV LED technology presents plenty of advantages over traditional mercury lamps and some of the prominent advantages, specific to the UV range of the spectrum, have been listed in Table 1.1 [58].

Table 1.1: Advantages of UV LEDs.

Mercury Lamps	UV LEDs
Single peak emission at 253.7 nm	Application–specific adjustment of wavelengths with narrow band coverage in UV–A/B/C region of the spectrum
Ozone generation	No unwanted creation of ozone due to narrow–band emission
Warm–up time of up to 30 minutes	Fully operational with no warm–up time. Instant ON/OFF capability
Large in size, making the application system bulky	Great degree of freedom for systems design, as the LEDs are small in size (ranging from 0.5 mm to 6.5 mm)
Contains mercury	Contains no toxic materials
Possible thermal radiation in the direction of emission	No thermal radiation in the direction of emission
Fragile and prone to breakage	Extremely robust and compact
High carbon footprint	Low carbon footprint

LEDs are made from a semiconductor material, typically gallium, arsenic or phosphorus. The semiconductor has two regions, one with an excess of electrons (n–type region) and the other deficient of electrons, also called holes (p–type region). Together the two regions form a p – n junction (Fig. 1.5) [56, 58]. When voltage is applied across the junction, the excess electrons move towards the holes in the p–type region of the semiconductor. As the electrons and holes recombine, energy is released in the form of light. The color of the light emitted depends on the semiconductor material used [59].

LEDs, centered in the visible region of the light spectrum, are highly efficient at converting electrical energy supplied into light energy. They also have a longer lifespan and are durable over the traditional incandescent light bulbs used for household lighting [56-59]. In the UV region of emission, however, the light output efficiency is very low (as of 2023 – highest output efficiency is 13% [60]) as this technology is still in its early stages. It is expected that within the next decade, the output efficiency will increase three–fold.

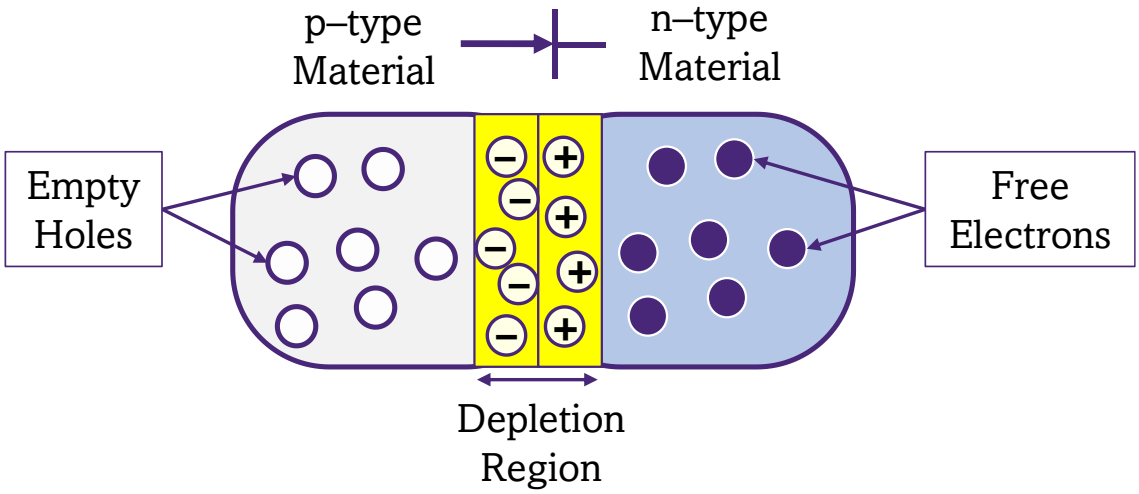

Figure 1.5: Light generation mechanism in LEDs (Source: [59]).

The manufacturing of LEDs takes place in a multi–step process. A representation of important steps can be seen in Fig. 1.6. As mentioned earlier, LEDs are made from bulk crystals of a semiconductor material (for instance, AlN bulk crystals in Fig. 1.6). These crystals are cut into thin slices for epitaxial growth in the second step. To produce wafers, a process called epitaxy is employed which involves depositing layers of semiconductor material onto a substrate of sapphire or silicon carbide [61-64]. Once the large wafers have been produced, they undergo a process called wafer mapping. In this process, based on the LED chip size, a tool maps the wafer into pieces and applies a layer of photoresist to the surface before exposing it to UV [62]. This creates a pattern which will, in the later stages,

determine the location of chips. Also, the wafers are cleaned to remove any impurities that may have accumulated during the earlier stages. Next, a layer of metal is deposited onto the wafer, which will later serve as contact for the LEDs before proceeding to the next stage of manufacturing process [63]. The next step is etching, which involves selectively removing material from the areas that were not covered by the photoresist during the wafer mapping step. This creates small indentations in the wafer that will later serve as the active regions for the LED chips [64].

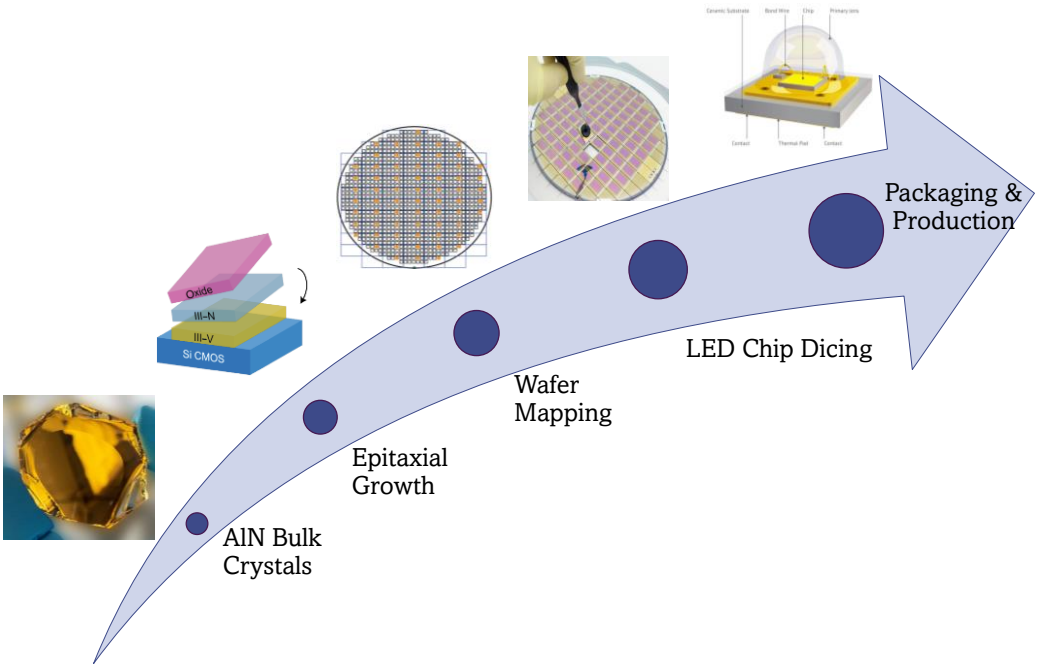

Figure 1.6: Stages in LED manufacturing (Source: [61]).

Upon etching, the wafer pieces undergo a process called doping. This involves introducing impurities into the semiconductor material to create the n–type and p–type regions that are necessary for the LED to function [62]. After the doping process, the wafer undergoes a series of deposition steps to create the various layers of the LED (Fig. 1.7). Once the LED chips have been fabricated, the following step involves the creation of contacts that will allow it to be connected to a circuit. This typically involves depositing metal onto the surface of the LED chip and annealing it to create good electrical contact. Finally, the LED chips are packaged into a housing that protects them from the environment and allows them to be mounted onto a circuit board. The packaging process typically involves encapsulating the LED chip in a plastic or ceramic package and attaching wires to the contacts [65]. In recent years, the development and commercialization of UV–C centered LEDs have accelerated, and manufacturing processes have seen a rise in speed, efficiency, and quality.

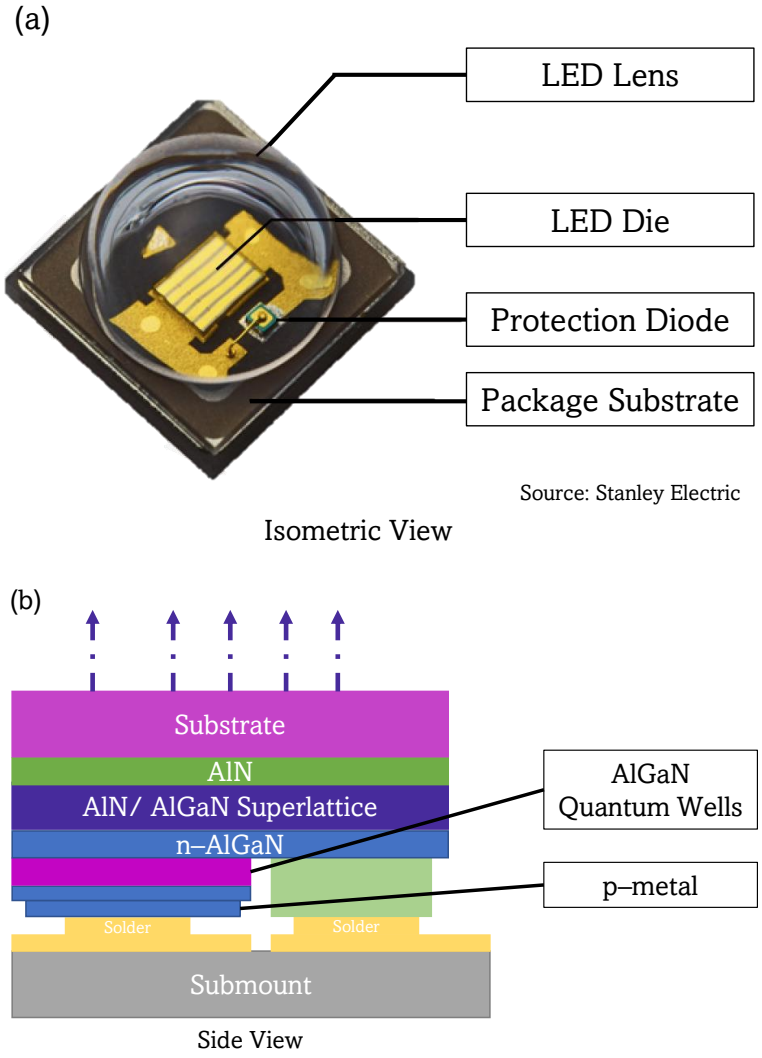

Figure 1.7: (a) UV LED chip and (b) Schematic of layer stack of LEDs (Source: [65]).

1.3. Water

Water is a precious and finite resource essential for the existence of life on Earth. It is thus crucial to ensure that the available water is clean and safe for human consumption. 71% of Earth is covered with water, however not all of it is accessible and, more importantly, consumable [66]. The primary sources of drinking water are surface water, groundwater, and rainwater. Surface water is found in rivers, lakes, and reservoirs, whereas groundwater is located beneath the surface and accessible through wells and boreholes. Rainwater is collected from rooftops during rain and stored for future use [66, 67]. In 2019, the United Nations General Assembly declared that access to clean drinking water and sanitation is a human right [68].

1.3.1. Availability

The accessibility and availability of safe drinking water varies depending on the region. In certain areas around the globe, there is an abundance of water while in others, water is scarce. According to a United Nations report (UN), over 2 billion people live in countries experiencing high water problems and predicts that, by 2050, this number is expected to increase up to 3.2 billion [69]. A report by the World Health Organization (WHO) further confirmed this data and stated that among them, nearly half of those people live in sub–Saharan Africa [70].

It can be seen in Fig. 1.8 how the continents of Africa and Asia (total population of 6.18 billion [71, 72]) have the lowest accessibility to safe drinking water. Unfortunately, there exist multiple challenges that prevent access to clean and safe drinking water like pollution, infrastructure, and scarcity. Consumable water can be easily contaminated via various pollutants such as bacteria, viruses, chemicals, and other substances and lead to a range of illnesses. These illnesses could vary from intestinal problems to more severe and life–threatening diseases like cholera or typhoid.

1.3.2. Contamination

Contaminated water is responsible for more than 500,000 deaths per year from diarrheal diseases, according to a study by WHO in 2017. Rotavirus and *Escherichia coli* (*E. coli*) are the two most common etiological agents of moderate–to–severe diarrhoea in low–income countries. [73]. Human waste is one of the most common and hazardous sources of water contamination. This also translates to inadequate sanitation and has been traced in countries such as Nigeria, India, etc. [74, 75]. When human waste is not treated properly and released into the environment, it can contaminate the nearby water sources and also seep into the groundwater sources. This also leads to the spread of waterborne diseases. Agricultural run–offs, industrial releases, and natural harmful contaminants are also sources of contamination [76]. The need to treat both drinking water and wastewater is of the utmost importance. Consumable water must be free from harmful pollutants and treated to ensure it is safe to drink. This is the same in the case of wastewater wherein the wastewater must meet certain criteria before release into the environment or for other uses.

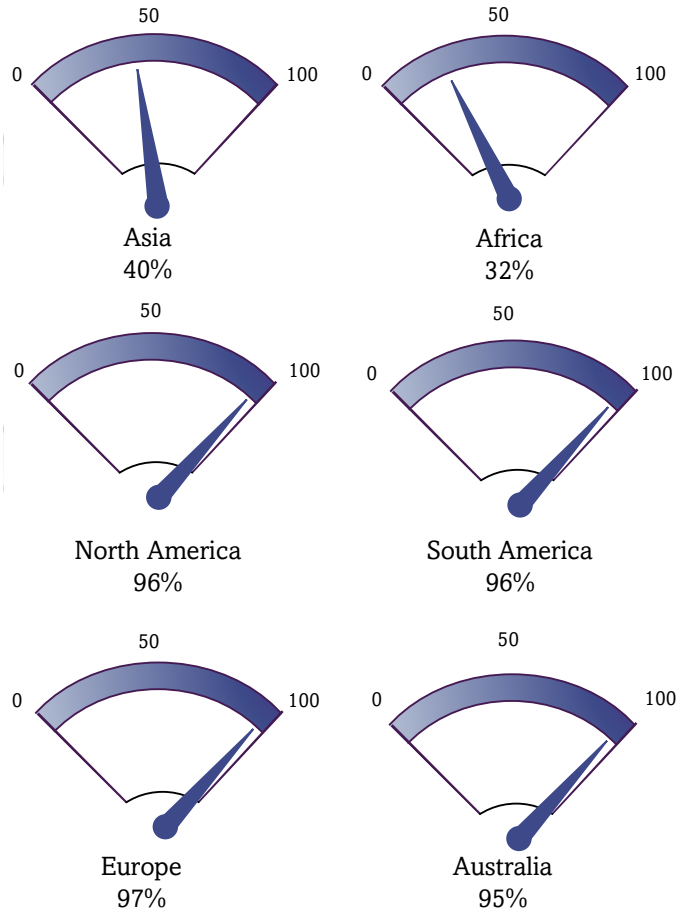

Figure 1.8: Water accessibility statistics by each continent as of 2017 (Source: [73,74]).

The WHO issues yearly guidelines on the definition of drinking water in terms of quality standards, nutrient concentration, and certain other parameters that help companies and governments ensure that their customers and citizens are consuming WHO recommended water quality [77]. It has also been found that aging infrastructure can cause contamination. This can happen when distribution pipes, in the case of point–of–use systems, and excretion systems, in the case of wastewater disposal, are corroded or damaged with time. It is necessary to ensure that the infrastructure is up–to–date and working to ensure low levels of water contamination. To this note, in 2020, it was found that over 80% of wastewater generated globally was discharged without adequate treatment leading to contamination of rivers, lakes, and oceans [78]. In low–income countries, only 27% of healthcare facilities have access to basic water services, which can lead to the spread of waterborne diseases and inadequate hygiene practices [79].

1.3.3. Treatment

To ensure the safety of drinking water and wastewater to the environment and citizens, it is crucial that it is effectively treated before use. Water treatment is the process of removing harmful contaminants from water and varies depending on the source and type of pollutants present. Multiple primary treatment methods exist to ensure the safety of water [80]. In a water treatment plant, coagulation and flocculation processes are used wherein chemicals are added to aggregate small particles for easier removal from the matrix. Another commonly used process is sedimentation, which involves settling down of larger particles in the water matrix where they can be easily removed [80]. In certain places where smaller pollutants are present, filtration is used. Filtration is the process of passing the water through a series of filters (based on removal requirements) which remove any particles and contaminants from the matrix. Finally, disinfection is conducted to remove any bacteria and viruses present in the matrix. This process uses chemicals such as ozone or chlorine that are known to be effective against microorganisms. In most cases, all the above treatment processes are combined to ensure that the water is safe for consumption.

Over the years, the process of disinfection has evolved rapidly. The use of chemicals has come down by about 50% since the early 2000s. Artificial sources, such as the ones discussed in Section 1.2.2., have replaced chemicals and are widely used in treatment plants. While there exist artificial sources for disinfection, not everyone has access to this technology and hence researchers have found ways to use natural sunlight for specific applications. One of the most notable applications is solar water disinfection, also known as SODIS. This is a method for the treatment of drinking water contaminated with pathogens. It involves the exposure of clear plastic bottles to sunlight for several hours. The UV light part of the sunlight kills the pathogens in water making it safe to drink. This process was first developed in the 1980s by Dr. Aftim Acra, a Swiss researcher working in Guatemala [81]. This method is a low–cost and low–tech way to disinfect water. This method is simple and easy to use in low–to–medium income countries and has been widely studied in recent years [82-86]. Multiple other technologies have also been employed for achieving effective disinfection of water such as photocatalysis and electrolysis [87-92]. These additional technologies contribute to the diverse arsenal of water disinfection methods, offering solutions to specific needs and conditions. By continually exploring and integrating innovative approaches, our ability to ensure safe and clean water for various applications has expanded rapidly in the past decade.

1.3.4. Improvement of Water Quality

As mentioned earlier, access to clean drinking water is still a major challenge in many parts of the world. However, there are many efforts underway to improve public access to clean water. Governments and other NGOs are investing in water infrastructure like building new treatment plants, repairing and maintaining the distribution pipelines, and monitoring the quality levels periodically [77, 80]. On the other hand, education and awareness campaigns have also seen a sharp rise in the last decade. These campaigns can help consumers understand the right water quality and promote good hygiene practices to avoid spreading waterborne diseases. For instance, the WHO released a social media video depicting the importance of handwashing, safe food preparation, and proper sanitation during the COVID–19 pandemic [93]. At the same time, water conservation has also been evaluated and planned for. Water conservation efforts can help reduce the strain on water resources around the globe. These steps include reducing water usage in agriculture and industries alongside promoting water–efficient practices [94]. While these efforts need to be two–sided, it is clear that local and national authorities need to monitor quality, limit over–usage, and avoid breaking the lowest threshold expected.

Therefore, plenty of Water Acts and laws have been put in place worldwide [95-99]. One of the most notable laws is the Safe Drinking Water Act (SDWA) of 1974. This law is a federal law enacted to ensure the safety of public drinking water in the USA. It establishes the minimum standards for treatment and disinfection of water and protects against harmful bacteria and viruses. Under this law, public water systems are required to regularly test their quality and notify consumers of any issues periodically [95]. Alongside the SDWA, the Clean Water Act (CWA, 1972) also describes the rules and regulations for protection of water resources in the USA. This law establishes minimum standards for treatment and enacts a standard operating procedure for municipal treatment plants [96]. The United States Environmental Protection Agency (EPA) monitors and regulates the enactment of these laws across the country while the WHO monitors the global situation [97-99]. Overall, there are plenty of laws such as the SDWA (1974), CWA (1972), both local and national, designed to protect public health and ensure the safety of water and other products. By following the laws and implementing effective strategies, the spread of waterborne diseases can be prevented by communities across the globe.

1.4. UV Disinfection

The history of UV–based disinfection dates back to the early 20th century when Niels Finsen won the Nobel Prize for his work on the treatment of skin diseases using UV [30]. Since then, researchers have been constantly studying UV light as a potential disinfectant in multiple applications. In 1910, the first use of UV light as a disinfecting agent was reported by Paul Vinogradsky, who utilized it to sterilize water containing bacteria. This led to many researchers, in this era, studying the efficacy of UV light as a disinfectant. By the 1920s, UV disinfection was being applied to the treatment of water and air [100, 101].

One of the most notable applications of UV was during World War II wherein UV disinfection was used to prevent the spread of infectious diseases among the military personnel, who were living in extreme conditions [33, 100]. By the 1950–1960s, UV disinfection rose as a budding technology, with its efficacy reported in the food and beverage industry [32]. It was in the 1970s, when governments across the world decided to use UV light in municipal water treatment plants. Today, UV disinfection is seen to be limitless, with applications in water and wastewater treatment, air purification, etc. It continues to play an important role in public health and safety [33]. The following sections aim at providing a comprehensive review of the research conducted using UV, specifically UV LEDs, for disinfection applications. It will cover the following topics: the mechanism of action of UV disinfection, the factors affecting the efficiency of disinfection, and studies involving UV LED based disinfection.

1.4.1. Mechanism of Action

Disinfection, as a concept, can be described as the reduction of viable microorganisms such as bacteria and viruses, to a desired concentration. Sterilization, on the other hand, means elimination of the microorganisms [101]. The process of disinfection does involve elimination, however, there exists no technique to ensure a 100% disinfection rate. The mechanism of disinfection involves at least two steps: (1) Penetration of the disinfectant through the cell wall and (2) reaction between enzymes within the cell (Fig. 1.9) [101]. The inactivation or reduction of microorganisms has been elucidated by the Chick's Law, which states that "rate of bacterial destruction is directly proportional to the number of organisms remaining at any time" and has been expressed in Eq. 1.1 [102].

$$-\frac{dN}{dT} = k \times N \qquad \text{Eq. 1.1}$$

where, N is the number of organisms per volume and k is a rate constant. This relationship implies a uniform susceptibility of all species at a constant concentration of disinfection, pH, temperature, and strength [102]. Many deviations from Chick's law have been described in the literature. One of them is the Chick–Watson's Law which explains the relationship between the number of active and inactive microorganisms as a product of concentration of the disinfectant and exposure time (Eq. 1.2) [103,104].

$$ln\frac{N_f}{N_o} = k \times C^n \times t \qquad \text{Eq. 1.2}$$

where, k is a rate constant, C is the concentration of disinfectant, n is the exponent (normally 1), and t is the exposure time. As mentioned earlier, UV–based disinfection is a process that involves exposing a contaminated matrix, consisting of microorganisms, to UV radiation (the disinfectant). This radiation can be delivered from mercury lamps, LEDs or plasma lamps and depends on multiple factors within the reactor set–up. In terms of mechanism of damage, in the literature, it has been reported that UV radiation damages the DNA of the microorganism and prevents them from replicating (Fig. 1.9) [105-108]. Specifically, the UV–C region of the UV light has been proven to be the most effective at disinfecting microorganisms [28]. A detailed description of the mechanism of the action of UV disinfection process, based on each wavelength range, will be provided in Chapter 5 and 6 of this work.

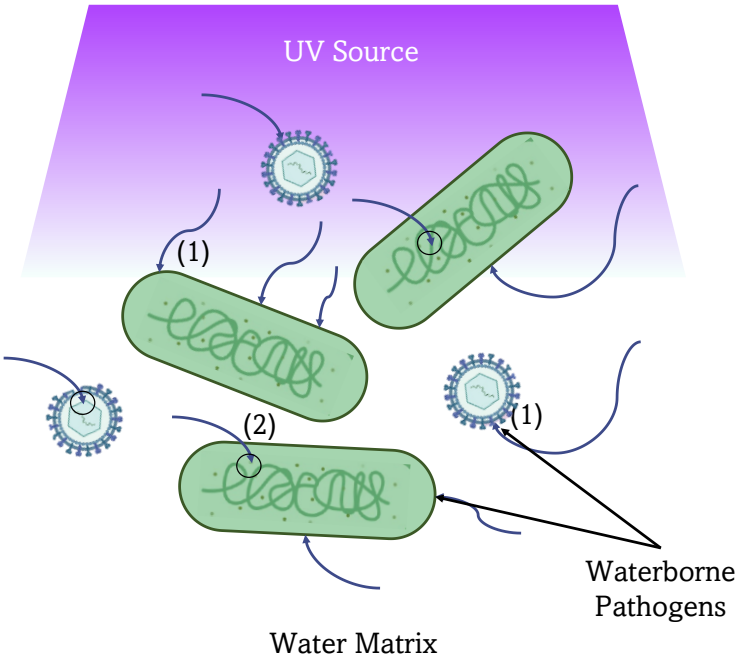

Figure 1.9: Mechanism of inactivation (Source: [106]).

1.4.2. Factors Affecting the Efficiency of UV LED Disinfection

The efficiency of disinfection depends on multiple factors, including wavelength, intensity, and exposure time. The wavelength of UV radiation determines the effectiveness of the disinfection process [108]. As noted by Bolton et al. (2008) [106], microorganisms absorb different wavelengths of UV light and behave differently at each point. It is also suggested that UV radiation in the range of 260 nm – 270 nm is highly absorbed by microorganisms and subsequently, is highly efficient for use in disinfection processes. UV–C radiation is the most effective at disinfecting microorganisms, followed by UV–B and UV–A radiation [105, 106]. The intensity of UV radiation is measured in terms of irradiance which is the emitted power per unit area. This parameter is denoted in W m^{-2} [109]. Theoretically, higher irradiance levels result in more effective disinfection. While this is true, it is important to note that excessive intensity of UV radiation can cause photon saturation, as shown by Che et al. (2017) and increase the risk of damage to materials and surfaces [109, 110]. Similar to the intensity of UV radiation, exposure time is another factor that impacts the disinfection process. Exposure time, also called dwell time, is the amount of time the microorganism is under UV radiation. This parameter is measured in seconds and must be optimized to balance the effectiveness of the disinfection process with the risk of damage. The product of exposure time and intensity gives rise to the commonly used term of UV dose or UV fluence. Most disinfection experiments are compared in terms of log reduction per unit of UV fluence [111].

1.4.3. Developments in UV LED Disinfection

UV LED disinfection has been applied in various fields, and its efficiency has been proven by multiple studies worldwide (Fig. 1.10). In the early 1990s, research in the area of UV LED was limited to homogenous systems. However, with time research has also extended to the development of hybrid systems combining UV LEDs with other disinfection technologies. One such technology is photocatalysis, which uses a photocatalyst, like titanium dioxide (TiO_2). The combination of UV LED and photocatalysis has been shown to increase the disinfection efficiency of both technologies. For example, a study conducted by Kim et al. (2017) found that the combination of UV–A LED and TiO_2 photocatalysis achieved a higher disinfection rate for *Escherichia coli* (*E. coli*) and MS2 bacteriophages than using either technology alone [112].

Another area of research in UV LED disinfection has been the development of sensors and monitoring systems for real–time detection of microorganisms in water. The use of UV LEDs in these systems allows for efficient and rapid detection of microorganisms, as the LEDs can be easily integrated into the sensor or monitoring device. For instance, a study by Grief et al. (2008) developed a microfluidic chip with integrated UV LED and fluorescence detection for the rapid detection of bacteria in water samples [113].

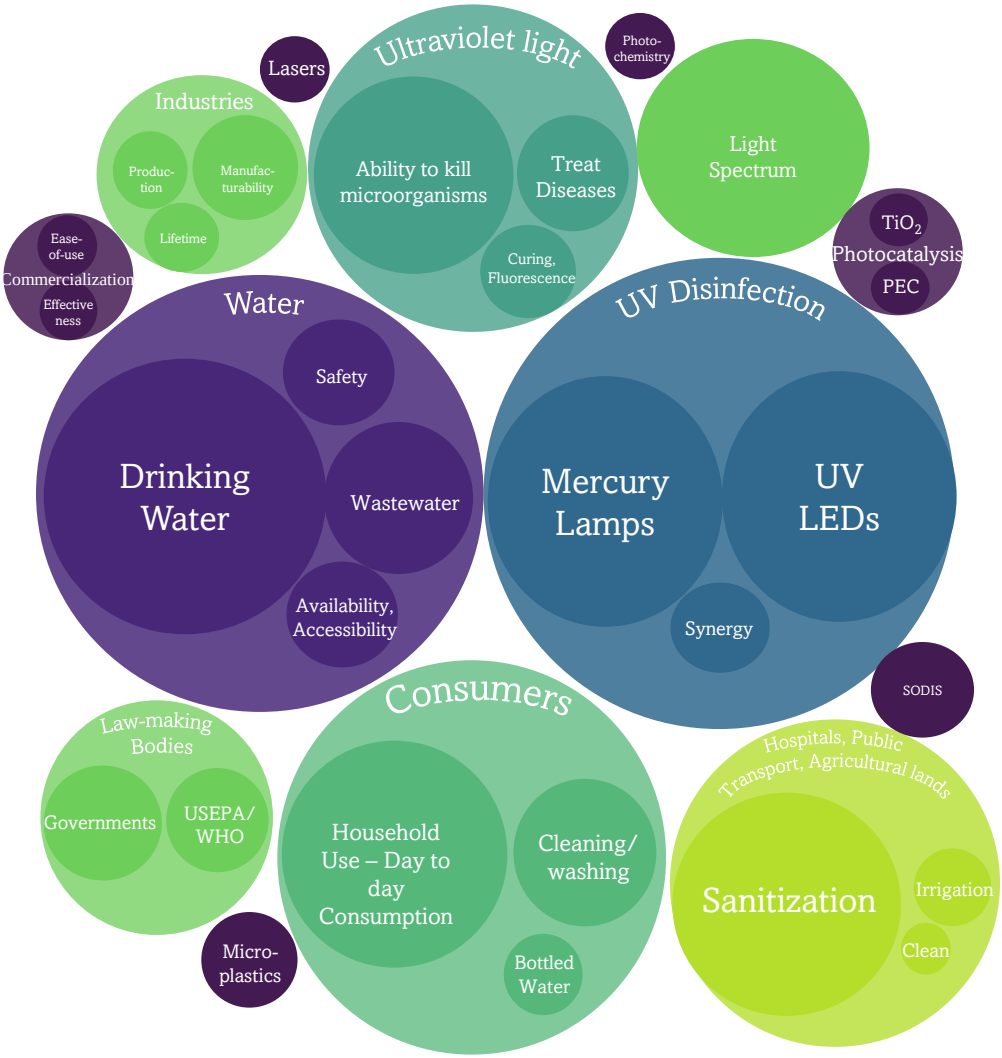

Figure 1.10: Areas of interest.

The development of UV LED technology has also led to significant advancements in the field of air disinfection [114]. UV LEDs can be used to disinfect the air in enclosed spaces, such as hospitals and airplanes, to reduce the transmission of airborne pathogens. as reported in a study by Kim et al. (2018). The study developed a portable air disinfection system using UV–C LEDs to reduce the concentration of airborne bacteria in a hospital ward [115-119].

In another area, UV LEDs were used for the disinfection of greywater (i.e., wastewater generated from household activities such as bathing and washing dishes). The researchers found that the use of UV LEDs resulted in a higher level of disinfection compared to using traditional chlorine–based disinfection methods [119, 120]. They also found that the use of UV LEDs resulted in a reduction in the amount of residual disinfection by–products in the treated water, which is an important factor in ensuring its safety [120].

Interestingly, although the applications of UV sources were already well–known by the early 2000s, it wasn't until the years 2004–2005 that their commercialization began in earnest. It was not until the subsequent years of research and innovation that their full potential was realized. One area in which UV LED technology was proving particularly effective is in water disinfection, with products like the SteriPen Adventurer emerging as early pioneers in this field [121]. Over the next two decades, numerous UV LED based water purification products gained widespread recognition and adoption, marking a major milestone in the development of this technology like the Klaran™ WR series disinfection system for dispensers and coolers [122] and the PearlAqua Deca™, a system for use in point–of–entry and POU applications [123]. Today, UV LED sources are used in a variety of applications, from medical and healthcare to food and beverage processing, and their potential continues to be explored and expanded [124-126]. Overall, the study of UV light spectrum has been a fascinating journey of discovery and innovation, with contributions from many different fields of science. It has led to a deeper understanding of the properties of light and matter, and it continues to play a crucial role in many areas of scientific research and technological development.

1.5. Challenges in UV LED Disinfection Process

To summarize, UV LEDs have emerged as a promising technology for disinfection applications due to their unique properties. However, there are still several challenges that need to be addressed to further advance this technology and facilitate the widespread adoption of UV LED based disinfection systems. The following section aims to identify key challenges and establish objectives for this thesis.

Drinking water and wastewater treatment using UV sources can be highly energy–intensive. Optimizing treatment processes to minimize energy consumption is an ongoing challenge [126], making it important to balance treatment effectiveness with cost and energy efficiency. The effectiveness of UV LED disinfection achieved in a particular water matrix is

largely determined by the light source used. Achieving a sufficient UV dose at the target can be challenging given the low light output efficiency of UV LEDs. It has also been found that efficiency further decreases at higher power levels [127, 128]. This also gives rise to the need for continuous monitoring and maintenance of the sources as they are prone to degrade faster. Certain microorganisms are more susceptible to specific UV wavelengths, and selecting the appropriate wavelength for a given application can be critical to achieving effective disinfection [102, 106, 128]. To ensure optimal performance and effective disinfection, it is essential to develop a customized LED system that operates at multiple wavelengths and to thoroughly understand the source before applying it in practice.

The measurement of UV sources presents another significant challenge in the field of UV LEDs, as it is difficult to obtain accurate and precise readings. Ensuring accurate calibration of instruments used and validating the measurements has been found to be challenging for researchers [129, 130]. It has been known that the output of UV sources can vary with time due to factors like aging, temperature changes, and operating conditions. Hence, ensuring stability during usage and measurements is key for further use in applications. Accurate measurement of UV radiation often requires specialized instrumentation that may not be widely available or affordable, limiting access to accurate measurements for some applications.

Furthermore, it has also been found that modeling the spectral output from UV sources can be challenging due to the complex, multi–peaked nature of the output and variations in intensity across different wavelengths [130-133]. A significant gap exists in the modeling of UV sources in a water medium and our understanding of their behavior. Very few researchers have attempted to model radiation in water, as creating different interactions can be difficult in complex environments [134]. There is still much that is not fully understood about the behavior of UV sources, particularly in complex environments. The lack of complete knowledge about the behavior of UV sources makes it challenging to accurately model their output and predict their impact in different applications.

1.5.1. Objectives of the PhD Thesis

Overall, this thesis aims to comprehensively evaluate the area of UV LED technology and the application of the potential synergistic effect of multi–wavelength systems in the disinfection of water. It has been carried out in the framework of the REWATERGY project (H2020-MSCA-ITN-2018, Project No.: 812574). Based on the aforementioned challenges,

this thesis has been split into 5 chapters in an attempt to provide solutions to each of them. Each chapter is aimed at one of the following objectives (Fig. 1.11).

- **LED Characterization** – This chapter aims to carefully select and assess UV–C LEDs at various wavelengths, utilizing multiple techniques to characterize the behavior of the device, the uniformity of emitted radiation, the amount of UV dose received at the point of interest, and the device's lifetime. The objective is to develop a comprehensive understanding of the light source that will be employed in subsequent chapters.
- **UV Sensors** – To tackle the difficulties encountered in measuring UV LED sources, this chapter assesses various parameters influencing radiation measurement and compares five distinct sensors capable of measuring in the UV region. The goal is to identify potential solutions to mitigate their impact on measurement accuracy.
- **Radiation Modeling** – To bridge the gap in the modeling of UV sources within water and to comprehend the system parameters that impact the total UV dose applied during the process, this chapter employs ray tracing as a technique to evaluate its efficacy and compares it with other contemporary tools and techniques used in research.
- **UV Disinfection** – This chapter aims to assess the impact of the chosen UV sources on the disinfection process by applying them to buffered water contaminated with a standard microbial contamination indicator (*E. coli*) and analyzing their disinfection efficacy. Furthermore, in addressing the issue of high energy consumption, the chapter explores the potential of wavelength synergy to achieve better results. Specifically, it investigates whether combining two or more wavelengths can produce a synergistic effect on the process and yield lower energy consumption.
- **Wastewater Disinfection** – Ultimately, the UV sources investigated in objective 1 are tested on an actual water matrix sourced from the secondary effluent of the wastewater treatment plant (WWTP) located at URJC facilities. This chapter conducts the same analysis carried out in the UV disinfection chapter, aiming to provide a comprehensive evaluation of the applied UV LED technology on the system. The findings from the preceding objectives are then integrated to provide a comprehensive explanation of any observed effects.

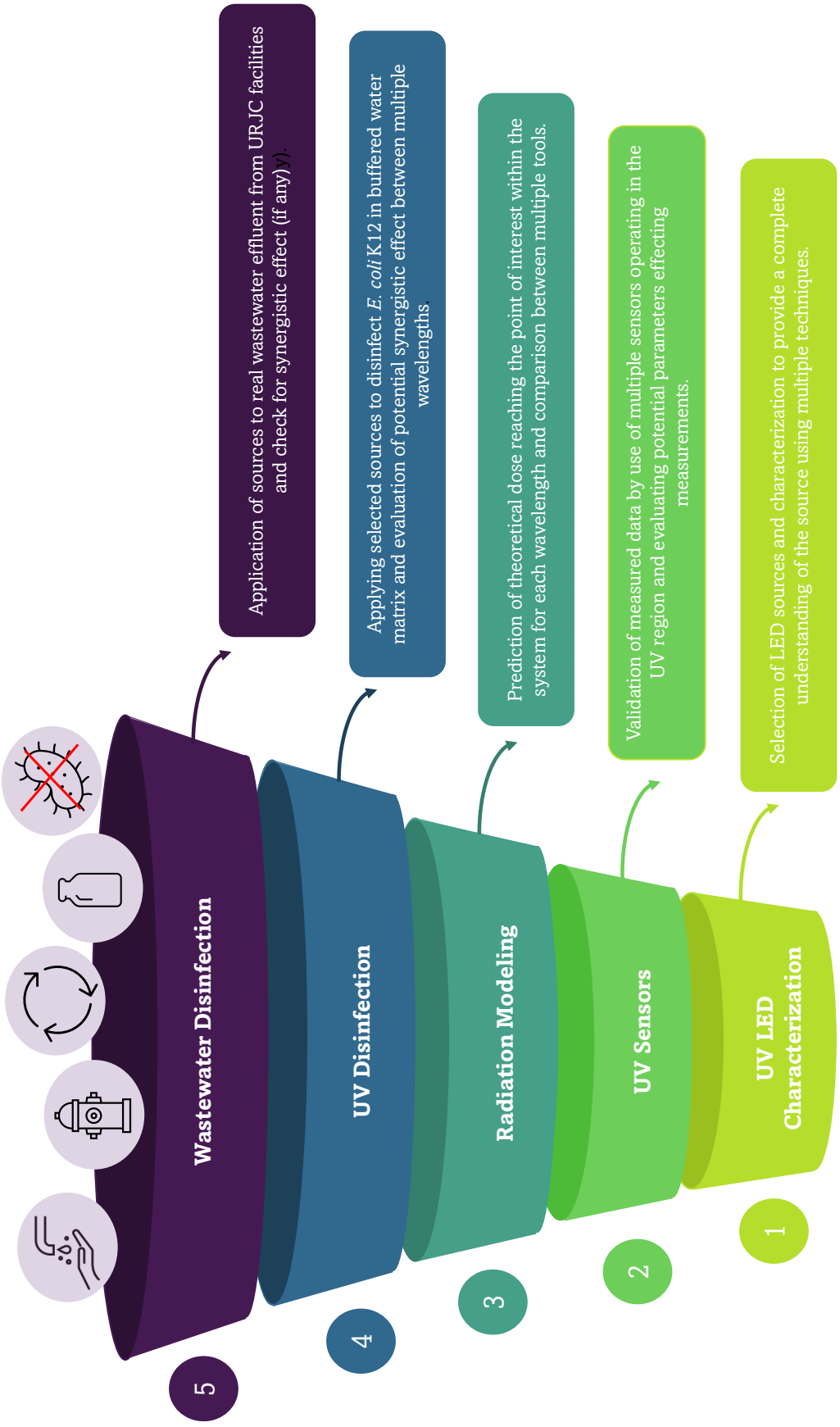

Figure 1.11: Objectives of this study.

CHAPTER 2

LED CHARACTERIZATION

2.1. Introduction

Over the past two decades, research using UV LEDs has increased drastically. These light sources have been applied to multiple fields including but not limited to; printing, coating and adhesive curing and, most recently to food, air, and surface disinfection [42, 107, 134, 135]. Since 2008, scientists have been tracking and cataloguing commercially available UV LEDs and observed a five–fold increase in the number of companies manufacturing these light sources [136]. Due to their advantages over traditional light sources, they have been considered an ideal replacement in applications and have been studied extensively. While there has been an increased use in various fields, the interest in understanding the light source has decreased significantly. Most UV LED research articles and industrial whitepapers delivered in the past decade have predominantly revolved around two topics. The first, promoting the technology by stating its advantages over traditional sources and second, using the possible integration benefits for consumers and researchers. The overall problem definition has evolved over the years to solve application issues rather than targeting the primary focus of the research i.e., use of particular light source to achieve the target solution [115]. Researchers have used UV LEDs in multiple applications, however, have encountered multiple issues with regards to the light source, as the technology is relatively new and in its phase of ongoing development and refinement [109, 114]. While UV LED technology has made a significant advancement in the recent years, there are areas where further improvements and advancements are desired by researchers and industrial companies [114]. Light output from the LEDs is one of the main parameters that can directly impact the application it has is being utilized for. The evaluation of light output parameters from the LEDs aids design optimization and can help understand what is occurring within a process or system [138]. LED systems are mainly characterized by irradiance and subsequent dose received on the target. Irradiance is defined as the radiant flux received by a surface per unit area. The SI unit is Watt per square meter (W m^{-2}) [139]. Dose is a measure of the amount of light received by a single particle as it passes under the light source, expressed in Joules per square meter (J m^{-2}). The relationship between the two parameters is shown in Eq. 2.1. below [139, 140].

$$D = I \times t \qquad \text{Eq. 2.1}$$

where, D is the dose acting in J m^{-2}, I is the intensity of light emitted by the source in W m^{-2} and t is the residence/dwell time of the particle under light source in seconds. The

residence/dwell time, in Eq. 2.1., is a function of speed of the particle (s), distance between the source and particle surface (x) and volume treated by the source (V) (Eq. 2.2 [140]).

$$t = f\ (s, x, V) \qquad \text{Eq. 2.2}$$

These parameters are key to understanding the application of LEDs to a process. A representation of how dose varies based on the parameters for a UV curing process can be seen in Fig. 2.1 [141].

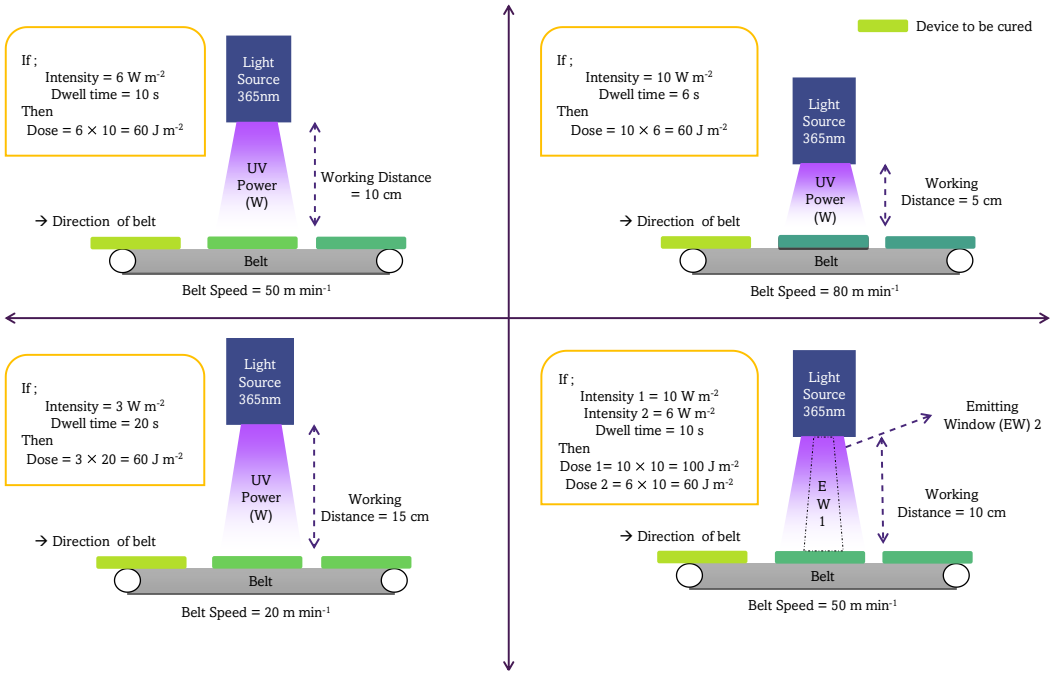

Figure 2.1: UV dose variation in a curing process (Source: [141]).

The above discussed parameters are controlled by numerous factors within the system operating the LEDs like temperature of the LED substrate, thermal management of the device, drive current, device optics, etc. Separate studies have been conducted on light optics and use of reflectors to enhance optical light output from the sources. However, no standardized procedure or techniques exist to do so [142]. While reflectors and optics are specific to the set–up and application, the understanding of LED emission has not been significant, as reported by Lawal et al. (2018) [114]. Chen et al. (2017) reviewed the prospects of UV disinfection applications and noted that there is an urgent need for research on improved heat–dissipation system of the LEDs alongside a monitoring system that can assess the functioning of individual LED elements on a device [109]. Questions have also been raised on reliability issues of UV LEDs in studies by Mitrenga et al. (2019), Nieland et al. (2019), and Piva et al. (2022), where factors like temperature, degradation, and heat dissipation were monitored and quantified [143-145].

Although these researches have been targeted at providing a better understanding of the sources', limited research has been conducted on the characterization of UV LEDs on a specific device and evaluating parameters that could assist in the optimization of light reaching a point of interest in different applications [146]. As mentioned in Chapter 1, LEDs allow the selection of narrow target wavelengths to be used in specific applications, but researchers have struggled to understand parameters like full width half maximum, thermal drift, that directly influence spectral emission of the LEDs used on their respective applications and hence need to be comprehensively studied [146, 147]. This new LED climate is great for generating an international market, but the challenge has now become about educating researchers and companies about the underlying technology in the application [114]. There are many studies in the field of light and optics to characterise and analyze the LED sources. However, it is important to note that the behavior of these light sources is a function of the device operating them [148-150]. Hence this chapter attempts to evaluate and choose UV–C LED sources from multiple suppliers in the market by establishing a criterion. The selected LEDs have been designed onto a device and used for an in–depth analysis. The study evaluates a safe drive current for the LEDs using a "rollover test" and monitors the light output over 48 h of continuous running [151, 152]. The chapter further characterizes the LED sources by studying the effect of current, working distance, on light output, in terms of the two main parameters (intensity and dose) using multiple test set–ups to obtain a detailed understanding of the light sources and identify any possible issues. It measures the uniformity of light from the device and monitors any shifts in peak wavelength of the device with an increase in current. It finally evaluates the lifetime of the selected sources under continuous running conditions and investigates the potential reason behind the trend obtained.

2.2. Methodology

2.2.1. LED Selection

For the purpose of the thesis work, LEDs were chosen as light sources over mercury lamps. LEDs have also attracted increased interest from researchers as they have the ability to emit controlled radiation at multiple wavelengths of interest whereas mercury lamps have a monochromatic emission peaking at 254 nm, thus enabling a wider research base [153]. While LEDs have their advantages, one key issue with LED sources, currently, is that these sources have low light output [114].

To decide on the light source among multiple manufacturers, a decision criterion was created based on both industrial and academic standards. This decision criterion took into account both efficiency and price per mW of power to help conclude the best light sources. Table 2.1 below summarizes the established decision criterion. As seen in Table 2.1, five key parameters were chosen based on previous studies and on certain key manufacturer datasheet numbers that helped build an understanding of the light source considered [154-156]. Based on the literature review, it was decided that light sources centered at 265 nm, 275 nm, 285 nm, and 310 nm would be effective in disinfection; hence, LEDs in this range have been researched. The listed parameters below were further ranked to create a balance between performance and cost of manufacturing before proceeding with the selection of the LEDs.

Table 2.1: Decision criterion for choosing the light source.

Parameter	Description (Manufacturer options)
Compatibility of the footprint of the LEDs	Package Size of the LED (3.5 mm /1.5 mm /1.3 mm / 6.5 mm / 6.35 mm) Number of Pads (1–3) Device to run the LEDs
Power (mW)	Test power on the datasheet of the manufacturer normally given as radiant flux (in mW)
Test Current and Maximum Ratings	Data from the datasheet of the light source. The data published is based on particular drive current set by the manufacturer.
Maximum Permissible power of the package	Manufacturer power output Calculation of mW/$ cost on each LED How much power per device is possible for the particular LED
Efficiency	Based on Datasheet – using forward voltage, drive current – input power can be known. Using the output power denoted as radiant flux, rough efficiency is calculated

2.2.2. Testing Equipment

To understand the complete emission profile of the device and other characteristics, an X–Y based motor gantry tester was used (Fig. 2.2 (a)). The tester consists of a workbench (where the device can be mounted and moved to multiple distances away from the optical sensor) and a motor gantry which supports the optical sensor (Fig. 2.2 (b)) and moves as

required in longitudinal and lateral directions. The entire set–up is controlled using a LabVIEW VI that has been configured and programmed to collect data from measurements for further analysis. The entire set–up is enclosed in a black box to avoid exposure to harmful UV radiation.

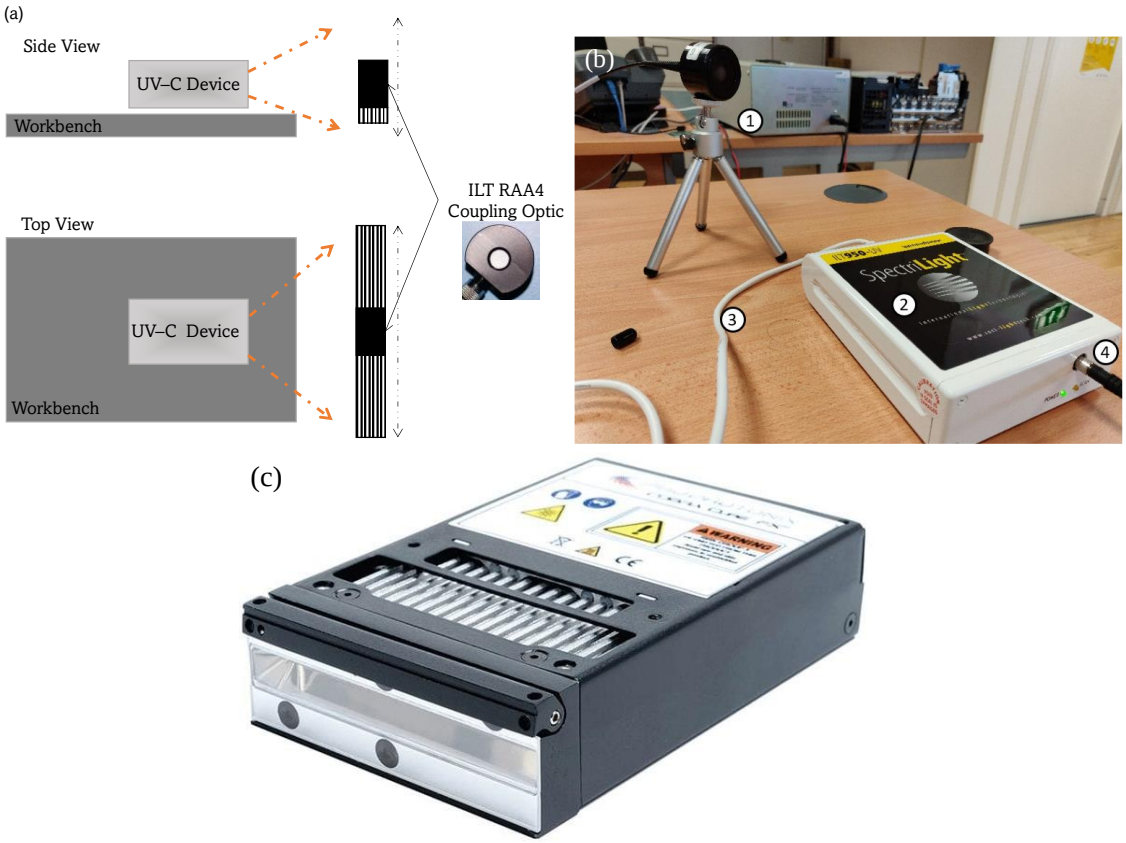

Figure 2.2: (a) Top view of X–Y tester for radiometry, (b) Optical sensor equipment, and (c) COBRA FX–1 device.

To characterize the light emitted from the device, a spectroradiometer has been used. The spectroradiometer is the ILT 950UV series measuring radiation in the range from 210 nm to 1100 nm [157, 158]. The optical sensor system consisted of 4 main components (Fig. 2.2 (b)) – (1) Detector Head, (2) Optic Fiber, (3) 950 Spectroradiometer, and (4) USB cable. Note that for certain characterization experiments, other sensors have been used. These sensors have been detailed along with their respective set–ups. The chosen LEDs have been built onto the ProPhotonix COBRA FX–1 series devices (Fig. 2.2 (c)) according to their specifications. Details on re–designing of the device and specifications are discussed in Section 2.3.2. The device was characterized in multiple ways using the main equipment discussed above. The following sections detail each experimental set–up used for the characterization of the LED device.

2.2.3. Rollover Test

Manufacturers typically characterize the light source using a single LED on a copper cooled block. The results of these tests determine light specifications, such as maximum input current for the LED datasheets, which are provided to potential customers [159]. In practice, multiple LEDs are often located together in a device mounted on a heat sink. Therefore, the specifications given by manufacturers can only serve as guide figures for the selection process. When a device has been designed with the selected LED, the LEDs altogether need to be tested, in the device conditions, to determine the maximum and ideal current to run the device at [160]. This test is called "rollover" test and involves measuring the optical power output from the device with gradual increases in LED input current. At a certain input current, any further increase does not result in a significant increase in optical power output. At this stage, any further increase means that the LEDs are generating more heat than light, hence are prone to degrade faster [145]. Lighting device manufacturers call this point the rollover point and program the device input current to a lower or higher level for safe operation and long lifetime of the LEDs [152]. To bypass the device electronics, a bench top power supply is connected to limit the current and adjust the voltage. Doing so, a direct connection of power to the LEDs is established as shown in Fig. 2.3. This enables the user to adjust the current going into the LEDs and measure the optical output. The fans used to cool the device are always switched "ON".

During the rollover test, the current input into the LED is increased in equal steps at steady state conditions, and the optical power output is measured along with the voltage required, to understand the relationship between the efficiency of the LEDs *vs* input power. The optical power output was measured using the ThorLabs S120VC detector head coupled to the PM100D radiometer.

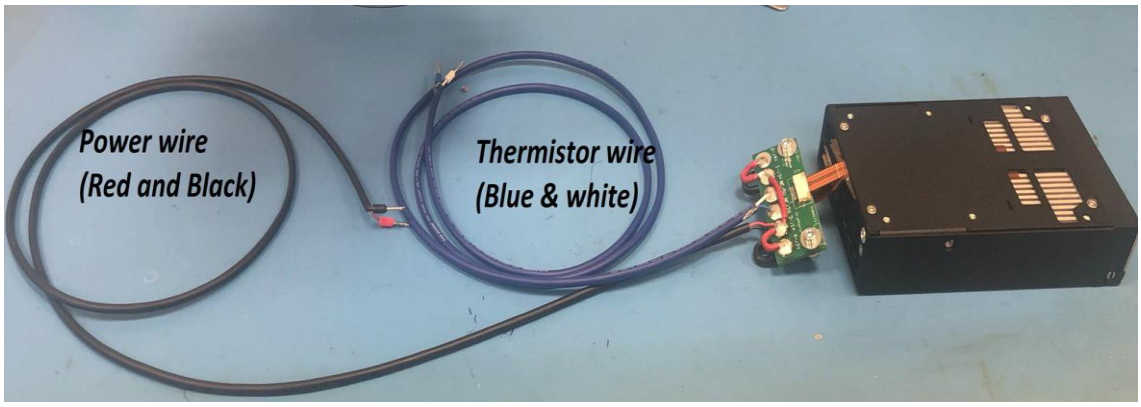

Figure 2.3: Device bypass for rollover test.

2.2.4. Balancing and Burn–In

A key quality step in the manufacturing process of a light device is ensuring that the device output is constant and reliable. A power meter (PD300RM–8W Starbright 7201580 Radiometer Dosimeter, Ophir [161]) to measure the intensity output from the device has been used. The device is placed at a 200 mm safe distance away from the power meter and connected to a software algorithm that is programmed to set the device to the defined target. The distance is chosen depending on the size of the device to ensure that all chains (set of 4 LEDs, in case of 265 nm, 285 nm, and 310 nm devices, and set of 16 LEDs for 275 nm device) can be evenly detected by the power meter. The resulting intensity output is used as a target for system balancing and to check if intensity varies significantly after the burn–in process (discussed below).

The software algorithm continuously heats and cools the device to ensure uniform light output is obtained from each chain. This is done to ensure that the light emission is consistent at a range of temperature conditions of the device. The device is switched "OFF" and "ON" multiple times by the program until a uniform light output is detected by the power meter. Fig. 2.4 shows the side view of the set–up used for balancing.

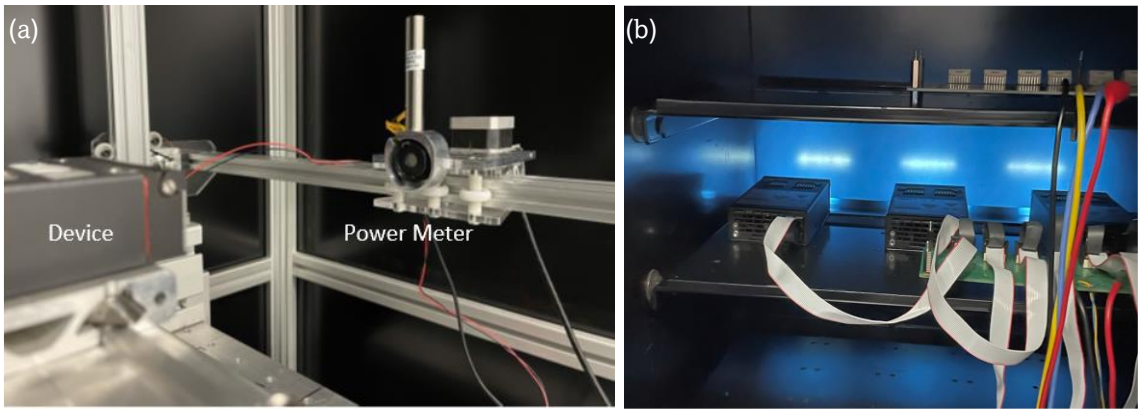

Figure 2.4: (a) Balancing set–up and (b) Burn–In Cabinet.

Once the device is balanced, it is important to ensure that the light output is consistent over time. The device is then placed on "burn–in" or running continuously at maximum intensity setting for 24–48 h (Fig. 2.4 (b)). After 24 h, the light output is measured and compared to potentially check for any increase or decrease in output. If the light output after 24 h is within 5% of the previous reading, the device is taken off the cycle.

2.2.5. Spectral Measurement

One of the objectives of the study was to comprehensively evaluate the performance of LEDs operating in the UV–C to UV–B region. The first step in doing this was to understand the emission spectrum. The emission spectrum is unique to the LED chosen and not the device, hence measuring the spectrum helped understand the LED behavior for further use in disinfection studies (Chapter 5, 6). Spectral measurement helps understand the underlying effect of a particular wavelength on substances and surfaces [162].

Fig. 2.5 shows a representation of the set–up used for spectral measurement. The device is mounted on the workbench and the sensor is placed at the center of the emitting window of the device. The device has been moved at multiple working distances away from the sensor to evaluate if the working distance shifted the peak wavelength of the LED used.

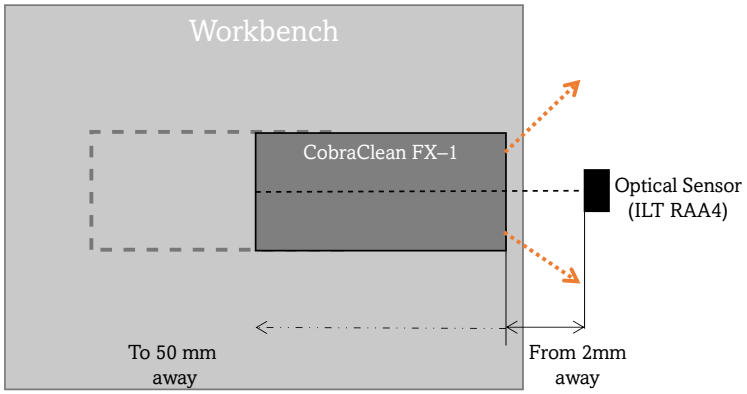

Figure 2.5: Representation of spectral Measurement set–up.

2.2.6. Uniformity Characterization

The same system set–up was used for these measurements as in Fig. 2.2 (a). As mentioned earlier, the motor gantry is linked to a LabView VI [163, 164], designed to capture the uniformity of the device under study. Using a custom program that allows input of gantry speed, the sensor (mounted on the motor gantry) is moved across the emitting face of the UV–C device, as shown in Fig. 2.6. At each point, the software commands the sensor to take a measurement and output the data to the LabView interface. For the uniformity measurements, an area of 120 mm × 30 mm was measured at a working distance of 10 mm between the sensor and emitting window. This area was decided based on the extent of light diversion from the device. The collected data builds a 3–dimensional surface intensity map that characterizes the overall uniformity of the device at a particular working distance and consequently, calculates the received dose at 1 cm s^{-1} speed of the motor. This

experiment has been conducted at different working distances to evaluate its effect on the uniformity of the device, an important criterion in any system design involving UV–C devices.

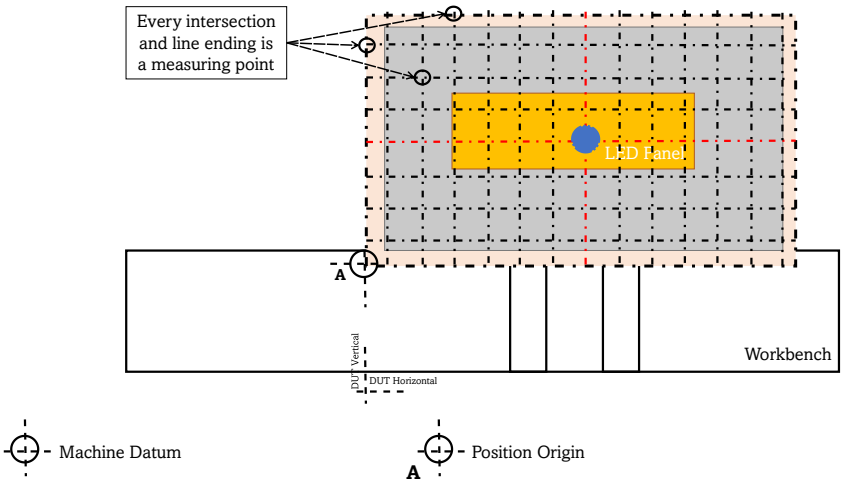

Figure 2.6: Representation of the area covered by the sensor in each measurement.

Two further measurements have been collected in this characterization step – longitudinal and lateral intensity distributions. For this, the LabView program was changed so that the sensor moved along the horizontal and vertical center lines of the device (see red lines in Fig. 2.6). All other characterization experiments were conducted with the sensor at the center of the emitting view (blue circle in Fig. 2.6).

2.2.7. Lifetime Set–up and Measurements

For real–environment applications of UV–C devices in disinfection application of drinking water or wastewater, it is necessary to ensure that the device output is monitored and evaluated, as it is known that the LED output decreases with time [143, 165]. While the device electronics have a long lifetime, the LED lifetime needs to be monitored carefully. Given that the UV–C LEDs have low efficiency, this means that more heat is released during emission than light output. Hence, it is important to monitor the intensity of the emission over time. Characterizing the lifetime of the devices helps understand the amount of intensity lost with time which can also be factored into the experiments [165]. For the purpose of lifetime testing, two devices of each wavelength have been manufactured. A chamber (hereafter called lifetime chamber, Fig. 2.7 (a)) has been used to keep the devices running continuously at an ambient temperature of 25°C. The devices were taken out of the lifetime chamber at certain intervals of time to measure and record the power output. The

output power from each device was measured every day for the first 2 weeks of operation, once a week for the next 2 months, and once a month until the output power dropped in intensity below 80% of the measured intensity on day 0 of the process. Two parameters were monitored to capture the lifetime of the device – overall light output and individual chain output. ThorLabs manufactured S120VC detector coupled to a PM100D radiometer was used for these measurements [166].

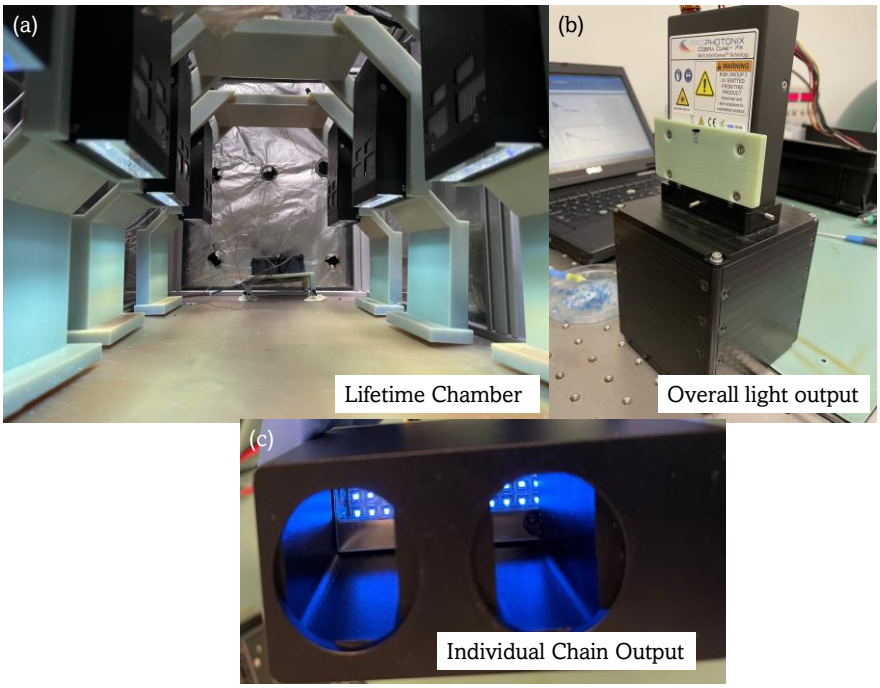

Figure 2.7: (a) Lifetime chamber, (b) Set–up for overall output measurement, and (c) Set–up for individual chain output measurement.

The test set–up for overall light output measurement consisted of a black box, where the device could be mounted on one end and the sensor on the other end to ensure operator safety from the UV–C radiation; see Fig. 2.7 (b). Measurements were taken only when the device reached a temperature of 40°C and above with all the fans running. This was done to replicate running experimental conditions and to avoid any possible cooldown of the devices during experimental set–up which could lead to different measurements. The temperature was monitored using a resister connected to the device electronics. During the LED lifetime, it is possible that a small section of LEDs could drop in intensity with time relative to the other LEDs on the device and need to be monitored to further establish device characteristics [165]. A test jig was designed that allowed for testing of these individual chains; see Fig. 2.7 (c). These measurements provide a good understanding of the device and the LEDs used with time and relative to each other.

2.3. Results and Discussions

2.3.1. LED Selection

As discussed in Section 2.2.1, firstly, all possible LEDs in the range of interest for disinfection have been studied and data input into a worksheet. A continuously updated *ad–hoc* library was created throughout the period of this thesis. Table 2.2 shortlists the possible manufacturers and LEDs considered in the initial phase of this work based on the decision parameters (see Table 2.1). See Appendix 2.A on other parameters that have been drawn from the datasheets for analysis.

The products **highlighted** in Table 2.2 are the products that have been selected for this study. Due to the COVID–19 outbreak, the market for UV–C LEDs has risen exponentially due to their ability to disinfect surfaces and air. As of 2022, the highest efficiency reported by any manufacturer for UV–C LEDs is 13% (SD3535-UVAC-X, 280+395 nm LEDs from Ivy Bridge Technology [60]). This can be seen in comparison to Table 2.2 (from 2019) where the maximum reported efficiency was 8% by Bolb, concurrent to the observations of Jasenak et al. (2018) [136, 167]. The chosen LEDs can be seen in Fig. 2.8 and their datasheet specifications are listed in Table 2.3.

Table 2.2: LEDs evaluated.

Model	Product Name	Wave-length (nm)	Efficiency	Manufacturer
3535 Packaged LED	-	275	8.035%	Bolb
BR35QF275M01X	-	275	3.500%	PEC
PU88S31	UVC 3535 Emitter	280	3.365%	Lextar
BR35QF275S01X	-	275	3.030%	PEC
3535 Packaged LED	-	275	3.000%	Bolb
EOLS-310-697	**UV SMD LED**	**310**	**2.380%**	**EQ Photonics**
IN-C35PUDTDU1	3535 UV LED	275	2.307%	Inolux
KL265-50W-SM-WD	**Klaran WD Series**	**265**	**2.285%**	**Klaran- Crystal IS**
PB2D-UCLA-TC	PB2D Series	275	2.205%	ProLight Opto
LTPL-G35UVC275GZ	G35 Series	275	2.165%	Liteon
LJU1106EAE-275	-	275	2.118%	Stanley Electric

Model	Product Name	Wave-length (nm)	Efficiency	Manufacturer
SCF35BUC00D1Z4	Sanan SCF35BUC Series	275	2.083%	Sanan
CUD7GF1B	CA3535	275	2.053%	Seoul Viosys
KL265-50V-SM-WD	Klaran WD Series	265	2.000%	Klaran- Crystal IS
ZEUBE265-2CA	-	265	1.976%	Stanley Electric
CUD7GF1A	CA3535	275	1.818%	Seoul Viosys
LTPL-G35UV275GR-E	G35 Series	275	1.794%	Liteon
LTPL-G35UVC275GH	G35 Series	275	1.791%	Liteon
LEUVK37B50HF00	UV 3535 LED PKG	280	1.785%	LG Innotek
KL265-50U-SM-WD	Klaran WD Series	265	1.714%	Klaran- Crystal IS
WS3535C20LF-310	UVB LED SMD	310	1.781%	VioLumas
LTPL-G35UVC275GM	G35 Series	275	1.677%	Liteon
S-S35J-F3-275-01-5-180	-	275	1.666%	Seti
CUD8GF1A	CA535	285	1.666%	Seti
XST-3535-UV	**SMD UV C**	**280**	**1.550%**	**Luminus**
ELUC3535NUB	2.4W Series	275	1.538%	Everlight
LTPL-G35UV275GC-E	G35 Series	275	1.538%	Liteon
RVXR-280-SM-073605	RayVio XR UV LEDs	280	1.538%	RayVio
CUD8GF1B	CA535	285	1.494%	Seti
PB2D-1CLA-TC	PB2D Series	275	1.470%	ProLight Opto
WS3535C30LF-310	UVB LED SMD	310	1.454%	VioLumas
PU35CL1 V0	UVC 3535 Emitter	275	1.333%	Lextar
XBT-3535-UV	**SMD UV C**	**275**	**1.318%**	**Luminus**
ELUC3535NUB	2.4W Series	275	1.282%	Everlight
ELUC3535NUB	2.4W Series	275	1.282%	Everlight
S-S35F-F3-310-01-4	-	310	1.250%	Seti
S-S35F-F3-285-01-4	-	285	1.250%	Seti
S-S35F-F3-275-01-4-110	-	275	1.250%	Seti

Klaran- Crystal IS 265 nm | Luminus 275 nm | Luminus 285 nm | EpiGap 310 nm

Figure 2.8: Selected LEDs for further analysis.

Table 2.3: Characteristics of selected LEDs.

Manufacturer	Klaran- Crystal IS [168]	Luminus UV [169]	Luminus UV [170]	EpiGap [171]
Part Number	KL265-50U-SM-WD	XBT-1313-UV-A150-AG270-00	XST-3535-UV-A60CD280-01	EOLS-310-697
Peak Wavelength (nm)	265	275	285	310
Viewing Angle (°)	130°	150°	60°	120°
Maximum Forward Current (mA)	700	100	800	600
Package size (mm)	3.5 × 3.5	1.35 × 1.35	3.5 × 3.5	3.5 × 3.5
Number of Pads	3	2	2	2

2.3.2 COBRA FX–1 Device

The COBRA FX–1 Series from ProPhotonix was used as the base platform to manufacture UV–C LED based lamps, see Fig. 2.2 (c). This section provides an overview of the device used and its manufacturing process. The device is 74.5 mm × 125.8 mm × 28 mm in size and typically uses UV–A based LEDs (COBRA Cure FX–1 Series, [172]). The UV–A version of the FX–1 has 40 LED chips, 10 LEDs per chain and 4 chains in series. Each chain is connected to an individual driver on the printed circuit board (PCB) and can be controlled by the user. The LEDs are wire bonded onto the substrate and mounted onto a light head (heat sink and other electronics). The device has a thermal heat sink mounted on the back

of the substrate and a fan cooled system. The thermal heat sink is made up of Aluminum 6061 material and is EDM wire eroded with 20 fins, in total, to maximize thermal efficiency. The device comes with 2 reflector options – D4 and DW. D4 is a divergent type of reflector whereas the DW is divergent–wide type. DW reflector with a divergent angle of 110° provides more dose and D4 with a divergent angle of 40° provides more intensity. The divergence profile is shown in Fig. 2.9. For this study, the D4 type reflectors have been chosen as there was a shortage of space between the reflector and LEDs in the DW version, such that a slight change in placement of LEDs on the substrate could short the entire circuit board. Additionally, the D4 version concentrated a significant amount of light emission towards the central region.

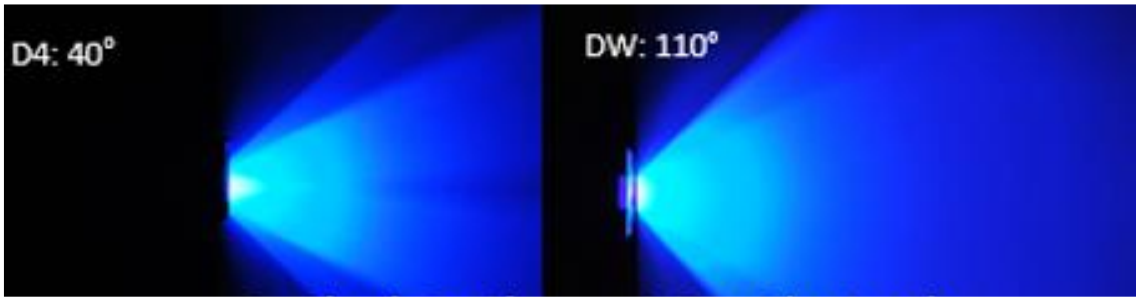

Figure 2.9: Optical options for COBRA FX–1 Series.

The FX–1 driver is a controlled conditioner driver that uses 48V DC safe current. It provides a controlled drive of the LEDs on substrate. The driver has a micro–controller, on the PCB, which monitors the temperature of the substrate and applies cooling via the fans on the device. The driver helps maintain a safe electric current so as to not short or burn out the LEDs. It uses a 0–10 volts analog signal corresponding to the 0–100 percent intensity range. The software of the FX–1 is a system of different algorithms working together to ensure safe running of the device. It has multiple outputs and inputs which help convert electrical input from the source to optical power output from the LEDs.

The above discussed device has been redesigned to fit in UV–C LEDs, chosen in Section 2.3.1, according to their respective footprint. To accommodate the UV–C LEDs, firstly, the substrate was redesigned. While the UV–A FX–1 accommodated 40 LEDs, the UV–C LED FX–1 device accommodated 16 LEDs, for the 265 nm, 285 nm, and 310nm LED sources, and 64 LEDs for 275 nm LEDs. The 275 nm LEDs are smaller in size (1.35 mm × 1.35 mm) compared to the other three wavelengths studied (3.5 mm × 3.5 mm). Fig. 2.10 shows the redesigned substrate for the UV–C FX–1 265 nm version. The design accommodated 4

LEDs per chain in 4 chains controlled by drivers in the case of the 16–LED sources whereas for the 275 nm source, the arrangement was 16 LEDs per chain.

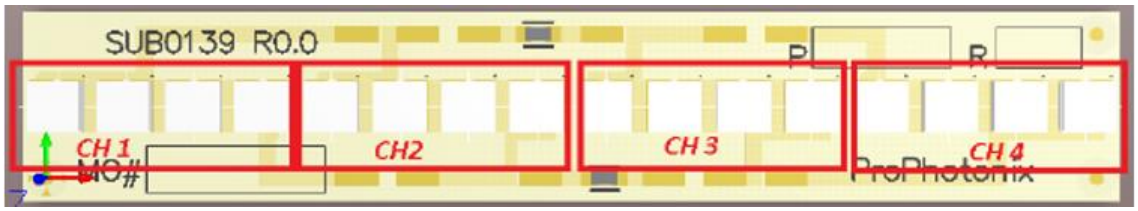

Figure 2.10: Redesigned substrate for 265 nm light source.

The LEDs are mounted onto AlN substrates in a clean room (to avoid contamination during placement) and sent to reflow through an oven to ensure accurate placement. The substrates are then mounted onto a light head before being enclosed in a mechanical housing. Fig. 2.11 (a–d) shows the LEDs built onto a COBRA FX–1 device (here onwards called COBRA Clean FX–1 device).

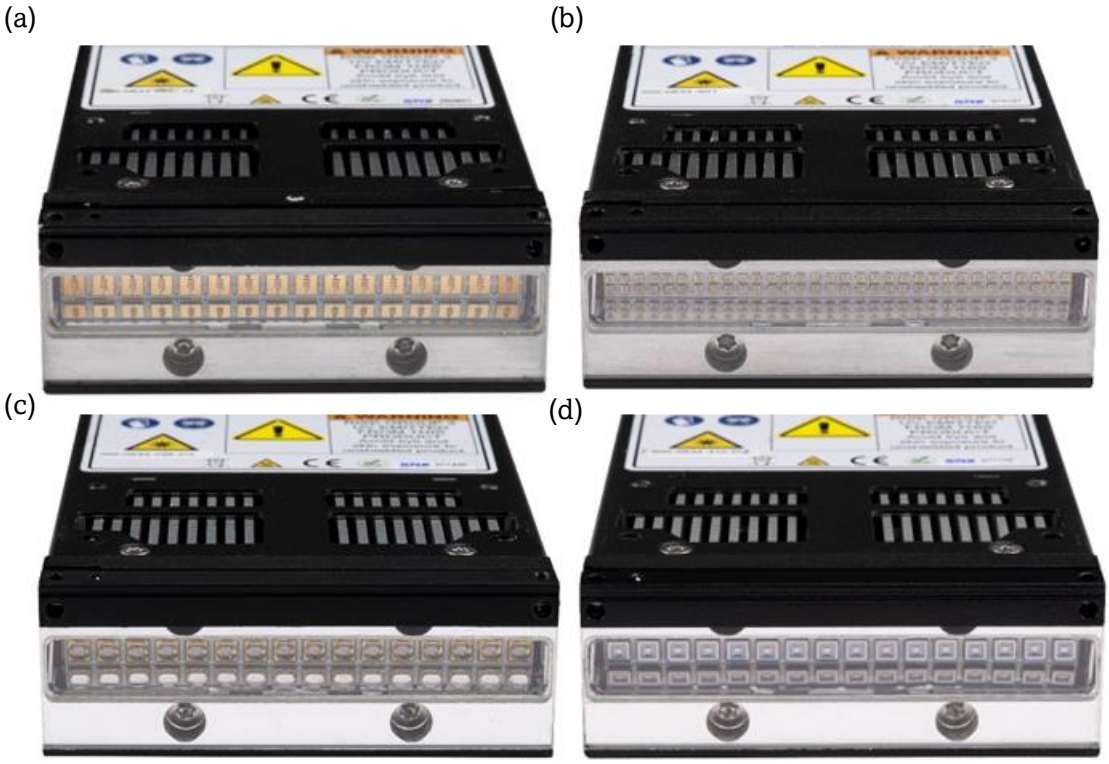

Figure 2.11: COBRA Clean FX–1 devices – (a) 265 nm, (b) 275 nm, (c) 285 nm, and (d) 310 nm [173].

2.3.3. Rollover Test

For LEDs, it is expected that with an increase in current the light output increases linearly [174]. For the LEDs selected, the datasheet maximum current has been listed in Table 2.4. In theory, at this current, the light output should be maximum. However, this is not the case as the LED light output is a function of other parameters specific to the device. As mentioned earlier, the test conditions of the manufacturer are near ideal hence can only be used as guide figure. This was proven by the data obtained from rollover tests. Fig. 2.12 (a–d) shows the plot of input current to measured power output for all the devices. Initially, it can be seen that the power output linearly increases with current but after a certain current, 200 mA for COBRA Clean FX–1 265 / 285 / 310 nm and 100 mA for COBRA Clean FX–1 275 (here onwards the devices will be referred to as FX–1 λλλ), the power output starts to stabilize or fall off the linear trend. This current value above where the linear relationship starts to drop off is referred to as the "*rollover current*" (listed in Table 2.4).

To calculate the rollover current (point of off–linearity), the raw data from measurements are fit to a polynomial trend (dark blue lines in Fig. 2.12(a–d)) and the equation of the line is extracted. Further a linear trend line is defined based on initial linear data for comparison. The data is input into a software and the point of off–linearity is extracted. This has been listed as "Rollover current" in Table 2.4.

Table 2.4: Comparison between manufacturer currents and device–controlled tests.

Wavelength (nm)	Manufacturer LED Datasheet		Rollover Current (mA)	Set Drive Current (mA)
	Typical Current (mA)	Maximum Allowable Current (mA)		
265	500	700	317	300
275	40	100	130	120
285	350	800	467	450
310	350	600	437	440 → 420

Rollover current provides the lighting device manufacturer with a safe operation limit within which the LEDs will provide the best lifetime possible. Once the rollover current was calculated, this served as a baseline for optical testing and determination of the system point. The system point is the programmed maximum current on the respective device to ensure adequate device lifetime. In the case of the COBRA Clean FX–1's used, upon rollover tests, the operating current for the devices was set to 300 mA for the 265 nm LEDs, 120 mA for

the 275 nm LEDs, 450 mA for the 285 nm LEDs, and 420 mA for the 310 nm LEDs. This was the programmed value as input for the balancing test (Section 2.2.4). It must be noted that for the FX–1 310 device, the set current was higher than the rollover point. This was decided as the 310 nm LED efficiency was the highest among the LEDs studied and for an additional power output, as it is known 310 nm inactivation requires high doses [175].

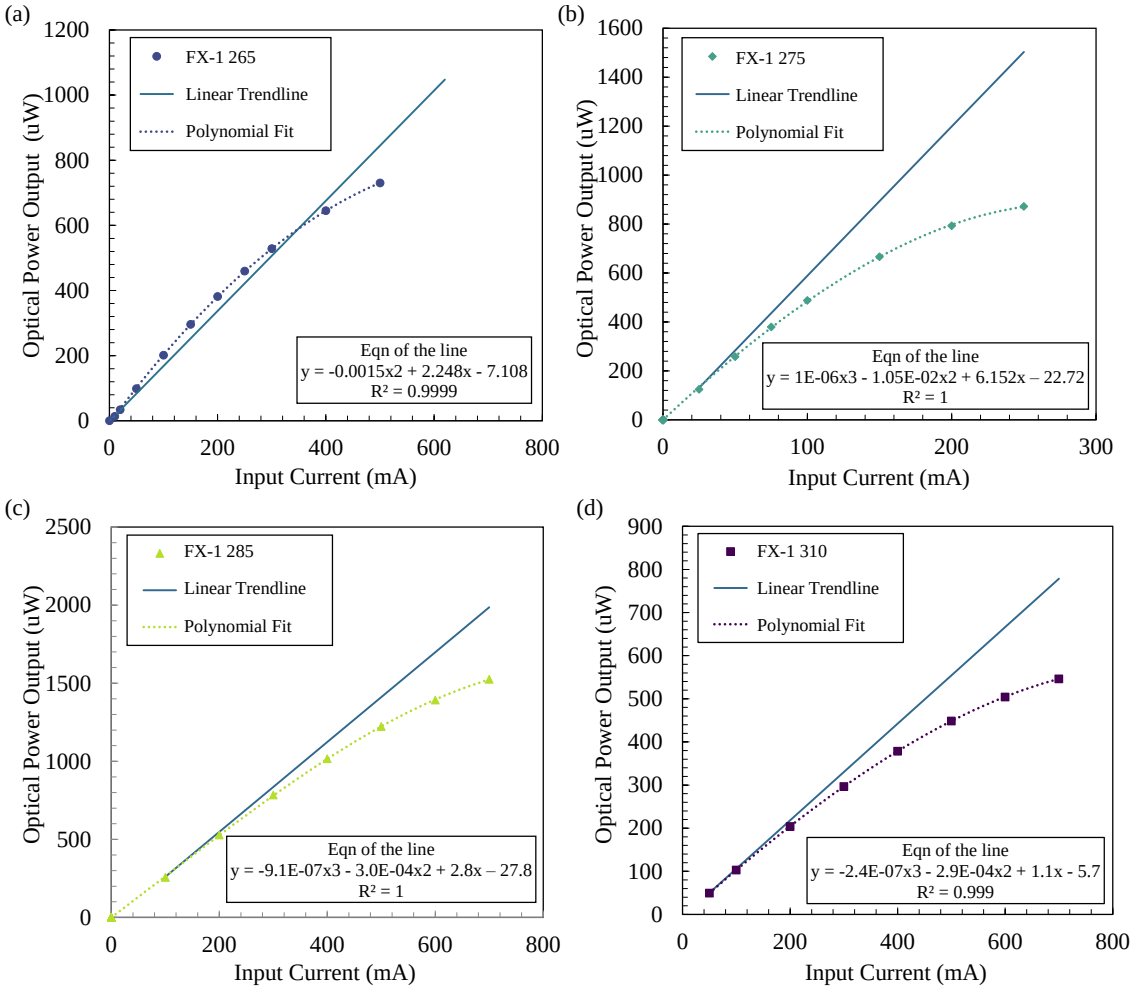

Figure 2.12: Rollover test results for the devices (a) 265 nm, (b) 275 nm, (c) 285 nm, and (d) 310 nm.

All the devices were then placed on continuous running for 24–48 h. Among the 4 devices studied, the 310 nm device intensity varied significantly (> 5%) after 48 h of running (Fig. 2.13 (a)). This was investigated further. The device was kept running for a further 3 days and the drops were monitored. It can be seen that, for instance, Device 1 (Violet line in Fig. 2.13 (a)), the difference in measured intensity of the device between Day 0 and Day 4 is nearly 15%. This meant that the device was possibly overheating, or the LEDs were not reliable with time and prone to degrade faster. In total after 9 days of operation, the relative

intensity drop was seen to be 9%. In an attempt to compensate for the intensity drop observed, the set current was reduced to 420 mA (Dark blue arrow in Table 2.4). The device was tested again, and the intensity measured was seen to be consistent with time; see Fig. 2.13 (b). While there was an intensity drop after certain hours of operation for most devices, the average variation in measured intensity, after 9 days of operation, was within ± 5% of Day 0 (Except in the case of Device 4).

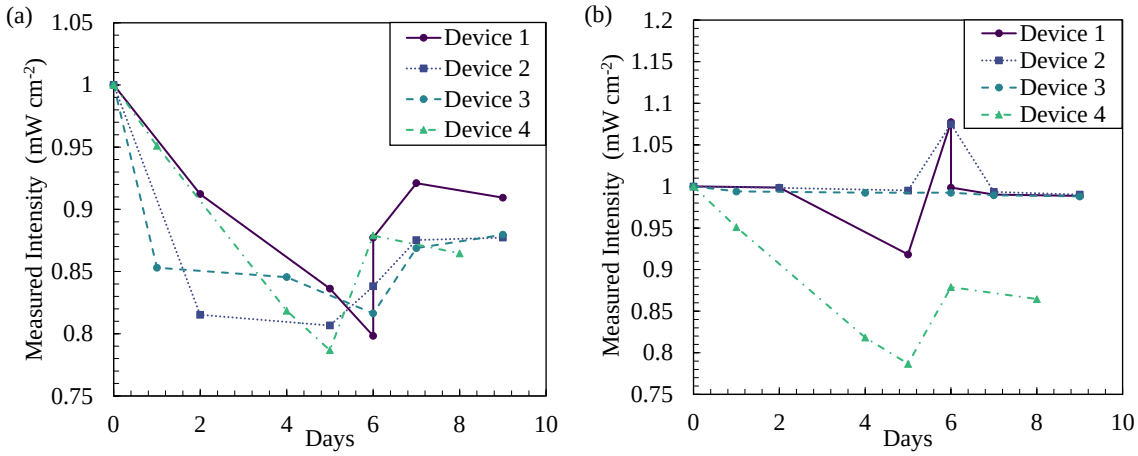

Figure 2.13: Measured Intensity with time – (a) At 440 mA set current and (b) at 420 mA set current.

In the case of FX–1 275, it can be seen that the set current was higher than the maximum allowable current for the LEDs. This was decided upon checking the temperature of the substrate and behavior of the LEDs after burn–in, as the LEDs could handle higher input current due to the device electronics. Each LED was constantly monitored to ensure that the increased current did not short the LED or cause possible substrate damage.

2.3.4. Emission Spectrum

The study of the emission spectrum helps verify the actual peak wavelength of the LEDs under study. Understanding the emission spectrum of the LEDs is critical for the use of the devices in different applications [160, 162]. In the case of this study, the emission spectrum of the LEDs was measured using the ILT RAA4 coupling optic connected to the 950UV series spectroradiometer. The measurements were conducted at a distance of 50 mm between the emitting window and sensor, at 5 ms integration time of the sensor. The working distance was chosen based on estimated safe exposure distance so as to not saturate the sensor, whereas the integration time was selected based on reducing the signal–to–noise ratio of the radiometer. The UV–C LEDs selected have low emission compared to

UV–A or higher wavelength LEDs, and hence at higher integration times, the noise was higher than the actual light signal obtained. The measured emission spectrum relative to their peak wavelength of each of the LEDs can be seen in Fig. 2.14 (a). During measurements, it was seen that the 285 nm LEDs are the most powerful LEDs compared to the other wavelengths. A comparison between the manufacturer specified peak wavelength of the LEDs to the measured peak wavelength of the LEDs has been listed in Table 2.5. Note that the manufacturers always specify an individual peak wavelength on the datasheets but within an error range of ± 5 nm. It can be verified from Table 2.5 that the peak wavelengths are within the manufacturer's specifications.

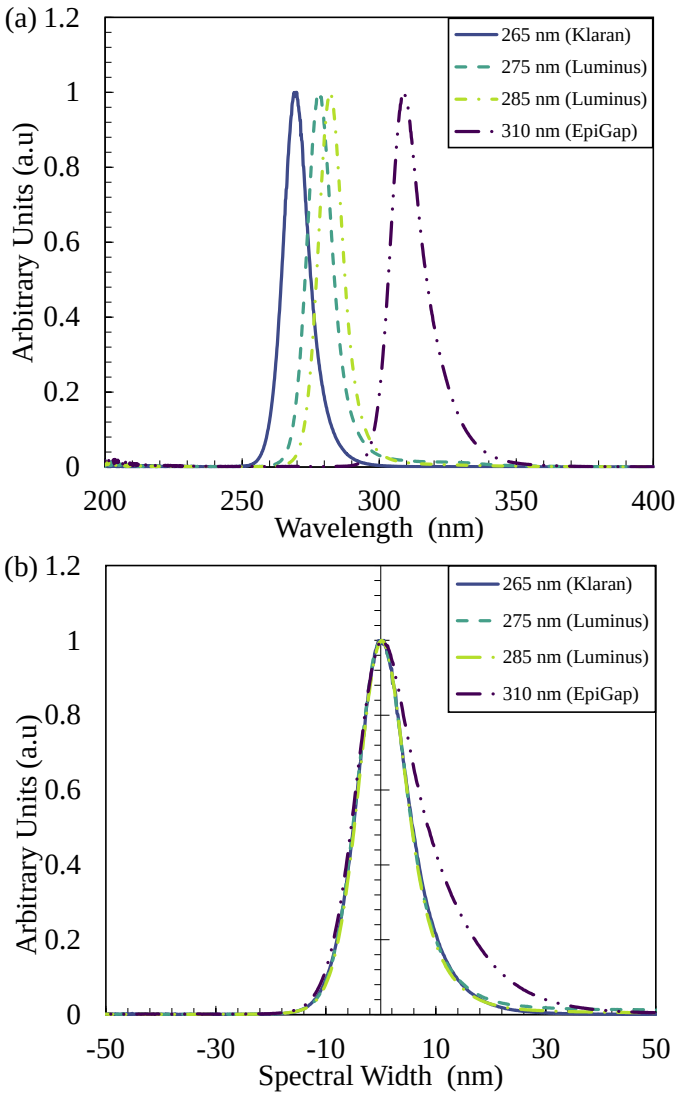

Figure 2.14: (a) Measured LED spectrum relative to their respective peaks and (b) Spectral width comparison.

Table 2.5: Comparison between manufacturer mentioned peak and measured peak wavelength.

Manufacturer Peak Wavelength (nm)	Measured Peak Wavelength (nm)	Full width half maximum (nm)
265	269.883	12.392
275	278.027	10.644
285	282.085	10.062
310	308.694	13.998

A key feature of the LED spectrum is the evaluation of the width by means of the full width half maximum (FWHM). The FWHM is the difference between the values of the independent variable at which the dependent variable is equal to half of its maximum value [175, 176]. In other words, it is the width of a spectrum curve measured between those points on the *y*–axis, which are half the maximum amplitude. To calculate the FWHM of each LED, the spectrum is centered relative to the peak wavelength, as shown in Fig. 2.14 (b), and the wavelength points, at which the relative intensity was 50% of the maximum, were extracted. This data will be further utilized in Chapter 5 and 6 of this thesis. It is evident that the 310 nm LED (from EpiGap) is wider than the other wavelengths chosen. Table 2.5 summarizes the measured spectral width data for each wavelength. Due to the FWHM, it can be seen that the FX–1 275 and FX–1 285 devices' emission are within each other's ranges. This meant that the use of one of the devices would be sufficient in further studies. It is important to note that all experiments were conducted in triplicates on 3 separate days to ensure the reproducibility and repeatability of the data obtained. The error obtained was in the third significant digit and hence is not visible in the plots.

2.3.5. Effect of Current on Intensity

The rollover test helps identify the safe limit of operation and is the point where the light emission goes off–linear with current [127, 177]. To ensure that the relation between optical power output and current is linear, this test has been conducted. The input current was increased from 10% of the maximum set current (Rollover current) to 100%, and the resultant optical power intensity was measured using an optical sensor. Fig. 2.15 plots the relation between relative intensity and current for each of the devices used in this study.

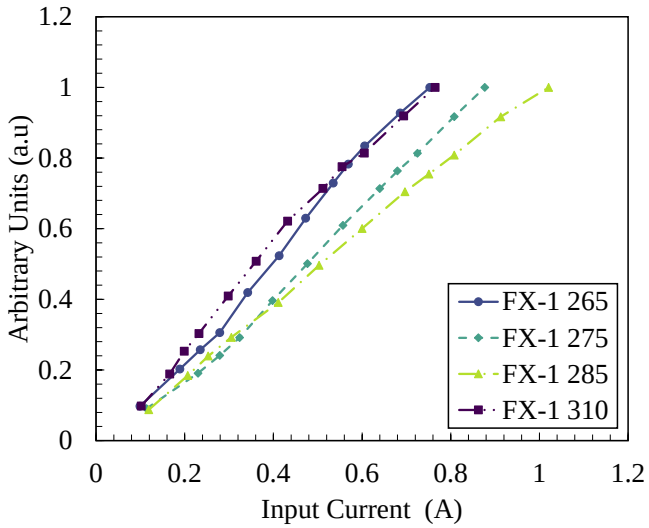

Figure 2.15: Relative intensity *vs* current measurements.

As these devices were set to a safe current from the rollover test, the relation between current and intensity was seen to be linear. Each device data, in Fig. 2.15, is plotted relative to its measured intensity at 100% current. This test was done with custom control in a lab environment i.e., the device was connected to an ammeter and voltmeter, that the operator could control. In application conditions, the device is connected to a potentiometer which regulates the current flowing into the device. This test helped in gaining confidence that a 10% turn on the potentiometer will mean 10% of the maximum deliverable intensity is emitted by the device, thus establishing complete control over the amount of light for disinfection experiments. Another key output from this test was the measured spectrum as the current input increases. LEDs are known to undergo thermal drift with the increase in temperature of the substrate [127]. This will occur if the substrate is not being cooled sufficiently by the device electronics. The resulting effect of a thermal drift would be on the potential application of the device. It has been studied that thermal drift causes the LEDs to shift to a higher wavelength by up to 15 nm. Certain applications that use LEDs as light sources require specific target wavelengths. Therefore, ensuring that no thermal drift occurs is necessary for the reliability of the device. As the intensity was recorded, the measured spectrum was extracted as well. Fig. 2.16 (a–h) plots the measured spectrum at each intensity alongside the peak wavelength at each input current for all the devices studied. It was seen that, in almost all the studied devices, the peak wavelength shift was not significant (maximum of ± 1 nm) with an increase in input current. This indicated that the device electronics are cooling the substrate sufficiently enough so as to not cause a wavelength shift due to temperature increase at the LED junction, with an increase in current input.

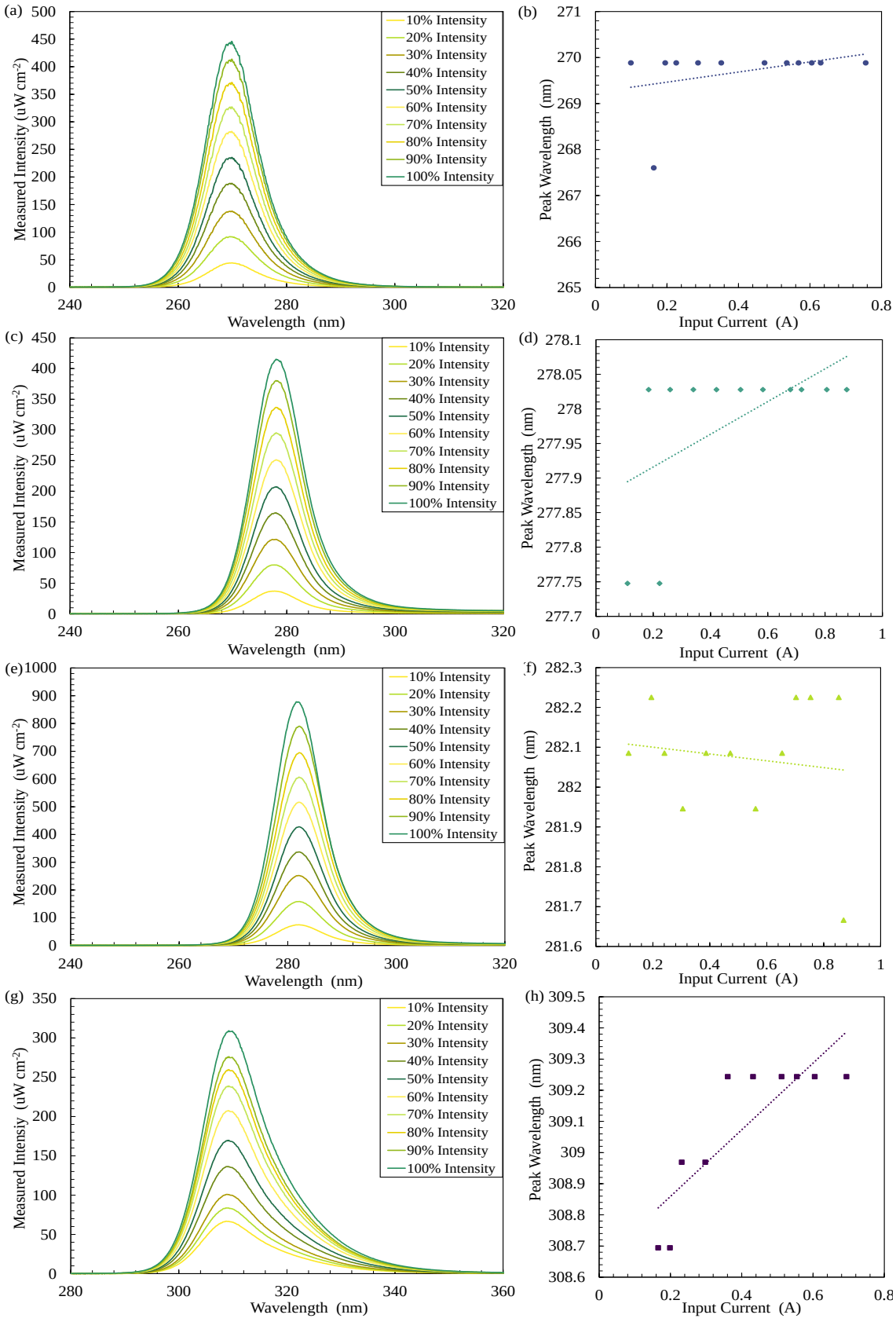

Figure 2.16: Measured spectrum at each intensity and peak wavelength shift with current for – (a–b) FX–1 265, (c–d) FX–1 275, (e–f) FX–1 285, and (g–h) FX–1 310.

2.3.6. Device Light Output

To use the devices for disinfection processes, it is necessary to understand the light distribution reaching the target area. The device uniformity test provided valuable input to understanding the light spread across an area in front of the emitting window [176]. This test was conducted at a working distance of 10 mm away from the sensor. Fig. 2.17 (a–d) shows the 3D uniformity plot for all the devices.

Among the devices tested, FX–1 285 can be seen to emit the highest intensity at 10 mm away from the window. It can be seen in the plot that the light intensity in the center is high compared to that of the top and bottom ends of the device. This is due to the optics used within the devices. The optic (in this case D4, Section 2.3.2) concentrates the light emitted by the LEDs to the central region with a gradual decrease as the sensor moves away from the center of the device. The color bands in Fig. 2.17 indicate the intensity range. The plots clearly show how light is distributed along the area scanned (120 mm × 30 mm). This will be used in further discussions of Chapter 5 and 6.

Using the same set–up and program, the lateral and longitudinal profiles were drawn along the central line of the light sources for distances between 5 mm to 40 mm away from the sensor. Fig. 2.18 plots the lateral and longitudinal profiles of the devices. From the longitudinal profiles, it can be seen that the side chains are at a higher intensity compared to the central LEDs (Fig. 2.18 (b–d) (L)). This can be attributed to the fact that during balancing (Section 2.2.4), the sensor is at a certain distance away from the device. The side chains (CH1 and CH4 in Fig. 2.10) are at an angle relative to the sensor receptive surface while the central chains (CH2 and CH3 in Fig. 2.10) are perpendicular to the center of the measuring sensor. When the whole device is set to the current value, the side chains will result in lower measurements due to the placement of the sensor. This can be avoided by balancing each chain individually, although this has not been done for this work.

From the lateral profiles in Fig. 2.18 (R), it can be seen that they are the same as the side view of the uniformity plots in Fig. 2.17. As the light source is moved away from the sensor, the plot starts to flatten out. In the case of 5 mm working distance (WD) profiles, the profile is concentrated vertically from -5 mm to 5 mm from the center of the device, whereas for 40 mm, the profile is broader between -15 mm to 15 mm from the center.

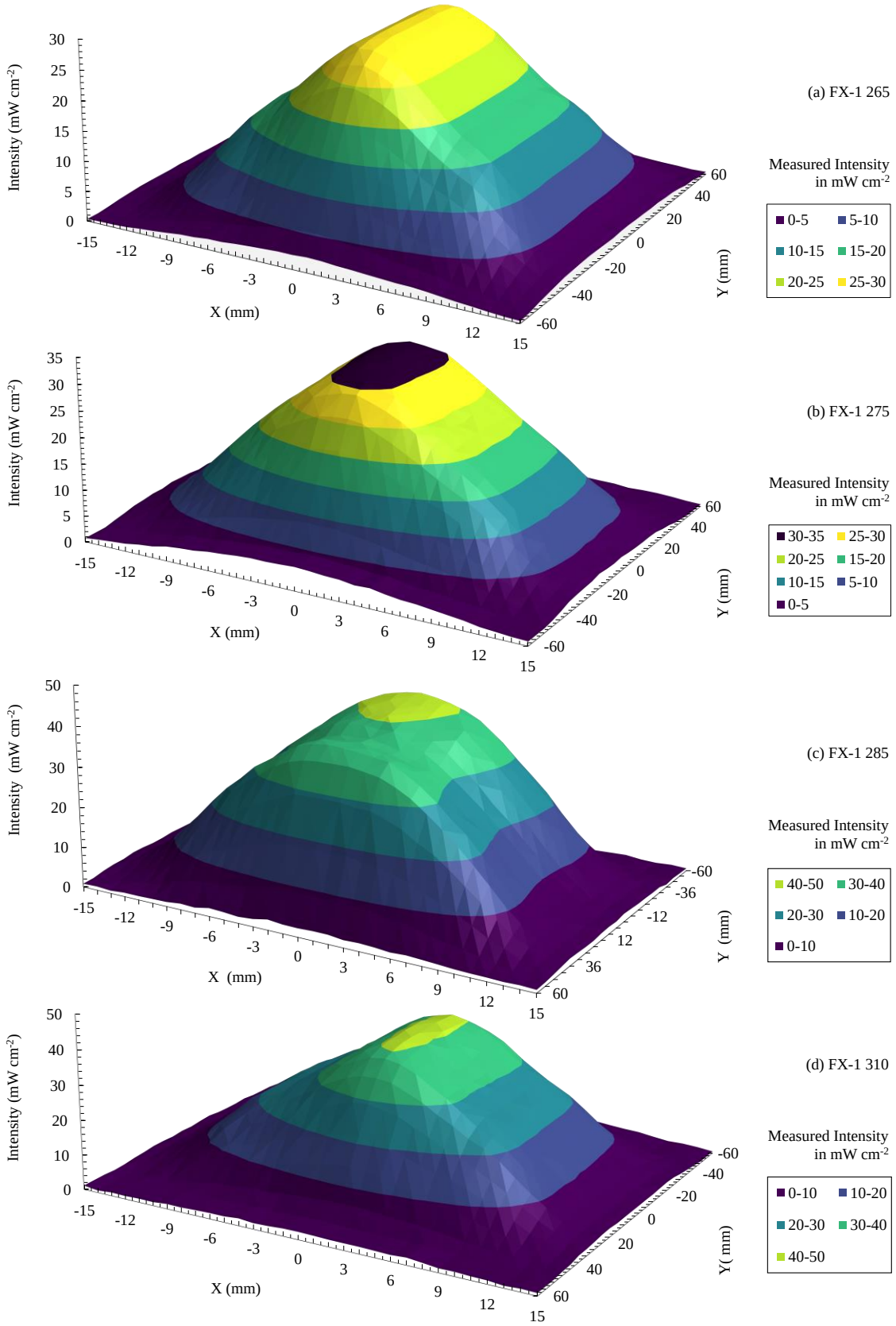

Figure 2.17: 3D Uniformity Plot at 10 mm away from the sensor for – (a) FX–1 265, (b) FX–1 275, (c) FX–1 285, and (d) FX–1 310.

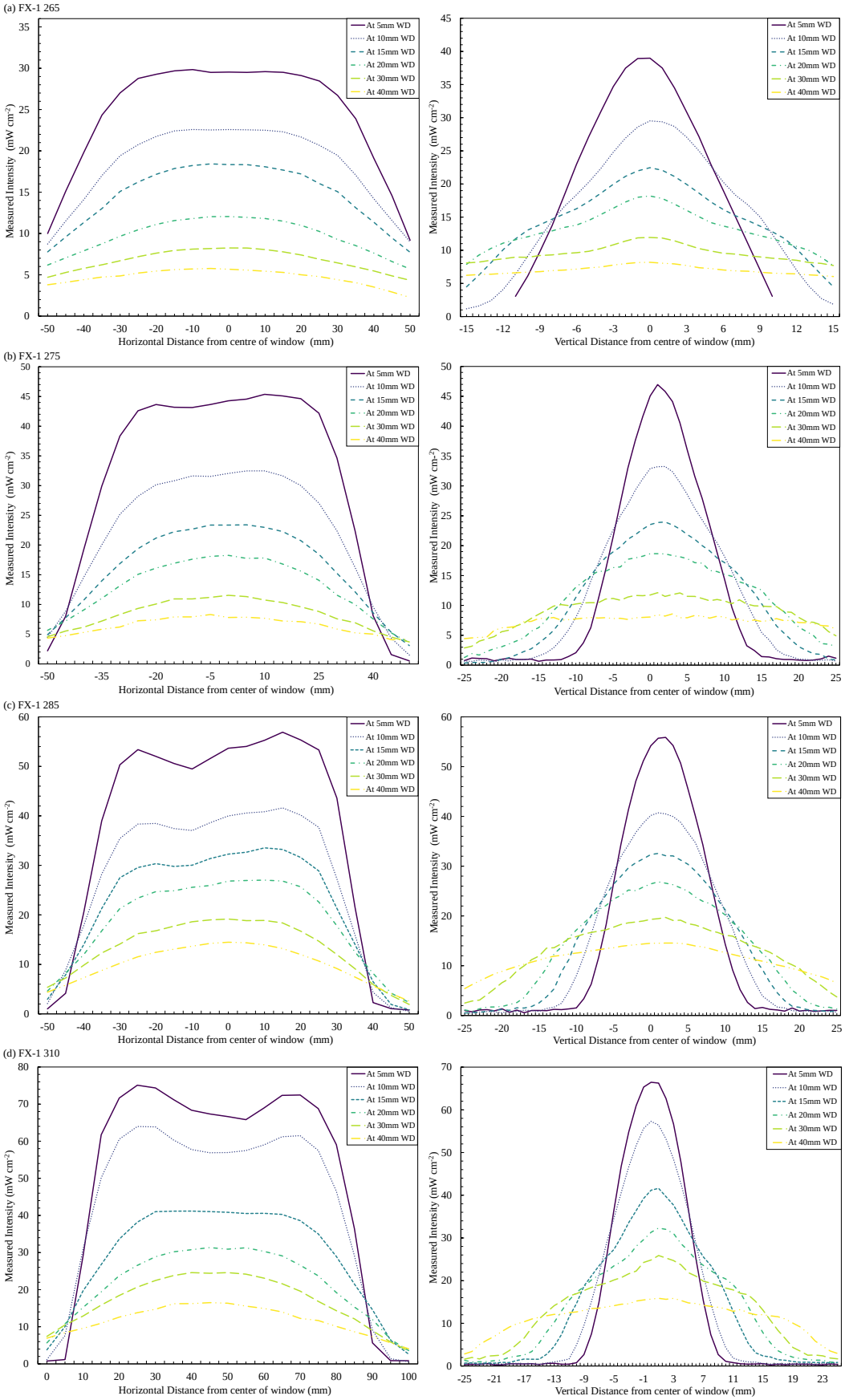

Figure 2.18: (L) Longitudinal profile and (R) Lateral profiles for FX–1 devices.

2.3.7. Effect of Working Distance on Intensity and Dose

The total intensity acting on a target area is a function of the light emitting source and the distance between the source and the target [178, 179]. With an increase in the distance from the target, the light intensity decreases as the spread of light is wider, as represented in Fig. 2.19 (a). The same amount of light is spread over a wider area, at a larger distance. The effect of working distance on intensity and dose has been studied for the devices built for further use in this thesis. Evaluation of the effect of working distance on intensity and, consequently, the dose helps factor in the actual values for calculating disinfection rates.

For this study, the sensor was positioned central to the emitting window of the device, and the workbench (see Fig. 2.5) was moved from distances of 2 mm to 30 mm away from the sensor. Fig. 2.19 (b) plots the measured peak intensities at each working distance. It can be seen that all devices follow the same trend with an increase in distance between the sensor and emitting window. The trend that followed was seen to be exponential. This is concurrent with other studies in literature that observed an exponential loss in intensity with distance [162, 179]. Given the exponential loss trend observed, it can be expected that the dose loss with working distance should follow the same. This was not the case when the calculated dose, at 1 cm s^{-1}, was extracted from the program. It is important to note that Fig. 2.19 (b, c) plots the peak intensities and peak dose values of the scans conducted.

Fig. 2.19 (c) plots the calculated dose loss with an increase in working distance. It is important to note that, as expected, there was a loss of UV dose with working distance, although, in contrast to the intensity loss, the loss observed in dose is gradual. This is due to the fact that UV dose is the integral under the curve of intensity measured [150]. While the intensity decrease is step down at each working distance, the dose decrease is much more gradual as it is a function of intensity, time, and speed considered. This trend was also observed in Raymont et al. (2002) [179]. Table 2.6 summarizes the results of the tests conducted and provides a comparison between the devices tested. FX–1 285 has the highest intensity and dose compared to the other wavelengths.

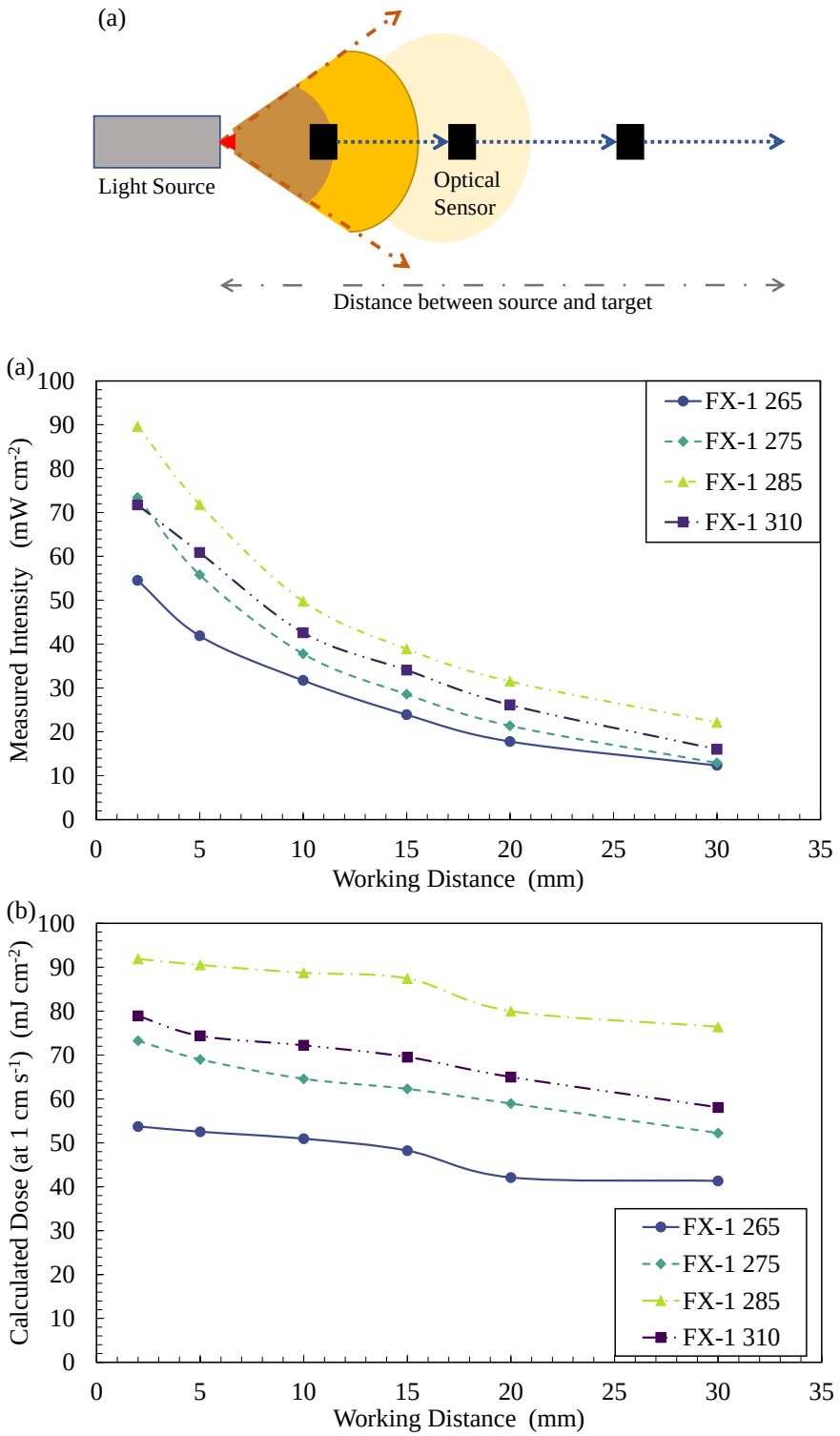

Figure 2.19: (a) Representation of effect of working distance, (b) Plot of measured intensity *vs* working distance, and (c) Plot of dose (at 1 cm s^{-1}) *vs* working distance.

Table 2.6: Measured Intensity (*I* in mW cm^{-2}) and dose (*D* in mJ cm^{-2}) at multiple working distances.

Working Distance (mm)	FX–1 265		FX–1 275		FX–1 285		FX–1 310	
	I	*D*	*I*	*D*	*I*	*D*	*I*	*D*
2	54.50	53.74	73.42	73.26	89.59	91.93	71.71	78.91
5	41.86	52.53	55.77	69.00	71.81	90.53	60.85	74.38
10	31.70	50.94	37.76	64.59	49.73	88.74	42.58	72.22
15	23.89	48.22	28.55	62.29	38.87	87.45	34.04	69.55
20	17.79	42.12	21.36	58.94	31.46	80.01	26.11	65.00
30	12.33	41.34	12.91	52.23	22.14	76.45	16.01	58.08

2.3.8. Device Lifetime

It has been known that many UV LED based devices are hampered by limited lifetimes due to degradation [180]. Reliability and lifetime improvement of the devices requires a better understanding of the failure feature and mechanisms within the LEDs chosen [181-185]. Gong et al. (2006) conducted a study on the degradation mechanism of 265 nm UV LEDs and found that the leakage current induced an optical degradation of the LED sources [183]. This experiment was conducted to evaluate the progress of an LED from the start of its use in the device until approximately 20% loss in overall intensity is obtained (L80). Understanding the lifetime helps estimate the useful operating lifetime of a device. Device lifetime data also provides insights on the reliability of the device electronics. While most drops can be associated to LED degradation, any unwanted drops will help realize device problems. The lifetime experiments of the FX–1's were conducted between November 2020 – December 2021.

Fig. 2.20 is the plot of measured data for all the devices after a certain number of operational hours. The plot shows the device's overall power output (teal diamond marker points) and the average chain output measured (navy blue square marker points). It provides a clear understanding of how the LEDs behave with time. For instance, initially, for about 145 and 400 h of operation of the FX–1 265 and 275, respectively, the optical power output keeps

increasing and then a dip in output can be observed. Initially, the power output of the LEDs increases because they are new. The LEDs have lower junction temperatures and the thermistors within them remain relatively cool, resulting in less heat dissipation to the cooling system [180]. However, as time passes, the junction temperature stabilizes and the LEDs return to their original emission power, as determined by system balancing. With continuous operation over an extended period, the LEDs start to degrade, leading to a decline in the overall power output [181]. This degradation can be attributed to various factors such as aging, wear and tear, and the cumulative effects of prolonged use. As a result, the power output of the LEDs experiences a dip as their performance gradually diminishes [180-184]. While the 265 nm and 275 nm LEDs were seen to reach about 80% of day 0 measurements in 3700 h of operation, the FX–1 285 was seen to reach L80 in 800 h of operation.

The degradation rate of the FX–1 285 LEDs was the highest compared to the other LEDs studied, almost exponential with the operation time, thus raising questions of its effectiveness. To further investigate potential reasons behind this drop, the power output per chain was evaluated (Fig. 2.21 (a)). It was seen that 2 of the chains (Chain 3 (triangles) and Chain 4 (X markers)) were causing the exponential drop. Chains 1 and 2 were seen to stabilize after approximately 800 h, although dropping nearly 15% at the same time. Between 800 and 3500 h of operation, chains 1 and 2 dropped 8–10% whereas chains 3 and 4 dropped 13–15%.

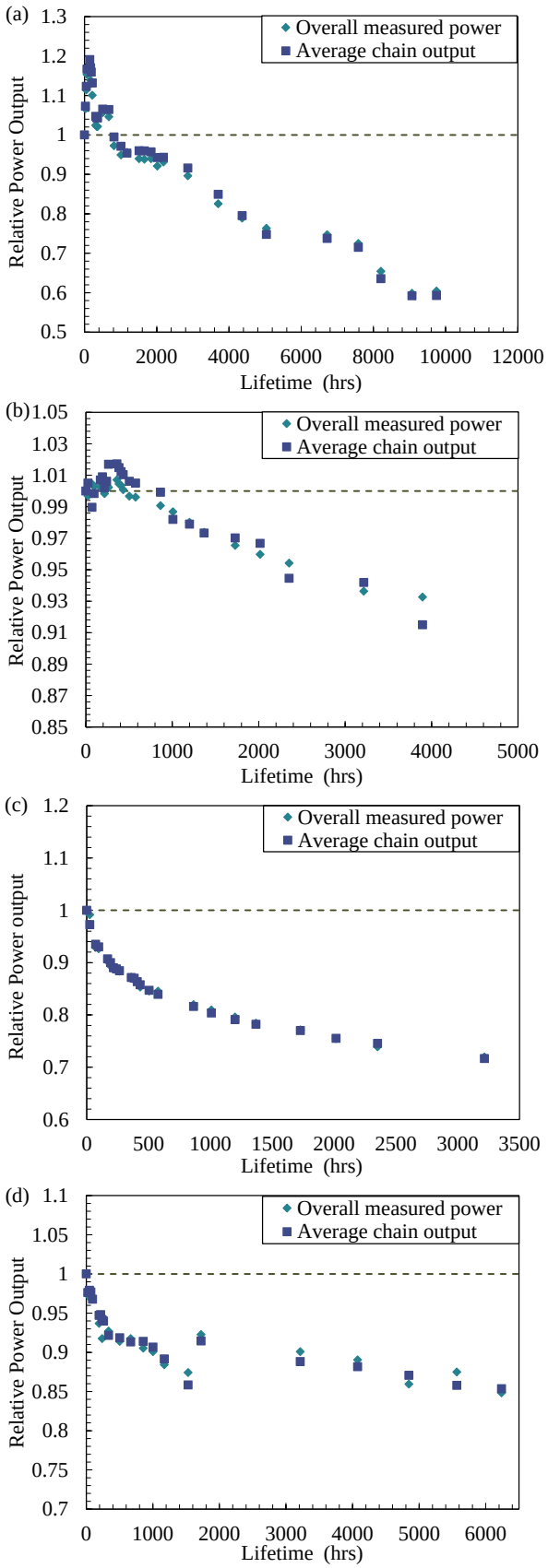

Figure 2.20: Lifetime data for – (a) FX–1 265 (after 9700 h), (b) FX–1 275 (after 3800 h), (c) FX–1 285 (after 3200 h), and (d) FX–1 310 (after 6200 h).

A closer look at the devices, found that the optical lens from one of the LEDs (Red circle in Fig. 2.21 (b)) had fallen off the LED body due to temperature rise during operation, explaining the chain 4 drop seen in Fig. 2.21 (a). It was also seen that the LEDs in chains 3 and 4 were dimmer compared to the other chains. This was due to the quality of the LEDs and associated with the manufacturing bin of the LED received from the manufacturer. Power output per chain for other devices is shown in Appendix 2.B (Fig. 2.B.1 (a–c)). For the FX–1 310, although no increase in light output was obtained, the power output stabilized with time (after 1500 h of operation) and hence no further investigation was conducted.

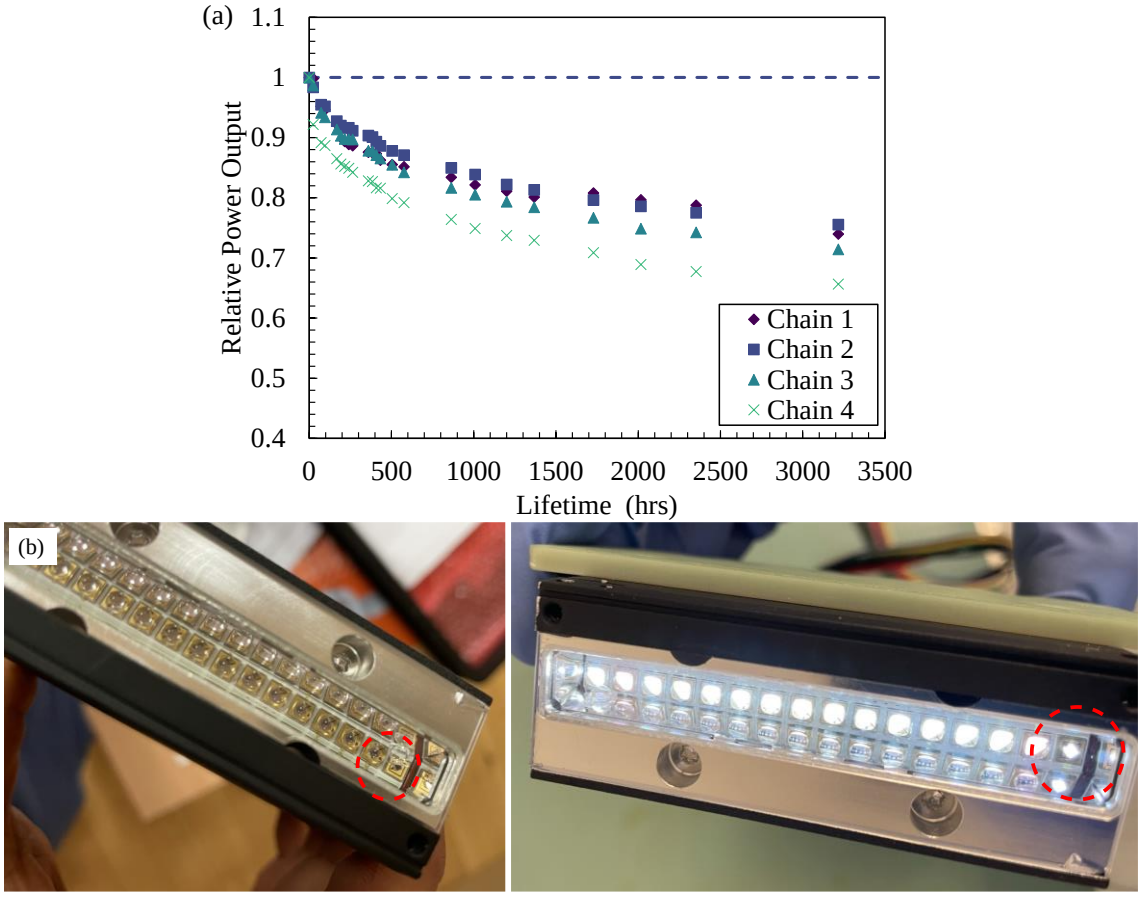

Figure 2.21: (a) Individual chain output with time for FX–1 285 and (b) FX–1 285 LED degradation.

2.4. Conclusions

This chapter evaluated multiple UV–C LED suppliers and chose LEDs centered at 265 nm, 275 nm, 285 nm, and 310 nm to be used in the manufacturing of the light sources. The LEDs obtained were incorporated into the ProPhotonix COBRA FX–1 series. The device was further characterized to understand the behavior of the LEDs within the device. Rollover tests assisted in setting a safe current to the LEDs for a longer lifetime and reliable operation of the device. Each wavelength's spectrum, intensity, and dose characteristics were evaluated for comparison and a better understanding of how best to use them in a disinfection system. The peak wavelength of the devices were found to be 269.8 nm, 278 nm, 282.1 nm, and 308.7 nm for FX–1 265, 275, 285, and 310 devices, respectively. It was further verified that the devices showed a linear response to an increase in input current. An exponential trend in loss of intensity was obtained while studying the effect of working distance on intensity and was seen to be similar for all the devices. Unlike the intensity profile, the dose loss with an increase in the working distance of the devices was found to be gradual. The device intensity profile and uniformity data will be further used to help model and characterize a UV–C LED based disinfection system in this thesis. The longitudinal profiles showed that the side chains of the device emitted slightly higher intensity compared to the central chains, due to the experimental procedure of balancing.

Amongst the LEDs studied, 285 nm LEDs possessed the highest radiant intensity output and were seen to possibly make the 275 nm LEDs redundant. Further characterization of the devices showed that the LEDs were prone to wavelength shift with an increase in input current. For the 265, 275, 310 nm LEDs, the wavelength shift was lower compared to the 285 nm LEDs, when the input current was increased. The lifetime analysis of FX–1 285 showed that the LEDs were not reliable and degradable after only 800 h of operation, possibly due to quality of the LEDs (adhesive failure of the optical lens) and the manufacturing bin of the LED received whereas the other devices showed a lower loss in intensity with operational time. Therefore, analyzing the data from FX–1 285, it was decided that the LED device will not be used for further studies in this work. An inspection of the discussed results in this chapter raised the question of the validity of the measurements conducted. It was necessary to ensure that the sensors used for each of the experiments were returning "true" and reliable data. To answer this question, the following chapter analyzes the parameters that could affect measurements from different optical sensors and elucidates how to choose a sensor depending on the application of use.

Appendix Chapter 2

2.A. LED Product Library

LED Database (as of 10/08/2022)

Package Size	Package Thickness	LED Size	Model	Product Name	Wavelength	Viewing angle	Lens Type	Number of Pads	Junction Temperature (°C)	Forward Voltage (V)	Rated Current(mA)	Power Output (mW)	Maximum Current (mA)	Input Power	Efficiency	Manufactuer	Status of product
3.5*3.5	1.3	1.7	3535 Packaged LED		275	150	Flat	2		5.6	20	9	20	0.112	8.035714%	Bolb	Under development
0.25*0.25	0.018		2010 LED Chip		275	170		2		5.8	20	5	20	0.116	4.310345%	Bolb	Released
1.3*1.3	1	0.5*0.5	XBT-131-UV	SMD UV	275	150	Flat	2	85	6.5	25	6.5	100	0.1625	4.000000%	Luminus	Released
4.5*4.5	1.8		BR45QF275M01X		275	75	Flat	2		5	20	3.5	50	0.1	3.500000%	PEC	Released
3.5*3.5	1.8		BR35QF275M01X		275	125	Flat	2		5	20	3.5	50	0.1	3.500000%	PEC	Released
3.5*3.5	1.1	0.5*0.5	PU88S31	UVC 3535 Emitter	280	140	Hemispherical	3	65	5.2	20	3.5	30	0.104	3.365385%	Lextar	Released
9*9	1.8		BR90QF275S25X		275	105	Flat	2		25.5	300	250	500	7.65	3.267974%	PEC	Released
6.8*6.8	2.12	4.35	NCSU334B		280	115	Flat	3	110	6.5	350	70	600	2.275	3.076923%	Nichia	Released
3.5*3.5	1.8		BR35QF275S01X		275	125	Flat	2		5.5	60	10	150	0.33	3.030303%	PEC	Released
4.5*4.5	1.8		BR45QF275S01X		275	75	Flat	2		5.5	60	10	150	0.33	3.030303%	PEC	Released
3.5*3.5	1.3	1	3535 Packaged LED		275	150	Flat	2		7.5	20	4.5	20	0.15	3.000000%	Bolb	Released
6*6	1.3	1.7	6060 SMD		275	150	Flat	2		7	350	72	350	2.45	2.938776%	Bolb	Released
3.45*3.45	1.78	1*1	MNU1109EAE-275		275	120	Flat	2		5.2	20	3	50	0.104	2.884615%	Stanley Electric	Released
18*18	1.8		BR180QF275S100X		275	105	Flat	2		11	3500	1100	5000	38.5	2.857143%	PEC	Released
1.5*1.5	0.5	0.5*0.5	PQ2A-UCLA-TC	PQ2A Series	275	35	Flat	2		6.8	20	3.5	30	0.136	2.573529%	ProLight Opto	Released
3.25*3.25	1.2	1*1	SCF35BUC00D1Z1	Sanan SCF35B UC Series	275	130	Flat	3	100	6	40	6	100	0.24	2.500000%	Sanan	Released
3.45*3.45	1.3	1*1	E275*3		275	130	Flat	3	180	6	30	4.5	40	0.18	2.500000%	ILT	Released
3.65*3.65	2.55	1.07*1.07	SCD35BUC0061Z1	Sanan SCD35B UC UVC	275	80	Hemispherical	2	125	7	350	60	500	2.45	2.448980%	Sanan	Released
3.5*3.5	1.8		BR35QF310S01X		308	125	Flat	2		5.4	60	8	100	0.324	2.469136%	PEC	Released
3.65*3.65	1.27	1*1	SCM35BUC00E1Z1	SCM35B UC Series	275	140	Flat	2	90	7	350	60	350	2.45	2.448980%	Sanan	Released
0.25*0.25	0.018		2010 LED Chip		275	170		2		6.5	20	3	20	0.13	2.307692%	Bolb	Under development
3.5*3.5	1.5	1*1	EOLS-310-697	UV SMD LED	310	120	Flat	2		6	350	50	600	2.1	2.380952%	EQ Photonics	Released
3.5*3.5	1.65	0.6*0.4	IN-C35PUDTDU1	3535 UV LED	275	125	Flat	2	60	6.5	20	3	20	0.13	2.307692%	Inolux	Released
3.45*3.45	2.95	3.2	BRT-B35DD7E1CSC	B35	275	30	Hemispherical	2		6.5	20	3	30	0.13	2.307692%	BioRaytron	Released
3.45*3.45	2.4		BRT-B35CD7E1CSC	B35	270	80	Hemispherical	2		6.5	20	3	30	0.13	2.307692%	BioRaytron	Released
3.45*3.45	2.25	3.2	BRT-B35LD7E1CSC	B35	275	100	Hemispherical	3		6.5	20	3	30	0.13	2.307692%	BioRaytron	Released
3.45*3.45	2.95	3.2	BRT-B35DD7D1CSC	B35	275	30	Hemispherical	2		6.5	30	4.5	30	0.195	2.307692%	BioRaytron	Released
3.45*3.45	2.4		BRT-B35CD7D1CSC	B35	270	80	Hemispherical	2		6.5	30	4.5	30	0.195	2.307692%	BioRaytron	Released
3.45*3.45	1.8		BRT-B35LD7D1CSC	B35	275	120	Hemispherical	2		6.5	30	4.5	30	0.195	2.307692%	BioRaytron	Released
3.9*3.9	2.56	1*1	3939C26501C000	3535 High Power UVC	265	60	Hemispherical	3	85	7	100	16	100	0.7	2.285714%	UVT Taiwan	Released
3.9*3.9	1	1*1	3939F26501C000	3535 High Power UVC	265	120	Flat	3	85	7	100	16	100	0.7	2.285714%	UVT Taiwan	Released
3.5*3.5	0.61	0.8*0.8	KL265-50W-SM-WD	Klaran WD Series	265	130	None	3	115	7	500	80	700	3.5	2.285714%	Klaran- Crystal IS	Released
1.3*1.3	1.1		SCM13AUC00F1Z1	Sanan SCM13A UI Series	275	130	Flat	2	75	5.5	40	5	100	0.22	2.272727%	Sanan	Released
3.5*3.5	1.05	2.4	PB2D-UCLA-TC	PB2D Series	275	120	Flat	3	85	6.8	20	3	30	0.136	2.205882%	ProLight Opto	Released
3.65*3.65	1.27	0.5*0.5	SCM35BUC00E1Z2	SMD Series	275	130	Dome	2	60	6	100	13	100	0.6	2.166667%	Sanan	Released
3.5*3.5	0.8	1*1	RVXR-308-SM-06500300	RayVio XR UV LED	308	120	Flat	3		6	100	13	100	0.6	2.166667%	RayVio	Released
3.5*3.5	1.78	1*1	LTPL-	G35	275	120	Flat	2	90	6.2	350	47	500	2.17	2.165899%	Liteon	Released
3.85*3.85	1.4		HQS-3535UVC005G		275	120	Flat	3		6.5	50	7		0.325	2.153846%	HuaQiSheng	Released
3.45*3.45	2.95	3.2	BRT-B35DD7C1CSC	B35	275	30	Hemispherical	2		7	50	7.5	50	0.35	2.142857%	BioRaytron	Released
3.45*3.45	2.4		BRT-B35CD7C1CSC	B35	270	80	Hemispherical	2		7	50	7.5	50	0.35	2.142857%	BioRaytron	Released
3.45*3.45	1.8		BRT-B35LD7C1CSC	B35	275	120	Hemispherical	2		7	50	7.5	50	0.35	2.142857%	BioRaytron	Released
3.5*3.5	1.3	1*1	LJU1106EAE-275		275	120	Flat	2		5.8	350	43	600	2.03	2.118227%	Stanley Electric	Released
3.65*3.65	1.31	0.6*0.4	SCF35BUC00D1Z3	Sanan SCF35B UC Series	275	120	Flat	2	75	6	40	5	60	0.24	2.083333%	Sanan	Released
3.5*3.5	1.2	1*1	SCF35BUC00D1Z4	Sanan SCF35B UC Series	275	120	Flat	3	115	6	100	12.5	200	0.6	2.083333%	Sanan	Released
3.5*3.5	1.2	0.6*0.4	CUD7GF1B	CA3535	275	120	Flat	3	120	5.6	100	11.5	250	0.56	2.053571%	Seoul Viosys	Released
3.5*3.5	0.61	0.8*0.8	KL265-50V-SM-WD	Klaran WD Series	265	130	None	3	115	7	500	70	700	3.5	2.000000%	Klaran- Crystal IS	Released
3.5*3.5	2.24	1*1	ZEUBE265-2CA		265	120	Hemispherical	2		6.9	440	60	500	3.036	1.976285%	Stanley Electric	Released
6.35*6.35	1.8	1*1	CUD8AF1C	AAP 1 Chip	275	120	Flat	2	120	5.6	30	3.3	60	0.168	1.964286%	Seoul Viosys	Released
3.85*3.85	1.4		HQS-3535UVC010G		275	120	Flat	3		6.5	100	12.5		0.65	1.923077%	HuaQiSheng	Released
6.8*6.8	1.3	4*4	SCF68AUC00D4Z1	Sanan SCF68A UC Series	275	130	Flat	3	85	27	350	175	500	9.45	1.851852%	Sanan	Released
3*3	0.9	0.5*0.5	PBLB-1CQA-TCL	PBLB Series	275	120	Flat	1		6.8	20	2.5	70	0.136	1.838235%	ProLight Opto	Released
3.5*3.5	1.2	1*1	CUD7GF1A	CA3535	275	120	Flat	3	120	5.5	30	3	60	0.165	1.818182%	Seoul Viosys	Released
3*3	1.05	1*1	CUD7QF1A	3030	275	120	Hemispherical	2	120	5.5	20	2	60	0.11	1.818182%	Seoul Viosys	Released
3.5*3.5	1.78	1*1	LTPL-G35UV275GR-	G35	275	120	Flat	2	90	6.5	150	17.5	200	0.975	1.794872%	Liteon	Released
3.5*3.5	1.78	1*1	LTPL-	G35	275	120	Flat	2	90	6.7	600	72	700	4.02	1.791045%	Liteon	Released
3.4*3.4	1.62		LEUVK37B50HF00	UV 3535 LED PKG	280	125	Flat	2		7	20	2.5	25	0.14	1.785714%	LG Innotek	Released
3.5*3.5	0.61	0.8*0.8	KL265-50U-SM-WD	Klaran WD Series	265	130	None	3	115	7	500	60	700	3.5	1.714286%	Klaran- Crystal IS	Released
3.5*3.5	1.18	1*1	WS3535C20LF-310	UVB LED SMD	310	130	Flat	2	90	5.5	50	4.9	120	0.275	1.781818%	VioLumas	Released
6.35*6.35	1.8	2*2	CUD8AF4D	UV AAP Series	275	120	Flat	2	120	5.9	600	60	800	3.54	1.694915%	Seoul Viosys	Released
3.5*3.5	1.78	1*1	LTPL-	G35	275	120	Flat	2	90	6.2	250	26	300	1.55	1.677419%	Liteon	Released
3.5*3.5	1.1	1*1	S-S35J-F3-275-01-		275	130	Flat	3		6	100	10	350	0.6	1.666667%	Seti	Released
3.5*3.5	1.2	1*1	CUD8GF1A	CA535	285	120	Flat	3		6	20	2	30	0.12	1.666667%	Seti	Released
3.5*3.5	1.2	1*1	CUD9GF1A	CA535	295	120	Flat	3		6	20	2	30	0.12	1.666667%	Seti	Released
5*5	1	1.2*1.2	DUV280-S-C-X	SMD Ceramics	280	140	Flat	3		6	20	2	30	0.12	1.666667%	QD Jason	Released
6*6	1.8		BR60QF275S04X		275	135	Flat	2		11	300	55	250	3.3	1.666667%	PEC	Released
5*5	1	1.2*1.2	DUV310-S-C-X	SMD Ceramics	310	140	Flat	3		6	20	2	30	0.12	1.666667%	QD Jason	Released
3.5*3.5	1.18	1*1	XST-3535-UV	SMD UV	280	60	Hemispherical	3	100	6.45	350	35	800	2.2575	1.550388%	Luminus	Released
3.45*3.45	1.3	1*1	E275-10		275	130	Flat	3	180	6.5	160	16	180	1.04	1.538462%	ILT	Released

3.5*3.5	1.13	2*2	ELUC3535NUB	2.4W Series	275	120	Flat	3	70	6.5	100	10	300	0.65	1.538462%	Everlight	Released
3.5*3.5	1.78	1*1	LTPL-G35UV275GC-	G35	275	120	Flat	2	90	6.5	100	10	150	0.65	1.538462%	Liteon	Released
3.5*3.5	0.8	1*1	RVXR-280-SM-07360	RayVio XR UV LED	280	120	Flat	3		6.5	100	10	100	0.65	1.538462%	RayVio	Released
3.75*3.75			HQS-3535UVC608G		275	60	Hemispherica	3		6.5	100	10		0.65	1.538462%	HuaQiSheng	Released
3.75*3.75			HQS-3535UVC008G		275	120	Flat	3		6.5	100	10		0.65	1.538462%	HuaQiSheng	Released
6*6	1.35		LEUVA66G00HF00	1in 1 LED PKG	280	121	Flat	3		6.5	20	2	30	0.13	1.538462%	LG Innotek	Released
3.5*3.5	1.2	0.6*0.4	CUD8GF1B	CA535	285	125	Flat	3		5.8	150	13	200	0.87	1.494253%	Seti	Released
3.5*3.5	1.05	2.4	PB2D-1CLA-TC	PB2D Series	275	120	Flat	3	85	6.8	100	10	150	0.68	1.470588%	ProLight Opto	Released
6*6	1.35		LEUVA66G00HF00	278 LED PKG	280	126	Flat	3		7	100	10	150	0.7	1.428571%	LG Innotek	Released
3.5*3.5	1.18	1*1	WS3535C30LF-310	UVB LED SMD	310	130	Flat	2	90	5.5	100	8	200	0.55	1.454545%	VioLumas	Released
3.9*3.9	3.12	1*1	3939A26501C000	3535 High Power UVC	265	30	Hemispherica l	3	85	8	150	16	100	1.2	1.333333%	UVT Taiwan	Released
3.5*3.5	1.45	0.5*0.5	PU35CL1V0	3535 Series UV	275	125	Flat	3	65	6	30	2.4	30	0.18	1.333333%	Lextar	Released
3.5*3.5	1.18	1*1	XBT-3535-UV	SMD UV	275	130	Flat	3	100	6.5	350	30	800	2.275	1.318681%	Luminus	Released
3.45*3.45	2.25	3.2	BRT-B35CD7B1CSD	B35	275	100	Hemispherica	2		7	100	9	100	0.7	1.285714%	BioRaytron	Released
3.5*3.5	1.13	2*2	ELUC3535NUB	2.4W Series	275	120	Flat	3	70	6.5	300	25	300	1.95	1.282051%	Everlight	Released
3.5*3.5	1.13	2*2	ELUC3535NUB	2.4W Series	275	120	Flat	3	70	6.5	300	25	300	1.95	1.282051%	Everlight	Released
3.5*3.5	1.01	0.55*0.55	S-S35F-F3-310-01-		310	125	Flat	3		6	20	1.5	30	0.12	1.250000%	Seti	Released
3.5*3.5	1.01	0.55*0.55	S-S35F-F3-285-01-		285	125	Flat	3		6	20	1.5	30	0.12	1.250000%	Seti	Released
3.5*3.5	1.01	0.55*0.55	S-S35F-F3-275-01-		275	125	Flat	3		6	20	1.5	30	0.12	1.250000%	Seti	Released
3.5*3.5	1.18	1*1	WS3535C20LF-265	UVB LED SMD	265	130	Flat	2	90	5.8	50	3.6	120	0.29	1.241379%	VioLumas	Released
3.45*3.45	2.25	3.2	BRT-B35CD7A1CSD	B35	275	100	Hemispherica	2		7	150	13	150	1.05	1.238095%	BioRaytron	Released
3.5*3.5	0.8	1*1	RVXR-280-SM-07310	RayVio XR UV LED	280	120	Flat	3		6.5	100	8	100	0.65	1.230769%	RayVio	Released
3.5*3.5	1.18	1*1	WS3535C20LF-275	UVB LED SMD	275	130	Flat	2	90	6.3	50	3.8	120	0.315	1.206349%	VioLumas	Released
3.5*3.5	1.18	1*1	WS3535C48LF-310	UVC LED SMD	310	130	Flat	2	90	5.7	350	23.4	700	1.995	1.172932%	VioLumas	Released
6*6	1.8		BR60QF310S04P		308	135	Flat	2		11.5	300	40	400	3.45	1.159420%	PEC	Released
3.75*3.75			HQS-3535UVC602G		275	60	Hemispherica	3		6.5	40	3		0.26	1.153846%	HuaQiSheng	Released
3.75*3.75			HQS-3535UVC002G		275	120	Flat	3		6.5	40	3		0.26	1.153846%	HuaQiSheng	Released
3.5*3.5	2.24	1*1	ZEUBE265-1BB		265	120	Hemispherica	2		6.9	440	35	500	3.036	1.152833%	Stanley Electric	Released
3.9*3.9	3.2	1*1	IN-C40PUATKU1	4040UVC LED	275	30	Hemispherica l	3	65	7	150	12	150	1.05	1.142857%	Inolux	Released
3.9*3.9	2.6	1*1	IN-C40PUBTKU1	4040UVC LED	275	60	Hemispherica l	3	65	7	150	12	150	1.05	1.142857%	Inolux	Released
3.9*3.9	1.6	1*1	IN-C40PUCTKU1	4040UVC LED series	275	120	Flat	3	65	7	150	12	150	1.05	1.142857%	Inolux	Released
3.45*3.45	1.4	0.6*0.4	300SMD		300	120	Flat	2		9	200	20		1.8	1.111111%	UV Photonics	Released
6.35*6.35	1.8	1*1	CUD1AF1C	UV AAP Series	310	115	Flat	2		5.5	30	1.8	45	0.165	1.090909%	Seti	Released
3.5*3.5	1.18	1*1	WS3535C30LF-275	UVC LED SMD	275	130	Flat	2	90	6.3	100	6.8	200	0.63	1.079365%	VioLumas	Released
3.5*3.5	1.18	1*1	WS3535C48LF-265	UVC LED SMD	265	130	Flat	2	90	5.9	350	22	700	2.065	1.065375%	VioLumas	Released
1.12*1.12	0.4		JS-DUV310 A	Flip Chip	310					5.5	20	1.1	20	0.11	1.000000%	QD Jason	Released
3.5*3.5	2.24	1*1	ZEUBE265-2BA		265	120	Hemispherica	2		6.9	440	30	500	3.036	0.988142%	Stanley Electric	Released
3.5*3.5	1.2	1*1	CUD1GF1A	CA3535	310	120	Flat	3	120	6.2	20	1.2	30	0.124	0.967742%	Seoul Viosys	Released
4.4*4.4	1.5		BRT-B44LD7A1CS0	B44	275	120	Flat	3		7	150	10	150	1.05	0.952381%	BioRaytron	Released
4.4*4.4	1.5		BRT-B44LD8A1CS0	B44	280	120	Flat	3		7	150	10	150	1.05	0.952381%	BioRaytron	Released
1.12*1.12	0.4		JS-DUV280 A	Flip Chip	280					6	20	1.1	20	0.12	0.916667%	QD Jason	Released
6.35*6.35	1.8	2*2	CUD1AF4D	UV AAP Series	310	118	Flat	2		5.5	600	30	700	3.3	0.909091%	Seti	Released
6*6	1.8		BR60QF275S09X		275	125	Flat	2		16.4	700	100	350	11.48	0.871080%	PEC	Released
6.35*6.35	1.8	2*2	CUD1AF1D	UV AAP Series	310	120	Flat	2		5.5	200	9.5	250	1.1	0.863636%	Seti	Released
3.45*3.45	1.4	0.6*0.4	HP310SMD		310	120	Flat	2		8.5	350	25		2.975	0.840336%	UV Photonics	Released
3.5*3.5	2.24	1*1	ZEUBE265-1BA		265	120	Hemispherica	2		6.9	440	25	500	3.036	0.823452%	Stanley Electric	Released
3.5*3.5	0.8	1*1	XP4-280-SM-07703	RayVio XP4 UV LEDs	280	120	Flat	3		26	300	60	200	7.8	0.769231%	RayVio	Released
3.5*3.5	1.28	1*1	OP255-10P-SM	Optan	255	120	Flat	3	115	8	100	6	100	0.8	0.750000%	Optan	Released
3.5*3.5	1.28	1*1	OP275-10P-SM		275	120	FLat	3	115	8	100	6	100	0.8	0.750000%	Optan	Released
3.45*3.45	1.4	0.6*0.4	318SMD		318	120	Flat	2		10	200	15		2	0.750000%	UV Photonics	Released
5*5	1	1.2*1.2	DUV265-S-C-X	SMD Ceramics	265	140	Flat	3		6	20	0.75	30	0.12	0.625000%	QD Jason	Released
3.5*3.5	0.8	1*1	RVXD-280-SM-07100	Vio XD UV L	280	120	Flat	3		6.5	100	4	100	0.65	0.615385%	RayVio	Released
6*6	1.8		BR60QF310S09P		309	125	Flat	2		17	700	70	900	11.9	0.588235%	PEC	Released
3.5*3.5	0.8	1*1	XP4-280-SM-07633	RayVio XP4 UV LEDs	280	120	Flat	3		26	300	40	200	7.8	0.512821%	RayVio	Released
3.45*3.45	1.4	0.6*0.4	325SMD		325	120	Flat	2		10	200	10		2	0.500000%	UV Photonics	Released
3.5*3.5	1.2	0.6*0.4	CUD5GF1B	CA535	255	125	Flat	3		7.5	100	3.5	200	0.75	0.466667%	Seti	Released
1.12*1.12	0.4		JS-DUV265 A	Flip Chip	265					6.5	20	0.5	20	0.13	0.384615%	QD Jason	Released

Note: The database consisted of over 600 LEDs. Only some LEDs have been listed above.

2.B – Lifetime Measurements

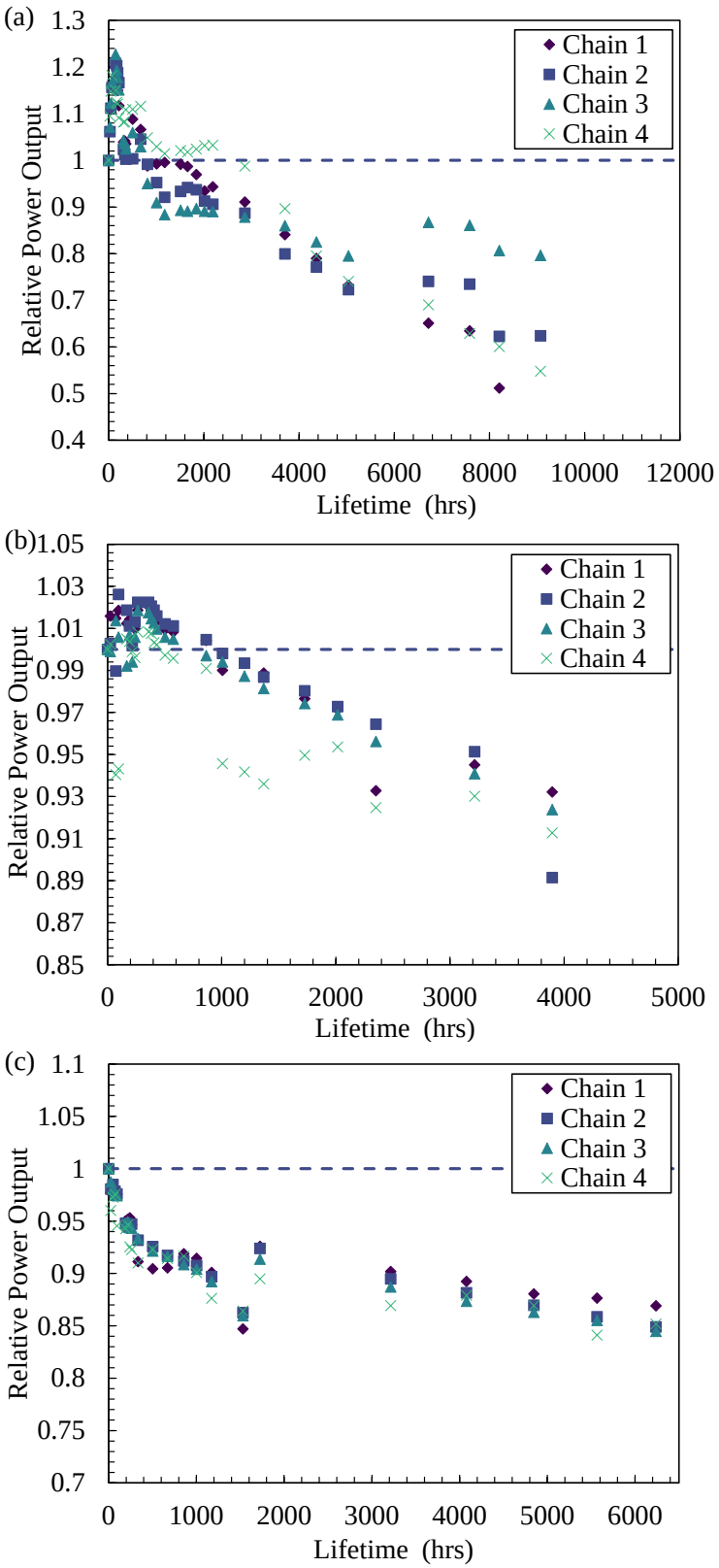

Figure 2.B.1: Individual chain power output measurements (a) FX–1 265, (b) FX–1 275, (c) FX–1 310.

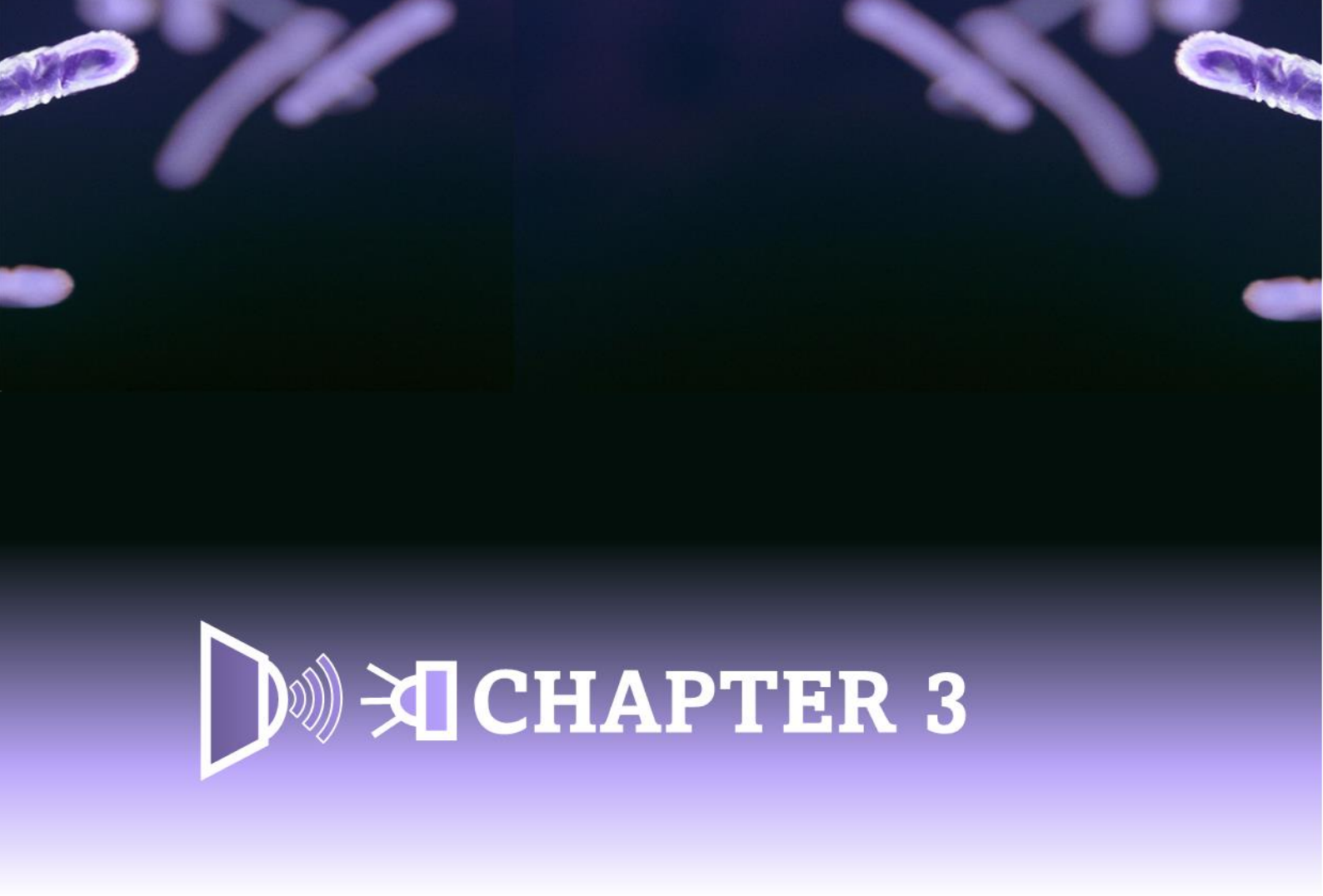

CHAPTER 3

UV SENSORS

3.1. Introduction

Ultraviolet light has a wide variety of applications in industry, including disinfection [185], lighting [186], photocatalysis, UV paint curing, and UV glue curing [186, 187]. The COVID–19 outbreak, in 2019, led to increased interest in finding solutions using ultraviolet light, specifically in the UV–C wavelength ranges (240 nm – 280 nm [185]), to achieve effective disinfection of surfaces and air. As of 2022, the shortest wavelength UV LEDs produced and available commercially is 230 nm [189]. Increased interest in UV–C LEDs has developed the need for a better understanding of light measurement techniques. Radiometry is the science and technology of measuring and quantifying electromagnetic radiant energy. Two commonly used terms in radiometry are intensity (or radiance) and flux (or irradiance) [190-192].

Sholtes et al. (2019) explored the development of a comparison protocol between measurements done using devices from different manufacturers [193]. Grum et al. (1979) [194] established different configurations of radiometric measurement systems, one of which can be seen in Fig. 3.1 (a). A typical light measurement system consists of a light source, transmission medium, and a sensor or detector that, when exposed to light, generates current or voltage proportional to the amount of light received. The signal processor then converts the incoming signal to a light–level reading in units such as W, W cm^{-2}, etc. The measurements systems can be configured with different optics to suit the set–up for a particular measurement [191, 194].

The light source is the main component of interest in these measurements. If the source is small in the context of the measurement to be conducted, the source approximates to a point source. However, in practical applications, all light sources are extended sources. Extended sources are sources where the size of the source is larger than the capability of the measurement system. If the system emission angle is higher than the acceptance angle of the detector, measurements taken will be lower than the actual light emitted by the source and hence not completely valid for further use unless the loss is factored in. Measurements will be valid only when conducted at long working distances so as to capture most of the light emitted (Fig. 3.1 (b)) [195].

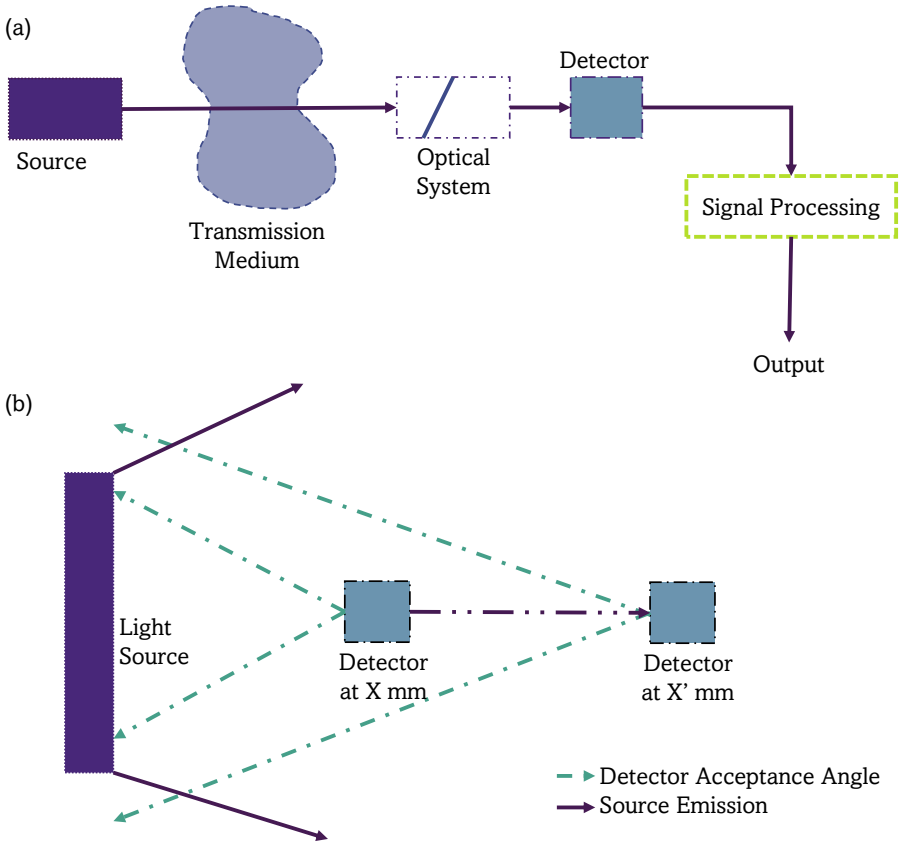

Figure 3.1: (a) Typical configuration of radiometric measurement systems adapted from [194] and (b) Schematic representation of an extended light source.

For industrial light systems and scientific experiments, where the light source consists of multiple LEDs running in series or parallel combinations, the concept of extended source is essential for the accurate measurement of light intensity. Different light measurement techniques are used by light system manufacturers and scientific experts to understand the behavior of light at a given point of interest, including chemical actinometry, radiometry/dosimetry, optical modeling, and discrete ordinate modeling [186]. The lighting industry also employs integration spheres for light measurement, although there are very few integrating spheres in the market that can be used for ultraviolet sources due to the effect of ultraviolet light on the inner coatings of the integrating sphere.

In radiometry, a detector/sensor plays a vital role in ensuring measurements are valid and acceptable. Every detector head has a light receiving surface where the light enters the detector head, a detector where the light from the source falls onto, and a cable that transmits the light received to be recorded by the sensor [196]. Most detectors are silicon photodiodes or CCD based multi–channel array detectors, which are very versatile and reliable. A detector's spectral sensitivity is equal to the product of its responsivity and the

transmission of the coupling optics within it [197]. An ideal detector measuring a light source would have a cosine response. A perfect cosine response is one where the device agrees with Lamberts cosine law. This law states that the radiant intensity from an ideal diffusing reflective surface and the cosine of the angle between the direction of incident light and surface normal are directly proportional [198]. A cosine response device is a Lambertian receiver [199]. As shown in Fig. 3.1 (a), while the set–up used to measure the light source can be simple, it is necessary to know if the measured values are valid and can be used for further calculations. For example, research has shown the variability of measurements done by equipment from different manufacturers [186].

Despite extensive research on measurement techniques and characterization for UV LED measurements [185, 193], there is a need to understand the data obtained from the measurements and explore the validity of these measurements. Questions associated with standard protocols used in radiometric measurement have been explored [193, 200], but possible effects of errors in measurement have not been quantified. While there are many books and papers on optical and light measurements [186, 190-198, 201], there is a need to establish common errors, such as placement of the detector with respect to the light source, temperature of the sensor, etc., that operators may induce, unknowingly, while measuring extended light sources. This chapter aimed to quantify the variability in the measurement of LED lamps centered in the UV range of light spectrum as affected by the equipment used. The study compares sensors that operate in the wavelength range of 265 nm – 395 nm of UV and discusses the importance of understanding the compatibility of the sensor for the measurements to be recorded.

3.2. Methodology

3.2.1. Sensors

While meters can have the same form factor, there can be a wide range of specifications that can differ between each manufacturer. For example, one of the principal differences between meters is their calibrated wavelength range and planar sizes. It is necessary to evaluate each measurement set–up on a case–by–case basis and to choose a meter that encompasses the range of measurements required for the specific application.

Table 3.1 lists sensors from four different manufacturers used in this study. Fig. 3.2 depicts the calibrated wavelength measurement ranges of each detector head and optic when the entire area of the detector head or coupling optic is evenly illuminated. These values are based on the parameters provided by the manufacturer in their datasheets.

Table 3.1: Sensor Specifications.

Detector Head	Manufacturer	Meter	Intensity Range	Aperture Diameter (mm)
UV A/B 1390323 [202] UV V 1265282 [203]	Loctite	UVA/B Radiometer Dosimeter UV-V Radiometer Dosimeter	5 mW cm^{-2} – 20 W cm^{-2}	0.75
S120VC [166]	ThorLabs	PM100D Radiometer	70 nW cm^{-2} – 70 mW cm^{-2}	9.5
PD300RM - 8W [161]	Ophir	Starbright 7201580 Radiometer Dosimeter	1 µW cm^{-2} – 8 W cm^{-2}	8
RAA4 Right Angle Cosine Adapter [158] ** W Optic Diffuser [158] **	International Light Technologies (ILT) [157]	ILT950UV Spectro-radiometer	1 nW cm^{-2} – 100 mW cm^{-2}*	6.9 24

* No specific information on the datasheet, range based on measurements done with SpectrLite software.

** RAA4 and W components from ILT are coupling optics and not detector heads [158].

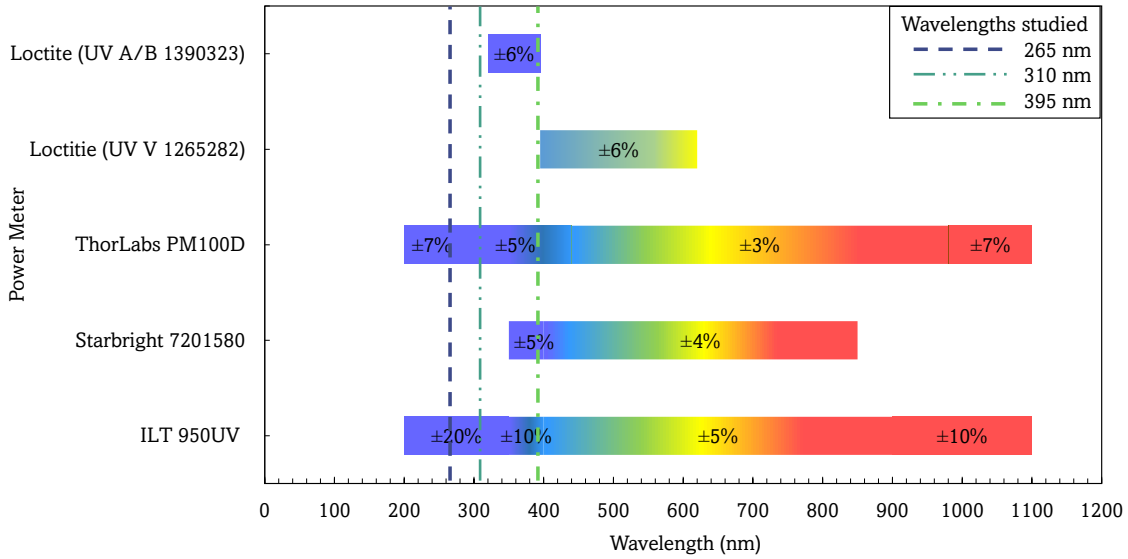

Figure 3.2: Peak wavelength of light sources studied (dotted line), wavelength range, and intensity calibration accuracy of the sensors used. Own elaboration based on manufacturers data [202, 203, 166, 161, 157].

Loctite dosimeters are built to measure narrow–band wavelengths, specifically for LED light curing devices. The meter has a screen display where the data and profile can be read [202, 203]. ThorLabs S120VC has typical applications for low power lasers and LEDs. The sensor uses a large active area combined with a reflective, diffused filter. Data measured using the ThorLabs sensor can be downloaded and accessed for further analysis [166]. Ophir sensors have diffusers that suppress out–of–band light. The meter has a built–in display and memory capacity that can be downloaded onto a computer for further analysis [161]. International Light Technologies (ILT) manufactured sensors are portable spectroradiometers with a wide range of calibrated wavelengths. These meters use a coupling optic that receives and transmits data to the detector array inside the ILT spectroradiometer. The data measured by the coupling optic can be read on the software provided by the manufacturer, SpectrILite III [157]. The Loctite, ThorLabs and Ophir based sensors employ a console for data measurement and storage while the ILT–based spectroradiometer employs a software layer meter head that supports user–based light measurement.

3.2.2. Sources – Light Emitting Diodes

Three light sources of different spectral emission in the UV–A, UV–B and UV–C ranges were analyzed. The LEDs chosen for this work were 265 nm (KL265–50U–SM–WD, Klaran), 310

nm (EOLS–310–697, EpiGap), and 395 nm (CUN96A1B, Seoul–SeTi). To conduct experiments, the LEDs were solder attached to starboards (601019.01, 60050, Lumitronix).

Spectral measurements were made to ensure that the emission of the chosen LEDs was centered at the wavelengths of interest and measured using the ILT spectroradiometer with the RAA4 coupling optic (2003357U1, ILT). Fig. 3.3 shows the spectrum of each LED relative to their peak wavelength.

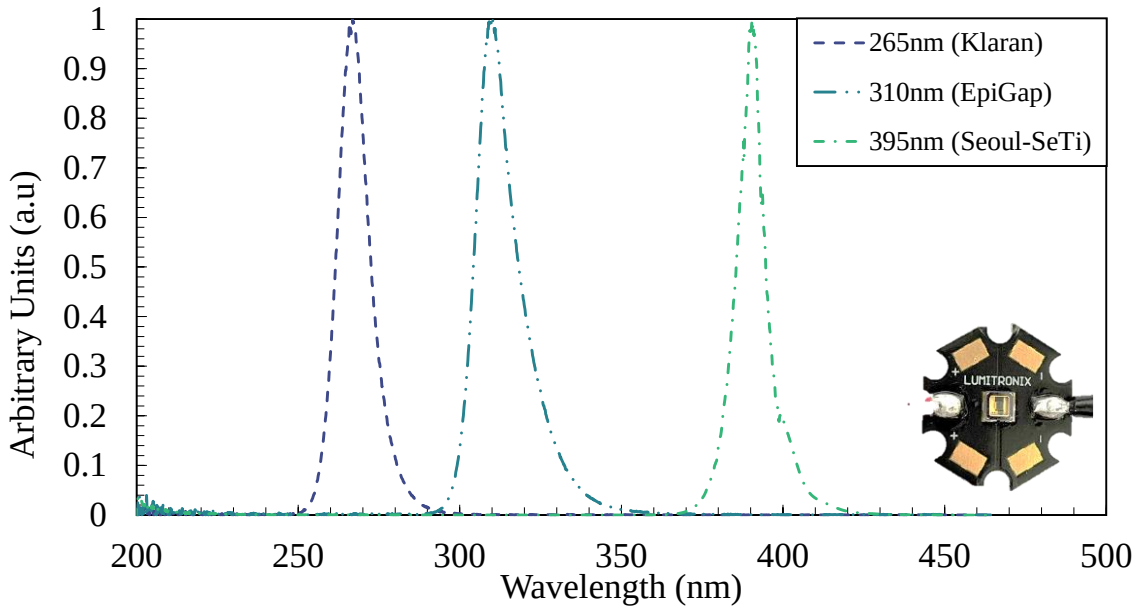

Figure 3.3: Relative spectral intensity of each light source.

3.2.3. Set–up for Experiments

The LED soldered onto a starboard substrate were mounted to a heatsink for cooling (as shown in Fig. 3.4 (a)).

3.2.3.1. Angle of Acceptance

The angle of acceptance is defined as the maximum incident angle at which an optical element (lens, fiber) will transmit light that can be detected and measured by the detector [191]. A rotating fixture was used to measure the maximum incident angle for each of the detector/coupling optics used in this study (see Fig. 4 (b)). The detector head was placed co–axial to the source. The light source selected was a single point source, which meant that the amount of light measured was lower than the range of the detector manufactured by Loctite (minimum of 5 mW cm^{-2} required). For Loctite detectors, a lens (Fresnel Tech #0.3) was used in front of the source to increase signal strength reaching the detector. Refer to

Appendix 3.A for the change in the set–up for the Loctite detectors (Fig. 3.A.5). For the purpose of this work, angles between 0° and 180° were studied in steps of 10°. A working distance of 100 ± 1 mm was maintained between the light source and aperture. Three replicate measurements were taken on separate days to ensure that measured data was repeatable and reproducible for each detector used in this study. For further information on the set–up and rotating fixture, refer to Appendix 3.A (Figs. 3.A.1 – 3.A.3).

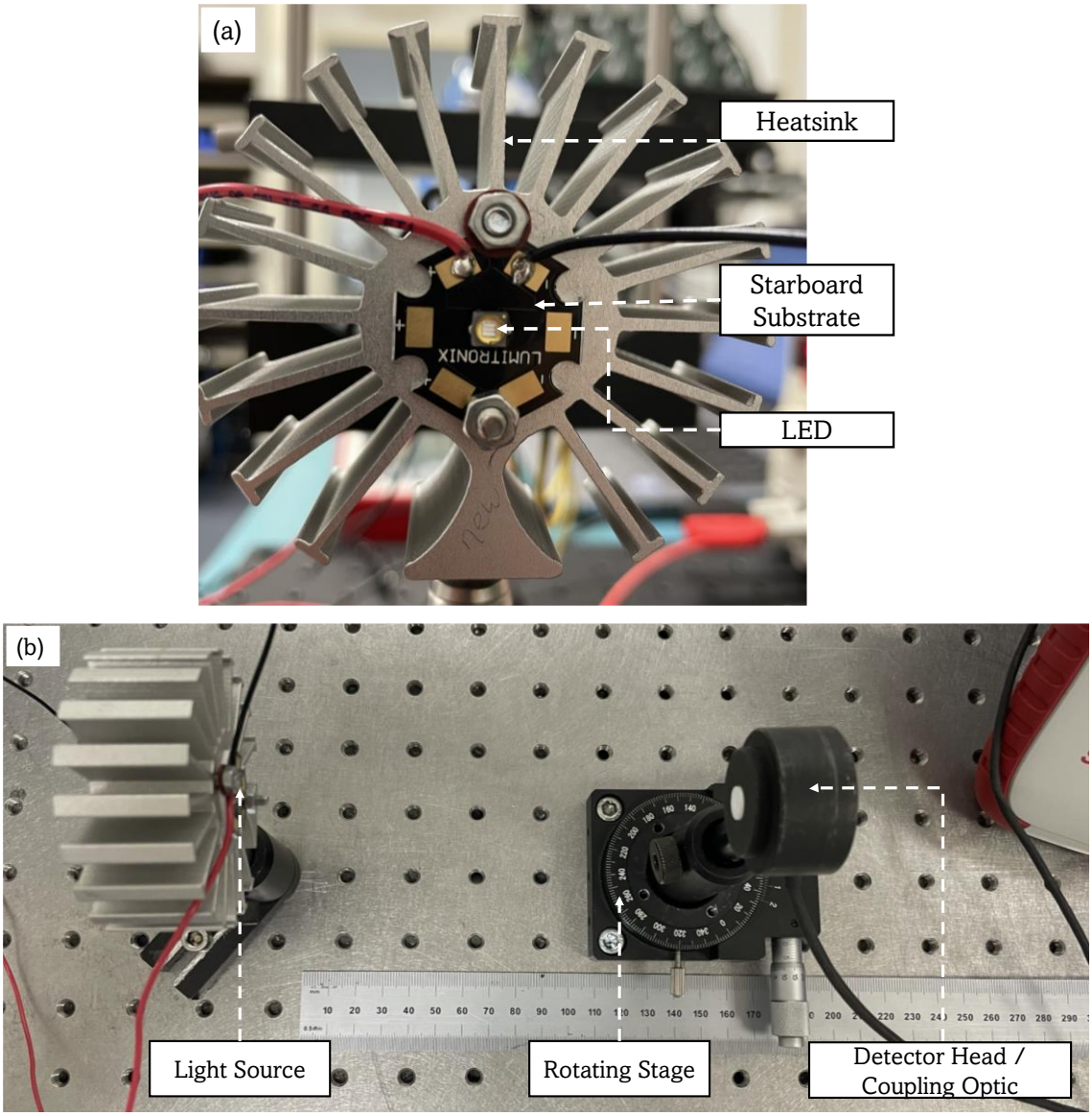

Figure 3.4: (a) Light source mounted on the heatsink and (b) Angle of acceptance test set–up using the Ophir detector.

3.2.3.2. Ambient and Stray Light

Ambient light is all the light present in the room before switching the light source "ON". In some situations, ambient light can also be considered stray light. Stray light is any light that is not intended to be in the system during a measurement or operation. It can be light from reflections or scattering from structures and surfaces that cannot be controlled during experiments [198]. This can be controlled by conducting the experiment in a dark room or "zeroing" out the ambient light at the position of measurement, before starting actual measurements. The room in which this experiment was conducted was a well–lit room with ceiling lights and no other light sources in the room. To provide an understanding of how much ambient light exists in a lab environment, each detector was laid flat onto the workbench, and a reading was taken to provide a guide figure on ambient light present in a lab environment.

3.2.3.3. Integration Time

Integration time is the period of time over which the detector or coupling optic collects photons of light at every measurement point. This time can range from a few microseconds to seconds. Most power meters and spectroradiometers use auto–integration time settings depending on the amount of light it detects [198]. The manufacturer programmed console within the ThorLabs sensor (PM100D) auto adjusts the range depending on the light input at the aperture, so as to return a valid reading for the signal received. On the other hand, the ILT sensor has an option for manual input and the ability to choose an auto setting of integration time to capture data. The integration time settings can be managed via the software interface provided by the manufacturer. Integration time settings can have a significant impact on the data obtained. The same experimental set–up for intensity measurements was used to investigate this effect. These experiments were conducted only for ILT manufactured RAA4 coupling optic as the remaining manufacturers either adjust their range based on the signal or use auto integration time setting.

3.2.3.4. Sensor Temperature

The effect of the change in temperature of the sensor on readings was evaluated. For these experiments, a panel resister (10 Ω ± 1% 12.5 W) was mounted onto the back of the ThorLabs S120VC detector head to initiate the required temperature rise. Fig. 3.5 shows a schematic representation of the set–up. The light output was initially allowed to stabilize for

30 min after which the detector head was then heated to 40°C and readings were taken for each degree Celsius drop of the detector head.

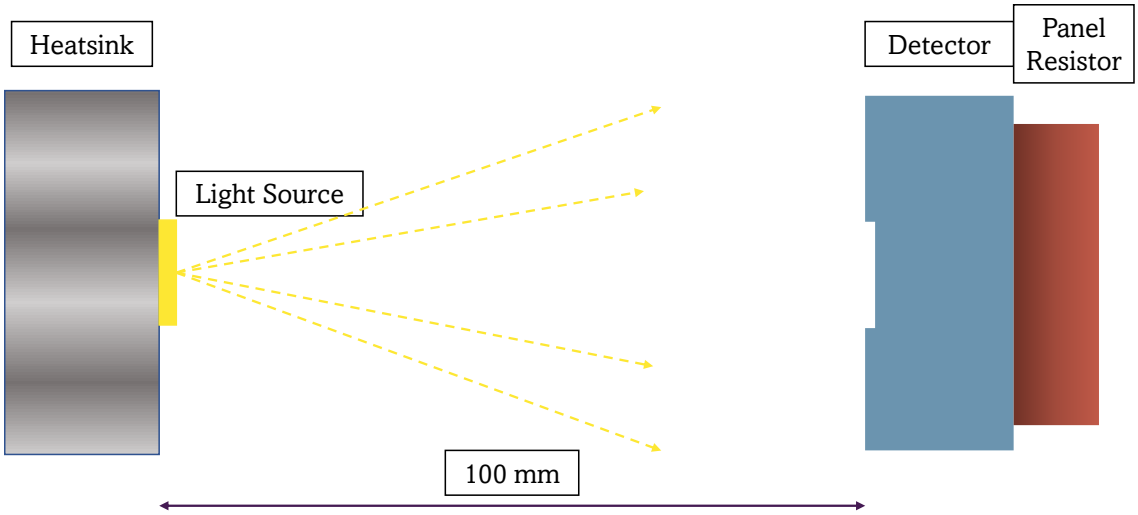

Figure 3.5: Schematic representation of the set–up for analyzing the impact of temperature on measurements.

3.2.3.5. Measurement of the Intensity

Another essential difference between sensors is their ability to return accurate intensity measurements. Different sensors operating in the same wavelength range will return different measured values, and it is critical to know if the intensity displayed is valid within the calibration of the meter. For this purpose, differences in the intensity measurements recorded with the different sensors have been evaluated. For these experiments, the light source was mounted at a 100 mm working distance from the detector, and the intensity was measured.

3.3. Results and Discussions

Before any experiments are conducted, it is important to understand non–measurement set–up parameters that can affect the final results. Firstly, the meter chosen must have a traceable and lasting calibration that can be depended upon. Quality of calibration ensures that the conversion of voltage to the corresponding light level reading is accurate. Most devices have NIST or ISO17025 traceable calibration [186]. Second, lenses and optics are sometimes used to increase the signal for measurements. Some lenses absorb ultraviolet light, so caution must be taken while using any optics to measure ultraviolet light. As in the case of this study, the lens could only be used to increase the measured intensity from the 395 nm light source and did not increase the measured intensity of light when used with the 265 nm or 310 nm light source. Third, LEDs are known for their ability to turn on and off with less time for stabilization [193]. It is important that readings be recorded after the source has stabilized. It is essential that while designing an experiment, the thermal resistance, specific heat capacity, and rate of heat dissipation of the light source are considered and accounted for [185]. Also, it is important to have sufficient thermal management as the LEDs tend to fade off or fluctuate until an equilibrium is reached. An unstable light source can result in inaccurate and non–reproducible measurements. Most sensors are designed to fit a specific application field. The selected sensor must be compatible and fit for the measurement system designed.

3.3.1. Angle of Acceptance

In an experiment involving the characterization of an extended light source, the source is normally fixed onto a mounting stand which can then be translated or rotated about an axis. To measure light output and intensity delivered to a point of interest, a suitable detector is placed for measurements. To deduce the angle of acceptance of the detectors/coupling optics used in this study, the light source was fixed while the detector was rotated about an axis. This experiment highlights the importance of accurate positioning of the light source and measuring device for accuracy of measurements obtained. Data were measured for every 10–degree tilt of the detector acceptance plane with respect to the light source. The measured data were then interpolated linearly to steps of 0.1° to calculate the angle of acceptance of the detector/coupling optic. The angle of acceptance has been calculated using the concept of full width half maximum (FWHM) with respect to the light source emission. Fig. 3.6 (a–e) shows the angle of acceptance of the detectors discussed earlier.

To understand the results obtained, the designs of these detectors/coupling optics have been taken into consideration (Fig. 3.6 (f)). In the case of sensors from Thorlabs, Ophir, and Loctite, the detectors have an aperture and a detector, while the ILT manufactured coupling optics have a fiber optic which transmits the light incident on the aperture to the detector house inside a box via the phenomenon of total internal reflection. The distance between the detector and aperture and the size of the aperture provides inputs about any light lost within the detector head. Large distances mean that some of the light incident on the aperture will be lost. The measurements have also been compared with an ideal cosine response to understand the behavior of each of the detectors used in the study. Table 3.2 summarizes the results of the angle of acceptance of detectors in this study.

The Loctite detectors (UV A/B 1390323 and UV V 1265282) have a narrow range of wavelength calibration and a small aperture diameter. There is very little space between the detector and the aperture. This means that most light entering the aperture will reach the detector, thus very little light is lost. It is evident in comparison with the ideal cosine response that it is close to the ideal response (Fig. 3.6 (a)).

In the case of PD300RM–8W (Fig. 3.6 (b)), the detector is nearly cosine. The angle of acceptance of the detector is 114.5 ± 0.5°, possibly due to a portion of the detector head protruding from the main housing (Fig. 3.6 (f)). With the diffuser protruding outside of the head, it can accept low angles of light incident onto the diffuser. Low or high angle reflections of light will reach the detector entrance, where it will be scattered onto the detector inside. This makes it ideal to obtain a cosine response i.e., the detector will measure most light reaching its surface.

Table 3.2: Summary of angular response of detectors.

Sensor	Width (°)		
Wavelength	265 nm	310 nm	395 nm
Loctite - UV A/B 1390323, UV V 1265282	N/A	N/A	107.0 ± 0.5
Ophir PD300RM-8W	N/A	N/A	114.5 ± 0.5
ThorLabs S120VC	74.5 ± 0.5	76.7 ± 0.2	80.7 ± 0.5
ILT RAA4	109.0 ± 0.5	109.0 ± 0.5	109.0 ± 0.1
ILT W Optic	26.5 ± 0.3	24.9 ± 0.2	23.7 ± 0.5

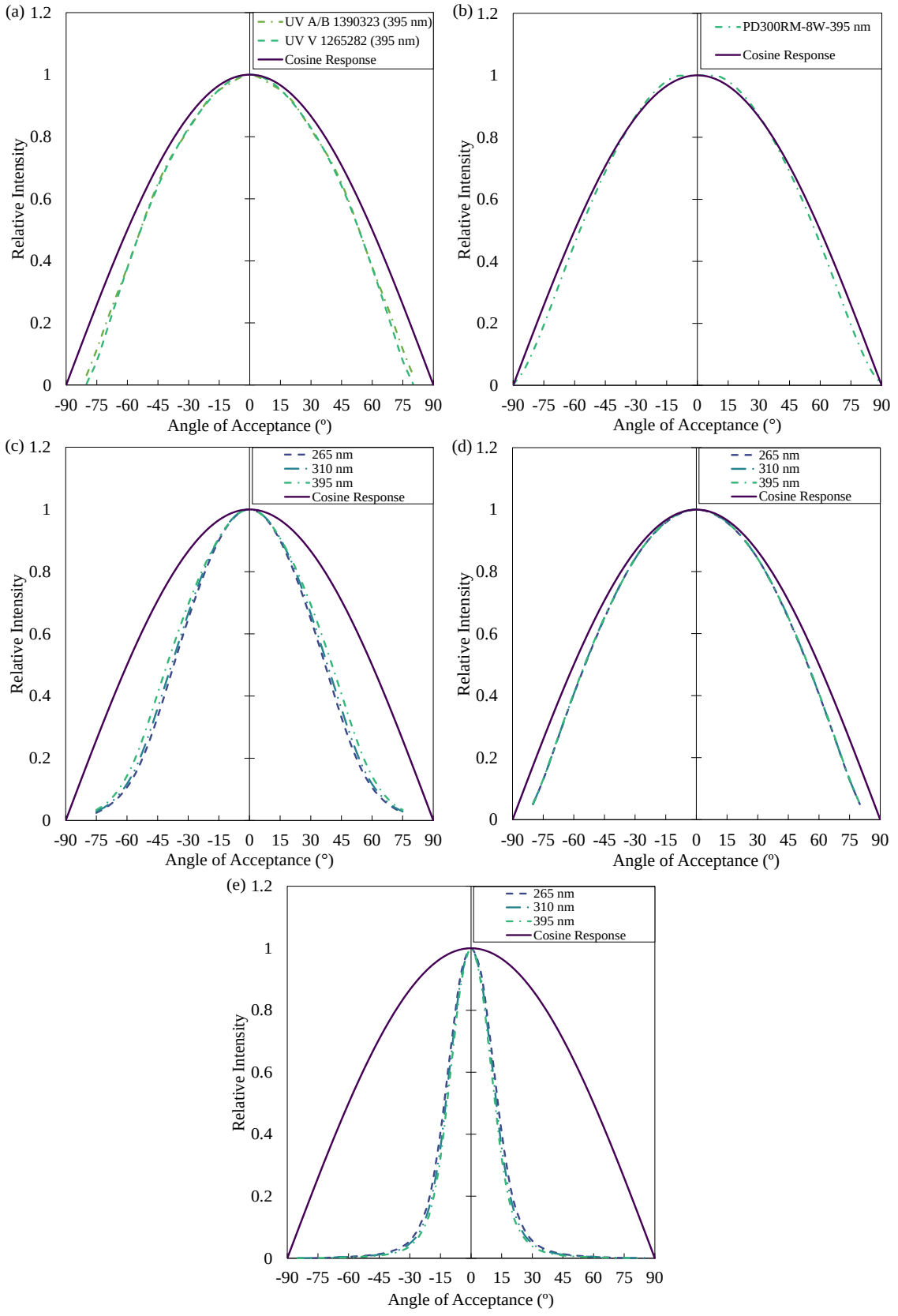
(a)
UV A/B 1390323 (395 nm)
UV V 1265282 (395 nm)
Cosine Response
Relative Intensity
Angle of Acceptance (°)
(b)
PD300RM-8W-395 nm
Cosine Response
Relative Intensity
Angle of Acceptance (°)
(c)
265 nm
310 nm
395 nm
Cosine Response
Relative Intensity
Angle of Acceptance (°)
(d)
265 nm
310 nm
395 nm
Cosine Response
Relative Intensity
Angle of Acceptance (°)
(e)
265 nm
310 nm
395 nm
Cosine Response
Relative Intensity
Angle of Acceptance (°)

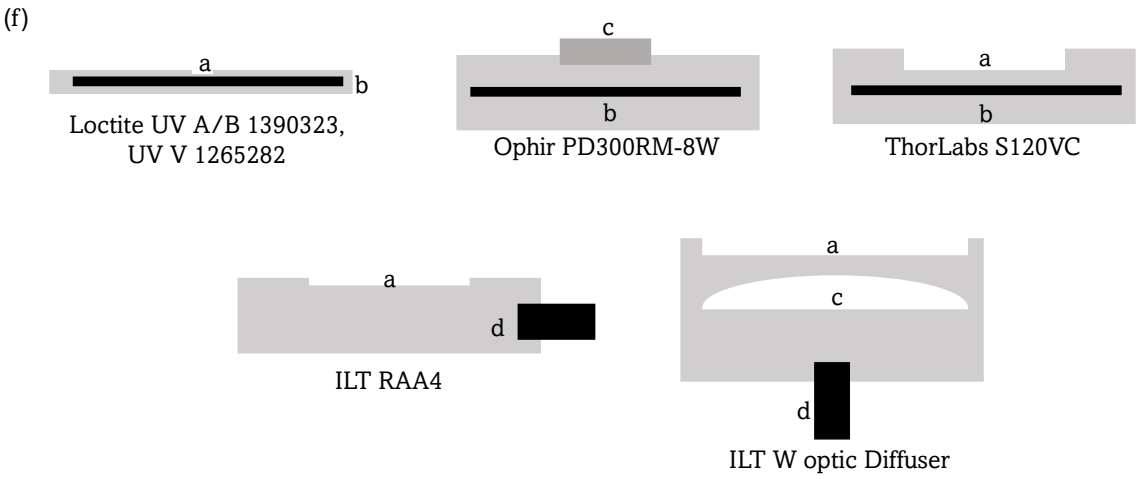

Legend - (a) Aperture (b) Detector (c) Diffuser (d) Fiber Optic

Figure 3.6: Angle of Acceptance of sensors– (a) Loctite – UV A/B 1390323, UV V 1265282, (b) Ophir PD300RM–8W, (c) ThorLabs S120VC, (d) International Light Technologies – RAA4, (e) International Light Technologies – W Optic, and (f) Schematic representation of the cross–sectional views of the detectors (not to scale) [202, 203, 166, 161, 157, 158].

With the ILT RAA4 and ThorLabs S120VC detectors (Fig. 3.6 (f)), the aperture sits a few millimeters inside the front plane of the detector head, which decreases the ability of the sensor to accept low angle light, including low angle reflections. For the ThorLabs S120VC detector, the aperture is located lower than that of the RAA4 coupling optic with respect to the detector head, which explains the difference in angle of acceptance between the two (Fig. 3.6 (c)). Due to its decreased ability to accept low angle reflections, the ILT RAA4 coupling optic, does not have a near ideal cosine response (109.0 ± 0.5° at 265 nm) as that of the Ophir PD300RM–8W, meaning that this loss needs to be factored in while using the coupling optic in measurements (Fig. 3.6 (d)). The ILT W optic diffuser has a low angle of acceptance compared to the others in this study (26.5 ± 0.3° at 265 nm (Fig. 3.6 (e)), this can be attributed to the dome–shaped diffuser design of the optic by the manufacturer. It is evident that the distance between the detector and aperture is longer compared to the others, which implies that there is light being lost during transmission.

During the experiments, it was observed that two of the detectors (W Optic and S120VC) showed a wavelength dependent angular response (Table 3.2). The ILT W Optic diffuser had a larger angle of acceptance towards shorter wavelengths, while the ThorLabs S120VC showed a larger angle of acceptance towards the longer wavelength light (Fig. 3.7 (a)).

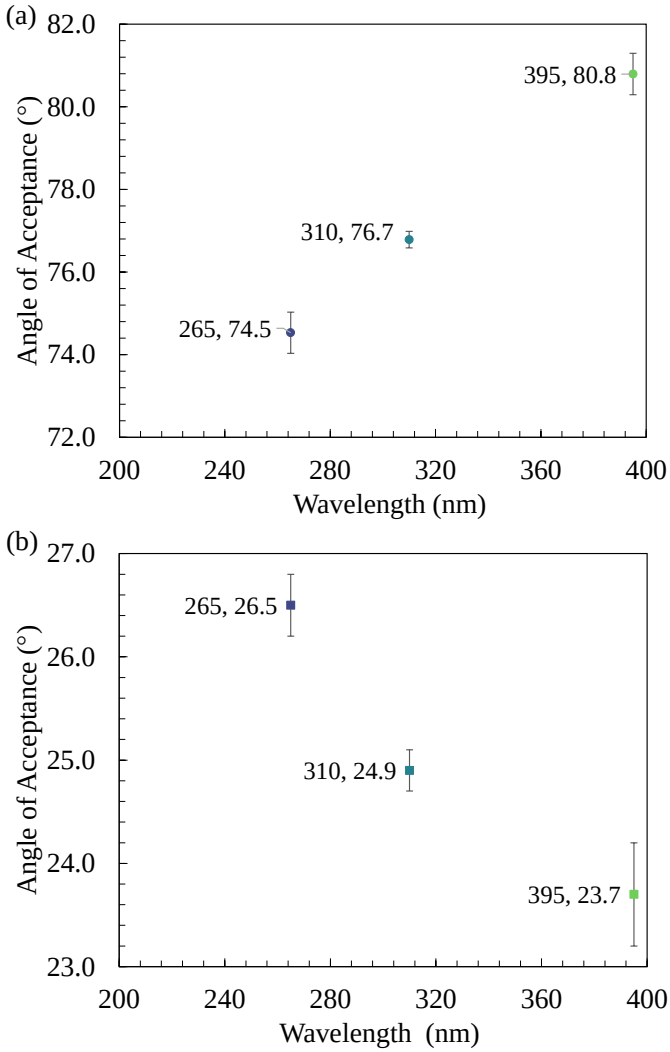

Figure 3.7: Change of acceptance angle of detectors with wavelength – (a) ThorLabs S120VC and (b) ILT W Optic Diffuser.

In the case of the ThorLabs S120VC detector, the decrease in angle of acceptance with the decrease in wavelength can be associated with the absorption and scattering element within the detector. It is possible that the material of the detector does not scatter the lower wavelengths enough, and the interactions between light and detector inside are causing this decrease of angular response combined with predominant optical loss due to Rayleigh scattering [204, 205]. As discussed earlier, the ILT manufactured optics employ an optical fiber to transmit light received to the detector housing. While no change in angle of acceptance with wavelength was observed with the RAA4 optic, the W optic diffuser measurements recorded a decrease with the increase in wavelength (Fig. 3.7 (b)). This could be due to the phenomenon of Brillouin shift within the optical fiber that needs to be investigated separately [206]. These are just possible reasons for the changes observed, and

the effect on the actual values measured corresponding to each wavelength needs to be investigated separately, as it is outside the scope of this study.

As discussed in this section, it can be seen that it is essential to ensure that the detector is flat, and the back plane is parallel to the source and perpendicular to the optical axis. This ensures the credibility and accuracy of measurements. A small degree of tilt in the detector could cause a significant change in measurements that will affect further calculations or further use of the data, especially in the case of extended sources of light.

3.3.2. Effect of Ambient Light

Measurements in ambient light can be challenging, as this light can be detected by the measuring device, thus impacting the final measurement result. Even stray light reflecting off surfaces or lab coats can be detected. Reflections from uncoated surfaces (~5%) or coated (~1%) surfaces can affect data measured by the optical sensor. Accounting for changes in ambient light when the source signal is at a comparable level to that of ambient light poses a big challenge to researchers. Ambient light in the room will be an issue if the ambient signal is large, as this will lower the detection range for the detector/sensor. For example, if a detector can only measure up to 20 mW cm^{-2} of intensity and the ambient light measured is about 15 mW cm^{-2}, it leaves the detector with only 5 mW cm^{-2} for the signal of interest.

Some meters or dosimeters are calibrated for a specific wavelength range (ex. Loctite UV A/B 1390323), while others are calibrated for a broad wavelength range (ex. ILT 950 UV, ThorLabs S120VC). This means that the meter reads any ambient light in the calibrated wavelength range (i.e., for ILT and ThorLabs 200 nm to 1100 nm). It is known that there is negligible UV–C light in solar, but due to the range of calibration of the meters, most of the surrounding light can be read by the detectors/sensors. For low efficiency UV–C LEDs, the signal is very low in comparison to other wavelength ranges. Therefore, it is important to account for the surrounding light to ensure the measured data is accurate. This measurement was carried out to demonstrate how large an ambient light signal can be in a lab environment. (For data on these measurements, refer to Table 3.B.1 in Appendix 3.B). While the Thorlabs, Ophir, and ILT sensors detected ambient light and data could be drawn, the Loctite detectors (UV A/B 1390323, UV V 1265282) detected no ambient light due to two reasons. One, Loctite detectors are calibrated for narrow band wavelength range with

possible inbuilt filters that filter–out of band wavelengths and second, detection range (5 mW cm^{-2} to 20 W cm^{-2}) which makes the detectors less susceptible to low ambient signals.

In the experiments conducted, it has been observed that typical ambient levels were approximately ~0.23 mW cm^{-2}. There can be a significant difference in readings, specifically for deep UV source measurements, if ambient light is not taken away from the measurements. For example, for the 310 nm LED used in this study, at a working distance of 100 mm, the recorded intensity was 0.13 mW cm^{-2}. If ambient light is not accounted for, the recorded intensity would have been 0.36 mW cm^{-2}. The increase in measured reading is approximately 180% more than the actual amount of source light received by the detector. This measurement is simply a guide to emphasize the importance of accounting for ambient light in any captured data.

Most detectors (ex. ThorLabs sensor) have a function to "zero" before conducting any measurements. This option helps detect ambient light and subtract the small fraction during actual measurements. Some detectors (ex. ILT sensors) in the market employ a preliminary dark scan measurement before the measurement scan. A dark scan is any signal present in the room in the absence of light. These scans are subtracted from the measured scan to provide data on the source light observed by the detector. The ILT detectors use a USB–interfaced device with a custom–controlled computer software tool – SpectrILite III, that assists in measurement using the detectors. The software shows the ambient light (positive peaks) and dark signal (subzero peaks) detected by the detector. There are 2 peaks, at 405 nm and 435 nm, in the frame. The intensity measured in the figure has been contributed by reflections from ceiling lights, stray light, and mercury lines from the fluorescent tubes (Refer to Fig. 3.B.1, Appendix 3.B).

Sometimes, in the case of open ceilings, the weather outside the building could affect the ambient light in the room. A rainy day could mean very little ambient light, which needs to be considered while taking measurements. It is possible to disregard ambient light conditions while taking measurements if there is a sufficient signal, but precautions must be taken to keep the surrounding light as consistent as possible. All experiments for the other parameters discussed in the work took place in a dark room, and any ambient light was "zeroed or subtracted" using the respective power meter.

3.3.3. Effect of Integration Time on Readings

Among all the sensors used in this study, only the coupling optics from ILT required the manual input of integration time for measurements. Control of integration time helps to maximize the signal–to–noise ratio and avoid sensor saturation. Signal–to–noise ratio (SNR) is a quantity that compares the level of the light signal received by the detector to the level of background noise. A higher SNR means that there is more signal than noise and vice versa [201]. Saturation occurs when the signal exceeds the measurement capacity of the sensor. Fig. 3.8 shows the difference between a saturated and an unsaturated sensor. When the intensity exceeds the upper limit of the detection system, saturation occurs, which is recognizable by a flat line (see dotted curve in Fig. 3.8). The data in Fig. 3.8 is from the RAA4 coupling optic measuring a 395 nm light source. At 250 ms integration time, the detector measured data for longer than its measuring capacity, causing it to saturate, whereas at 10 ms integration time, the detector measured data within its capacity. To understand the difference in measured intensity for a saturated and unsaturated sensor, a single scan was taken. Intensity scans with a saturated sensor resulted in a reading that was 43% less than that of the unsaturated sensor. The difference in measured intensity demonstrated the need to determine an ideal integration time before collecting data. In certain cases, depending on the measurement set–up, saturation can also be rectified by reducing the intensity of the source or increasing the distance between the source and detector.

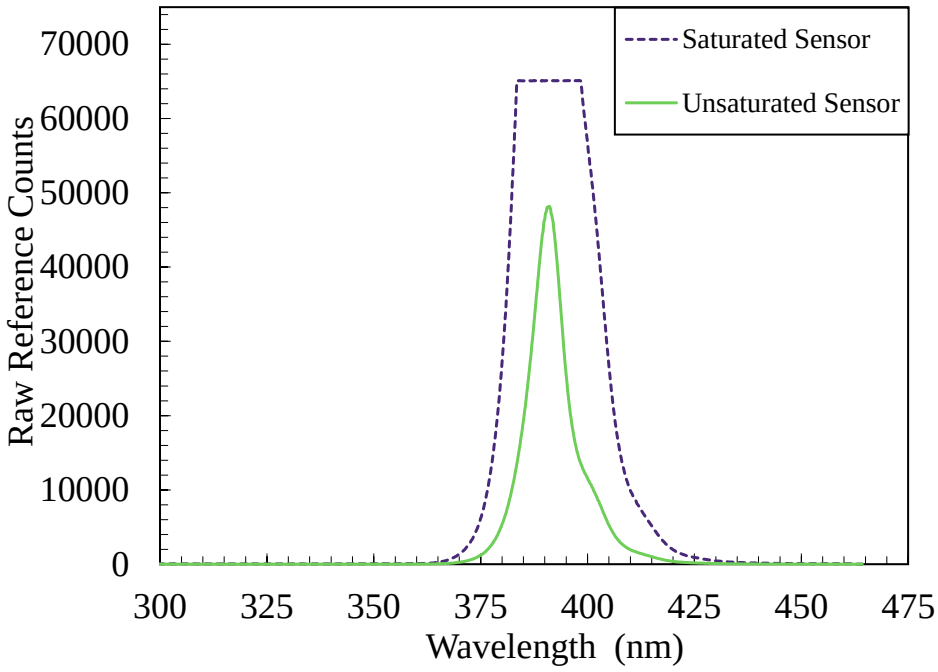

Figure 3.8: Raw reference counts measured by a saturated and unsaturated sensor.

It is also important to have the right integration time during measurements. Integration times depend on, but are not limited to, the current supplied to the LEDs, the optical output from the source, and the efficiency of the optical system. Lower integration times result in a lower signal–to–noise ratio, while higher integration times risk the saturation of the sensor. The experiment was conducted to understand the effect of integration time on the measurements using the ILT RAA4 coupling optic for 2 wavelengths, 265 nm and 395 nm. Fig. 3.9 shows the plots of the relative intensity measured against increasing integration time tested using the optic. All data presented in Fig. 3.9 (a) are relative to the intensity measured at an integration time of 1 ms. All data presented in Fig. 3.9 (b) are relative to the intensity measured at an integration time of 10 ms. The data in Fig. 3.9 was measured on three separate days and has been extracted from the ILT SpectrILite software. Measured data were consistent up to 3 significant digits after the decimal point.

For the 395 nm LED source, the integration time was varied between 0.03 ms to 20 ms. An integration time higher than 20 ms resulted in a saturated sensor, as 395 nm LED is efficient and emits a high signal compared to the 265 nm and 310 nm LEDs. It was observed that at an integration time lower than 10 ms, the intensity measured was nearly constant. For an integration time of less than 1 ms, the signal–to–noise ratio was very low, and hence the intensity measured is not a valid measurement of the source light. In the case of the 265 nm LED source, the integration time was varied between 0.03 ms to 1500 ms. Due to the low light output of the source, higher integration times were used to understand the impact. It was observed that for an integration time lower than 40 ms, the intensity measured was nearly constant. Similar to the 395 nm LED, at integration times less than 10 ms, it was observed that the measurement recorded too much noise. It is important to note that these integration times are ideal at a working distance of 100 mm only and will vary with any change in working distance between the source and measuring sensor.

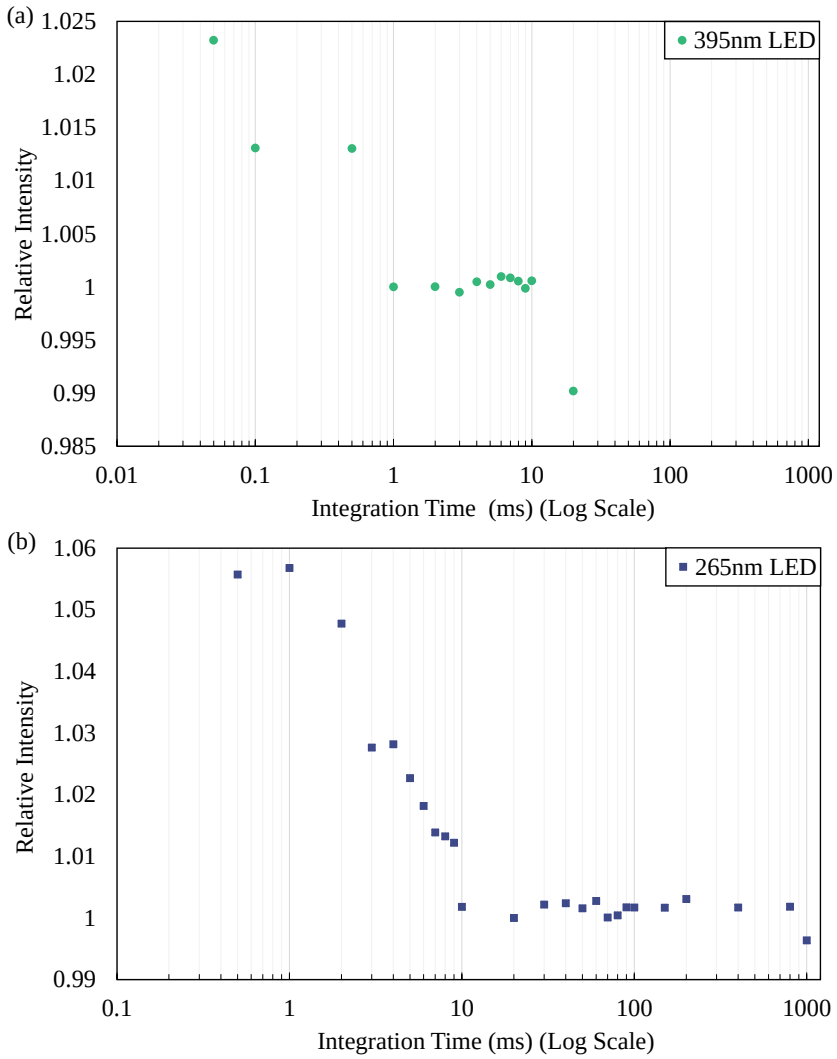

Figure 3.9: Change in measured intensity with integration time–(a) 395 nm and (b) 265 nm.

3.3.4. Effect of Temperature of the Sensor

Detector heads can slowly heat up with time when exposed to light. Temperature changes can significantly affect the readings displayed by the power meter. Sensors and meters used for measuring light are commonly made of semiconductor materials that are prone to deterioration upon heating or significant temperature rise of the body of the sensor. Prolonged exposure to light can lead to deterioration of the respective filter or aperture within the sensor. This deterioration can lead to permanent damage to the sensors and hence needs to be monitored carefully during measurements. Most meters do not display the temperature of the detectors. Amongst the sensors used in this study, ThorLabs PM100D power meter could display temperatures. To understand the effect of temperature on the sensor, the ThorLabs S120VC detector was heated to 40°C using a panel resister,

and the signal from the 395 nm LED source was monitored while the detector started to cool. The room temperature during this experiment was measured to be 20°C.

Data from the experiment can be seen in Fig. 3.10. All data measured have been normalized to the room temperature reading. The results from the experiment showed that there is an average of 0.2% change of measured intensity when the temperature rises. The change is low compared to the change seen in integration time experiments, but this provides a valuable understanding of how temperature impacts data measured by the detector. It is also possible that there is a temperature compensator designed into the detector head. Since the experiment employed artificial heating on the back of the detector, so as to not harm the detector permanently, it is possible that the change in measured data is a lot higher when the detector is heated over a prolonged time.

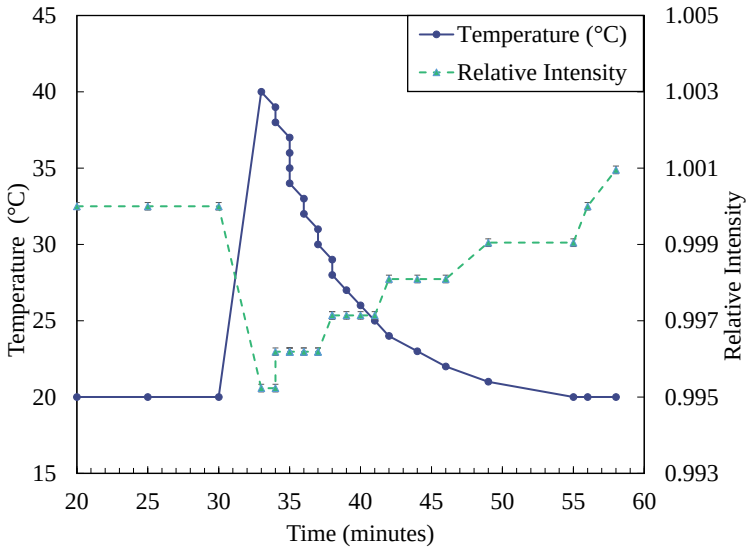

Figure 3.10: Effect of temperature on intensity measured by the sensor.

Another reason for the low change in intensity reading could be due to the mechanical design of the detector. While the display temperature does rise due to the heat applied, the aperture (light entering part of the detector) could be at a much lower temperature. Furthermore, the light source needs a certain amount of time to stabilize. It is important to note that no significant error was observed in the data measured between experiments, possibly due to artificial heating and reading of only 3 significant digits after the decimal point. However, this may change when the sensor temperature rises due to the light source. To avoid inaccurate readings, it is recommended to shield the detector from light until the source stabilizes.

3.3.5. Differences in Intensity Measurements between Sensors

Table 3.1 lists the intensity ranges of each sensor studied in this chapter. This experiment was conducted to show the difference in values returned by each sensor. Thorlabs and ILT manufactured sensors captured all the wavelengths used in this study, whereas the others could only detect the 395 nm LED light source. All measurements were taken on three separate days to evaluate repeatability and accuracy and averaged before plotting them in Fig. 3.11. For comparable data between detectors in this study, a separate experiment was conducted using a magnified signal for Thorlabs and Loctite Detectors.

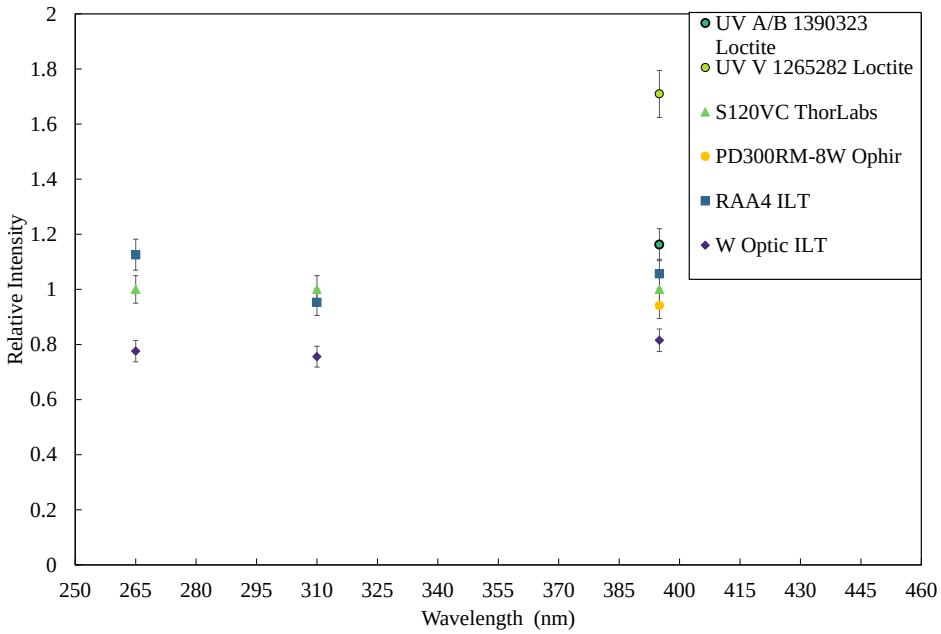

Figure 3.11: Comparison between sensor measurements.

To ensure reproducibility of data, calculated error between measurements and between consecutive days of measurement was observed to be 1% between the measurements. Data measured by ThorLabs Sensor (S120VC) has been used as a normalization point for the graph plotted in Fig. 3.11, as the average radiometric accuracy of the detector is approximately 5% across the entire range of wavelengths in this study. For the 395 nm LED source, the Ophir and Thorlabs sensors are in good agreement of ± 6% with each other. Even though all the sensors used could detect intensities in the range of the 395 nm LED source, all of them returned different values. For Loctite detectors, given their higher angle of acceptances, they measure higher intensities relative to the ThorLabs sensor measurements. The Loctite detector UV A/B 1390323 measured approximately 17% higher intensity, while the UV V 1265282 measured 70% higher intensity compared to the Thorlabs S120VC sensor.

It is evident from Fig. 3.11 that the RAA4, which is a right–angle cosine receptor, captures data very close to that of the ThorLabs sensor (a difference of ± 5%) while the W optic diffuser returns data approximately 20% lower than the ThorLabs sensor. Due to the lower angle of acceptance of the W optic, it is evident that less light is detected by the head, and thus it is important to understand its compatibility and calibration before use in an application. For the 265 nm and 310 nm LED sources, only the RAA4, W optic, and S120VC detector heads could be used. It was also observed that even though the RAA4 has a higher angle of acceptance than the S120VC, for the 310 nm source, the data measured was lower. This could be due to the radiometric accuracy of the two devices specified by the manufacturers, ± 20% and ± 5%, respectively.

3.3.6. Recommendations

The light industry is moving towards a common standard for light measurements in the form of LM–92, which is a new lighting measurement standard developed by Illuminating Engineering Society (IES) and the International Ultraviolet Association (IUVA) [207]. It is important to understand the differences between different sensors when comparing results between studies or evaluating UV LED based systems for purchase where manufacturers state the system irradiance and energy density. While multiple options are available for both the kind of meter and sensor measuring the light source, key importance must be given to the kind of application and set–up available to the user. The concept of extended light source needs to be applied while measuring large sources of light to ensure most light irradiated is captured by the detector. The kind and material of the detector must be investigated while choosing the measuring system. A close to cosine receptor is highly recommended as this means most light emitted by the source will be captured by the detector, if not, other errors are in the system and need to be factored in calculations. The concept of ambient light must be considered while measuring low light signal sources as this can significantly change the measurement obtained. Although LEDs are known to have instant ON/OFF capability, it is recommended to shield the light sensor from the source while it stabilizes before measurements so as to not damage the sensor during measurements. Not all sensors/coupling optics behave the same between different manufacturers and care must be taken while comparing measurements at all times.

3.4. Conclusions

This chapter showed that there are significant differences between sensors from different manufacturers used in the measurement of ultraviolet light systems. The chapter evaluated the different angular responses of the sensors and related them to their mechanical designs to understand the reason behind the response. The study showed that some sensors have different angular responses to different wavelengths and highlights the effect of ambient light on readings. The study observed that, for the ThorLabs sensor, there is a difference of 0.2% in the readings for a temperature rise of 20°C. This study also observed that even though two sensors can have the same wavelength ranges, it is not necessarily true that the readings will be the same. As seen for the 265 nm LED, an average difference of 17% between measured data from different sensors operating in the same wavelength range. It was concluded that measurement results are application specific and need to be evaluated first before proceeding towards characterizing the light source. For extended light sources, it is important to consider the angle of acceptance of the detectors and the working distance to ensure data is captured accurately. Change in the angle of acceptance with wavelength was seen for the ThorLabs S120VC and ILT W Optic diffuser. The reason behind this change needs to be investigated further. LED output can change with time, and the ability to measure a wide range of light signals is important to keep in mind while selecting a power meter. Measurements taken and data recorded need to be used and interpreted correctly before further use. Ensuring that the sensor is positioned precisely with respect to the source provides some assurance that the data received is accurate. Interpretation of the data recorded plays a key role in further use of the measurements. The study also highlighted the importance of ensuring the compatibility of the sensor with the specific application. This chapter validated and verified the measurements conducted using various sensors in Chapter 1 of this work and could be used for further analysis in the following chapters. It was seen that while measurements in air could be done using sensors and radiometric systems, measurements in a water medium faced a range of issues that needed to be examined closely.

Appendix Chapter 3

3. A. Experimental Set–up

The rotating stage used to conduct experiments can revolve between 0° and 360° as seen in Fig. 3.A.1 below. However, for the purpose of the experiments conducted, only angles between 0° and 180° were measured. (Or -90° to +90°).

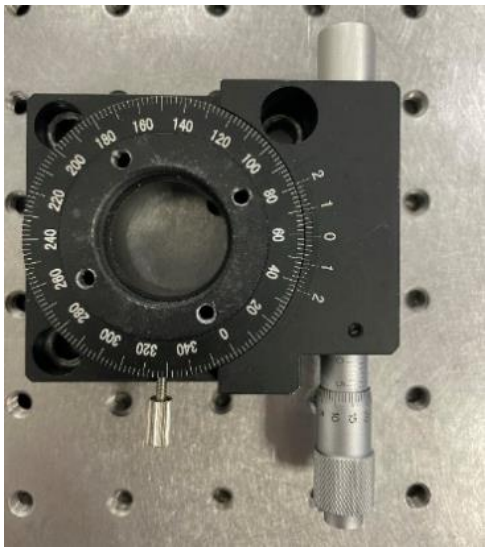

Figure 3.A.1: Top view of the rotational stage used for the angle of acceptance experiments.

Fig. 3.A.2 below shows the experimental setup used for the experiments involving the Ophir Detector. Figs. 3.A.3 and 3.A.4 show the detector position at -90° and +90° on the optical axis.

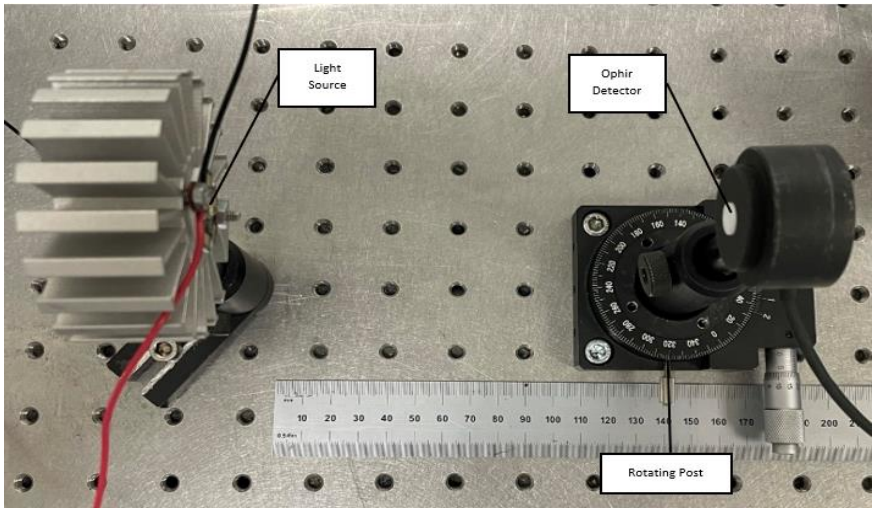

Figure 3.A.2: Experimental set–up using the Ophir Detector at 0°.

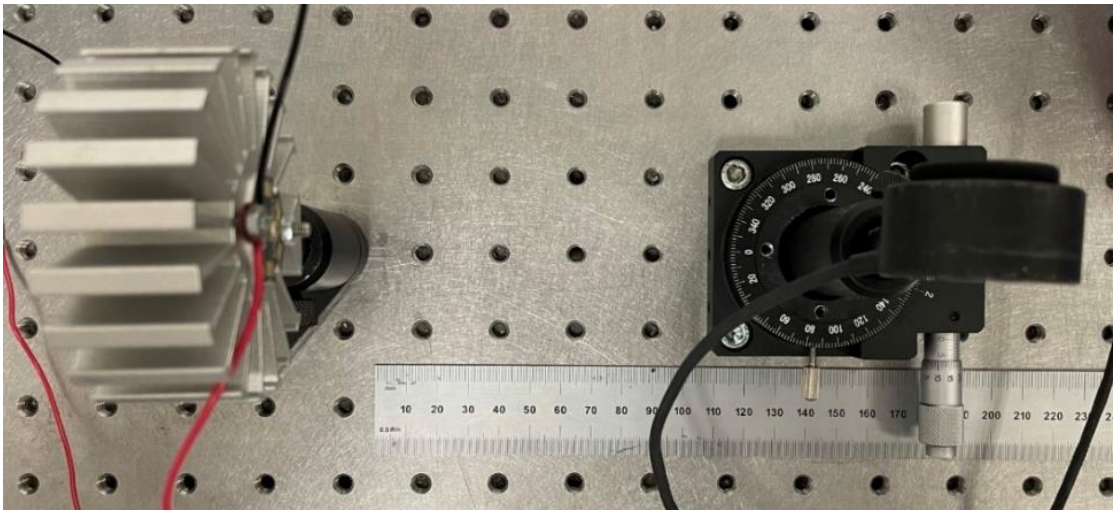

Figure 3.A.3: Experimental set–up using the Ophir Detector when the detector is at -90°.

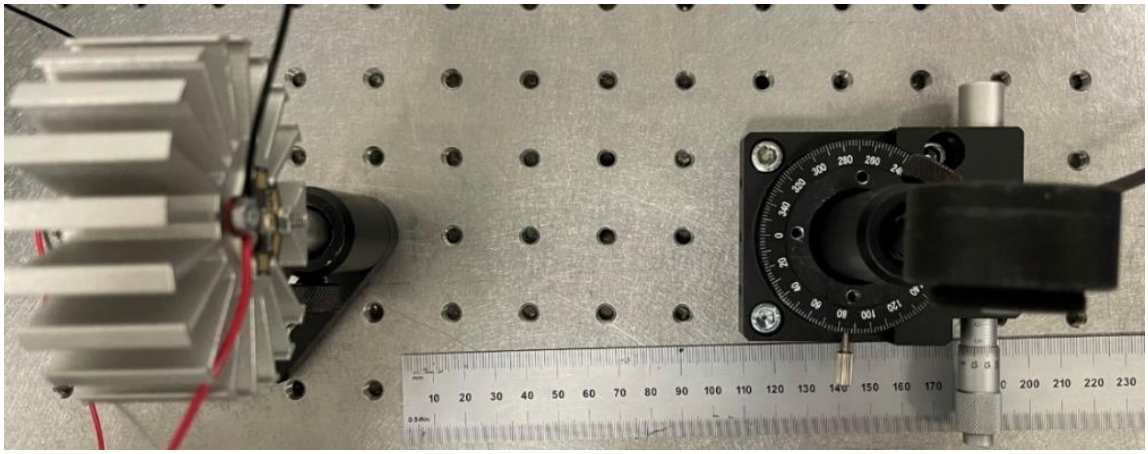

Figure 3.A.4: Experimental set–up using the Ophir Detector when the detector is at 90°.

- Loctite Setup: For the Loctite detectors studied, a minimum signal of 5 mW cm^{-2} was required for measurements to be recorded. Hence, the experimental set–up seen in Fig. 3.A.2 was modified by the placement of a #0.3 Lens in front of the light source as seen in Fig. 3.A.5. The lens was centered to concentrate more signal from the light source onto the detector surface.
- Set–up for other experiments: For experiments involving the study of the effect of integration time and ambient light on data measured the rotating stage has been replaced with a standard post as seen in Fig. 3.A.6. Fig. 3.A.6 shows the Ophir detector mounted onto a post for the experiment.

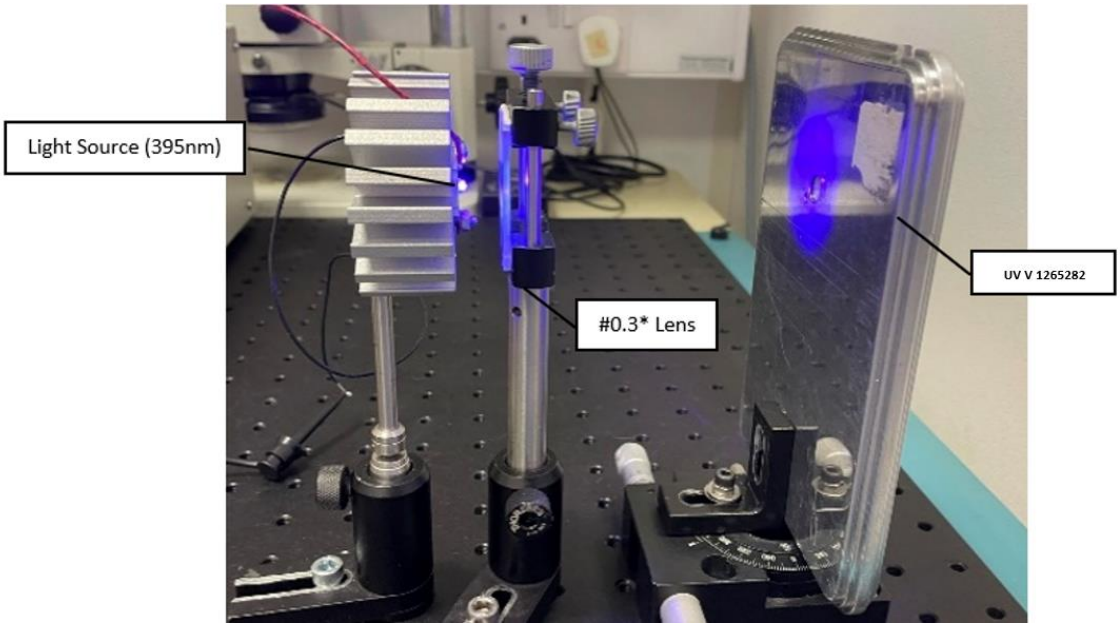

Figure 3.A.5: Test set–up for measurements using the Loctite detectors.

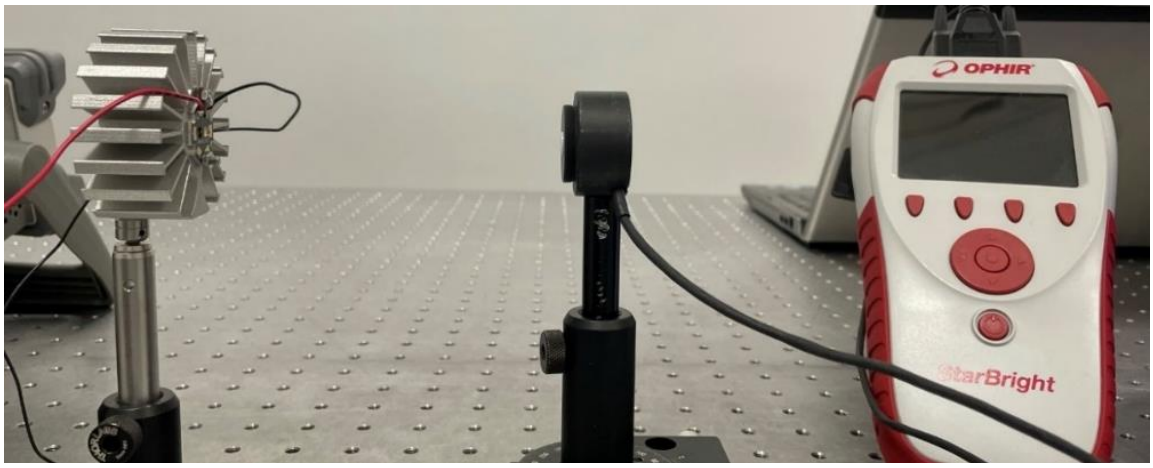

Figure 3.A.6: Test set–up for intensity and integration time measurement experiments.

3.B. Ambient Light Measurements

As discussed in Section 3.3.2, Table 3.B.1 lists the ambient light guide figures measured in the test facility. These figures are only guide figures as to the range of ambient light that can be measured in a particular area.

Table 3.B.1. Measured ambient light figures at the lab facility.

Manufacturer	Ambient Light Measured ($mW\ cm^{-2}$)
Thor Labs	0.26227
Ophir	0.2103
ILT RAA4	0.2334

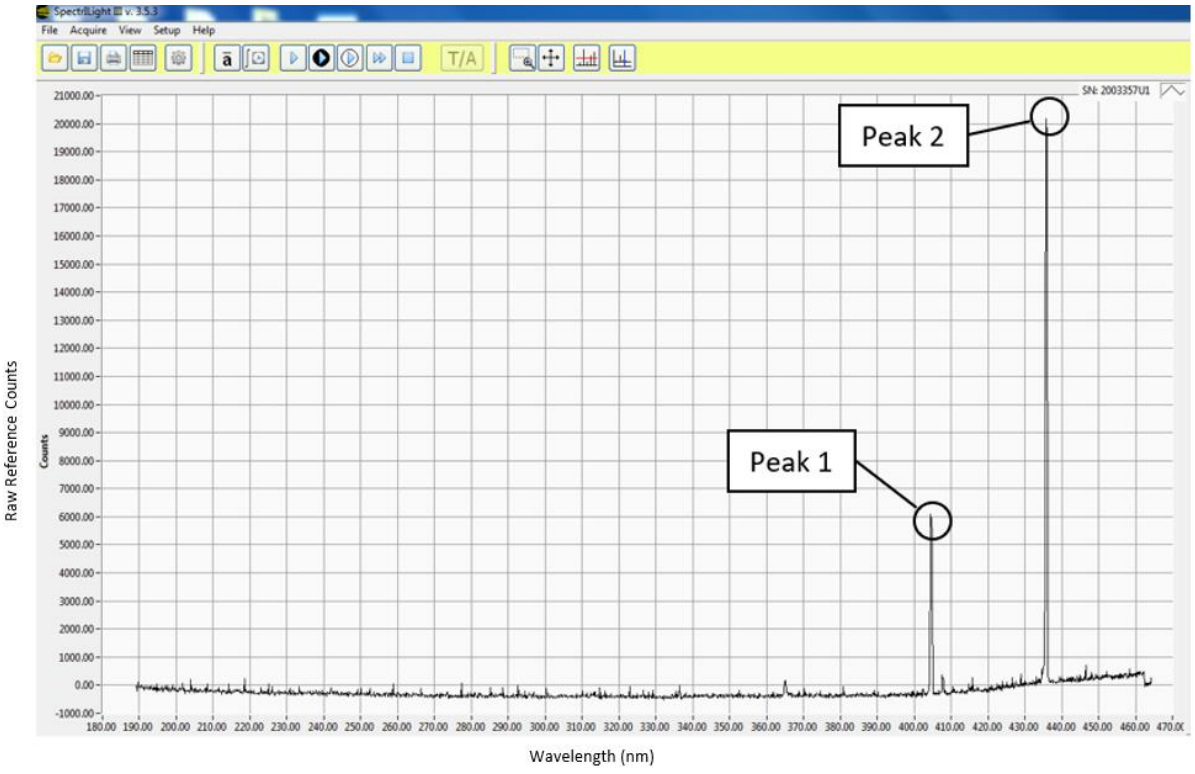

Figure 3.B.1: Ambient light and dark signal measured on SpectrLite III

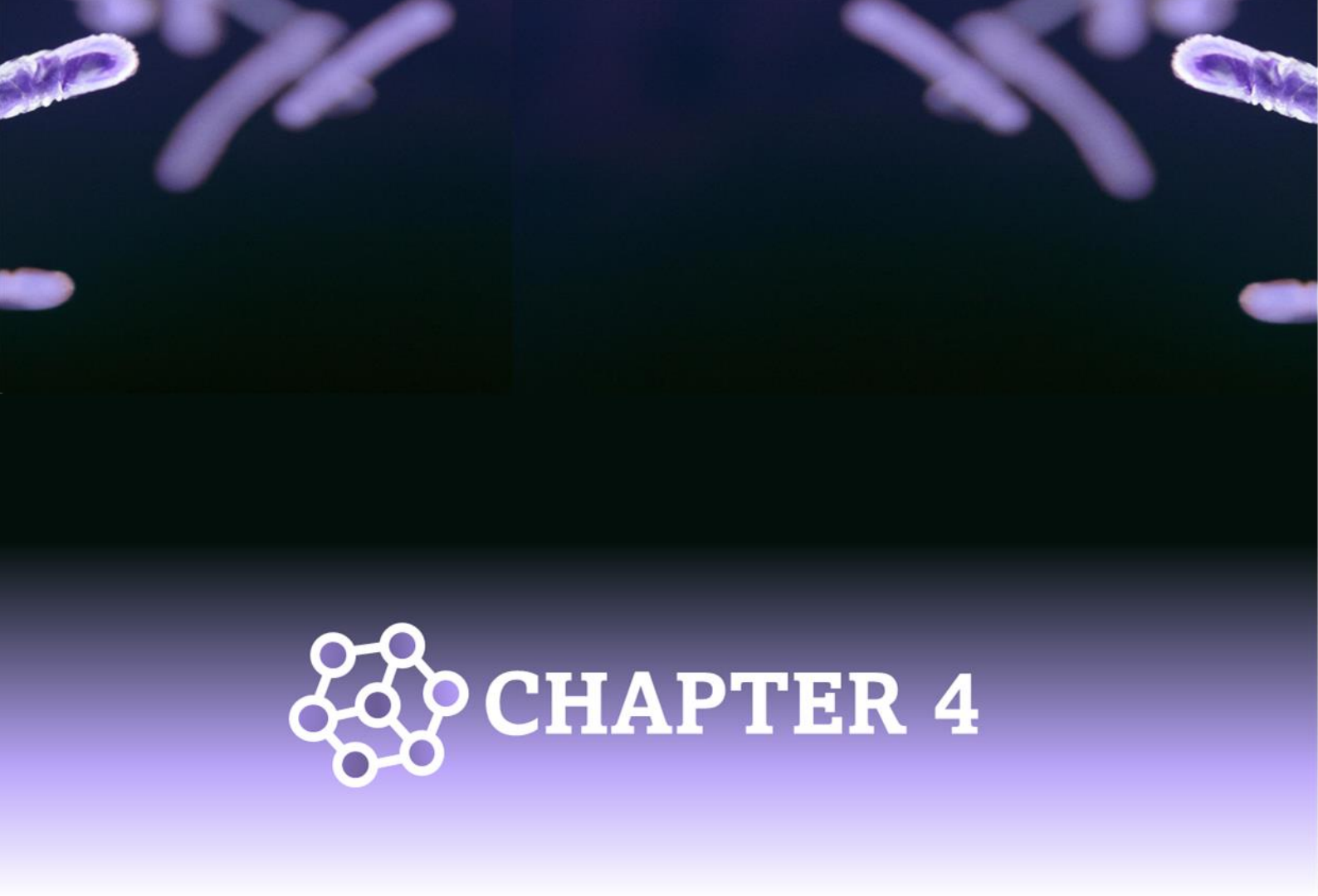

CHAPTER 4

RADIATION MODELING

4.1. Introduction

One of the key aspects to evaluate and optimize the efficiency of a UV reactor is to understand the path of light as it travels through the system. Many methods have been applied theoretically and experimentally to understand the path of ultraviolet light as it travels through a specific medium since the idea of its germicidal effectiveness was observed by Downes et al. in 1877 [29]. Experimental techniques like radiometry and actinometry are physical techniques that require the use of a physical validated set–up for measurements of light. Radiometry is widely used in the lighting industry for measurement of light sources [190]. This technique employs a radiometer (consisting of a sensor or detector and a signal processing unit) which measures the amount of light reaching its receiving surface when subjected to light. While very useful in air mediums, it faces challenges in water–based environments. Very few detectors and radiometers exist in the market that are waterproof or can measure light in water [208-210]. These detectors are of high cost and/or require special attachments, which could cause other issues such as leaks, inaccurate measurements etc., within the system. Another experimental tool employed in the laboratory is chemical actinometry. This technique involves the use of chemicals that absorb photons as the light passes through the system leading to a measurable chemical reaction from which the number of photons absorbed is estimated using a known quantum yield [211, 212]. Actinometry, while useful to measure light, does not provide inputs to help optimize the light source as the measured data only signifies the cumulative number of photons absorbed by the utilized chemicals as it is exposed to light over a period of time.

As discussed above, experimental techniques have worked well in an air medium. However, in a water–based medium multiple operational challenges have been faced by the operators [213]. To overcome these challenges, simulation techniques have been employed to understand the radiant intensity in a water medium. Simulation techniques like discrete ordinate are models on a virtual environment that help understand theoretical light irradiations acting at the point of interest.

Over the years, researchers have considered multiple simulation approaches. Two main approaches have been used in the literature – Eulerian (volumetric reaction rate based) and Eulerian–Lagrangian (particle tracking based) frameworks [214-217]. Several models have been proposed for radiation distribution and to evaluate the kinetic rate constants of microbial inactivation. [218-221]. It has been shown that reactor dynamics, radiation, and

kinetics can be solved using simulation packages such as COMSOL, ANSYS or OpenFOAM based on Computational Fluid Dynamics (CFD) for reactor modeling. Within the Eulerian framework, the conservation equations of mass and momentum are solved. The comparison of the average particle (in this case, simulated microorganisms) values help determine the overall performance of the UV reactor [222]. Within the Lagrangian simulation framework, the trajectories of microorganisms (considered dispersed particles) are computed assuming the Newtonian equation of motion. The inactivation is determined using the accumulated light energy within the described path [222]. Unluturk et al. (2004) [223] and Wright et al. (2000) [215] used the combined Eulerian–Lagrangian framework to simulate UV photoreactors for microbial water disinfection. Keshavarzfathy et al. (2019) [224] elaborated on the need to conduct studies on design concepts that lead to a better understanding of the hydrodynamic interactions and reactor performance. The research studied the development of a model for simulation of UV LED based reactors in the Eulerian framework.

The Monte Carlo method is another approach considered in the literature [225, 226]. This approach is a stochastic method that allows for a flexible geometry and adapts well to complex statistical simulations [227]. The technique involves tracking the trajectory of a large number of photons and computing the location where they are absorbed in a 3–Dimensional space. Busciglio et al. (2016) [228] further considered a probabilistic approach to radiant field modeling in a system and validated the model using Monte Carlo simulations. The research found significant agreement between the two techniques. The above discussed approaches can cover all domains within the reactor if enough particles are taken into account for analysis. Nevertheless, the subject of radiation modeling and transfer in the type of media has been approached from multiple directions in literature and multiple challenges have been observed. Shah et al. reviewed two methodologies for modeling – SURF (simultaneous UV fluence rate and fluid dynamics) and TURF (three step UV fluence rate and fluid dynamics) and concluded that the CFD models can predict the dosage received by water better than applying the average dosage to the system based on the power of lamps [229]. The performance of a reactor depends on multiple factors within the system including interaction between radiation type, radiation dynamics, and the design of reactor [230]. In a 3–Dimensional domain, obtaining an accurate prediction of radiant field and intensity reaching a point of interest requires powerful computing capability and space.

Although the above discussed simulation and experimental techniques are used for their respective applications, these models and tools also lack some inputs that are necessary for

accurate and valid prediction of light irradiation in a flow–based system due to the inability to incorporate certain parameters that play a key role in the amount of irradiation reaching the point of interest, including: i) Accurate source modeling to accommodate the radiation pattern of the light source; ii) Scattering and reflections incurred due to design of the emission system and turbulent flow of water through the system, and iii) Inputs on how to optimize the light reaching the point of interest, given that UV–C LEDs operate at low efficiencies. However, the exact knowledge of optimizing the amount of light reaching the point of interest remains unknown in most cases, and these parameters have continuously evolved with time. Light sources have moved from mercury lamps to the use of LEDs, which are much smaller than the former, making the recent germicidal systems less bulky. In this present study, multiple methods have been utilized to validate the modeling predictions.

In this chapter, a method for prediction of radiant intensity a reaching a point of interest within a water–based medium is studied using optical ray tracing, by considering the actual radiation profile of the UV–C LED selected, optical phenomenon occurring within the medium, design optimization, and change in intensity at interfaces to overcome challenges faced in both experimental and simulation techniques currently used. Ray tracing technique is mainly used in pre–production stages of light source manufacturing. It has been widely debated as to how effective ray tracing is in comparison with the traditionally used Monte Carlo algorithms. Li et al. (2022) [231] compared the two techniques for spine lesions, observing that ray tracing significantly overestimates the volume of target covered by the dose for one case but saw that the estimated dose difference was within 3% between the two techniques for the three other cases studied. The main difference in the former case was the presence of multiple air cavities in the study. In conclusion, the authors mention that the ray tracing technique is “adequate” for use in most cases, but it would need to be validated with other techniques for further use of simulated data [231]. In a similar type of study comparing ray tracing with reverse Monte Carlo method for application to a GEO orbit, Benacquista et al. (2019) concluded that the ray tracing method is fast but presents intrinsic limitations that need to be verified before further use [232]. Monte Carlo simulations have been used in the literature for reactor modeling and have been proven to be time–consuming, while also requiring a large computational space [233-235].

This study applies ray tracing in a germicidal system and attempts to trace the path of ultraviolet light as it propagates through the system and water medium. There exist multiple tools from different manufacturers that employ ray tracing theory like 3Delight [236], POV–

Ray [237], and ZeMax [238]. ZeMax optic studio has been used for the design and simulation of the system for this study. Given the limitations seen in the literature, this study analyzes the validity of the method via comparison with existing techniques employed in academia and industry. The study conducts a step wise analysis of the designed system by comparison with radiometry in an air medium and uses obtained data to quantify the effect of a quartz tube on the irradiation in air. This quantification provides insights into the amount of light lost at multiple working distances within this method. DOM simulations, commonly employed in photoreactors simulations [239-242], have been used to understand the steps and challenges between the two simulation techniques. The study also develops a model to simulate the presence of water and compares it with a lab–based method, used to calculate the number of photons entering water i.e., ferrioxalate actinometry, and compares the increase in radiant intensity as the light passes through the set–up. Finally, a model has been built to provide insight into the radiant energy distribution within a complex system of 4 wavelengths and an understanding of how light intensity changes as it propagates within the tube.

4.2. Methodology

4.2.1. LED Source, Fixture Design, and Spectral Characterization

Three LED light sources of spectral emission in the UV–B and UV–C ranges, characterized in Chapter 2, have been used for this study. The emission spectrum of the devices can be found in Chapter 2, Section 2.3.4. To conduct actinometry and further tests, a custom designed fixture was manufactured. The fixture can be seen in Fig. 4.1 (a, b). The fixture can accommodate up to 8 COBRA Clean FX–1's [243] and a quartz tube (For details on design considerations and analysis, see Appendix 4. A.). The quartz tube can be connected to the sampling tank and outlet to enable a flow through system. The quartz tube used for this study has an external diameter of 23 mm, an inner diameter of 20 mm and a length of 100 mm (FAB028553, MultiLab Ltd). The devices, when mounted on the fixture, can be moved to multiple working distances (from 14 mm to 34 mm away from the center of the quartz tube – see Fig. 4.1 (c) representation). The fixture, seen in Fig. 4.1(b), is made up of aluminum material to ensure any light lost can be reflected back into the quartz tube.

To characterize and quantify the intensity of light emitted from the device, a spectroradiometer has been used. The same measurement sensor (ILT 950UV Spectroradiometer coupled to RAA4 optic) used in Chapter 2 for the characterization of the device has been used. To understand the complete emission profile of the device and other characteristics, the X–Y based motor gantry tester was used (Fig. 2.2 (Chapter 2)).

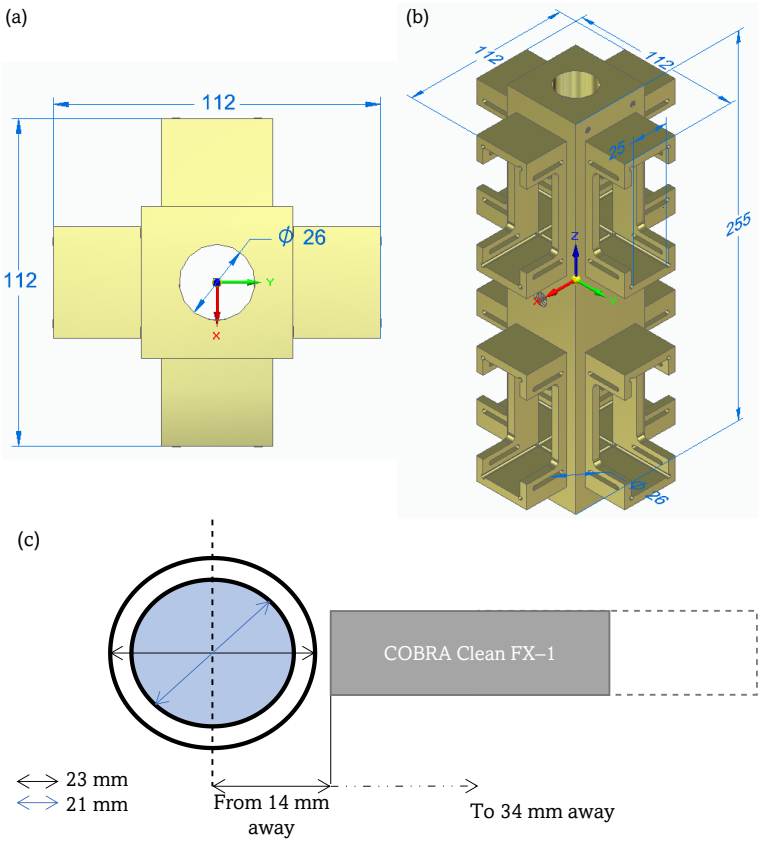

Figure 4.1: UV Fixture – (a) Top View, (b) Isometric View, and (c) Representation of distance between center of the tube to source window.

4.2.1.1. Set–up to Quantify the Effect of the Quartz Tube

One of the objectives of this study was to quantify the effect of quartz tube and compare it with the results obtained from the ray tracing model. To do this, a custom manufactured half–quartz tube, cut along its length has been used. The tube is from MultiLab Ltd (FAB027469, 23 mm outer diameter, 20 mm inner diameter, and 100 mm length). Fig. 4.2 is a schematic representation of the change in set–up for this experiment and Table 4.1 summarizes the quartz tube properties, including the transmittance data as obtained from the manufacturer. The quartz tube and device have been placed as per the dimensions on the UV–C fixture, discussed above, and tested at the same working distances as available on the fixture.

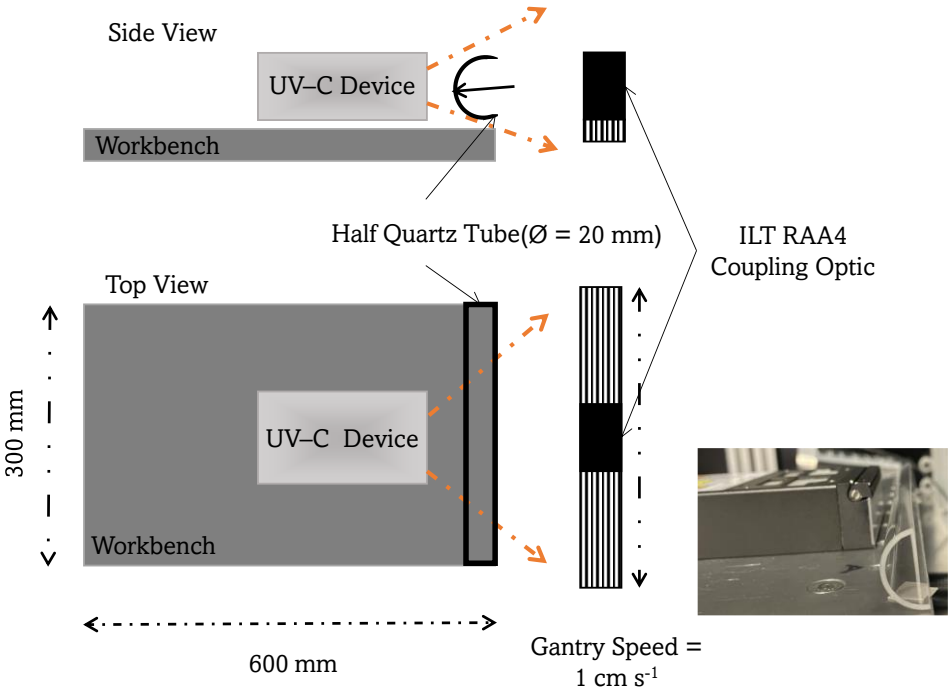

Figure 4.2: Top view of X–Y tester for half–quartz tube radiometry.

Table 4.1: Material and optical properties of the quartz tube.

Property	Typical Value
Density (ρ)	2.2×10^3 kg m^{-3}
Refractive Index	1.485
Transmittance	At 265 nm - ≈0.89
	At 275 nm - ≈0.90
	At 310 nm - ≈0.92

4.2.2. Optical Modeling of the Devices with Ray Tracing

ZeMax Optic Studio has been used for optical simulations. This tool is commonly used by device manufacturers in the early stages of device production, as this tool helps understand the ray paths, predicts theoretical peak intensity (according to LED datasheet optical power output), and provides inputs on ways to optimize the use of reflectors and/or optical components within the device. The tool employs a low cost and quick technique of ray tracing. The software models the propagation of light from the source designed, through the system, and on to the final point of interest. The resulting distribution of rays within the system is used to predict a wide range of light parameters as per interest [238]. Ray tracing

involves the use of two fundamental properties of a ray – position and direction. The position and direction of the ray in a Cartesian coordinate system is defined in Eq. 4.1 and 4.2.

$$\vec{r} = \{x, y, z\} \quad \text{Eq. 4.1}$$

$$\hat{k} = \{l, m, n\} \quad \text{Eq. 4.2}$$

In Eq. 4.1, $\vec{r}$ is the position of the ray and (*x, y, z*) are coordinates measured in units of length depending on the type of system analyzed. In Eq. 4.2, $\hat{k}$ is the direction of the ray and (*l, m, n*) are the direction cosines of the unit vector that points along the ray. Both these quantities are measured based on local coordinates or global coordinates relative to the reference frame input by the operator. If a ray is propagated by distance *x*, where *x* is the length in SI units, the new coordinates of the ray is given by Eq. 4.3.

$$\vec{r'} = \vec{r} + x\hat{k} \quad \text{Eq. 4.3}$$

To predict ray path by refraction, reflection or diffraction within the set–up, the tool employs Snell's law in vector form at the point of intersection with a surface (Eq. 4.4).

$$n'\left(\hat{N} \times \hat{k'}\right) = n(\hat{N} \times \hat{k}) \quad \text{Eq. 4.4}$$

where, *N* is the unit normal vector of the surface at the point of contact and *k* is the ray direction cosine vector. The above Eq. 4.4, changes with the kind and type of optical phenomenon detected at the point of intersection between the surface and ray. To optimize and understand the ray path and associated light system, the tool has the option for two types of ray tracing – sequential and non–sequential. In sequential mode, light rays are limited to propagating from one point to the next and are not flexible for complex systems. Non–sequential ray tracing allows the rays to propagate through the components within the system and allows ray splitting, scattering, and reflections to occur during simulation. This method of ray tracing means that there is no specific sequence for movement of rays within the system i.e., the rays may hit any part of the system designed and move in any direction based on the optical phenomena detected at the point of contact by the software [238]. For this reason, non–sequential mode of ray tracing has been employed in this study.

Contrary to the case of Discrete Ordinate Method (DOM) simulations, the media between the LED array and the radiometer need not be included in the simulation to calculate radiation transport. In the case of ZeMax, the body is designed using shapes available on the software like point sources, ray sources, two angle sources etc. [238]. In the case of this

study, the source has been designed as radial source and the other parts were designed using multiple shape options available on the tool based on the device used to match and replicate the actual device manufactured. Each LED footprint was taken into consideration while designing the device on the tool. Dimensions like thickness of the LED package, size of the actual light emitting surface, and optical power output from the source were drawn from the datasheet, while other parts were designed according to dimensions provided by ProPhotonix. A screen grab of the modeling stage on the optic studio can be seen in Appendix 4.B. (Fig. 4.B.1). In the ZeMax user interface, the entire emission radiation pattern can be input in the source properties ensuring the simulated source irradiation is similar to the manufactured light source. From the datasheet of the LEDs, the radiation pattern has been extracted and used as an input in the tool. The 265 nm and 310 nm LEDs have a viewing angle of 120° and 130°, while 275 nm LEDs have a higher viewing angle of 150°.

A key parameter that controls the simulated values is optical power. Simulations were conducted, initially, using the power output of the LED (in mW) specified in the LED manufacturers datasheet to understand the theoretical intensities delivered to points of interest. Using radiometric experiments conducted in air (Chapter 2, Section 2.3.7), the actual power output of the LEDs has been recalculated to ensure that the model behaves closely to actual measurements. This provides an understanding of how the LED behaves within the device controlling the light output. Once this is done, the model can then be used to simulate the presence of a quartz tube and water in front of the source. A quartz tube is not readily available on the interface and multiple object types were considered before arriving at the use of a cylindrical object type. The quartz tube was modeled using a Boolean technique to simulate the hollow tube and the inner material of the pipe was changed to "*water*" for water–medium simulations. The properties of the quartz tube are as per the quartz library–loaded material properties on the tool. On the tool, the main parameter dictating simulation accuracy is the number of rays within the simulation. For a rough understanding of the light emission and path within the system, a low ray count will work, but for accurate simulations, a higher ray count is recommended. In the case of this study, all simulations have been conducted at 10^6 rays per model simulated. To quantity and analyze the data from light simulations, detector rectangles (here onwards called analytical detectors) were designed within the model. Analytical detectors were created at multiple working distances to simulate and quantify the effect of working distance on the intensity of light from the source. Fig. 4.3 (a, b) shows a sectional view of the 265 nm source designed

on the software depicting the light source, the mechanics within the device, and detector objects as black lines in the *x* direction. For simulations involving a water–medium, the refractive index was changed with each wavelength. The input data for this model has been listed in Table 4.2.

Table 4.2: Refractive index and quantum yield input from literature studies [244, 245].

Wavelength	Refractive Index	Quantum Yield (ϕ)
265 nm	1.3572 [244]	1.2281 [245]
275 nm	1.3540 [244]	1.2629 [245]
310 nm	1.3478 [244]	1.2281 [245]

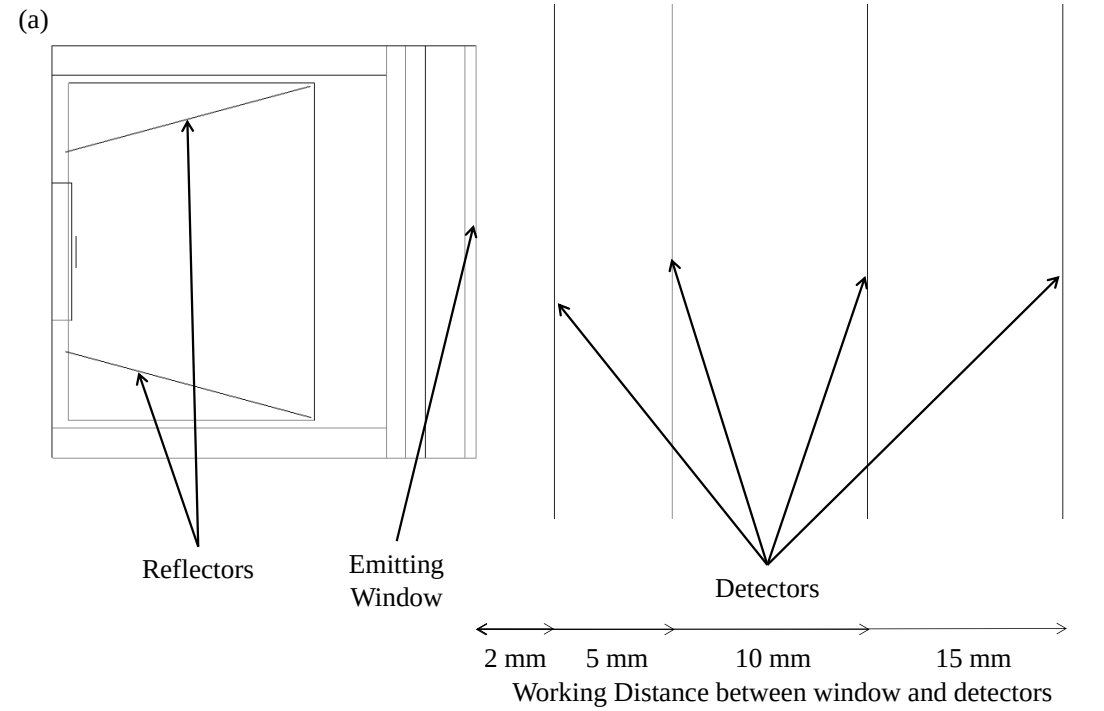

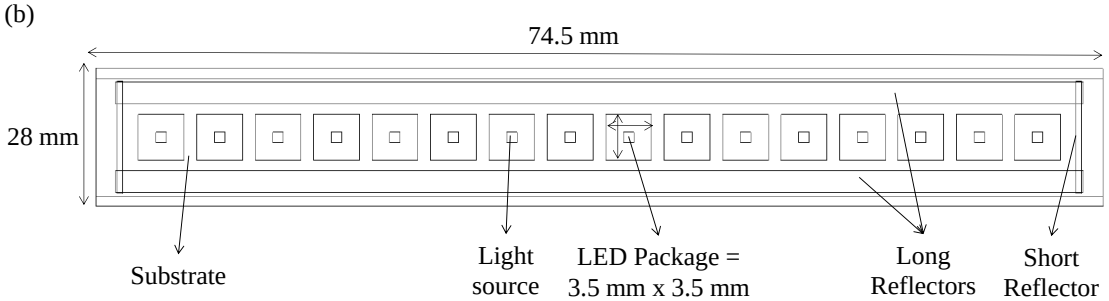

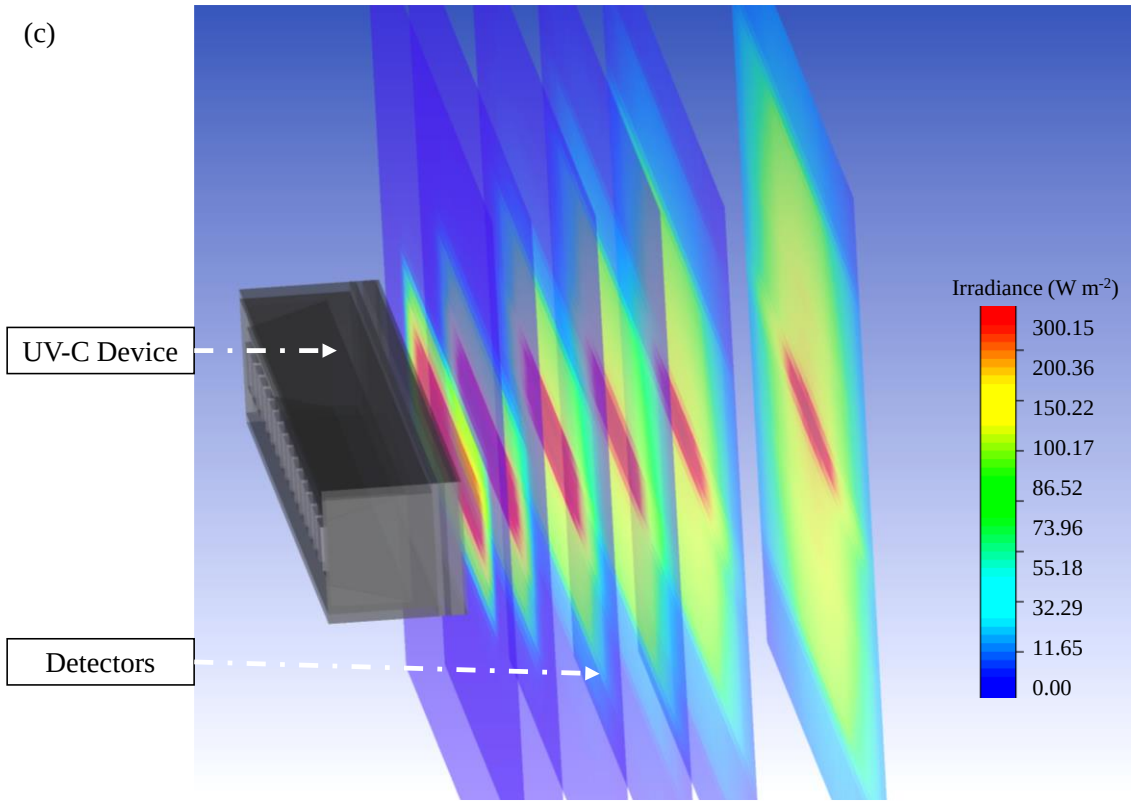

Figure 4.3: (a) Side view of the designed model on ZeMax interface, (b) Top view of the designed model, and (c) Section view of simulated 265 nm Optical Model.

4.2.3. Characterization using Chemical Actinometry.

Actinometry is a method by which the number of photons in a beam can be measured by use of a chemical system that absorbs the incident radiation in a defined space of a reactor. The method determines the number of photons integrally with time. Reactants used within this chemical system undergo a light–induced reaction for which the quantum yield is known. The quantum yield, $\Phi(\lambda)$, of a photochemical reaction can be defined as the number of events, like molecules formed, divided by the number of absorbed photons of that wavelength [246]. Measuring the reaction rate allows the calculation of absorbed photon flux (Eq. 4.5).

$$q_p(abs,\lambda) = q_p^o(\lambda)\left(1-10^{-A(\lambda)}\right) \qquad \text{Eq. 4.5}$$

where, q_p^o is the incident photon flux and $A(\lambda)$ is the decadic absorbance. There are different chemical systems listed by the International Union of Pure and Applied Chemistry (IUPAC) like solid and micro heterogeneous–phase chemical actinometers, gas–phase chemical actinometers, and liquid–phase chemical actinometers. Based on the wavelengths studied

and the type of set–up, a liquid–phase chemical actinometer has been selected. Specifically, potassium ferrioxalate ($K_3[Fe(C_2O_4)_3].3H_2O$) based chemical system has been used for this study. The chemical system is also recognized as the Hatchard–Parker actinometer by IUPAC and widely accepted as a standard actinometry test for ultraviolet wavelengths. The actinometer has a wavelength range of 250 – 500 nm with a quantum yield (Φ) of 1.25 – 0.9 [247, 248]. The quantum yield, used in calculations, for each wavelength has been listed in Table 4.2. The chemicals used for this procedure were as follows:

1. Oxalic Acid ($H_2C_2O_4.2H_2O$, Scharlau)
2. Ferrous Sulphate ($Fe_2(SO_4)_3.5H_2O$, ThermoScientific)
3. 1 N Sulfuric Acid (H_2SO_4, Scharlau)
4. 1,10 Phenanthroline ($C_{12}H_8N_2$, Scharlau)
5. Buffer Solution - Water (H_2O), 96% Sulfuric Acid and Acetic Acid sodium salt trihydrate ($C_2H_3NaO_2.3H_20$, Scharlau)

To characterize the device using chemical actinometry, the UV fixture has been used. For each test, only one device of a specific wavelength has been used within the fixture at a distance of 14 mm away from the center of the quartz tube. A magnetically coupled pump (Flojet, RS Pro 266-597) with a flow rate of 2 L min^{-1} has been used to flow the prepared solution through the fixture. Fig. 4.4 is a schematic representation of the set–up used. 2 L of milliQ water have been used as the base water matrix for these experiments. The experimental procedure is that proposed by Hatchard et al. (1956) [248]. 3 tests have been conducted for each wavelength with samples extracted at different time intervals to ensure repeatable and reproducible data is obtained.

4.2.4. Discrete Ordinate Method (DOM) Modeling

Discrete Ordinate Method is one of the available models used to calculate radiation transport implemented in Fluent in the multiphysics ANSYS™ platform [249]. The method solves the radiative transfer equation over a domain of discrete solid angles. In this technique, the incident radiation is calculated by integrating the radiant intensity along spherical space. The method employs discretization of spatial directions and solves the Radiative Transfer Equation (RTE, Eq. (4.6), [249]) for each direction. It calculates radiation intensity as a function of absorption, scattering, reflection, and emission. The equation describes the conservation of radiative intensity in a direction of space.

$$\frac{dI_{\lambda,\vec{\Omega}}}{ds} = \underbrace{-k_\lambda I_{\lambda,\vec{\Omega}}}_{Absorption} \underbrace{- \sigma_\lambda I_{\lambda,\vec{\Omega}}}_{Out\ Scattering} \underbrace{+ \frac{k_\lambda T^4}{\pi}}_{Thermal\ Emission} + \underbrace{\frac{\sigma_\lambda}{4\pi}\int_{\Omega'=4\pi} p(\vec{\Omega}' \rightarrow \vec{\Omega}) I_{\lambda,\vec{\Omega}} d\overrightarrow{\Omega'} I_{\lambda,\vec{\Omega}}}_{InScattering} \quad \text{Eq. 4.6}$$

where, $I_{\lambda,\vec{\Omega}}$ is the intensity of photons with wavelength, λ, propagated along direction $\overrightarrow{\Omega}$; k_λ is the volumetric absorption coefficient; σ_k the volumetric scattering coefficient; σ is the Stefan–Boltzmann constant; T is the temperature in degree kelvin, and $p(\vec{\Omega}' \rightarrow \vec{\Omega})$ is the phase function that describes the directional distribution of scattered radiation.

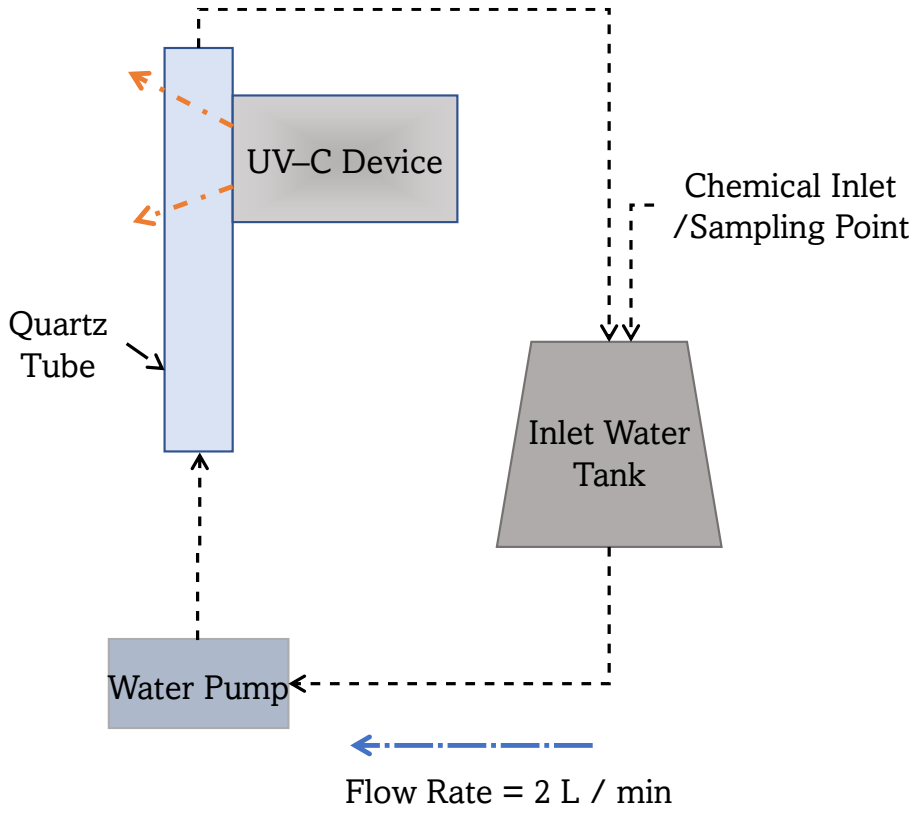

Figure 4.4: Schematic representation of the set–up used for actinometric experiments.

The device was designed on Solid Edge CAD software and converted to ANSYS™ Workbench for radiation simulations on ANSYS™ Fluent. For this study, the light has been assumed to be monochromatic. Each LED within the device has been simulated as a flat surface emitting light. The following assumptions have been made before conducting simulations: i) Thermal emission is neglected and temperature is set to 0 K, ii) Density and viscosity are considered constant, as per standard material properties, for the wavelength range studied, iii) Absorption coefficient of 0.00074 m^{-1} and scattering coefficient of 0.00049 m^{-1} have been assumed for air at the wavelength range (250 nm – 320 nm) from previous studies [250].

To simplify simulation time and the number of equations within the model, only the emitting window section (light head) of the device has been modeled (see Fig. 4.5(a)), with the same dimensions of the experimental system: 76.8 mm × 28 mm with 4 reflectors inside the emitting window. For each wavelength, the LED size and number of LEDs have been modeled as per the supplier design and datasheet specifications (Chapter 2, Table 2.3). For the simulations, the reactor has been considered as a simple black box that absorbs any radiation irradiated by the source. The reactor has slightly larger dimensions than that of the emitting window. Before extracting data from the simulations, a mesh sensitivity analysis has been conducted. For further information, refer to Appendix 4.C. (Table 4.C.1, Fig. 4.C.1 – 4.C.3).

For simulation on Fluent, the following conditions have been used:

a) Boundary Conditions: (i) Light source – Direct irradiation and beam width as per manufacturer specifications; (120° for 265 nm, 150° for 275 nm, and 130° for 310 nm FX–1) (ii) Reflectors – Zero internal emissivity and diffuse fraction; (iii) Reactor, emitting window, and LED substrate –100% internal emissivity and diffuse fraction.
b) Refractive index of air has been accounted for each wavelength from literature studies (265 nm – 1.00029777, 275 nm – 1.00029570 and 310 nm – 1.00029023 [244]).
c) For the light source, angular discretization of 15 × 15 solid angles per octant has been used, enough to capture the LED beam angle.
d) Optimum mesh size from the mesh sensitivity resulted in an average of 417,876 cells per wavelength, by use of an inflation mesh at the LED surface and surface mesh for the reactor body.
e) Second order upwind solution method for the DOM model with up to 500 iterations for calculation of the solution.
f) Convergence of numerical solution was ensured by monitoring the scaled residuals to a criterion of at least 10^{-6} for discrete ordinates and energy variables.

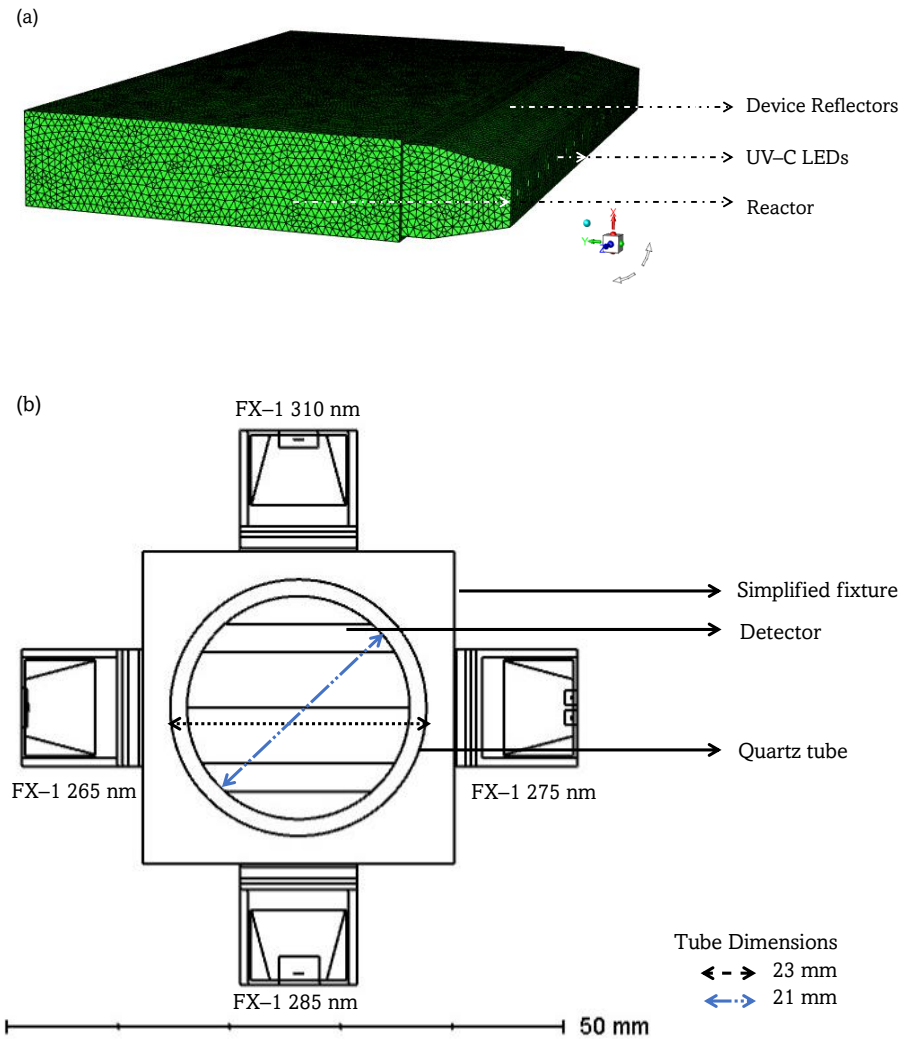

Figure 4.5: (a) Isometric view of the meshed DOM model for 265 nm source, modeled in ANSYS Fluent and (b) Upper view of the 4–wavelength complex system. (CW from the left) FX–1 emitting window of 265 nm, 310 nm, 275 nm, and 285 nm, respectively.

4.2.5. Modeling of a 4–Wavelength Germicidal System

Upon validation of the simulated model using the ray tracing method, a complex system consisting of 4 FX–1 devices operating at different wavelengths was modeled. The model was modified to replicate the fixture shown in Fig. 4.1 (a, b). The design was simplified for lower simulation time. The same number of rays (10^6) as mentioned earlier was used in simulations. Fig. 4.5 (b) depicts the model of the complex system.

4.3. Results and Discussions

4.3.1. Ray Tracing and Radiometry

As mentioned earlier, one of the key inputs into the simulation software is the optical power output per LED source. To understand how the tool is used in industrial applications, initial simulations have been conducted using the data sheet mentioned optical power output (in mW) of the source. The brown line in Fig. 4.6 (a) shows the predicted peak intensity, at multiple working distances. The result predicted by the simulation is higher than the actual peak intensity delivered by the device, experimentally determined.

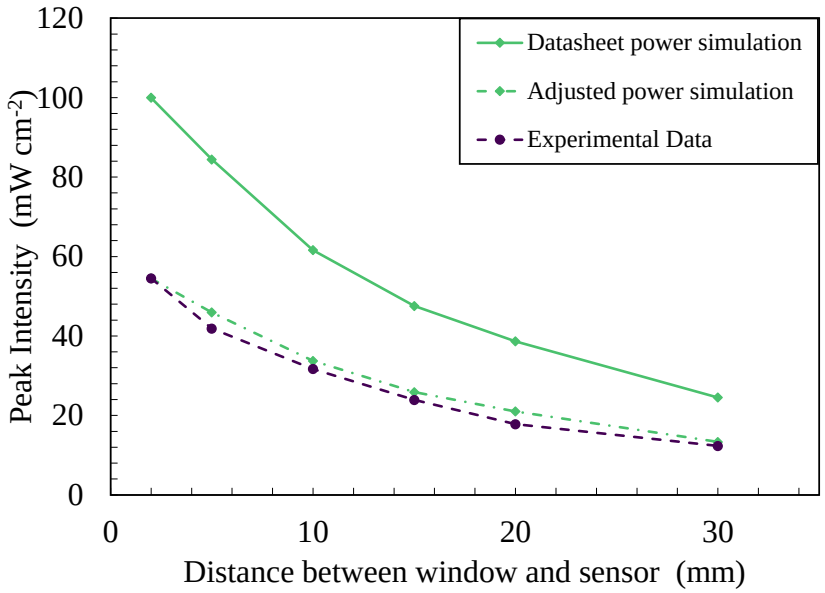

Figure 4.6: Ray tracing data *vs* experimental data (265 nm).

As per the manufacturer datasheets, the 265 nm and 275 nm LEDs have an optical power output of 70 mW (at 500 mA) and 8 mW (at 40 mA), respectively, while the 310 nm LED has an optical power output of 50 mW (at 350 mA). As discussed in Chapter 2 (Section 2.3.3), the LED manufacturer conducts tests on the LED in a near ideal environment and hence the theoretical peak intensity observed is considerably higher than the actual power output from the device. The actual power output from each LED must be determined on a case–by–case basis depending on the system and electronics driving the light source. In the case of the COBRA Clean FX–1's used, upon rollover tests (Section 2.3.3, Fig. 2.12 (a–d)), the operating current for the devices was set to 300 mA for the 265 nm LEDs, 120 mA for the 275 nm LEDs and 420 mA for the 310 nm LEDs.

For example, the 265 nm COBRA Clean rollover test results indicated a LED safe current for the device of 300 mA and corresponding optical power output from each LED of 33 mW. Using this value as the input required for the source, the input power on the software was adjusted to check if the model behaved the same as the experiments. It can be seen in Fig. 4.6 (a) that the data from the adjusted power simulation (green dotted line) is very close to the data measured by the spectroradiometer (orange line) (± 5%). Data on comparison between simulations for other wavelengths can be seen in Appendix 4.D (Fig. 4.D.1 (a, b)). By obtaining a close agreement, between the experimental data and simulated data, it was concluded that the device–based optics designed in the model are very similar to actual device conditions. The base model of the light source can now be used to simulate other conditions and compared with alternative techniques.

For any light source, it is understood that the total intensity acting on a target area is a function of the light emitting source and the distance between the source and target [251]. With an increase in the distance from the target, the light intensity decreases as the spread of light is wider. The same number of photons emitted by the light emitting surface is spread over a wider area at longer distance from the source. A representation depicting how light intensity decreases with increase in distance away from the source can be seen in Fig. 2.19 (a) (Chapter 2). To characterize the light source using a spectroradiometer for this work, working distances of 14 mm to 34 mm away from the source window (in 5 mm steps), as designed within the fixture, have been selected for measurements. The selected working distances provide an understanding of the behavior of light in air within the fixture. Radiometric measurements were conducted on 3 separate days to ensure the repeatability and accuracy of the obtained data. The experimental error obtained from measurements was low. Although all wavelengths have been measured and tested, only 265 nm based FX–1 data has been presented as the other wavelengths showed similar behavior and were in close agreement with the ray tracing simulation data.

Fig. 4.7 (a) plots the peak intensity measured at each working distance between the source emitting window and coupling optic for 265 nm source. It was seen that all the 3 wavelengths selected for this study, also seen in Chapter 2 (Section 2.3.7), follow the expected trend of decrease in light intensity with increase in working distance for both the techniques. Ray tracing simulations can be seen to have the same trend as the radiometric measurements with an average of ± 7% difference between the two techniques for 265 nm source while an average difference of 7% was observed for the other two wavelengths. Similar to findings in

the literature, the ray tracing technique overestimates the actual light intensity in the simulations. The difference and higher peak intensity observed can be attributed to the fact that in radiometric measurements, light bouncing off the workbench surface is lost, while this does not happen in the simulation environment. Although designed as per dimensions and specifications, the design models do not fully replicate the actual environment and hence a difference is expected. Within the X–Y tester, the sensor/coupling optic moves in X–Y direction for a period of time and captures data at each set point and displays light measured at each point at that instant of time, which could be another source of error to explain the difference between techniques.

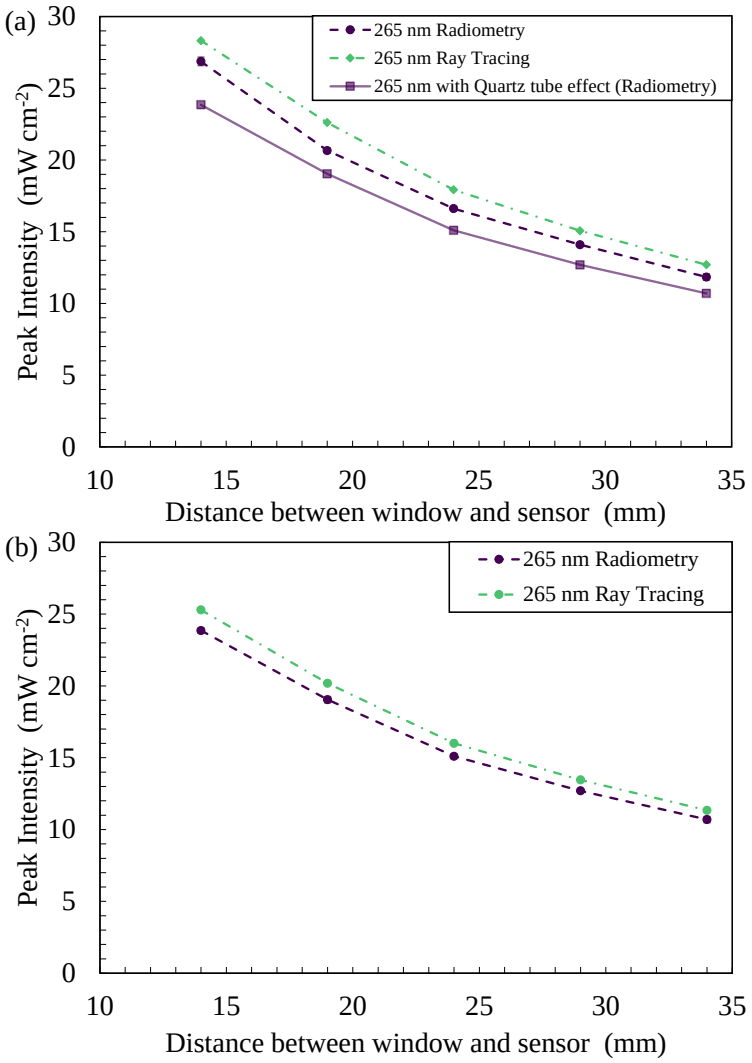

Figure 4.7: (a) Plot of peak intensity *vs* working distance for 265 nm source and (b) Comparison between radiometry and ray tracing in the presence of a quartz tube in front of the light source.

To summarize the comparison between the radiometric measurements conducted in air and the optical ray tracing simulations, Table 4.3 provides data on measured peak intensities at each working distance for the data seen in Fig. 4.7 (a). Plots of peak intensity versus working distance for 275 nm and 310 nm sources can be found in Appendix 4.D.2 (Fig. 4.D.2 (a, b) and Table 4.D.1). Compared to the 265 nm source, the 275 nm source emitted 1.4% lower intensity while the 310 nm source emitted 23% higher intensity at 14 mm working distance away from the center of the system.

Table 4.3: Recorded peak intensity at multiple working distances using radiometry and ray tracing.

Working Distance (mm)	Peak Intensity (265 nm) (mW cm^{-2})			
	Absence of quartz tube		Presence of quartz tube	
	Radiometry	Ray Tracing	Radiometry	Ray Tracing
14	26.8 ± 0.3	28.3	23.8 ± 0.4	25.3
19	20.7 ± 0.2	22.6	19.0 ± 0.3	20.2
24	16.6 ± 0.2	17.9	15.1 ± 0.2	16.0
29	14.1 ± 0.1	15.1	12.7 ± 0.4	13.4
34	11.8 ± 0.2	12.7	10.7 ± 0.4	11.3

4.3.1.1. Effect of Quartz Tube

To analyze the impact of the quartz tube on the incident light, Fig. 4.7 (a) provides a comparison between the radiometry measurements done in the presence (blue line) and absence of the quartz tube (orange line) at different distances from the light source for the 265 nm source. The quartz tube reduces the amount of irradiation reaching the target surface by 11%, at a working distance of 14 mm away from the center of the quartz tube, and follows the same trend as expected. In the same way, the ray tracing simulations resulted in similar data to that of the radiometric measurements, as shown in Fig. 4.7 (b) (orange line). Table 4.3 summarizes the measured and simulated data from these experiments and can be compared with data measured in the absence of a quartz tube to understand the impact of quartz thickness on the light irradiated for the 265 nm light source. In the presence of a quartz tube in front of the source, a good agreement can be observed between the two techniques, within ± 6% of the radiometric measurements, for all the wavelengths studied. Plots of peak intensity *vs* working distance for 275 nm and 310 nm sources can be found in Appendix 4.D.3. (Fig. 4.D.3 and Table 4.D.2). Compared to the 265

nm source, the 275 nm source emitted nearly the same intensity (a difference of about 0.004%), while the 310 nm source emitted 32% higher intensity at 14 mm working distance away from the center of the quartz tube.

As mentioned earlier, this study attempts to analyze and quantify the effect of quartz tube or quartz material on the light emitted. This study employs the use of a custom manufactured quartz tube cut along the length to understand the impact. The tests provided both an understanding of the impact of using a quartz material in front of the light source and an input for the simulations. To better understand the effect of quartz, the manufacturer of the quartz tube provided the transmission curve of the quartz material used by the tube (see Appendix 4.E). The measurements were conducted, and data were validated to ensure that the loss due to quartz material was well within the range expected as per the material specifications.

In Fig. 4.8 (a) and 4.8 (b), the average of all losses observed at multiple working distances in the radiometric measurements has been compared with the ray tracing simulations and the transmission curve obtained from the manufacturer. While the data for 265 nm and 275 nm sources show a good agreement between the techniques and the transmission curve, the error bar and loss for 310 nm source is high due to the 21% loss of light seen at 34 mm working distance (see Fig. 4.8 (b)). On the ray tracing, a constant loss was observed throughout all working distances and all wavelengths. In optical simulations, when the light travels within a device or system, the intensity does not vary unless other structures or objects affect the ray trajectory. Therefore, no change in loss is observed with an increase in working distance.

The data obtained in the presence and absence of a quartz tube was compared to calculate the amount of light lost as it travels through the walls of the quartz tube. In the case of the 265 nm source, an average loss of 10.0 ± 0.5% was observed with a maximum of 11% loss (at 14mm working distance) and a minimum of 8% (at 19 mm working distance).

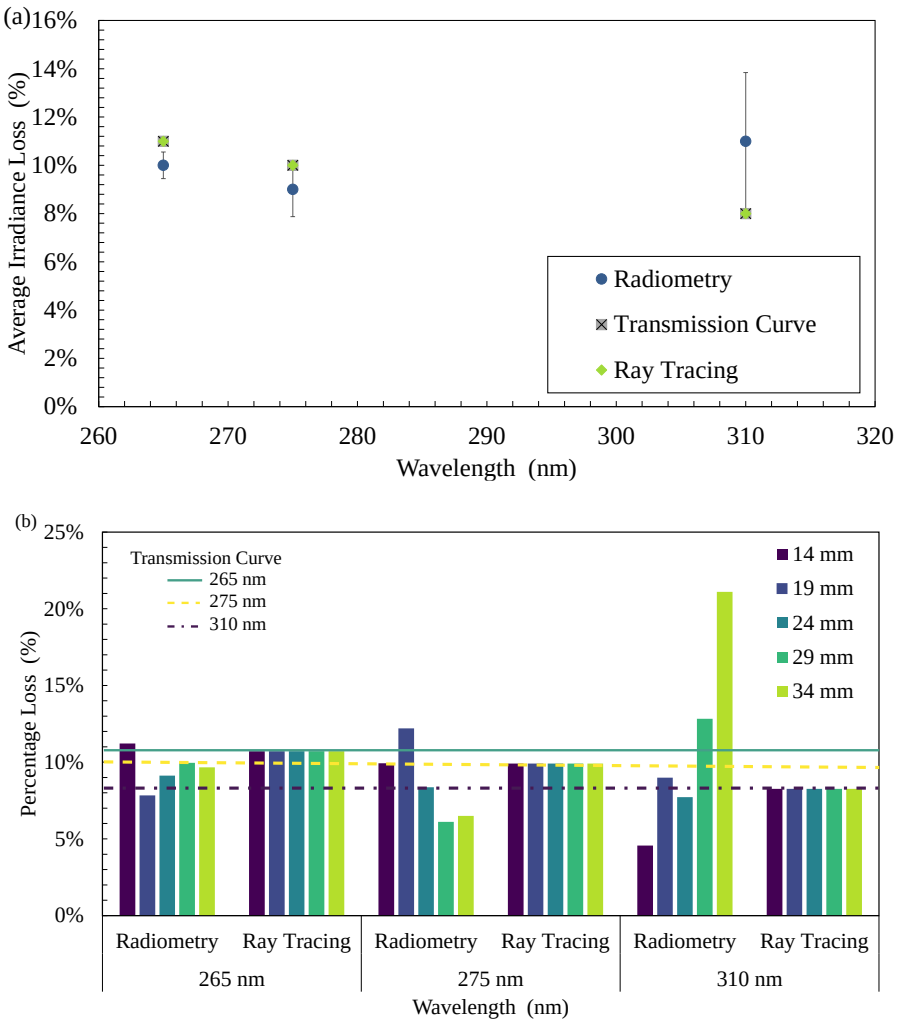

Figure 4.8: (a) Comparison between the average loss at multiple distances in radiometry, ray tracing, and transmission curve and (b) Plot of percentage loss of intensity for all wavelengths at multiple working distances.

In the case of 310 nm, the highest loss observed (21%), can be attributed to multiple reasons within the measuring system. In Fig. 4.2 (Section 4.2.1.1), it can be seen that there is a gap between the workbench (that moves the device to multiple working distances) and the measuring sensor (which is on a motor gantry). It is possible at higher working distances that the light is being lost due to the gap and the surrounding environment within the working set–up. Also, in the case of these radiometric measurements on the half–quartz tube, data was measured along the line of the tube rather than a rectangular space, which means any light not within the length of the quartz tube, at the instant of time when the sensor captures light signal, has not been measured. Table 4.4 summarizes the average loss observed with wavelength and data comparing the techniques.

Table 4.4: Data on the loss of intensity in comparison with the transmission curve.

Technique / Wavelength	Radiometry	Ray Tracing	Transmission Curve
265 nm	10.0 ± 0.5%	11%	11%
275 nm	9.0 ± 1.1%	10%	10%
310 nm	11.0 ± 2.8%	8%	8%

4.3.2. Discrete Ordinate Method

To further understand the method and tool's capability, this study conducted simulations using the DOM to compare and validate the ray tracing–based modeling technique. Table 4.5 summarizes the data obtained from the simulations for the 265 nm source. It can be seen that the data follows the same trend in both types of simulations. An average difference of 5.0 ± 0.9% was seen between the two simulation techniques for the 265 nm source. This difference could be due to the input value for direct irradiation on the DOM model. The input value, for DOM simulations, has been extrapolated from the radiometric measurements in Section 4.3.1 (Fig. 4.7 (a)). While on optical ray tracing, the LED optical power was input for the simulations. Data from DOM simulations can be seen to be closer to the radiometric measurements than that of optical ray tracing simulations (± 1.7%). Fig. 4.9 (a) plots the comparison between the two simulation techniques alongside the radiometric measurements from Section 4.3.1. For 275 nm and 310 nm sources, results can be found in Appendix 4.F. (Fig. 4.F.1 and Table 4.F).

To further understand the difference between the two simulation techniques, uniformity data has been extracted. Fig. 4.9 (b – d) compares the uniformity plots obtained from the two simulations at 14 mm away from the source along with the uniformity plot from radiometric measurements. While all three techniques display a similar profile, due to the size of the reactor design in DOM, the plot is cut off after the reactor size. In optical ray tracing, the analytical detector size does not impact simulations or simulation time and hence a wider plot could be obtained. The uniformity plot, in Fig. 4.9 (d), can be seen to be noisy as the data obtained from DOM simulations is a collection of more than 10,000 data points while the radiometry plot is a collection of ~600 high resolution points measured by the radiometer at an instant of time during the measurements. The plot, in Fig. 4.9 (d), can be smoothed by extracting data with fewer decimal points from the software. This has not

been done so as to provide an overview and comparison between the solutions obtained from respective simulation and experimental techniques.

Table 4.5: Recorded peak intensity at multiple working distances between simulation tools.

Working Distance (mm)	Recorded Peak Intensity (265 nm) (mW cm^{-2})	
	Ray Tracing	DOM
14	28.32	26.90
19	22.60	21.70
24	17.92	16.84
29	15.07	13.86
34	12.69	12.31

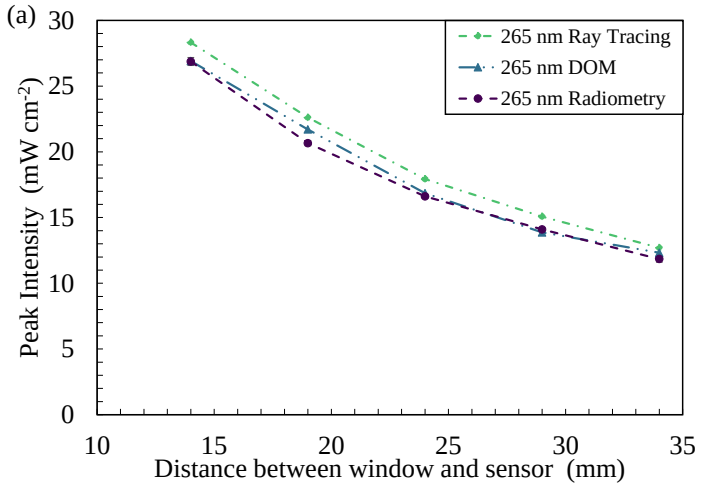

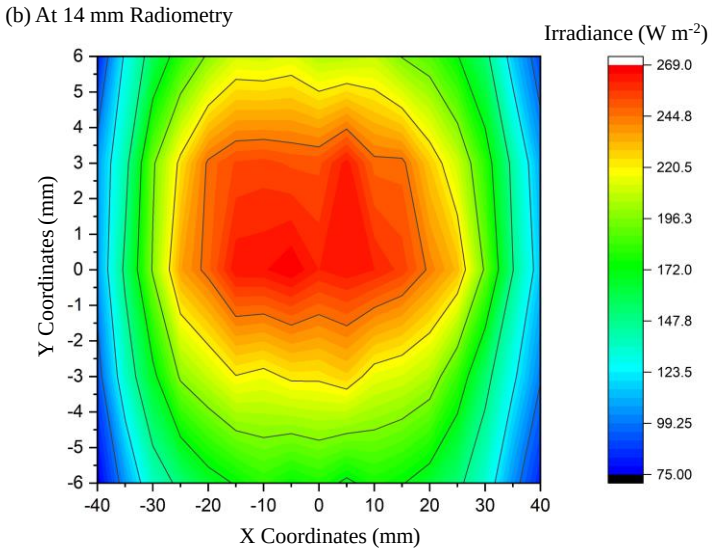

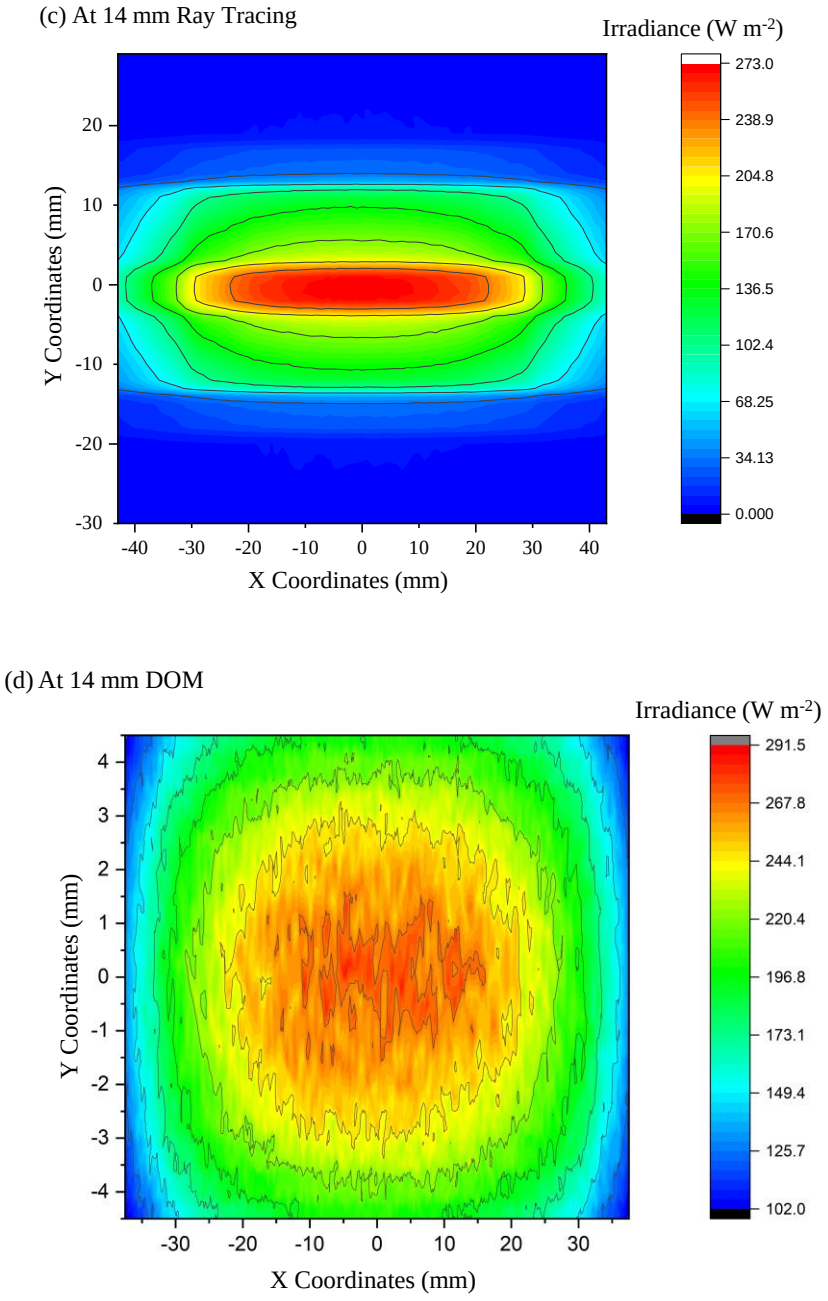

Figure 4.9: (a) Comparison between radiometry, ray tracing, and DOM, (b) Uniformity plot obtained from radiometry, (c) Uniformity plot obtained on ray tracing interface, and (d) Uniformity plot observed on DOM.

Both simulation techniques have their respective challenges and disadvantages. Both simulations are time–consuming and need an elaborate amount of computation and space for each simulation. In DOM, one of the main parameters controlling accuracy and precise simulations is the angular discretization of the light source. An increase in angular discretization significantly increases the simulation time. On the ray tracing tool, the main

parameter dictating simulations is the number of rays within the simulation. A low ray count will work for a rough understanding of the light emission and path within the system, but for accurate simulations, a higher ray count (greater than 10^6) is recommended. The simulation time for ray tracing averaged up to 1 h for high number of rays whereas on DOM, for a high angular discretization (above 15 × 15) of the light source, an average simulation time of 2–3 h was required.

The input of a number of rays is similar to conducting mesh sensitivity analysis in DOM. In DOM simulations, it is important that the entire system is built as a solid in a specific space to obtain results. In ray tracing–based simulations, the design of the system is based on an X–Y–Z coordinate system that enables easier design and can be built as per the design and dimensions. In both simulations, the main body can be simplified to reduce simulation time and processing. As in the case of this study, the whole body of the device has not been designed, only the light head section as this is the only part that contributes to simulating light travel. Both methods can simulate the presence of water and air in front of the source. However, it was seen that with ray tracing methods it is easier than DOM for both the design and simulation steps. Unlike DOM, each part can be designed independently. Hence, any issues incurred during or after simulations can be detected specific to the part and not the system as a whole. This helped reduce the time for correction and changes, whereas on DOM, the time required for understanding the issue and making changes was significantly higher. In simulations where the light source data is of importance, an advantage of ray tracing over DOM simulations is the useful input of the radiation pattern of the light source. In ray tracing, the light source can be programmed as per the manufacturer's datasheet and optimized for the device design. The ray tracing technique is mainly an optical tool and hence any particle tracking simulations cannot be conducted in this tool, while this can be done on DOM [240].

4.3.3. Characterization using Actinometry

Once the ray tracing model was validated in an air medium, the model was then developed to understand its behavior in a water–medium. To do this, multiple changes were made within the designed model discussed in Section 4.2.2:

- To design a tube on the tool, multiple "object types" were considered and tried. A hollow cylinder type object was not readily available and hence to build the quartz tube within the model, Boolean operation techniques were applied. Two cylinders have been

designed and using Boolean operations, the inner cylindrical area has been subtracted from the outer solid cylinder to obtain a hollow cylinder of the dimensions of the quartz tube within the fixture. In doing so, the software enables the input of two materials for each of the cylinders. The inner cylinder material was changed to "water" while the outer cylinder material was set to "quartz." [252]

- While conducting actinometry, the device was placed within the UV fixture and samples were taken. Within the UV fixture, the environment is different to the standard workbench set–up and it can be seen that there exist multiple design bodies and/or surfaces ensuring little light is lost within the system. To ensure that the simulation model replicates the actinometry measurements conducted on the fixture, two extra design bodies on top and bottom of the light source body (see Fig. 4.10 (b)) have been designed as per the fixture model.
- Analytical detectors or measuring points in the model have only been placed within the tube and the software assumes the remaining simulation space as air.
- The refractive index of water within the simulation was changed for each wavelength based on data from literature studies [244] and have been listed in Table 4.2.

Actinometric measurements have been conducted on 3 separate days to ensure reproducible and repeatable data is obtained. The quantum yield used to convert the measured data to mW cm^{-2} has been listed in Table 4.2. The technique was subjected to all three wavelengths in this study and only conducted at a working distance of 14 mm away from the center of the quartz tube. This technique was used to validate the ray tracing model and check if the simulation agreed with the measurements. Conducting actinometry for each working distance can be time–consuming whereas the simulation displayed data for all points of interest in lesser time. Measured data from actinometric measurements can be seen in Table 4.6, in comparison with the extracted peak intensity data at the center of the quartz tube on the simulated model. It can be seen that both the measured and simulated data are in close agreement with each other i.e., within the error range of the actinometric measurements for all the sources studied (see Fig. 4.10(a)). The 275 nm source can be seen to have the closest agreement 51.8 ± 4.4 mW cm^{-2} in actinometry to 50.22 mW cm^{-2} on the ray tracing model. The difference between the two techniques is seen to be about 3%. Data on actinometry measurements can be found in Appendix 4.G. (Table 4.G and Fig. 4.G.1).

Table 4.6: Data on comparison between actinometry measurements and ray tracing.

Wavelength	Measured Intensity (mW cm^{-2})	
	Actinometry	Ray tracing (Peak Intensity)
265 nm	35.0 ± 5.5	40.2
275 nm	52.0 ± 4.4	50.2
310 nm	52.7 ± 9.8	54.9

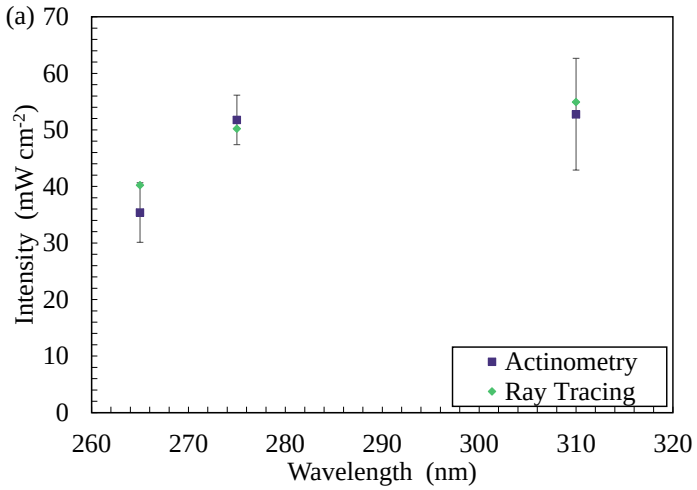

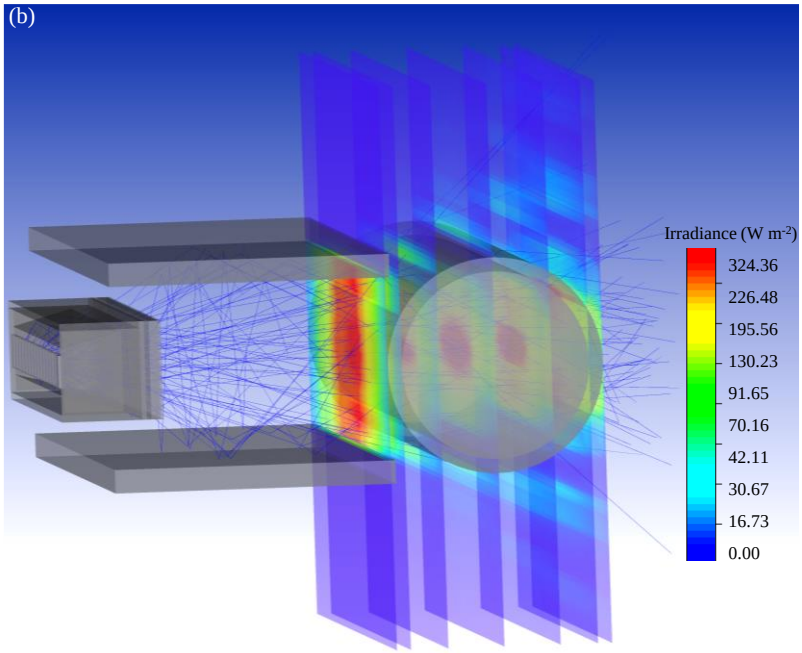

Figure 4.10: (a) Plot of intensity with wavelength between the two techniques and (b) Isometric view of changed ray tracing model.

Upon observing considerable agreement between the two techniques, the effect of water has been quantified using the same model, seen in Fig. 4.10 (b). Simulations have been conducted at multiple working distances within the fixture in air and water mediums. Table 4.7 summarizes the comparison between air medium and water medium for the 265 nm source. It can be seen that there is an increase in irradiation at all working distances when light passes through a water medium. It is known that very little light in the ultraviolet range is absorbed by water, and hence the increase is predominantly due to multiple optical phenomena occurring, within the medium, as the light propagates [228]. As the light passes through the water medium, it undergoes refraction and reflection, meaning multiple rays can be interacting at a given point within the simulation and system. Also, due to the design and material of the fixture, very little light is lost, and there is a high probability that any light not entering the quartz tube directly is reflected back due to the aluminum material manufactured fixture. Within the fixture set–up, due to supporting structures, light can be seen to reflect off the surface of the fixture and measured within the simulation and in actinometry as seen in the ray traces in Fig. 4.10 (b).

Table 4.7: Comparison between measured intensity in air and water medium for 265 nm source.

Working distance (mm)	Measured peak intensity. within the set–up (mW cm^{-2}) (Ray tracing)		% Increase in irradiation
	Air–Medium	Water–medium	
14	25.28	40.22	37.15%
19	20.18	37.42	46.07%
24	16.00	33.91	52.82%
29	13.45	37.76	64.38%
34	11.33	31.32	63.83%

By creating multiple analytical detectors. along the diameter of the quartz tube, the model also enabled an understanding of how the light intensity progresses from the window until the end of the quartz tube (see Fig. 4.10 (b)). Fig. 4.11 traces the measured peak light intensities as the light passed through the system designed, at multiple working distances, as available on the fixture (Fig. 4.2 (a, b)), starting from the emitting window of the device.

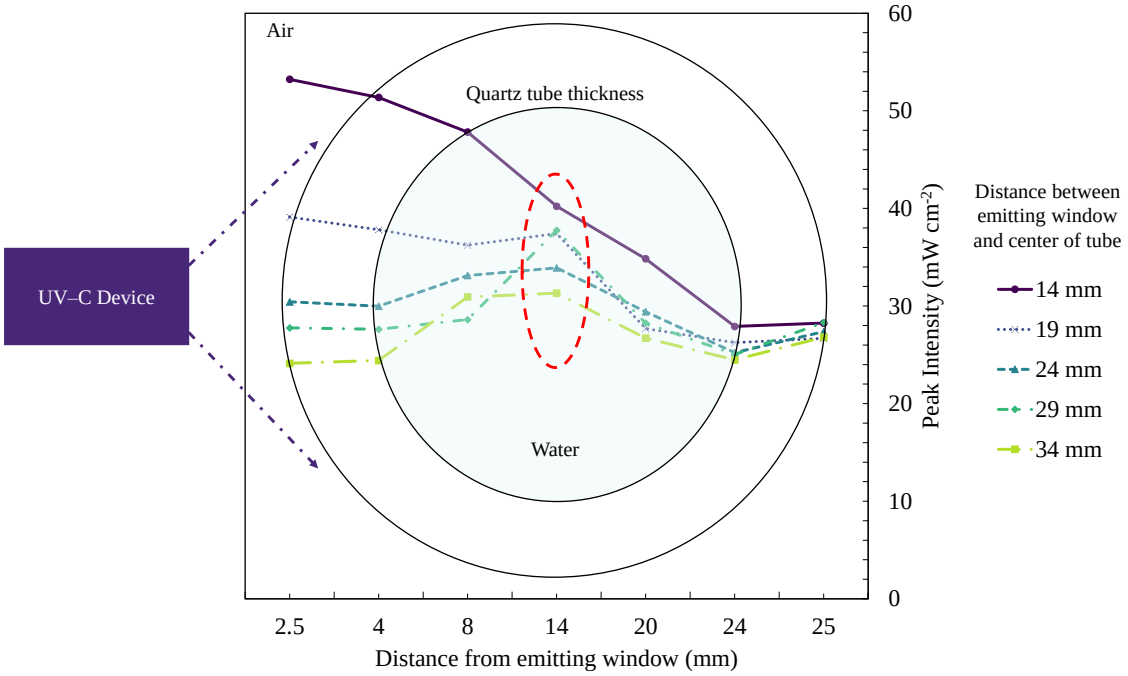

Figure 4.11: Plot of change in peak intensity as light propagates through the quartz tube within the fixture at multiple working distances for the 265 nm source.

At 14 mm, the peak intensity profile with working distance follows nearly the same trend as expected (a drop is expected in the maximum peak intensity with distance) but at other working distances, the trend observed is significantly different. It can also be seen that once the light enters the quartz tube, the highest intensity simulated is seen in the center of the quartz tube (red circle in Fig. 4.11). This is due to multiple reasons, including reflections from inside the fixture body as the distance increases between the source and tube, total internal reflections in water, light reflecting from opposite walls of the fixture, and due to multiple optical phenomena occurring as the light passes through the thickness of the quartz tube.

4.3.4. Analysis of a 4–Wavelength Germicidal System

From previous sections, it is clear that the ray tracing tool estimates intensity values within the error ranges of validated and known methods in the literature. In the case of a complex system involving more than 1–wavelength, experimental methods do not provide any information or data on the contribution of individual wavelengths to the overall intensity measured by the respective method. Ray tracing provides this data.

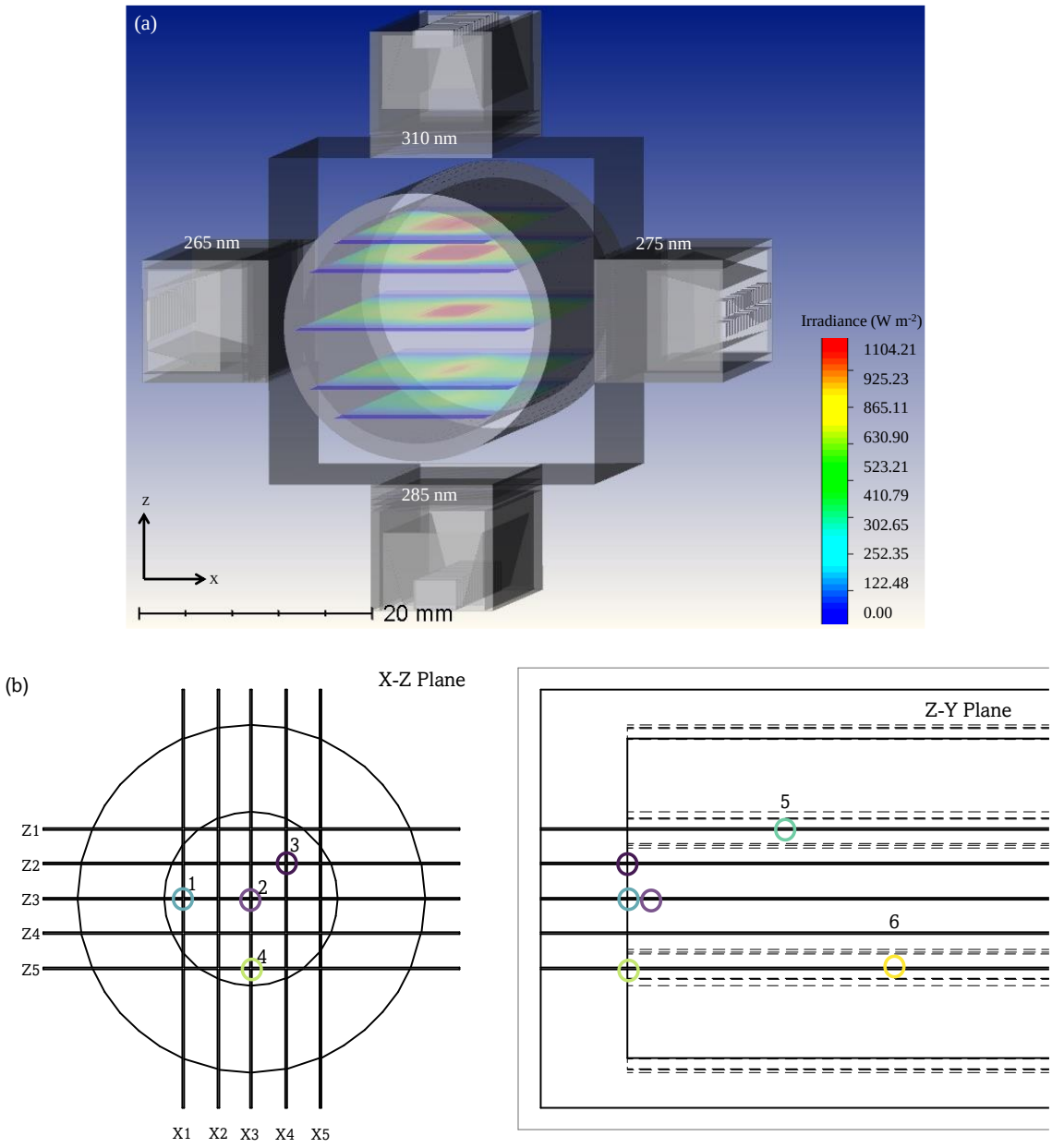

Figure 4.12: (a) Ray tracing model for a complex system involving multiple devices operating at different wavelengths (CW from the left: FX–1 emitting window of 265 nm, 310 nm, 275 nm, and 285 nm, respectively) and (b) Depiction of points of interest in a complex system.

To design a complex system involving multiple wavelengths and devices, the tool allows the use of mirror and rotation functions, to reduce modeling time in the case of this study. Water was simulated in the model using the technique discussed in Section 4.3.3. To simplify the amount of time taken for simulations and to better understand the data observed, two simulations were conducted. In the first simulation seen in Fig. 4.12 (a), the analytical

detectors are parallel to the *x–axis* to obtain data from the 310 nm and 285 nm devices. For the second simulation, the analytical detectors were moved parallel to *z–axis* to obtain data from 265 nm and 275 nm devices. The data from the two simulations were combined to provide information on light propagation within the tube, considering, for example, points 1–6 in Fig. 4.12 (b). Table 4.8 summarizes the data observed in these simulations. The simulation time for such a complex model was about 3–4 h, but this simulation provided valuable insights on the amount of light and wavelength reaching points of interest within the tube.

Table 4.8: Simulated intensity in water at different points within the tube.

Point number (Fig. 3.12 (b))	Total intensity (mW cm^{-2})	Spectral intensity in mW cm^{-2} (%)			
		FX–1 265	FX–1 310	FX–1 275	FX–1 285
1	135.38	50.63 (37%)	20.62 (15%)	13.78 (10%)	50.35 (37%)
2	199.60	40.45 (20%)	54.66 (27%)	50.22 (25%)	54.27 (27%)
3	147.64	37.25 (25%)	35.22 (24%)	29.80 (20%)	45.36 (31%)
4	160.03	46.55 (29%)	17.43 (11%)	34.65 (22%)	61.40 (38%)
5	131.11	16.35 (12%)	44.26 (34%)	27.55 (21%)	42.95 (33%)
6	111.92	22.68 (20%)	10.45 (9%)	27.37 (24%)	51.41 (46%)

Ray tracing has been seen to be effective and efficient in understanding the path of light as it travels through the system. Optimizing a system needs to be dealt with on a case–by–case basis and specific to the design of the system. For example, in the case of this study, using data from primary models in air and water, simulated data provided inputs on the behavior of each wavelength within the designed system. When irradiated at the same time, each wavelength contributed a certain percentage irradiation to the overall intensity. In Table 4.8, it can be seen that at point 2 (center of the quartz tube), 285 nm device irradiates the majority of the total irradiance reaching the point followed by the 310 nm device. To optimize the system, to achieve effective and efficient disinfection of water, the 285 nm and 310 nm devices can be moved within the fixture to 24 mm away from the center of the quartz tube, enabling a reduced contribution of the respective wavelengths to the total irradiation (24.82% and 20.06% respectively). Depending on the type of microorganism being evaluated and disinfected, the germicidal systems' effectiveness can be enhanced.

4.4. Conclusions

In summary, the present chapter reports on the application of an optical ray tracing method for prediction of irradiation reaching the point of interest as the light propagates through water in a germicidal system. The optical ray tracing modeling method was compared with radiometry, DOM and ferrioxalate actinometry. The results in comparison to these techniques have been seen to be in close agreement (±6%). This proved that the proposed method can be used to overcome major challenges faced during the measurement and simulation of irradiation in water. The study also quantified the effect of quartz material on irradiations in the UV–C range of light spectrum and observed a decrease of light intensity by 10.0 ± 0.5% for the 265 nm source. The comparison between the light transmission curve for fused quartz material used in this study provided an understanding of light behavior at multiple working distances as it passes through the thickness of the tube. A constant light loss was observed in simulations, whereas a variable light loss was seen in radiometric measurements. The study also validated measurements in water using ferrioxalate actinometry and provided an understanding of the increase in light intensity in water medium due to total internal reflections and scattering of light in water. The study found an average 52% increase in light intensity across multiple working distances in water for the 265 nm source with respect to air medium in the presence of a quartz tube. The method was further used in a 4–wavelength complex system and enabled a better understanding of the system design. The data obtained showed individual wavelength contributions at multiple points of interest within a complex system. Although the predictions of radiant intensities by optical ray tracing simulations are higher than experimental and other simulation methods, differences are within the error range. Each application needs to be worked on a case–by–case basis. In conclusion, the method provides a valuable understanding of how the light source propagates through the system, how to optimize the light irradiation within the system designed and the difference between air and water–based systems.

The simulation of light behavior in air and water provided a comprehensive understanding of the sources and devices selected for this thesis. The following chapters attempt to apply the selected sources to evaluate their disinfection potential and investigate the potential synergistic effect of multiple wavelengths.

Appendix Chapter 4

4.A. UV Fixture Design

The UV fixture was designed for manufacturability (limit cost), flexibility (allow LED lamp to be positioned at different working distances), simple usability for the operator, safety (no light leakage), and optical efficiency (to maximize disinfection). The UV fixture (Fig. 4.A.1) has been designed for the following objectives:

1. Provide effective disinfection of water.
2. Provide flexible working distances for the light source to move from 0–10 mm away from the quartz tubes' outer diameter.
3. Enable variable control of UV–C light intensity and allow continuous or pulsed irradiation.
4. Ensure safety is maintained by designing a fixture so that the UV–C light is not exposed to the external environment.
5. Enable easy removal of the quartz tube and LED lamps for cleaning and replacement, respectively.

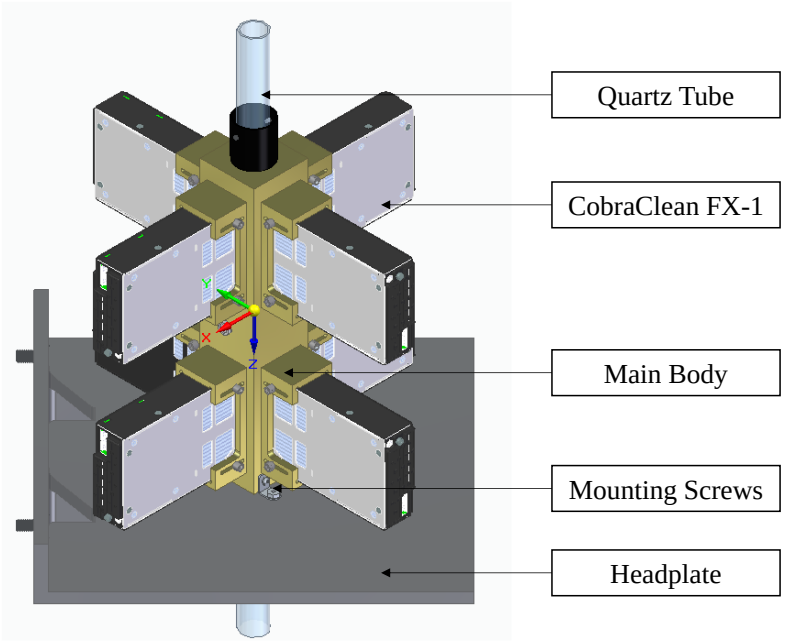

Figure 4.A.1: Constituents of UV Fixture.

The fixture set–up consists of a headplate, main body, quartz tube, and mounting screws. The main body is made of aluminum material to facilitate easy manufacturing and avoid possible breakdown due to UV light exposure. In order to ensure that the holder can

withstand the weight and pressure exerted on it, a basic finite element analysis of the design has been conducted as seen in Fig. 4.A.2.

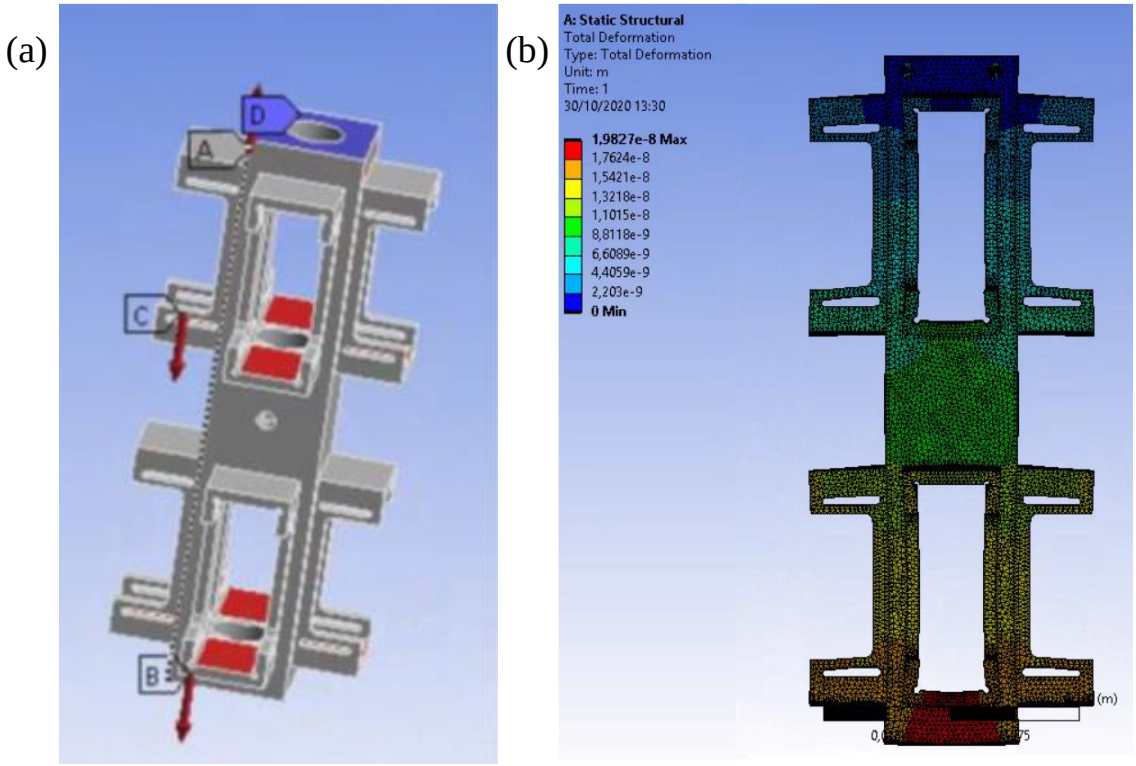

Figure 4.A.2: FEA Analysis conducted on UV Fixture – (a) Forces applied – where A is the upward force exerted by the headplate, B is the downward gravitational force, C is the force applied by the device and D is the contact force between main body and headplate, and (b) Static structural analysis indicating low fracture possibility.

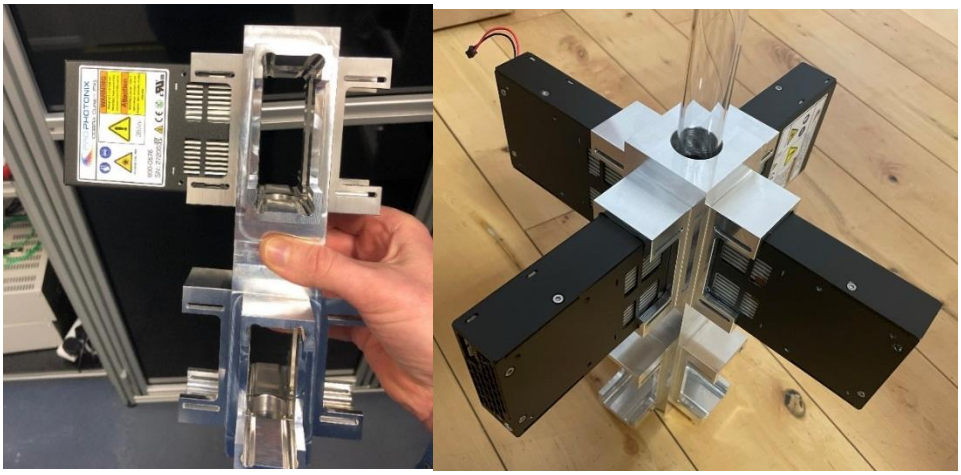

Figure 4.A.3: Manufactured Fixture.

Fig. 4.A.3 shows the manufactured main body with COBRA Clean FX–1's mounted on it. The fixture was manufactured by MAAS, Ireland.

4.B. ZeMax Optic Studio Design Layout

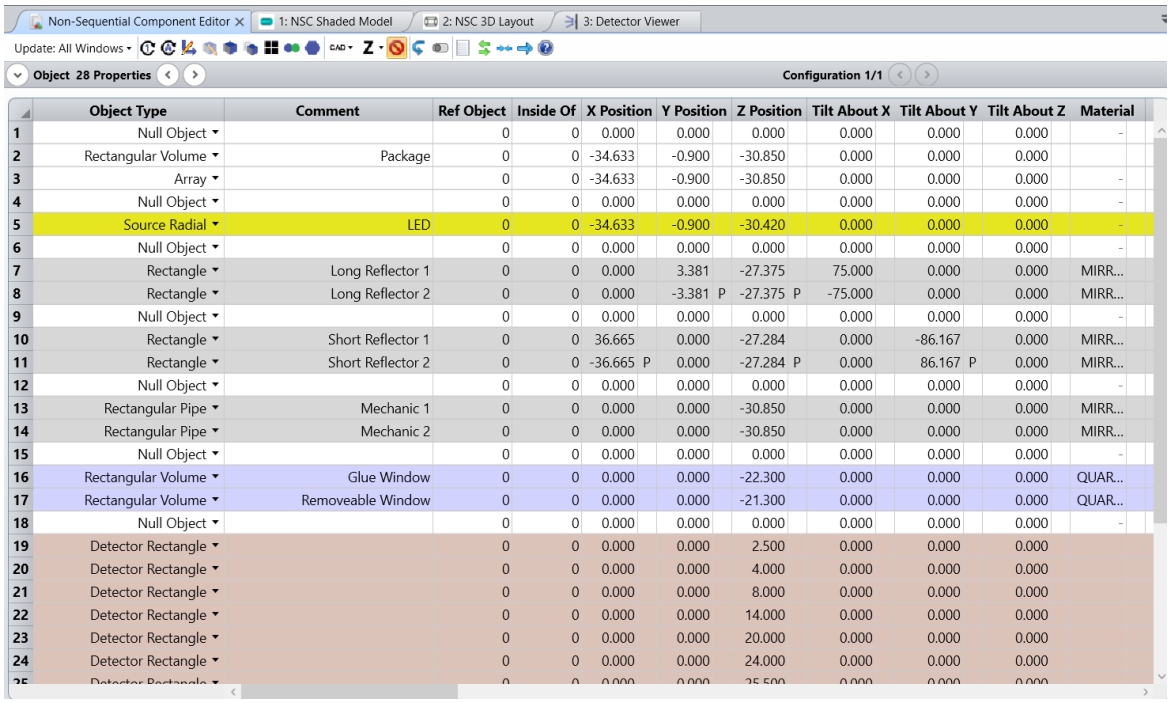

	Object Type	Comment	Ref Object	Inside Of	X Position	Y Position	Z Position	Tilt About X	Tilt About Y	Tilt About Z	Material
1	Null Object		0	0	0.000	0.000	0.000	0.000	0.000	0.000	-
2	Rectangular Volume	Package	0	0	-34.633	-0.900	-30.850	0.000	0.000	0.000	
3	Array		0	0	-34.633	-0.900	-30.850	0.000	0.000	0.000	-
4	Null Object		0	0	0.000	0.000	0.000	0.000	0.000	0.000	-
5	Source Radial	LED	0	0	-34.633	-0.900	-30.420	0.000	0.000	0.000	-
6	Null Object		0	0	0.000	0.000	0.000	0.000	0.000	0.000	-
7	Rectangle	Long Reflector 1	0	0	0.000	3.381	-27.375	75.000	0.000	0.000	MIRR...
8	Rectangle	Long Reflector 2	0	0	0.000	-3.381 P	-27.375 P	-75.000	0.000	0.000	MIRR...
9	Null Object		0	0	0.000	0.000	0.000	0.000	0.000	0.000	-
10	Rectangle	Short Reflector 1	0	0	36.665	0.000	-27.284	0.000	-86.167	0.000	MIRR...
11	Rectangle	Short Reflector 2	0	0	-36.665 P	0.000	-27.284 P	0.000	86.167 P	0.000	MIRR...
12	Null Object		0	0	0.000	0.000	0.000	0.000	0.000	0.000	-
13	Rectangular Pipe	Mechanic 1	0	0	0.000	0.000	-30.850	0.000	0.000	0.000	MIRR...
14	Rectangular Pipe	Mechanic 2	0	0	0.000	0.000	-30.850	0.000	0.000	0.000	MIRR...
15	Null Object		0	0	0.000	0.000	0.000	0.000	0.000	0.000	-
16	Rectangular Volume	Glue Window	0	0	0.000	0.000	-22.300	0.000	0.000	0.000	QUAR...
17	Rectangular Volume	Removeable Window	0	0	0.000	0.000	-21.300	0.000	0.000	0.000	QUAR...
18	Null Object		0	0	0.000	0.000	0.000	0.000	0.000	0.000	-
19	Detector Rectangle		0	0	0.000	0.000	2.500	0.000	0.000	0.000	
20	Detector Rectangle		0	0	0.000	0.000	4.000	0.000	0.000	0.000	
21	Detector Rectangle		0	0	0.000	0.000	8.000	0.000	0.000	0.000	
22	Detector Rectangle		0	0	0.000	0.000	14.000	0.000	0.000	0.000	
23	Detector Rectangle		0	0	0.000	0.000	20.000	0.000	0.000	0.000	
24	Detector Rectangle		0	0	0.000	0.000	24.000	0.000	0.000	0.000	

Figure 4.B.1: Screen grab of ZeMax optic studio.

4.C. Mesh Sensitivity Analysis on DOM

Mesh sensitivity analysis was conducted for each of the wavelengths. Fig. 4.C.1 – 4.C.3 show a plot of simulated peak intensity values *vs* number of cells in mesh. The optimum mesh used for simulations are shown in Table 4.C.1.

Table 4.C.1. Optimum mesh data.

Wavelength	Optimum Element Size (m)	Number of cells	Number of nodes
265 nm	0.0007	416887	80103
275 nm	0.0007	419567	80611
310 nm	0.0007	417174	80135

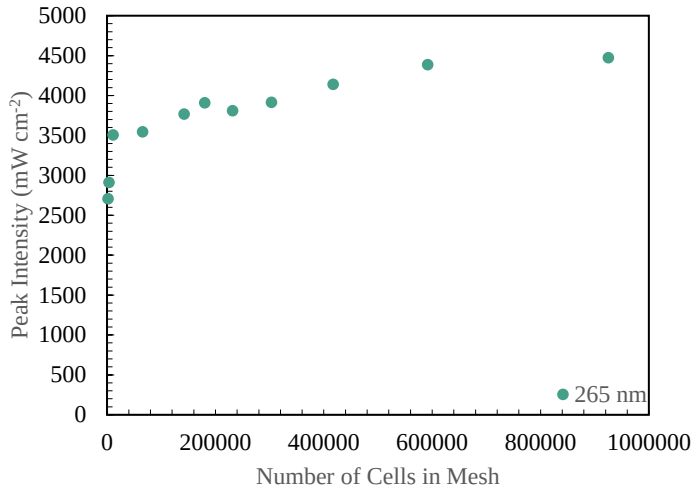

Figure 4.C.1: Mesh sensitivity analysis for 265 nm source.

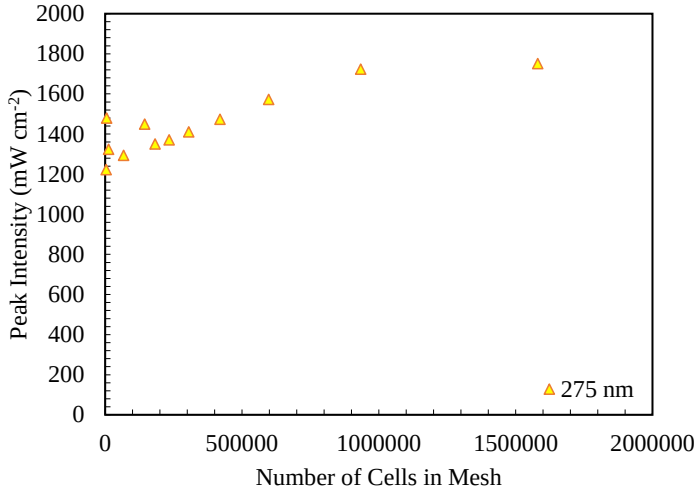

Figure 4.C.2: Mesh sensitivity analysis for 275 nm source.

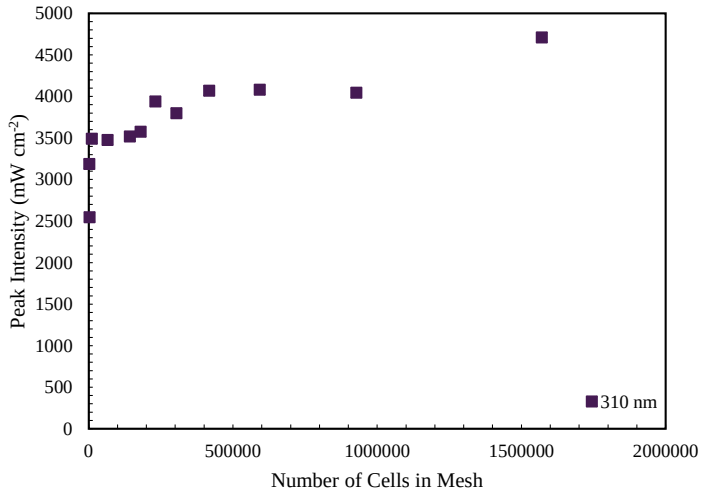

Figure 4.C.3: Mesh sensitivity analysis for 310 nm source.

4.D. Other Wavelengths

4.D.1. Optical Model *vs* Experimental Data

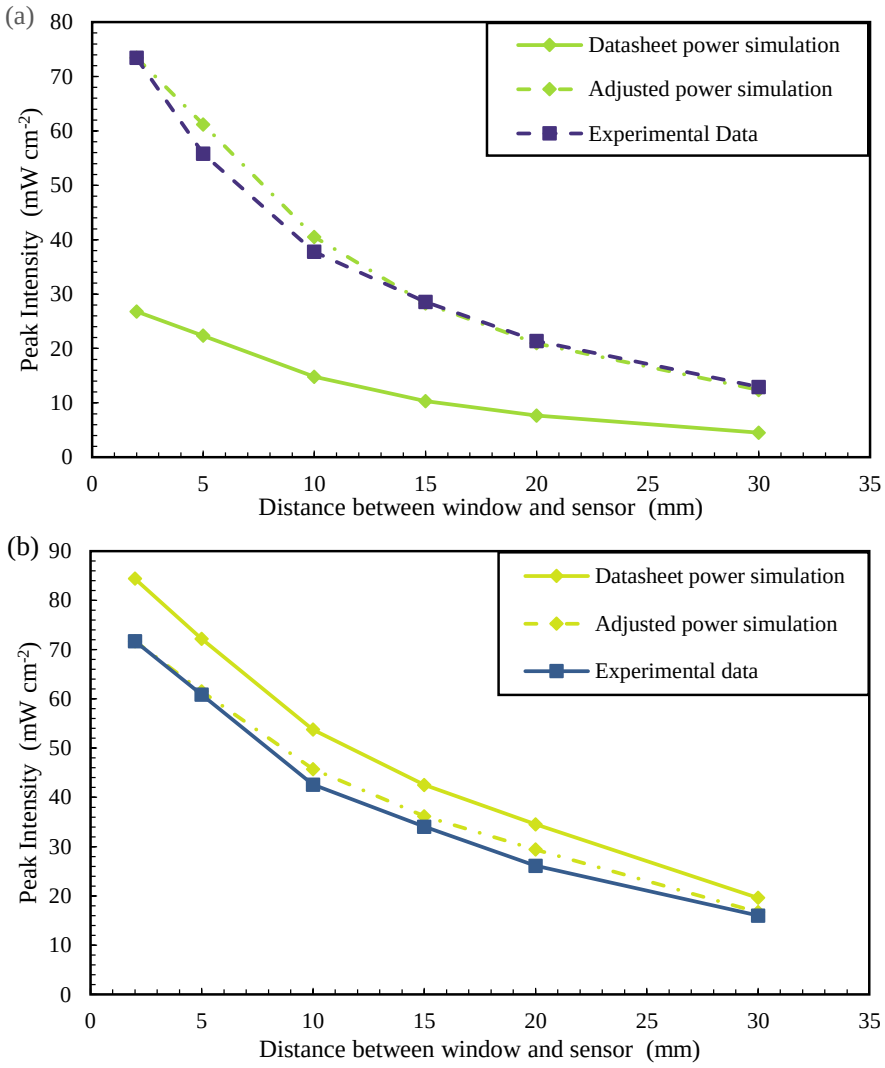

Figure 4.D.1: Optical model comparison between datasheet and actual power simulations (a) 275 nm and (b) 310 nm.

4.D.2. ZeMax and Radiometry

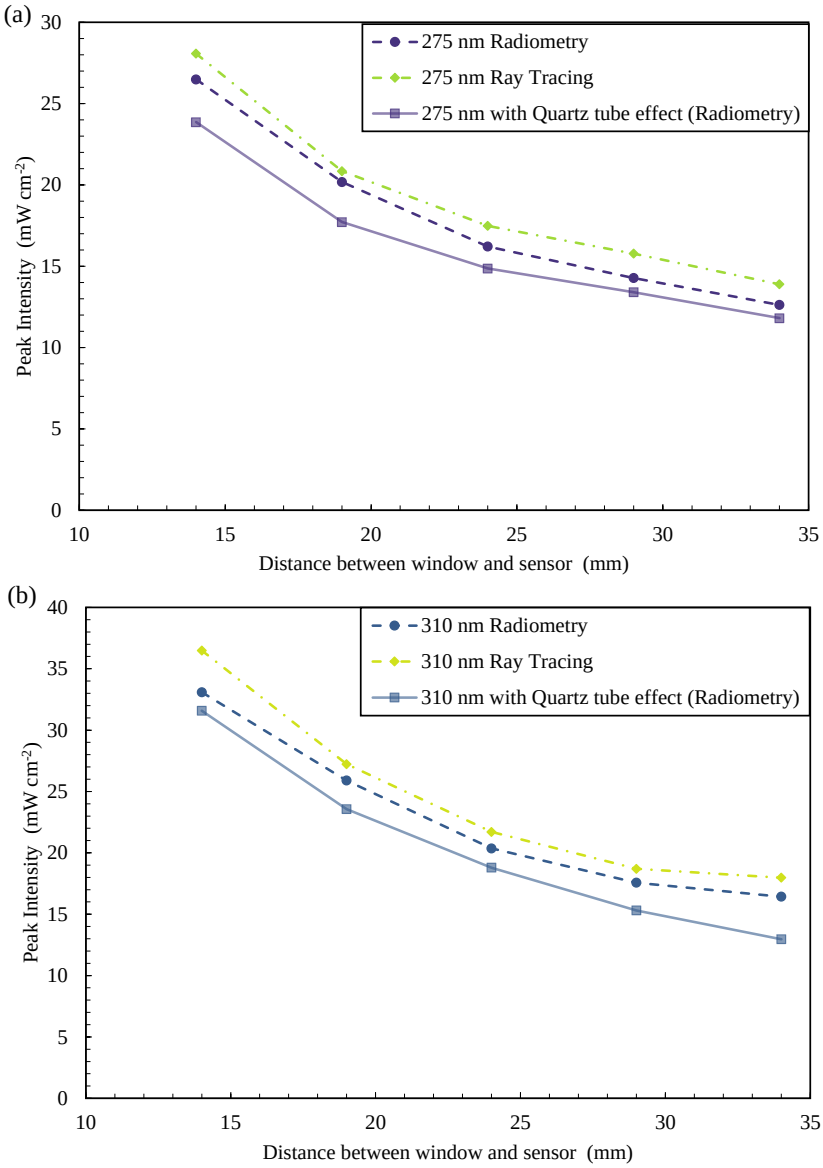

Figure 4.D.2: Plot of peak intensity *vs* working distance (a) 275 nm and (b) 310 nm.

Table 4.D.1: Recorded peak intensity at multiple working distances using radiometry and ZeMax (without the effect of quartz tube).

Working Distance (mm)	Measured Peak Intensity (275 nm) (mW cm^{-2})		Measured Peak Intensity (310 nm) (mW cm^{-2})	
	Radiometry	ZeMax	Radiometry	ZeMax
14	26.5 ± 0.2	28.0	33.1 ± 1.2	36.5
19	20.2 ± 0.6	20.8	25.9 ± 0.2	27.2
24	16.2 ± 0.4	17.5	20.4 ± 0.3	21.7
29	14.3 ± 0.2	15.8	17.6 ± 0.2	17.7
34	12.6 ± 0.1	13.8	16.4 ± 0.1	14.9

4.D.3. Effect of Quartz Tube

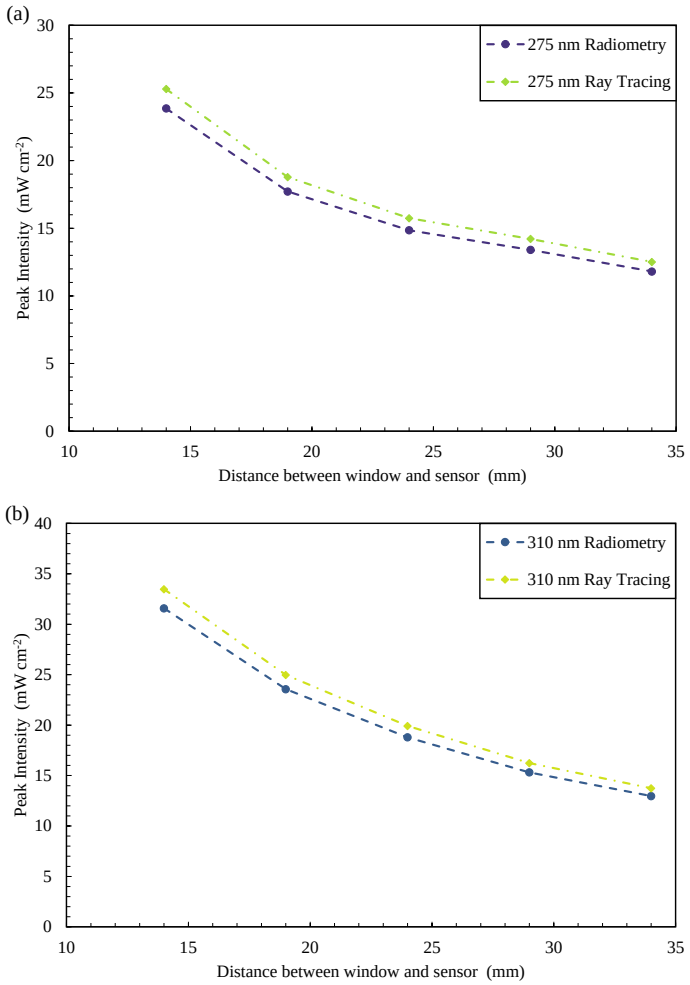

Figure 4.D.3: Plot of peak intensity *vs* working distance in the presence of quartz tube (a) 275 nm and (b) 310 nm.

Table 4.D.2: Recorded peak intensity at multiple working distances using radiometry and ZeMax for effect of quartz.

Working Distance (mm)	Measured Peak Intensity (275 nm) (mW cm^{-2})		Measured Peak Intensity (310 nm) (mW cm^{-2})	
	Radiometry	ZeMax	Radiometry	ZeMax
14	23.8 ± 0.8	25.3	31.6 ± 0.3	33.5
19	17.7 ± 0.6	18.8	23.6 ± 0.3	25.0
24	14.9 ± 0.1	15.7	18.8 ± 0.1	19.9
29	13.4 ± 0.2	14.2	15.3 ± 0.4	16.2
34	11.8 ± 0.2	12.5	13.0 ± 0.1	13.7

4.E. Quartz Tube Transmission Curve (FAB027469, GE214)

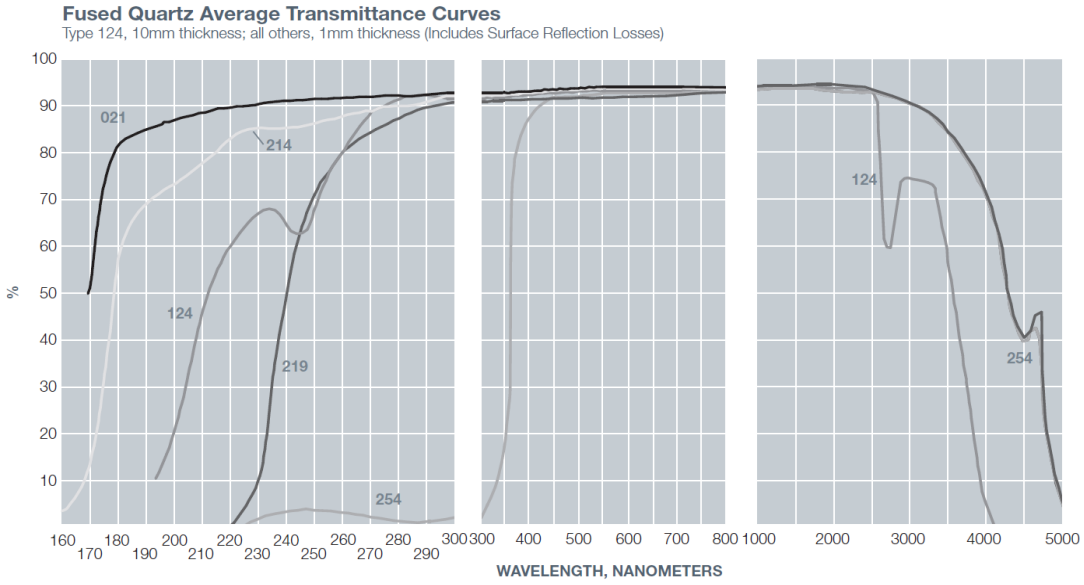

Figure 4.E.1: Fused quartz transmittance curve as obtained from the manufacturer (see white line for GE214 material type).

4.F. ZeMax *vs* DOM (other wavelengths)

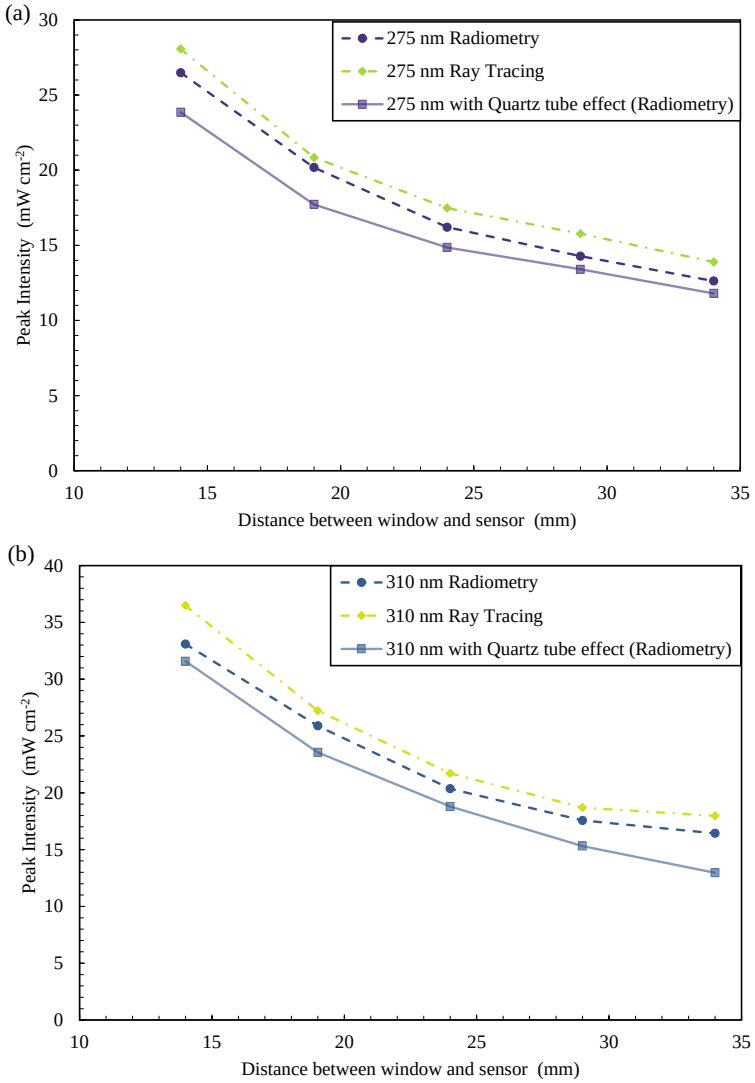

Figure 4.F.1: Comparison between ZeMax, DOM, and radiometry (a) 275 nm and (b) 310 nm.

Table 4.F.1: Recorded peak intensity at multiple working distances using DOM and ZeMax (in air).

Working Distance (mm)	Measured Peak Intensity (275 nm) (mW cm^{-2})		Measured Peak Intensity (310 nm) (mW cm^{-2})	
	ZeMax	DOM	ZeMax	DOM
14	28.06	27.22	36.48	34.29
19	20.84	19.80	27.22	25.86
24	17.47	15.90	21.70	20.62
29	15.77	14.35	18.69	17.57
34	13.88	12.63	17.97	17.43

4.G. Data on ferrioxalate actinometry

- Incident Area – 0.004712389 cm^2

Table 4.G.1: Actinometry data on incident irradiation.

Wavelength (nm)	Incident Irradiation in E s^{-1}			Average Incidence Irradiation in E s^{-1}	Error
	1	2	3		
265	3.66×10^{-6}	3.61×10^{-6}	3.79×10^{-6}	3.69×10^{-6}	0.000005%
275	5.56×10^{-6}	5.55×10^{-6}	5.70×10^{-6}	5.60×10^{-6}	0.000005%
310	6.28×10^{-6}	6.68×10^{-6}	6.37×10^{-6}	6.44×10^{-6}	0.000012%
Wavelength (nm)	Incident Irradiation in W m^{-2}			Average Incidence Irradiation in W m^{-2}	Error
	1	2	3		
265	351.32	346.21	363.93	353.82	5.26
275	513.89	512.73	526.40	517.67	4.37
310	514.25	546.98	521.94	527.72	9.88

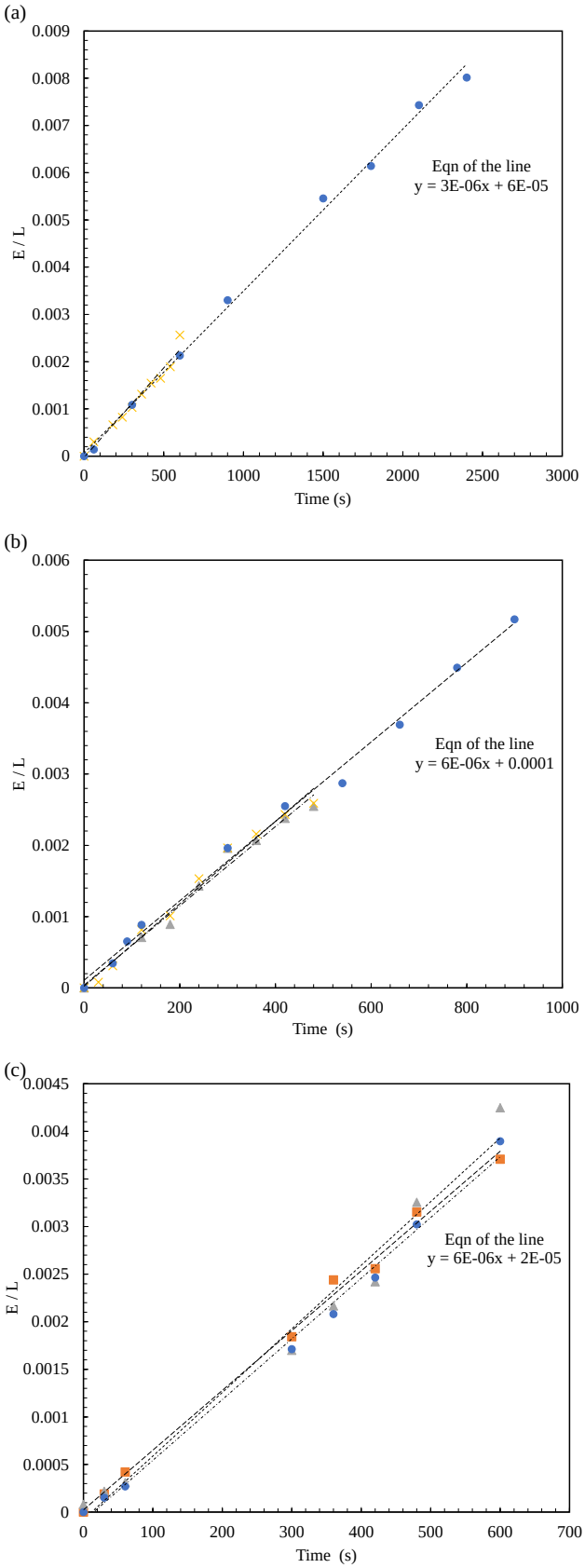

Figure 4.G.1: Plots of E/L *vs* time for ferrioxalate actinometry – (a) 265 nm, (b) 275 nm, and (c) 310 nm.

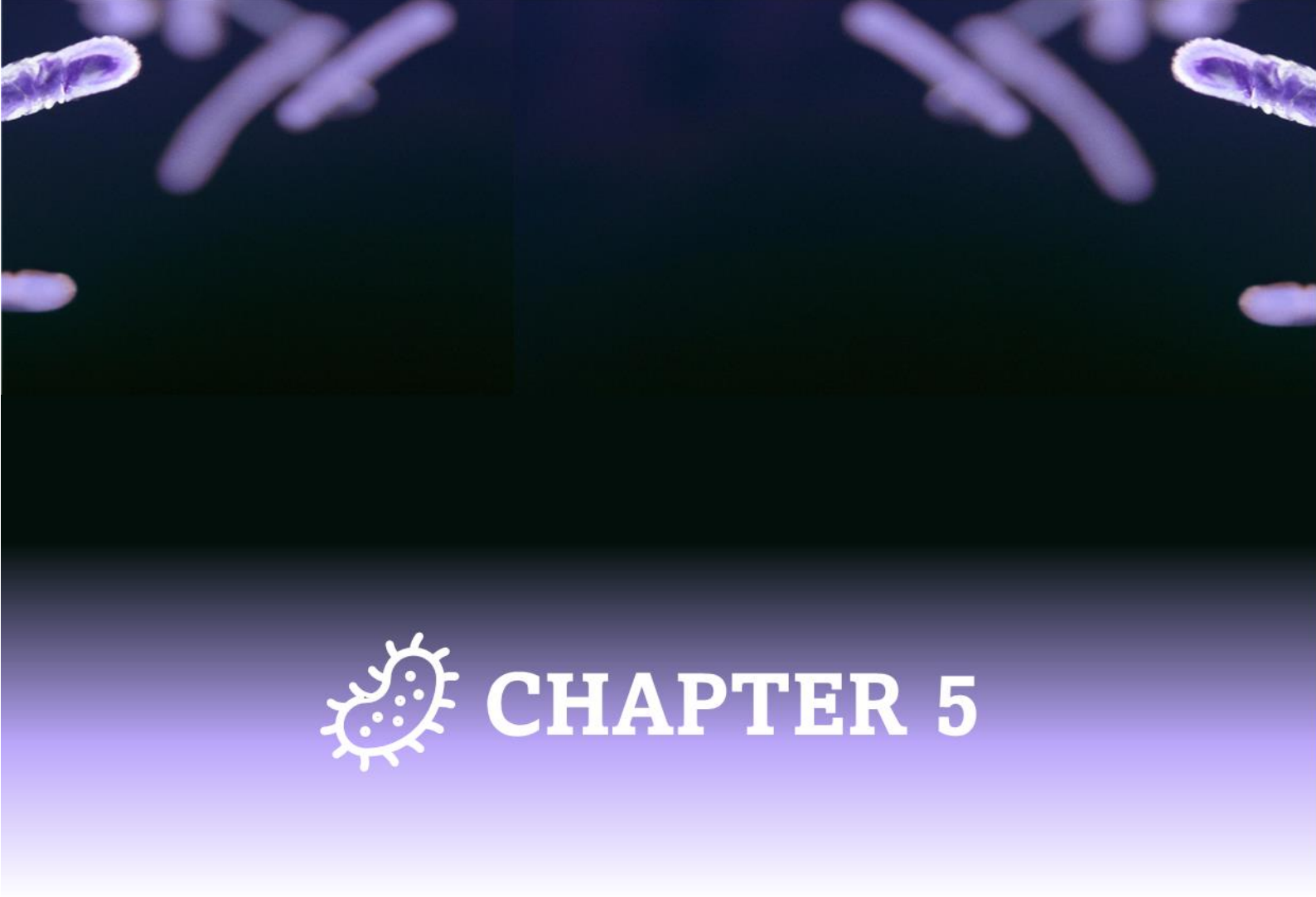

CHAPTER 5

UV DISINFECTION

5.1. Introduction

Water has been widely used across the world for various applications. Water is used for agricultural production, industrial processes, and drinking and cleaning at the household level [33]. While water has been a source of great help to human life, it has also been known as a transmission medium for bacteria and other microorganisms [29]. Governments across the world have put in great efforts to ensure clear and safe water is available to the common man [95-97]. The market for clean water has been developing since the early 1900s, with many researchers and scientists working on finding technologies to clean water at different levels of water supply and distribution [33]. As mentioned in Chapter 1, in the early days, industry utilized mercury lamps for drinking water and wastewater treatment. Mercury lamps with emission centered at 253.7 nm were found to disinfect water and surfaces effectively [48]. Since the early 2000s, LEDs hold promise to replace UV mercury lamps in water treatment. The evolution of the use of UV LEDs for disinfection in the past decade has led to a lot of research. There have been studies on different materials to harness lower wavelengths of light, tests to combine other process variables, and attempts to combine multiple wavelengths for a synergistic effect, are among the many areas explored [254-257].

Synergy of multiple wavelengths in disinfection has been widely debated across the literature. Synergistic effect between multiple wavelengths occurs when the combination produces an effect greater than the sum of their separate effects [255]. Some researchers have found no synergistic effect [255-258], while others have reported a significant synergistic effect [259-261]. This has led to questions being raised on other possible parameters that could be influencing the results obtained like inactivation mechanisms, light control etc., [107, 108, 262].

For instance, Beck et al. (2017) conducted experiments to study potential synergy between 260 nm and 280 nm UV–C LEDs and concluded that synergy was not possible due to the 2nd Law of photochemistry [255]. The law, also called the Stark–Einstein Law, states that for each photon of light absorbed by a chemical system, only one molecule is activated for subsequent reaction. This “photo equivalence law” was derived by Albert Einstein during his development of the quantum (photon) theory of light. On the same lines, the first law of photochemistry, the Grotthuss–Draper Law, states that light must be absorbed by a compound in order for a photochemical reaction to take place [14]. While the argument stated by Beck et al. (2017) is true, it is important to note that the inactivation mechanisms

of the two wavelengths used on the microorganisms, are similar, hence any combined effect would merely be the result of the sum of individual wavelength effects [255]. Another research, akin to this, was conducted by Woo et al. (2019) using the same wavelengths on the inactivation of human enteroviruses. The authors mention that the wavelength contribution to the total emission was 0.38 – 0.62 for 260 nm and 280 nm, respectively, but do not have any control on varying this ratio [258]. A slight synergistic effect was observed in the study by Hull et al. (2018), who conducted experiments using KrCl excimer lamps in sequential exposure with low–pressure mercury lamps and UV–C LEDs and concluded that there can be a use of excimer lamps in disinfection products but did not comment on synergistic damage mechanism of LEDs with excimer lamps [256].

Contrary to the above–mentioned researches, Nakahashi et al. (2014) found synergistic effect while testing the combination of 254 nm and 365 nm UV lights, due to the attenuation of a DNA repair pathway [261]. Also, Green et al. (2018) concluded that there was synergistic inactivation of three common foodborne pathogens when illuminating the water surface with a combination of 259 nm and 289 nm UV light, due to possible alternative inactivation mechanism at 289 nm leading to enhanced disinfection [259]. Other researchers have concluded synergy in their experiments as well using different experimental procedures and LED systems [259-261].

Comparing all the above–mentioned studies, the type of light source, corresponding UV dose received, and experimental set–up are some of the major differences. In the case of Beck et al. (2017), the light was irradiated with a prototype UVinaire® dual wavelength UV–C LED unit from Aquisense [255], whereas Green et al. (2018) used a Pearl Beam™ collimated beam unit by Aquisense [259]. One set of researchers used a flow–through type reactor set–up, whereas a few others used a batch reactor system. Also, in some cases, the type of statistical analysis tool used to conclude synergistic effect or vice versa is unclear. The need to bridge the gap between synergy and disinfection is of much importance as the potential synergistic effect could have a significant positive impact on the process. In all the studies on synergy, so far, authors have had little to no control over the light sources used [255-261, 263-271]. However, factors like emission spectrum, type of device, and contribution of each wavelength, when in combination, play a key role in comprehensively understanding possible synergistic effect between multiple wavelengths for inactivation of microorganisms, as highlighted by Green et al. (2018) [259].

The need for faster and more effective disinfection processes is of growing need, given the extremities of water safety being discussed worldwide. Synergy of multiple wavelengths could provide a solution to this growing demand and also possibly result in lower energy consumption for higher disinfection rates. The present chapter attempts to fill these knowledge gaps and take advantage of the previously established understanding and control of the light source to study its resulting effect on the inactivation of *E. coli* K12 in a buffered water matrix. The study verifies any possible synergistic effect by the use of robust statistical analysis tools and attempts to correlate the observed effect with inactivation mechanisms of the employed wavelength ranges. This is the first time that synergy between multiple wavelengths is evaluated by approaching it from the light perspective of establishing a complete understanding of the light source, device, and emission characteristics. The experimental set–up allows exposure of multiple wavelengths to a single pass flow reaction. It further evaluates the inactivation effect of each combination and conducts an extensive spectral analysis of the sources. The inactivation mechanisms of each wavelength range have also been analyzed to provide insight into the mechanisms of possible synergy. Finally, the study conducts an investigation of electrical energy per unit order of inactivation to conclude if the combination of wavelengths increased or decreased the energy efficiency of the overall process.

5.2. Methodology

5.2.1. Test Water

The test water, used in all the experiments of this chapter, consisted of 0.9% sodium chloride (NaCl) in ultrapure water (MilliQ 7003, 18.2 MΩ cm [272]) with a starting *E. coli* concentration of 10^6 colony forming units per mL (CFU/mL). The solution was prepared by adding 9 g of NaCl (Scharlab, SO0227 [273]) per liter of ultrapure water. 2 L have been used for each disinfection experiment in this study.

5.2.2. Microorganism Propagation and Enumeration

A frozen culture of *E. coli* K12 (Colección Española de Cultivos Tipo, CECT 4624) was added into 20 mL of sterile Luria–Bertan (LB) broth (Scharlab, 02-384 [274]) and incubated in an Orbital Shaker–Incubator (Biosan, ES-20 [275]) at 37°C for 18 h – 24 h, under stirring at 100 rpm, until a concentration of 10^9 CFU/mL was obtained. 5 mL of the broth solution was then centrifuged (Orto Alresa, Minicen [276]) at 3500 rpm for 25 min.

The cells were washed off the LB broth and resuspended in 5 mL of 0.9% NaCl solution, then, 2 mL was diluted in 2 L of test water to obtain an initial concentration of 10^6 CFU/mL. For enumeration, extracted samples were serially diluted in 0.9% NaCl solution before plating in prepared Miller's LB agar plates (Scharlab, 01-385-500 [277]), as demonstrated in Fig. 5.1. A minimum of 3 drops of 10 µL were spread on LB agar and incubated inverted at 37°C for 18 – 24 h. Samples were plated in triplicates. Plates yielding 10 to 100 colonies were included in the analysis and counted using a colony counter (JP Selecta, 4905002 [278]), that records colonies on the plate using pressure applied by the operator on each colony observed; see Fig. 5.1.

The plating procedure was dependent on initial observed results, for instance in case of t = 0 samples, the plating was done in terms of D0 – D3 and a separate plate for D-1 (100 µL drops). In contrast, irradiated samples were plated at D-2, i.e., 1 mL sample, to ensure the number of colonies was statistically significant (> 10 CFU/mL). For all the experiments, the bacterial inactivation, expressed as logarithmic reduction value (LRV), has been evaluated with respect to the initial concentration.

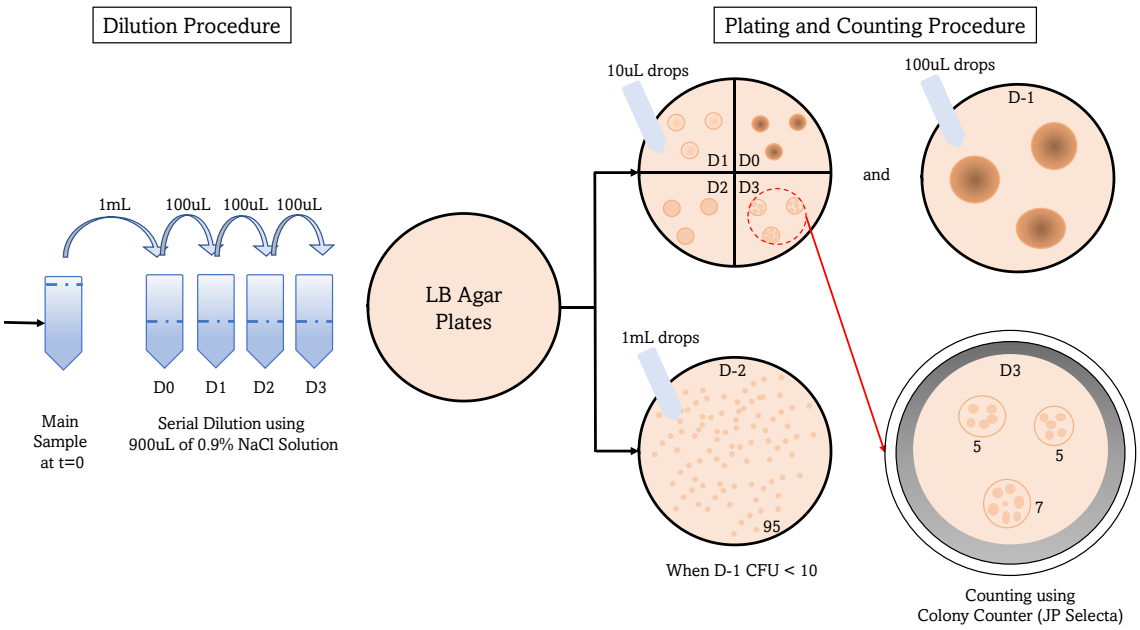

Figure 5.1: Representation of dilution, plating, and counting procedure.

5.2.3. UV Irradiation

The sources analyzed in Chapter 2 have been used as UV irradiation sources in this chapter. FX–1 265, FX–1 275, and FX–1 310 have been employed for disinfection experiments. The relative spectral output of the devices can be found in Fig. 2.14 (Chapter 2) of this thesis.

5.2.4. Experimental Set–up

To conduct disinfection experiments using multiple combinations, the UV fixture (Section 4.2.1, Chapter 4) has been used. The fixture can be found in Fig. 4.1 (a, b). The designed fixture can accommodate up to 8 COBRA Clean FX–1's and a quartz tube. The quartz tube has been connected to the sampling tank and outlet to enable two types of set–ups; see Fig. 5.2 (a, b). The first set–up (Fig. 5.2 (a)) studied is a recirculating batch–type reactor, where the water is recirculated for a certain period of time as per the wavelength studied and enables an understanding of disinfection rate with time and UV dose. One sample was collected at each time and plated in triplicate. The second type of set–up studied was a single pass flow–through reactor, wherein the water was circulated through the reactor only once. A minimum of 4 samples have been extracted from the outlet tank for this set–up and each sample has been plated in triplicate.

The set–up was connected to a magnetically coupled pump (Flojet, RS Pro 266-597 [279]) (at flow rate of 2 L min^{-1}) and stirred using a magnetic stirrer set–up for the recirculating batch reactor (Fig. 5.2 (a)). Each combination has been tested a minimum of 4 times, on separate days, to ensure the repeatability and reproducibility of the data. For the single pass system (Fig. 5.2 (b)), two radiant intensities (50% of the maximum and maximum intensity) of the devices have been tested for each combination to evaluate the overall UV dose response. It is important to note that since 310 nm is known to require longer exposure times for significant logarithmic reduction of the model bacterium [280], the 310 nm individual wavelength irradiation experiments were conducted, in recirculation mode, until 1–log reduction was observed to estimate the equivalent logarithmic reduction per pass in the flow–through system.

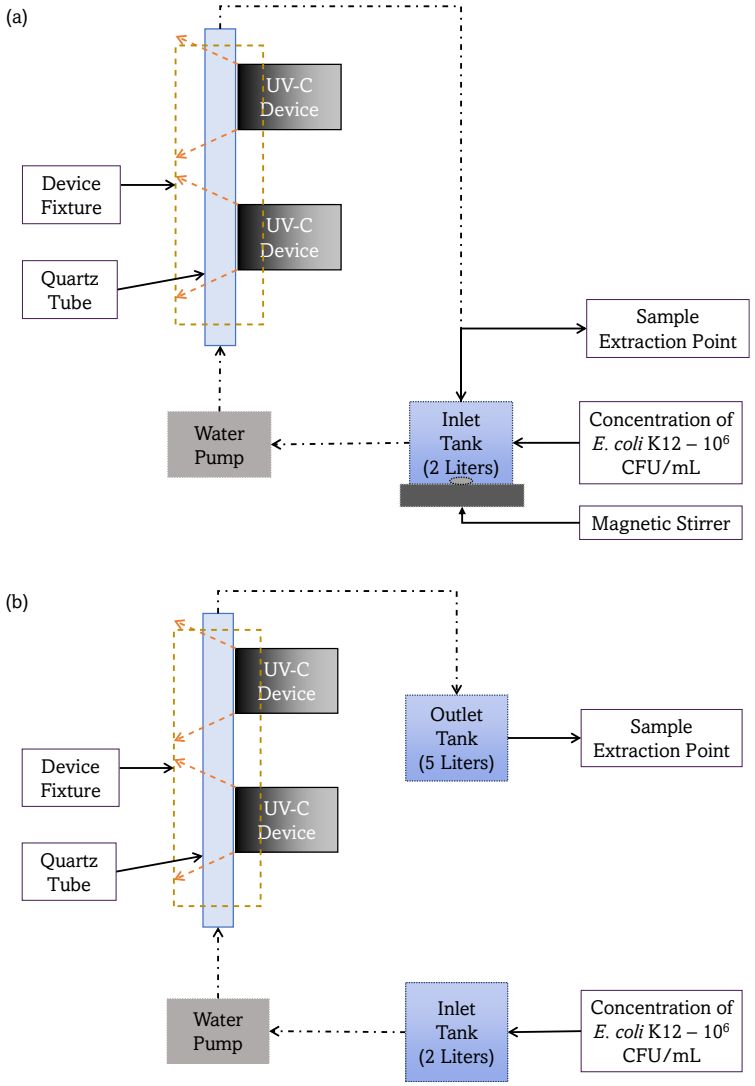

Figure 5.2: Schematic representation of – (a) recirculating batch reactor set–up and (b) single pass flow–through set–up.

5.2.4.1. Combinations of UV Sources

Multiple combinations of the chosen light sources have been tested. Fig. 5.3 represents the different combinations attempted in this study. Individual wavelength mode (IW, Fig. 5.3 (a)) involves the use of only one device on the UV fixture. Sequential mode (SE, Fig. 5.3 (b)) involves irradiation with 2 wavelengths, one after the other, on the water flowing through the system. In this SE mode of irradiation, both possible arrangements of wavelengths have been attempted in each combination (e.g. 265 followed by 310 and vice versa) to evaluate if the order of irradiation impacted the obtained disinfection rates.

In simultaneous mode (SI, Fig. 5.3 (c)), both wavelengths are acting at the same point at an instant of time. Finally, in sequential + simultaneous mode of irradiation (SS, Fig. 5.3 (d)), all 3 wavelengths selected are irradiated at the same time wherein 1 wavelength acts in sequence and 2 wavelengths act at the same point as the water passes through the system.

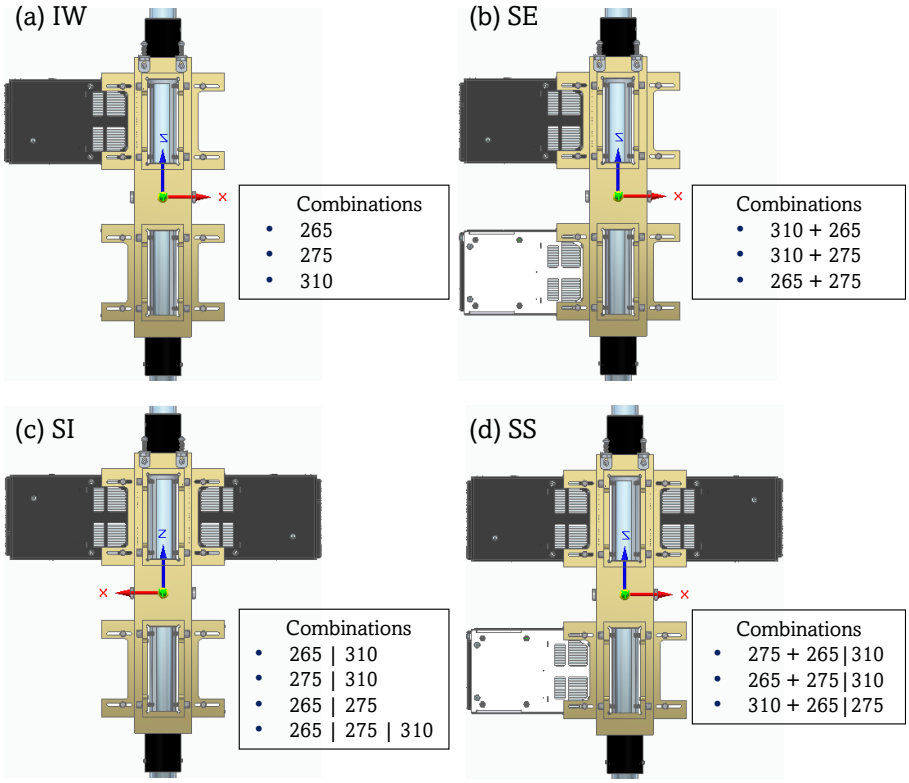

Figure 5.3: Possible combinations on UV fixture – (a) Individual wavelengths (IW), (b) Sequential Mode (SE), (c) Simultaneous Mode (SI), and (d) Sequential + Simultaneous Mode (SS).

5.2.4.2. Flow Rates

To evaluate the overall disinfection ability of the light sources selected, it was necessary to interpret the effect of flow rate on disinfection. This test has been conducted on the single pass flow–through system. To do this, the set–up in Fig. 5.2 (b) was modified to include a flow control valve after the exit of the water pump. This allowed manual control of the flow rate of water passing through the reactor. Fig. 5.4 is a schematic representation of the modified set–up showing the valve positions tested. 4 valve positions have been tested for one of the light sources in this study (FX–1 265).

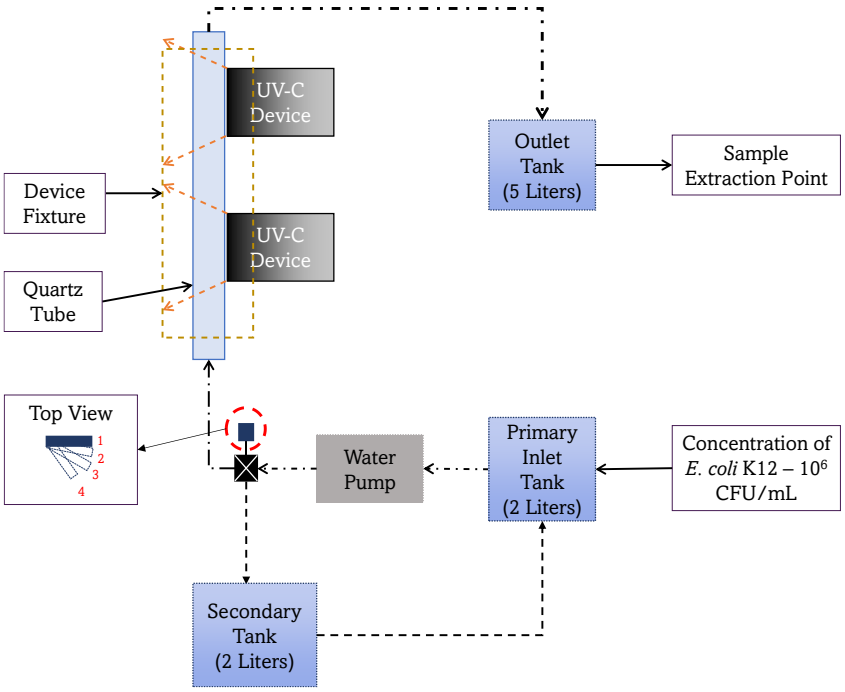

Figure 5.4: Representation of set–up change for study on the effect of flow rate.

Water exiting the water pump enters the flow control valve and depending on the position (see arrow from the red dotted circle), a fraction of the water is deviated to the secondary tank, while the rest is driven to the reactor. The water from the secondary tank is recirculated, manually, to the primary inlet tank. The 4 different valve positions have been fixed by experimental determination of the flow rates exiting the reactor (Table 5.1). The corresponding residence time, calculated according to Eq. 5.1, is also included in Table 5.1.

$$t = \frac{V}{Q} \qquad \text{Eq. 5.1}$$

where, V is the volume of the reactor in L, and Q is the flow rate of the pump in L s^{-1}. For the flow–through set–up, it can be seen that the contact times between the microorganism and light sources are short.

Table 5.1: Flow rates tested.

Valve Position	Flow Rate (L min^{-1})	Flow Rate (L s^{-1})	Residence Time (s)
1	2.00	0.033	0.743
2	1.75	0.029	0.850
3	1.50	0.025	0.990
4	0.75	0.012	1.981

5.2.5. Residence Time and Kinetic Constants

The kinetic constant (k_c in s^{-1}) for each combination was calculated using Eq. 5.2 assuming a first–order reaction according to the Chick's law [102, 103, 106, 281].

$$k_c = -\left(\frac{Log_{10}\left(\frac{Co}{C}\right)}{t}\right) \quad \text{Eq. 5.2}$$

where, C_o is the number of CFU/mL of the unirradiated sample, C is the CFU/mL for each sample and t is the residence time in seconds (s). The term $Log_{10}(C_0/C)$ is, by definition, the inactivation of bacteria expressed as LRV. It is well known that UV inactivation is fluence–based [255]. Therefore, the UV dose response data were fit linearly and the $\log_{10}$ fluence–based inactivation rate constant, k_d ($cm^2\ mJ^{-1}$) was determined as shown in Eq. 5.3.

$$k_d = -\left(\frac{Log_{10}\left(\frac{C_o}{C}\right)}{f_\lambda}\right) \quad \text{Eq. 5.3}$$

where, f_λ is the fluence at the given wavelength, λ, in mJ cm^{-2}, determined as shown in Eq. 5.4.

$$f_\lambda = I \times t \quad \text{Eq. 5.4}$$

being I the intensity delivered by the light source in mW cm^{-2}.

5.2.6. Synergy of Inactivation

The synergy of inactivation has been calculated using Eq. 5.5 [282].

$$Synergy = \frac{k_{combination}}{k_1 + k_2 + \cdots k_n} \quad \text{Eq. 5.5}$$

where, $k_{combination}$ is the LRV obtained from actual combination of wavelengths and $k_{1\ldots n}$ is the LRV obtained from individual wavelength disinfection experiments. Note that the analysis has also been conducted in terms of k_c (in s^{-1}), however all discussions have been presented in terms of LRV.

5.2.7. Statistical Analysis

5.2.7.1. Student's *t*–Distribution Analysis

To analyze the statistical significance between the sum of individual disinfection rates and the combined disinfection rates, a *t*–Student distribution analysis was conducted. A one–sided analysis with a confidence interval of 95% has been chosen for comparison, as there exists only one factor of comparison between the two datasets under study [282]. The

analysis was conducted for each UV source combination tested and compared to the theoretical sum of individual wavelength disinfections obtained. The value of "*t*" has been extracted from Student et al. (1908) [283]. Data has been collected in triplicates and presented as error bars representing the 95% confidence interval (*CI*) obtained from *t*–Student analysis. *CI* was calculated using Eq. 5.6.

$$CI\ (95\%) = \frac{t \times SD}{\sqrt{n}} \qquad \text{Eq. 5.6}$$

where, *t* is the value obtained for *v* degrees of freedom from the distribution table, *SD* is the standard deviation of all the collected samples and *n* is the number of samples in the range [283]. The interval of comparison is shown in Eq. 5.7. In its essence, the analysis was aimed to check if the theoretical addition of the individual disinfection effects is significantly lower than the actual disinfection rates obtained in the combination to conclude synergy and vice versa, if it is significantly higher, to conclude possible antagonism when wavelengths are irradiated in combination.

$$X \pm CI\ (95\%) \cong Y \pm CI\ (95\%) \qquad \text{Eq. 5.7}$$

The *t*–test determines if two populations, in this case theoretical disinfection rates and actual disinfection rates, are statistically different from each other whereas ANOVA tests can be used to test more than two levels of significance within an independent variable [284]. Hence ANOVA analysis has also been conducted on the data to further establish the validity of data obtained.

5.2.7.2. Codified Analysis of Variance (ANOVA)

ANOVA is a statistical test used to determine if there is a statistically significant difference between two or more categorical groups by testing for differences of means using variance [284]. The test assumes that there is no relationship between the datasets, the samples are normally distributed, and homogenous. It also requires that the different datasets have equal sample sizes. This study attempted a one–way ANOVA analysis on the data obtained for a fixed number of samples. Individual wavelength log–reduction values were summed randomly to ensure that the significance (if any) is seen in any possible sum of individual wavelengths. The statistic test for ANOVA is the *F* value. The formula can be seen in Eq. 5.8.

$$F = \frac{Variance\ caused\ by\ treatment}{Variance\ due\ to\ random\ chance} \qquad \text{Eq. 5.8}$$

The value of F shows if there is a significant difference between the independent variables tested for the chosen level of significance, in this case $p < 0.05$. ANOVA analysis is a built–in feature in Microsoft Excel and can be used to analyze the differences between two or more groups. The plug–in employs traditional ANOVA analysis to analyze categorical variables and assumes that the data follows a normal distribution [284]. In the practical application for this study, the variables are both continuous and interdependent. Therefore, the use of traditional ANOVA analysis is not entirely appropriate. On the other hand, codified ANOVA is a variation of ANOVA that can be used to analyze continuous variables. It involves codifying continuous variables into a set of indicator variables or functions, which are then used to perform ANOVA on the transformed data. The main difference between ANOVA and codified ANOVA is that the first can only be used to analyze categorical variables, while the latter can be used to analyze continuous variables, which is of need in this study [284,285]. The analysis involves codifying each experiment set as -1 / +1 for each factor (in this case, individual wavelength effect and their combination effect) under investigation, in blocks, depending on the total number of experiments conducted. The code -1 implies the device is switched "OFF" and +1 for switched "ON". Table 5.2 exemplifies the analysis with an example for test on two wavelength combination of 265 nm and 275 nm devices and three wavelength combination of all sources under study [284]. This technique is based on fitting the data to a surface response corresponding to a balanced two–level factorial design [284], whose model is shown in Eq. 5.9.

$$Y = a_0 + \ (a_1 \times x_1) + (a_2 \times x_2) + (a_3 \times x_1 \times x_2) \qquad \text{Eq. 5.9}$$

where, a_0 is a coefficient signifying no effect (in this case – dark), a_1 is the coefficient for x_1 effect (265 nm), a_2 is the coefficient for x_2 effect (275 nm) and a_3 is the coefficient for $x_1 \times x_2$ interaction effect (265 + 275) and Y is the response, k or LRV in this case. If the last factor $(a_3 \times x_1 \times x_2)$ is statistically significant, it means that the sum of the two $(a_1 \times x_1) + (a_2 \times x_2)$ factors is not enough to describe the global results of the combination of the two factors. If $a_3 > 0$, then the analysis can conclude possible synergistic effect and $a_3 < 0$ means possible antagonism between the wavelengths under study [284]. In total, for each combination (and each experimental design), the number of replicates that have been tested has been maintained at 18. Note that for the 3 wavelength combinations, in SI and SS mode, the above analysis has been changed to a three factor–two level experimental design (Table 5.2).

Table 5.2: Codified ANOVA example for 265 + 275 and 265 | 275 | 310 combination.

Two wavelength combinations (265 + 275 SE mode)				
Code		Meaning	LRV Response	k_c (s^{-1}) Response
x_1: 265 nm	x_2: 275 nm			
-1	-1	Dark	0.021	0.0292
+1	-1	265 nm ON	2.834	3.8163
-1	+1	275 nm ON	2.698	3.6331
+1	+1	265 + 275 ON	5.241	7.057
Three wavelength combinations (265 + 275 | 310)				
Code			Meaning	LRV Response	k_c (s^{-1}) Response
x_1: 265 nm	x_2: 275 nm	x_3: 310 nm			
-1	-1	-1	Dark	0.022	0.029
+1	-1	-1	265 nm ON	2.834	3.817
-1	+1	-1	275 nm ON	2.699	3.634
-1	-1	+1	310 nm ON	0.001	0.001
+1	+1	-1	265 + 275 ON	5.314	7.156
-1	+1	+1	275 | 310 ON	2.699	3.634
+1	-1	+1	265 + 310 ON	2.658	3.579
+1	+1	+1	265 | 275 | 310 ON	5.118	6.892

5.2.8. Error Propagation

In this study, error analysis plays a vital role in understanding the results and forming evidence–based discussions on the data obtained. For this reason, a detailed error propagation has been conducted [286]. In cases involving the calculation of error in sum (for instance Eq. 5.10), Eq. 5.11 has been used.

$$(Z \pm \Delta z) = (X \pm \Delta x) + (Y \pm \Delta y) \quad \text{Eq. 5.10}$$

$$\Delta z = \sqrt{(\Delta x)^2 + (\Delta y)^2} \quad \text{Eq. 5.11}$$

In the case of synergy of inactivation (Eq. 5.5), where the error needs to be calculated in a division (for instance Eq. 5.12), the error propagation has been done as seen in Eq. 5.13.

$$(Z \pm \Delta z) = \frac{(X \pm \Delta x)}{(Y \pm \Delta y)} \quad \text{Eq. 5.12}$$

$$\Delta z = Z \times \sqrt{(\frac{\Delta x}{X})^2 + (\frac{\Delta y}{Y})^2} \quad \text{Eq. 5.13}$$

5.2.9. Dark Control Experiments

To ensure the photoactivated nature of the disinfection results and to ensure a robust statistical analysis, dark control experiments were also conducted. To do this, the water matrix was spiked with the microorganism and run through the reactor in the absence of any irradiation. The experiment was conducted a minimum of 4 times and samples were plated in triplicates.

5.2.10. Electrical Energy Consumption

Electrical energy per order of inactivation is an important parameter in evaluating the efficiency of a disinfection process [287]. It is defined as the energy required to reduce the microbial population by one order of magnitude (i.e., ten–fold reduction, LRV = 1.0). To compare the electrical efficiency of each wavelength with possible combination of wavelengths, the electrical energy per order (E_{EO}, kWh m^{-3}) has been calculated according to Eq. 5.14 [286].

$$E_{EO} = \frac{P}{Q \times Log_{10}(\frac{C_o}{C})} \quad \text{Eq. 5.14}$$

where, P is the electrical energy consumed in each process (the sum of energy consumed by pump and lamps) in kW, Q is the inlet flow rate in m^3 h^{-1}, and $Log_{10}(C_o/C)$ is the LRV [287].

5.3. Results and Discussions

5.3.1. Inactivation Mechanism

To understand the disinfection process occurring within the reactor, it was necessary to draw a picture about the mechanism of inactivation the model bacterium undergoes when exposed to UV radiation. The following section captures different modes of inactivation reported in the literature and draws possible mechanisms for further use. The shortest wavelength studied for disinfection process is 172 nm [288], although this did not show any significant damage as this range of wavelength is highly absorbed by water. With an increase in emission wavelength, the absorption by water decreases and DNA strands within the microorganisms become a primary chromophore [289, 290].

Chromophore is a region in the molecule where the energy difference between two orbitals falls within the range of the incident spectrum [291]. A result of this is that the shorter wavelengths of UV were shown to induce protein damage as reported by Rastogi et al. [292]. It has also been reported that amino acids within the microorganism have the highest absorbance in the 200 – 254 nm range [293]. Overall, it can be concluded that the range of 190 – 260 nm primarily destructs the proteins and cell components within the organism that subsequently prevent photo– and dark– repair mechanisms. This mechanism will henceforth be termed as "UV-1".

Over the years, a lot of research has been conducted in multiple ways to evaluate the mechanism of damage for *E. coli* bacterium. As UV light passes through a microorganism, it is absorbed by components in the cell. It has been seen that proteins and nucleotides (consisting of DNA and RNA) absorb a significant amount of UV light in the wavelength range of 200 – 300 nm [106]. DNA absorption peaks in the range of 250 – 270 nm and has been widely reported as optimum for effective disinfection [28, 29, 106, 255]. Within this mechanism, the pyrimidine bases in the microorganism absorb the 250 – 270 nm range of the spectrum causing irreparable damage. The direct UV absorption by DNA results in the formation of lesions, which inhibit the transcription and replication processes [294-296]. In this range of UV, indirect damage holds another possible mechanism. Indirect damage is caused when the light in the UV region (specifically UV–B and UV–C) excites the internal photosensitizers (like porphyrins, sepiapterin, etc.) and produces reactive oxygen species (ROS) that promote DNA damage by oxidizing guanine [294]. At the same time, it has also been seen that protein components within the microorganisms show absorption of UV light between 275 – 285 nm range (peaking at 280 nm), in the literature, leading to irreversible effects on the DNA repair mechanisms in the host cell [255, 258]. To summarize, this wavelength range (250 – 310 nm) causes damage to different cell components (DNA, RNA, and proteins) of the microorganism, directly and indirectly. This mechanism of inactivation will henceforth be termed as "UV-2".

The next wavelength range considered is 320 – 400 nm (UV–A). This has been studied extensively mainly due to the fact that the output efficiency and cost of the devices in this range are much higher and cheaper, respectively over the UV–C wavelength-based LEDs and devices. Wavelengths in this range have been reported to excite both endogenous and exogenous photosensitizers that, in turn, oxidize biomolecules leading to cellular death [297,

298]. Most studied photosensitizers are flavins [294], porphyrins [299], and coproporphyrin III [300]. These photosensitizers are known to absorb UV–A light, in the above range, causing ROS generation and subsequently death. This mechanism of inactivation will be termed as "UV-3". At first glance, based on the wavelengths selected, the mechanism of inactivation followed would be UV-2 i.e., direct and indirect damage to the microorganism. This will be discussed later in this chapter.

5.3.2. Recirculating Batch Reactor

Disinfection experiments have been conducted for a recirculating batch reactor seen in Fig. 5.2 (a). Initially, the experimental plan involved conducting tests for all combinations and possibilities seen in Fig. 5.3. However, the data obtained with individual wavelengths discourages working in this operation mode, and therefore only single wavelength data are presented here. Fig. 5.5 plots the log inactivation obtained *vs* recirculation time for the individual wavelength tests conducted on *E. coli* K12. It can be seen that the log inactivation plots are not linear with the increase in time. This contradicts the kinetics of inactivation observed by Chick–Watson and Bolton–Cotton [102-104, 106]. In Fig. 5.5 (a, b), a closer look at the behavior showed a tailing effect at a longer operation time corresponding to a high UV dose received by the matrix. Considering the first and second laws of photochemistry, the tailing phenomenon could not be clearly explained with the theoretical mechanisms of inactivation for the microorganism tested. While the above–mentioned contradictions are valid for the FX–1 265 nm and 275 nm devices, the FX–1 310 nm device showed a behavior that has already been seen in the literature for the UV–B to UV–A regions of light spectrum. The initial slow disinfection is followed by a shoulder phase and finally, complete disinfection at a high dose, as shown in Fig. 5.5 (b) [301, 302]. The reason behind FX–1 310 behaving as expected while the other wavelengths showed tailing is due to the fact that the rate of disinfection is slow for UV–B LEDs [303] and for a significant LRV, a high UV dose is required. This is not the case for the other wavelengths in this study. An attempt was made at finding potential explanations for the behavior seen in Fig. 5.5 (a, b). Firstly, the assumption of first–order kinetics needed to be re–evaluated. For this reason, two initial concentrations of bacteria were tested for the recirculating batch reactor to verify first–order kinetics within the reactor set–up for a linear loss in bacterial concentration with time. Fig. 5.5 (c) plots the logarithmic concentration of bacteria *vs* time observed for the two concentrations (10^6 CFU/mL and 10^3 CFU/mL) alongside the slope of the line seen.

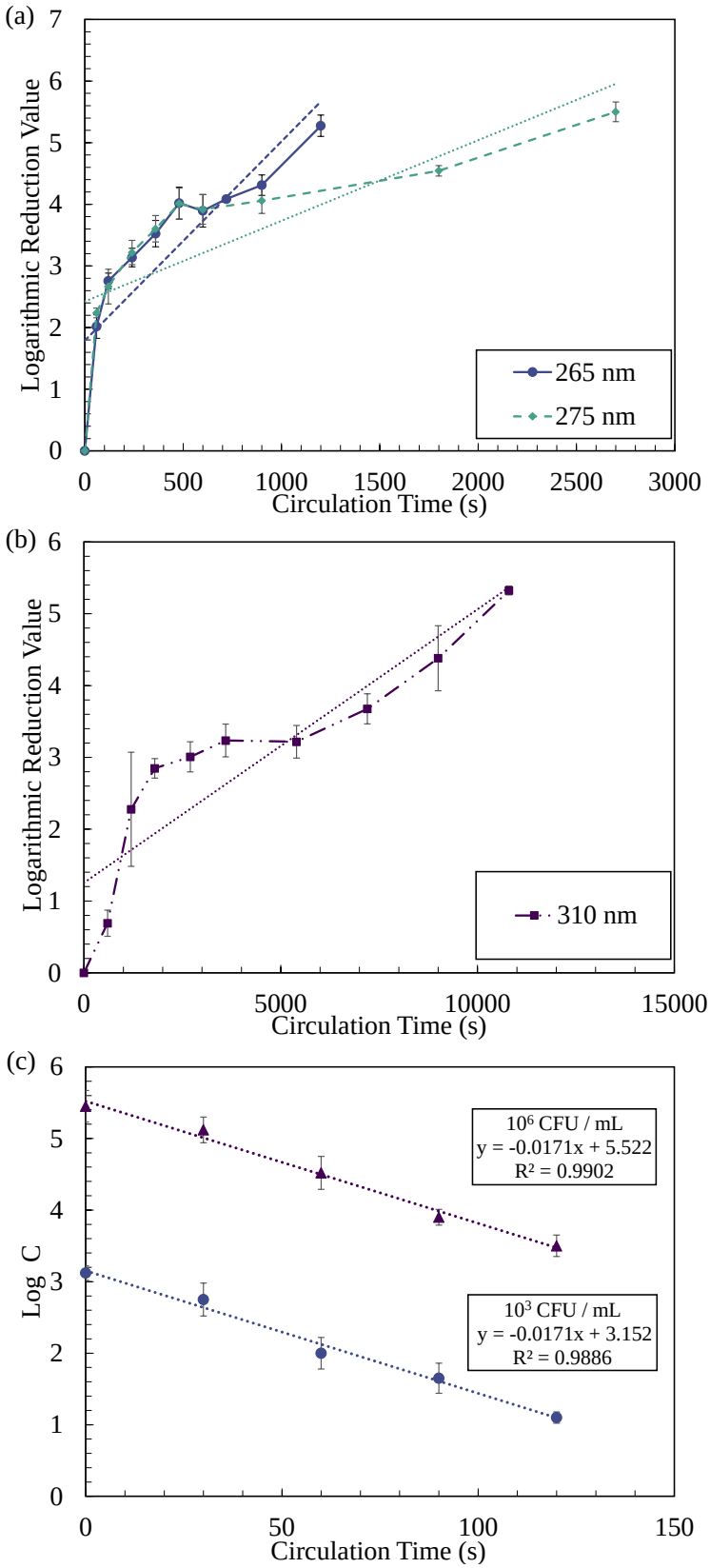

Figure 5.5: Disinfection rates in a recirculating batch reactor for (a) FX–1 265, 275, (b) FX–1 310, and (c) evaluation of first–order kinetics within the reactor.

It can be seen that the experiments follow a first–order kinetics as a change in concentration of the bacterium does not result in a change in the slope of the line and they are within the experimental and analytical errors of each other. Upon verification of the first–order kinetics, it was decided that the non–linear behavior obtained could be due to potential experimental conditions within the reactor. The behavior obtained could be fit to a 4^{th} degree polynomial curve, although no explanation of the inactivation mechanism could be provided. A literature review was conducted to examine if other researchers have obtained a similar trend and found that a few researchers observed a similar trend in the inactivation of bacteria for recirculating batch reactors [281,304,305]. It was seen that batch reactors show a linear behavior, although some studies have observed tailing at high UV doses corresponding to long residence times for batch reactor systems. For instance, in a study by Beck et al. (2017), the authors observed a short tailing in the system during exposure with 265 nm LEDs but did not comment on possible reasons behind this observation [255].

In a study by Lee et al. (2018), the study explores the underlying mechanism in the declining efficiency of a reactor and clearly saw a tailing of the inactivation curves. The authors claim a UV–induced microbial aggregation being a disinfection hindering factor, leading to longer times being necessary to achieve inactivation [304]. Similar to these findings, Oguma et al. (2013), observed tailing at high fluences during exposure with 265 nm and 280 nm LEDs. The authors do not investigate it in detail, however, they mention that "Tailing may have arisen from the aggregation of microorganisms because the flow–through reactor required a longer time of operation than a batch reactor and hence provided a higher possibility for microbial aggregation" [305]. Further studies by Gravetz et al. (2015) and Mattle et al. (2018) attempted to prove the above theory, however, stated that microbial aggregation is a "probability" and hence cannot be fully justified [306, 307]. This theory was also tested in our study to see if any potential microbial aggregation was achieved in this reactor. The samples were blotted with methylene blue indicator (Scharlab, 52015) and observed under the microscope (Motic, SMZ-160). Fig. 5.6 (a, b) shows the images captured from the microscope at t = 0 and t = 300 s, respectively.

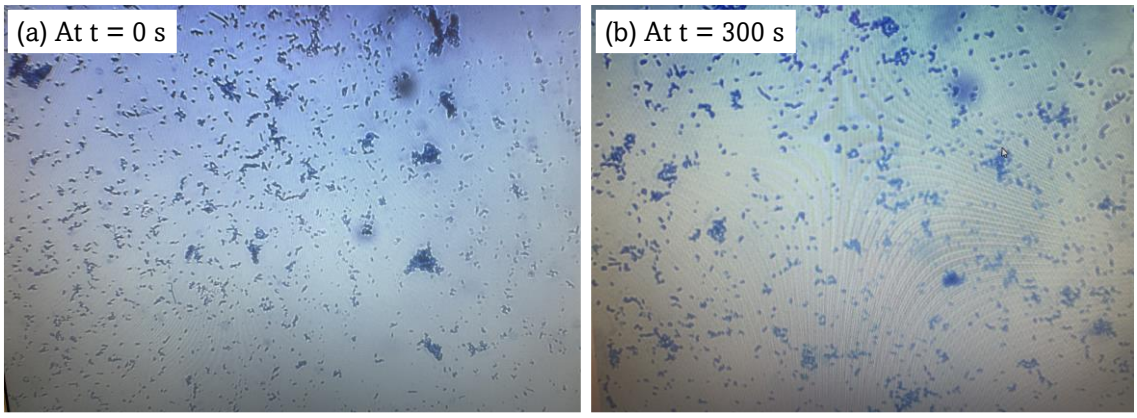

Figure 5.6: Observation of (a) unirradiated sample and (b) irradiated sample under the microscope for potential microbial aggregation.

According to the pictures in Fig. 5.6, there was no obvious microbial aggregation that could be substantiated. The large blue dots are the indicator agglomerating on the microscopic slide. Microbial aggregation has not been observed for multiple reasons including, but not limited to, low sample size under observation or that the aggregates could be inside the reactor pipes in the crevices, edges, and bends. Hence, with respect to the reactor under study, microbial aggregation was not considered as a possible cause for tailing seen.

Another parameter influencing the process was possible biofilm formation, on the inner surface of the tubing in the set–up, as studied by Papciak et al. (2022) [308]. However, this hypothesis was rejected in our system, as the set–up was rinsed with one cycle of 70% ethanol followed by three cycles of ultrapure water between each experiment. This ensured that any residual bacteria from the previous experiments were not influencing the next set of tests as ethanol kills all microorganisms when it comes in contact [309] (Fig. 5.7 (a)). Possible inhomogeneity of the water suspension was also considered. With regards to this, it is important to note that the main inlet tank, seen in Fig. 5.2 (a), was stirred during experiments using a magnetic stirrer set–up. Tests were conducted with and without the presence of a magnetic stirrer in the inlet tank. Fig. 5.7 (a) plots the observed log inactivation *vs* the circulation time for the FX–1 265 nm source. The presence or absence of a magnetic stirrer did not affect the disinfection rate, nor was it seen to induce tailing. This experiment confirmed that the water matrix is homogenous but could not assist in justifying the issue under investigation.

Interestingly, it was seen that not cleaning with 70% ethanol did induce a linear trend initially (until 10 min (gold (circle marker) and teal (diamond marker) lines in Fig. 5.7 (a)) but this could be attributed to the fact that *E. coli* K12 is sticky by nature [308] and can remain in the inner surface of the pipes during sample extraction.

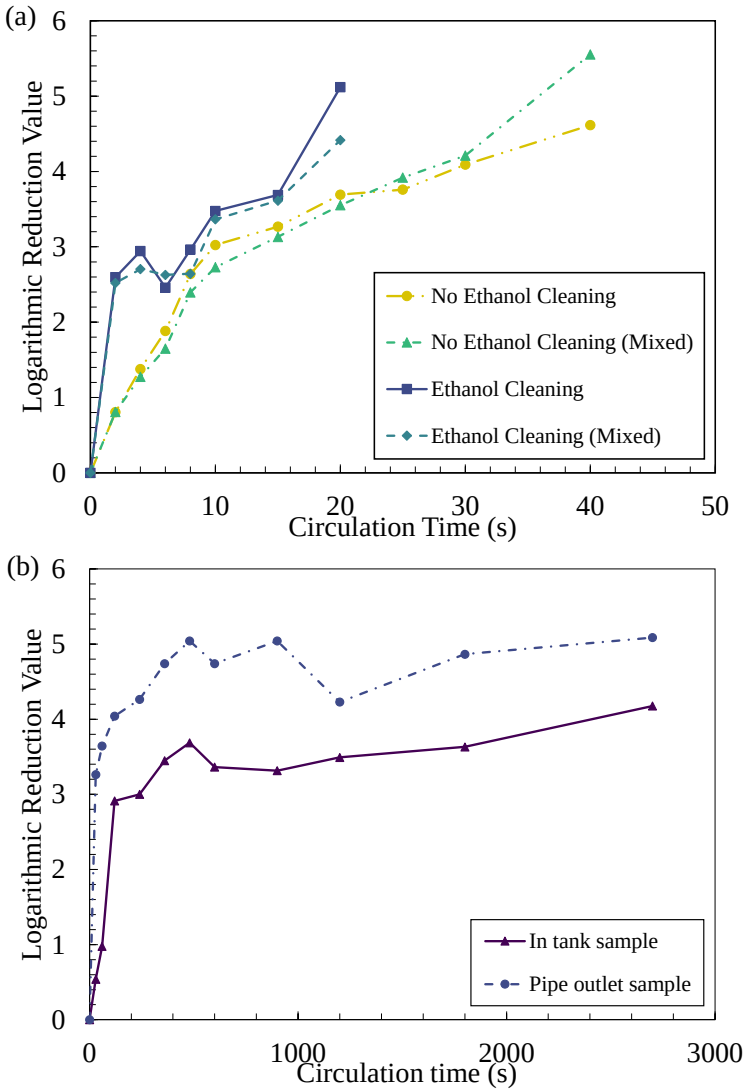

Figure 5.7: (a) Effect of cleaning the system in the presence/absence of magnetic stirrer and (b) difference between measured log inactivation at the tank and outlet of the pipe.

An inspection of the set–up conditions showed that a possible dilution effect was occurring within the system. This was investigated by collecting samples at two points in the system, i.e., at the pipe outlet and inside the tank. It is important to note that for the other discussed experiments in this section, the samples were extracted from inside the main tank. The results from these tests have been plotted in Fig. 5.7 (b). Although there was a clear difference between the measured concentrations of bacteria in the two points, the trend

observed was similar to the other experiments and did not aid in finding any conclusive explanation for the phenomenon. In any case, the results shown in Fig. 5.7 (b) confirm that a significant LRV is achieved in a single pass through the reactor. Therefore, from a practical point of view, there is no need to work under batch recirculation.

5.3.3. Kinetic Order and Effect of Dose

For the single pass flow reactor, it was necessary to verify that the reaction follows first–order kinetics with respect to the concentration of bacteria, and a linear dependence with the radiation dose. For this purpose, two bacterial concentrations (10^6 and 10^5 CFU/mL) were tested at two UV dose levels, the maximum emitted by the device (100%) and half this value (50%) for FX–1 265 device. The experiments were repeated a minimum of 3 times to ensure repeatable and reproducible data were obtained. The plot of LRV *vs* UV dose can be found in Fig. 5.8. It was seen that a change in the initial concentration of bacteria did not affect the inactivation rate within the reactor. The slopes of the two bacterial concentrations were compared to verify the similarity and it is clear that the two concentrations behave similarly within the reactor set–up. Hence, it has been concluded that the single pass flow reactor experiments are of the first–order. Moreover a clear linear trend is observed in the effect of the radiation dose on the inactivation.

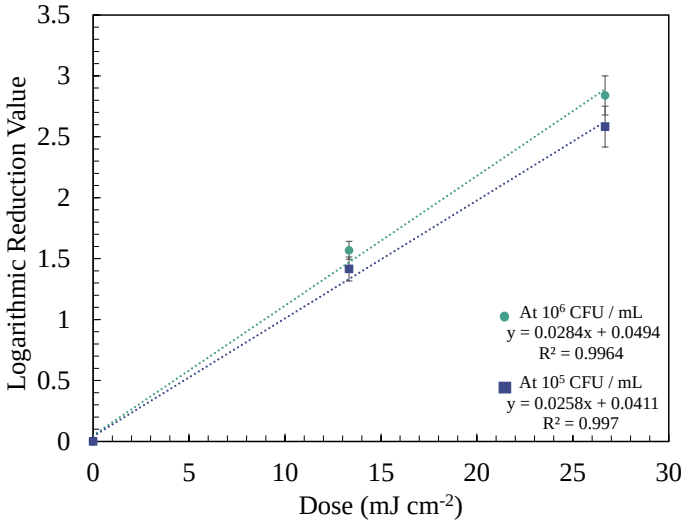

Figure 5.8: Comparison between inactivation rates for two bacterial concentrations within a single pass reactor for FX–1 265.

5.3.4. UV Inactivation by Individual Wavelengths

To elucidate any possible synergistic effect between multiple wavelengths, it was necessary to completely understand the effect of individual wavelengths on the *E. coli* K12 inactivation. Table 5.3 summarizes the main data of the UV devices used in the experiments.

Table 5.3: Intensity and spectrum details at 100% intensity.

Device name	Measured peak intensity (mW cm^{-2})	Calculated dose at 2 L min^{-1} (mJ cm^{-2})	Measured peak wavelength (nm)	Full width half maximum (nm)
FX–1 265	35.0 ± 5.5	26.7	269.03	12.39
FX–1 275	51.8 ± 4.4	39.0	277.74	10.64
FX–1 310	52.8 ± 9.9	39.8	309.51	13.99

Fig. 5.9 plots the LRV with an increase in UV dose on the water matrix. It is worth noting that the FX–1 310 experiments were attempted in a single pass, but the LRV values were negligible. Therefore, the average log reduction per pass for the FX–1 310 was estimated from the recirculation experiments (Data can be found in Appendix 5.A).

All wavelengths show linear behavior with an increase in dose, as shown in Fig. 5.9. FX–1 265 showed the highest LRV over the other two wavelengths as the emission from this device peaks at 269.039 nm which caused direct inactivation by UV-2 mechanism. While FX–1 275 is in the same inactivation mechanism range as that of FX–1 265, the absorption of this wavelength by *E. coli* K12 is lower than that of FX–1 265 LEDs [106]. The order of inactivation rates for highest disinfection at shorter UV exposure is LRV (FX–1 265) > LRV (FX–1 275) > LRV (FX–1 310). The average LRV of the FX–1 310 is extremely low, almost insignificant in a single pass reactor. The LRV's achieved with every light source and the corresponding k_d values can be found in Table 5.4.

Table 5.4: LRV for individual wavelength disinfection.

UV Source	Average LRV (50% Dose)	Average LRV (100% Dose)	R^2	k_d ($cm^2\,mJ^{-1}$)
FX–1 265	1.52 ± 0.12	2.8 ± 0.2	0.9977	0.1047
FX–1 275	1.13 ± 0.27	2.5 ± 0.3	0.9979	0.0627
FX–1 310	0.0003 ± 0.00008	0.00062 ± 0.00015	0.9981	2×10^{-5}

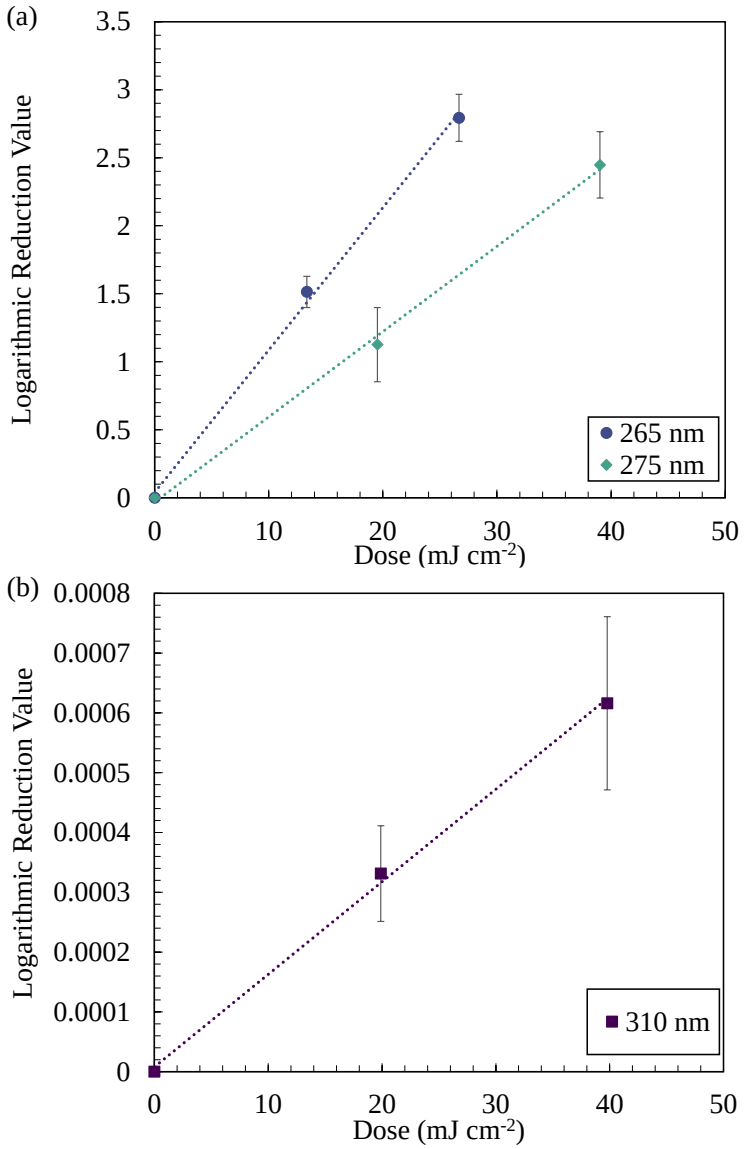

Figure 5.9: LRV *vs* dose for (a) FX–1 265 and 275, (b) FX–1 310.

5.3.5. UV Inactivation by Combination of Wavelengths

Disinfection experiments were conducted for all possible combinations shown in Fig. 5.3, for a minimum of 4 times on separate days to ensure that the data obtained is repeatable and reproducible. LRV and k_d value (kinetic constant based on UV Dose) for each combination are listed in Table 5.5. For data on the first–order kinetic constant (k_c in s^{-1}), see Appendix 5.B.

5.3.5.1. Sequential Mode (SE)

As mentioned earlier, the sequential mode involves the exposure of the water to two devices, one after the other. Fig. 5.10 (a) plots the observed LRV against the UV dose acting

on the water matrix. It is important to note that the order of exposure in the legend is the first wavelength followed by the other i.e., 310 + 265 corresponds to first exposure to FX–1 310 and then FX–1 265. The other arrangement has also been attempted and will be discussed later in this chapter. As expected, considering the UV-2 mechanism may be occurring at both wavelengths, the combination of FX–1 265 and 275 presented the maximum loss in bacterial concentration at similar dose levels compared to the other combinations in this mode. The order of inactivation rates for highest disinfection at ~60 mJ cm^{-2} is LRV (265+275) > LRV (310+265) > LRV (310+275).

5.3.5.2. Simultaneous Mode (SI)

In the simultaneous mode of operation, all the wavelengths under study act at the same instant of time and the same point, in contrast with the SE mode of operation where there are two points of reaction. For this set of experiments, two wavelength and three wavelength combinations have been tested (Fig. 5.10 (b)). Similar to the observations in SE mode, the combination of FX–1 265 and 275 resulted in the highest inactivation at ~60 mJ cm^{-2} compared to the other combinations tested. It can be seen that the combination of FX–1 310 with FX–1 275 resulted in lower inactivation compared to its combination with FX–1 265. As stated earlier, the FX–1 265 is more effective than FX–1 275 for *E. coli* K12 and thus helps understand the reason behind the lower inactivation rate. Interestingly, the combination of three wavelengths resulted in a similar inactivation at 100% UV dose, of all three devices, when compared to the combination of 265 | 275, whereas this 3–wavelength combination used nearly 1.6 times higher dose than the 265 | 275 combination. Therefore, the statistical and energy consumption analyses will key to understanding if there was any synergistic or antagonistic effect, when in combination, and whether it was effective when compared to the other combinations.

5.3.5.3. Sequential + Simultaneous Mode (SS)

This mode of operation is similar to the 3–wavelength combination discussed in SI mode above. Fig. 5.10 (c) plots the obtained loss in bacterial concentration against the UV dose. As in the SE mode, the first wavelength in the legend is in sequence, followed by the other wavelengths emitting simultaneously. The key observation, in this mode of operation, was that it resulted in a similar inactivation rate as that of the SI mode of operation using all three wavelengths. It has been plotted for comparison in Fig. 5.10 (c) (pink triangle marker).

Henceforth, this mode will be discussed together with the SI mode of irradiation of 3 wavelengths.

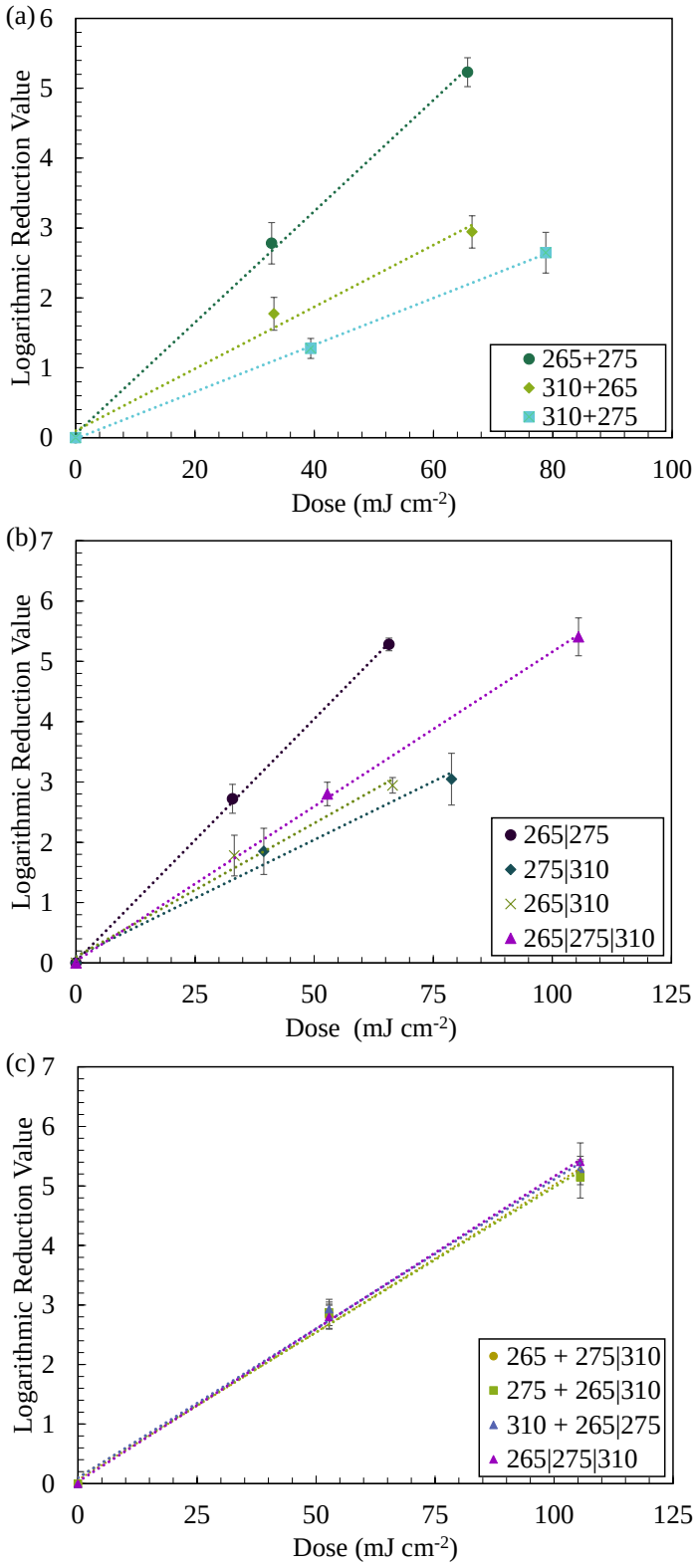

Figure 5.10: Plot of LRV against UV dose for (a) SE mode, (b) SI mode, and (c) SS Mode.

Table 5.5: LRV of UV combinations.

UV Combination	Average LRV (50% Dose)	Average LRV (100% Dose)	R^2	k_d (cm^2 mJ^{-1})
265 + 275	2.8 ± 0.3	5.2 ± 0.2	0.998	0.079
310 + 265	1.8 ± 0.2	3.0 ± 0.2	0.986	0.044
310 + 275	1.3 ± 0.2	2.6 ± 0.3	0.999	0.033
265 | 275	2.7 ± 0.2	5.3 ± 0.1	0.999	0.080
275 | 310	1.8 ± 0.3	2.9 ± 0.1	0.984	0.038
265 | 310	1.8 ± 0.4	3.0 ± 0.4	0.985	0.044
265 | 275 | 310	2.8 ± 0.2	5.4 ± 0.3	0.999	0.051
265 + 275 | 310	2.8 ± 0.2	5.2 ± 0.2	0.998	0.049
275 + 265 | 310	2.9 ± 0.2	5.2 ± 0.4	0.995	0.048
310 + 265 | 275	2.9 ± 0.1	5.3 ± 0.1	0.996	0.050

5.3.6. Effect of Arrangement

Prior to the analysis of potential synergistic effect in the combinations, it was necessary to understand if the order of exposure to different wavelengths, in SE mode of irradiation, affects the overall inactivation obtained. Also, it was essential to explore the difference between SE and SI mode of irradiation. Fig. 5.11 (a – c) compares the different combinations (in SE mode) in two possible arrangements with error bars representing the calculated experimental error. Note that the legend follows the same order as the exposure.

For the 265/275 nm LED device combinations, it can be seen that there is no significant difference between the two arrangements. This was also confirmed by the *t*–Student analysis conducted on the raw data for a confidence interval (*CI*) of 95%. The codified ANOVA analysis pointed to a difference between the order of arrangement at 50% UV dose from both devices when compared at 95% significance ($p = 0.0334$). However, if considered at a slightly lower significance level of 94%, both orders of arrangement showed similar behavior. Fig. 5.12 plots the obtained LRV for each combination with the error bars representing 95% *CI* obtained from the analysis. The reason behind no difference between the two arrangements can be attributed to the fact that both wavelengths inactivate the bacteria by the same mechanism (UV-2). Therefore, the order of exposure cannot significantly impact the inactivation rate.

In the case of combinations of 310 nm device with either 265 nm or 275 nm devices (Fig. 5.11 (b, c)), the order of wavelength exposure could have an effect on the process as in this case the 310 nm device, on its own, does not result in significant log–reduction [301]. For combinations involving 265 nm and 310 nm devices, the error bars do not overlap at 100% UV dose of both wavelengths (~65 mJ cm^{-2}) and at 50% UV dose, the bars just overlap. However, a *t*–Student analysis of the raw data showed that there is a significant difference between the two arrangements (Fig. 5.12 (a, b) – dark green and teal bars). Further, *p* values of 3.64×10^{-5} and 1.67×10^{-5}, at 50% and 100% UV dose, respectively, obtained from codified ANOVA, confirmed a significant difference between the two orders of arrangement. The exposure of FX–1 310 followed by FX–1 265 resulted in a higher logarithmic inactivation compared to the other arrangement. This is because the exposure first to FX–1 265 damages the microorganism completely (given the high absorbance of this wavelength for *E. coli*), and the effect of FX–1 310 is redundant in such combinations. On the other hand, exposure of FX–1 310 followed by FX–1 265 meant that there is a possibility that the 310 nm weakens the microorganism, making them more susceptible to the 265 nm killing mechanism.

Similar to the 265/310 nm combinations, it was seen that 275/310 nm combinations show the same behavior. The comparison between the two arrangements showed significant differences when analyzed using *t*–Student (Fig. 5.12 (a, b) – light green and lime bars) and codified ANOVA ($p = 9.8 \times 10^{-5}$ (50%) and 4.8×10^{-5} (100%)) despite error bars overlapping at 50% and 100% UV dose (Fig. 5.11 (c)). Overall, it was seen that the exposure of FX–1 310 followed by FX–1 265/275 resulted in higher log inactivation of the microorganisms, while the order of arrangement for FX–1 265/275 combinations did not show any significant difference. Here onwards, the analysis and results for combinations are discussed for the arrangements with a higher inactivation rate i.e., FX–1 310 followed by FX–1 265/275.

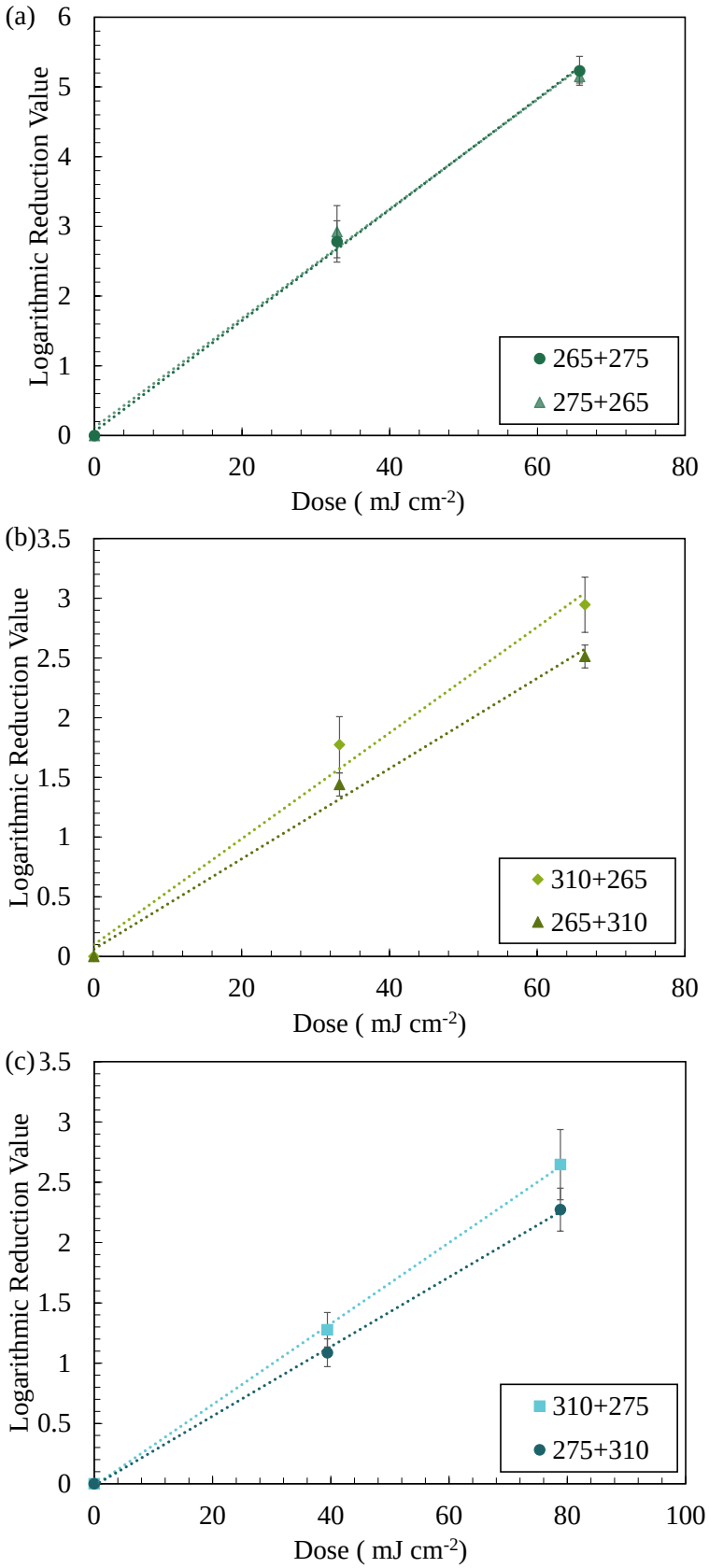

Figure 5.11: Comparison between arrangements in SE mode for (a) 265/275, (b) 265/310, and (c) 275/310 combinations.

Further a comparison between the different irradiation modes was conducted (see Fig. 5.12 yellow, orange, light green bars for SI Mode). For combinations involving 265 nm and 275 nm devices, the mode of irradiation had no significant effect on the inactivation obtained when compared using the test case in Eq. 5.7. Similarly, the combination of 265 nm and 310 nm devices showed no significant difference between the two modes. In contrast, in the case of FX–1 275 / 310 nm combinations, there existed a significant difference between the modes of irradiation.

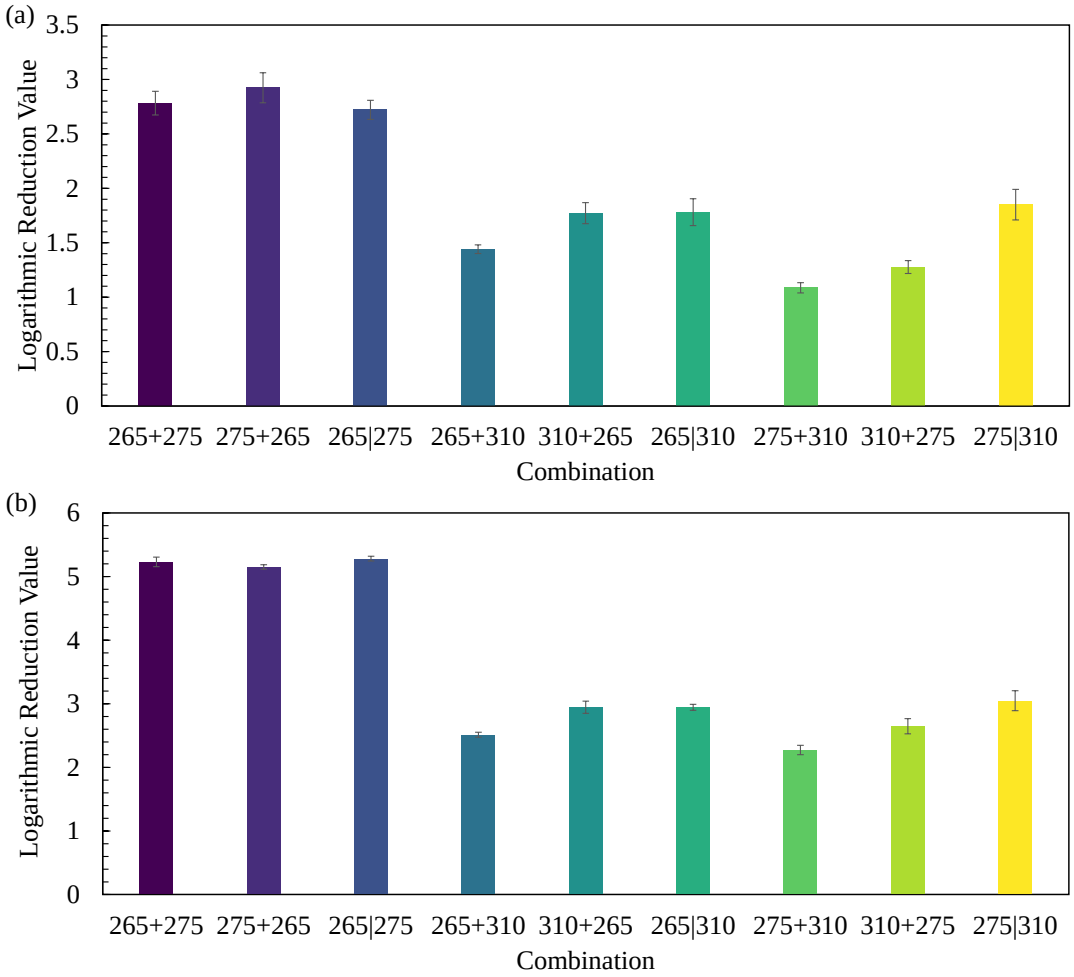

Figure 5.12: Comparison between obtained LRV for each combination at (a) 50% Dose and (b) 100% Dose with error bars representing 95% *CI*.

A priori it was expected that the SI irradiation mode would result in better inactivation rates over the SE mode. An investigation of the above results pointed out that only for combinations involving the FX–1 265 nm device, the mode of irradiation did not impact the inactivation obtained. This could be due to the fact that the 265 nm device emits the lowest intensity and, consequently, lowest dose compared to the other two wavelengths studied.

The dose contribution from FX–1 265 nm was found to be about 40.59% and 40.13% of the total UV dose when in combination with FX–1 275 nm and FX–1 310 nm, respectively. This means that irrespective of the mode of irradiation, FX–1 265 nm determines the global results given its high absorbance by the microorganism.

On the other hand, for combinations involving FX–1 275 with FX–1 310, the contribution is equal (49.51% and 50.49% respectively). Therefore, both devices play a significant and active role in the inactivation of such combinations. This could be clearly seen when the SE and SI modes of irradiation were compared for this combination. The SI mode of irradiation resulted in significantly greater disinfection compared to the SE mode. The concept of high UV fluence at a single point will result in better inactivation over multiple points has been discussed in Kowalski et al. (2009) [101]. In the SE mode of irradiation, there are two points of UV contact for the microorganisms, whereas, in SI mode, all the light is received at a single point. The SI mode offers more photons at an instant of time at one point compared to the SE mode and hence results in higher inactivation [101].

5.3.7. Effect of Flow Rate

The effect of flow rate on the disinfection process was only tested for the FX–1 265 device, as it is known the behavior does not change with wavelength, as this parameter is specific to the reactor set–up [235]. Fig. 5.13 plots the log–inactivation observed for the four flow rates discussed in Section 5.2.4.2. With the decrease in flow rate through the reactor, the residence time of the microorganism under the light source increases (Table 5.1, [106]).

Fig. 5.13 (a) plots the log–inactivation obtained as a function of intensity input (%), to demonstrate the effect of increase in residence time on the process and to compare the different flow rates. As expected, as the flow rate decreases the inactivation rate increases. This showed that the behavior of the reactor is linear with increase in residence time (Fig. 5.13 (b)).

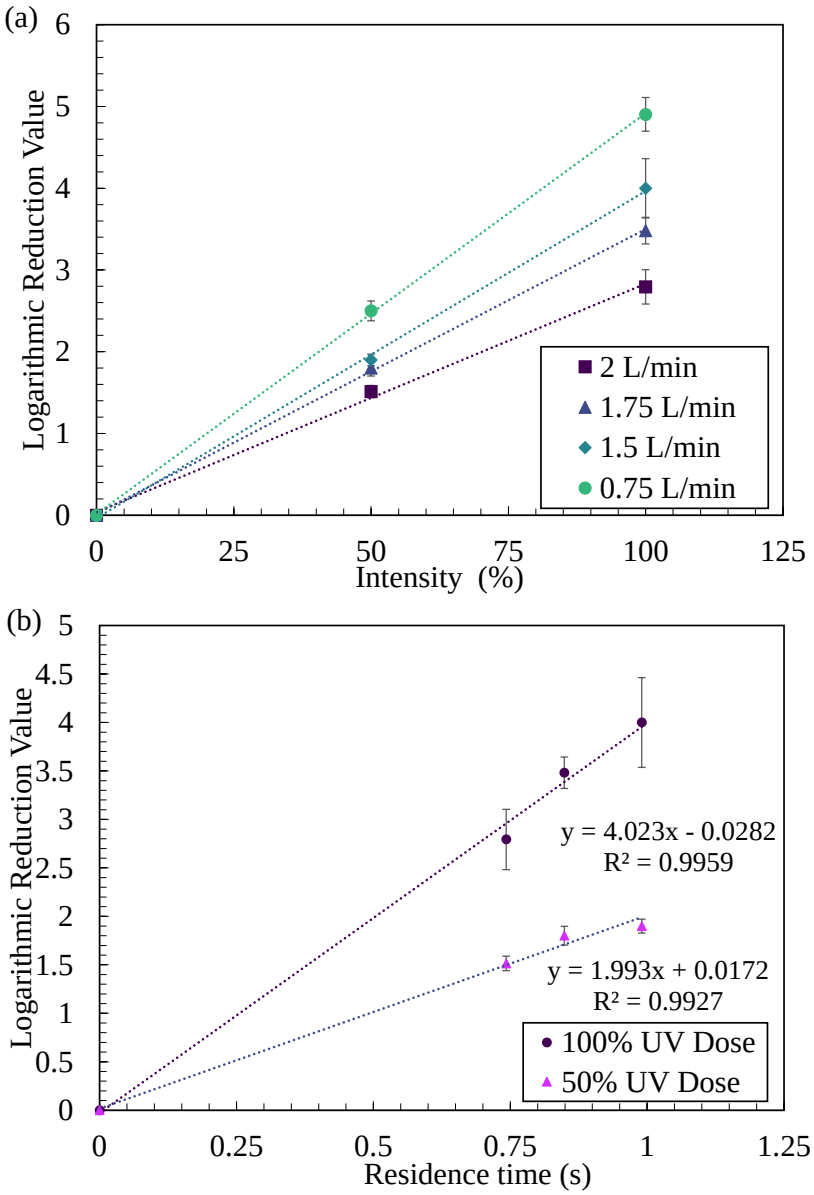

Figure 5.13: Inactivation rates at multiple flow rates as a function of (a) Input intensity and (b) Residence time.

5.3.8. Synergy of Inactivation

Synergy of inactivation values have been calculated using the definition discussed in Section 5.2.6, whereas the overall error has been propagated using Eq. 5.11 and Eq. 5.13. Theoretical LRV has been calculated using the sum of individual wavelength LRV's in Table 5.4. Table 5.6 and 5.7 list the theoretical LRV's and actual LRV's for each combination tested, at 50% and 100% UV dose, respectively. This analysis has also been conducted in terms of kinetic constants (k_c) and data can be found in Appendix 5.C.

At first glance, it can be confirmed that, for all combinations tested, no antagonism can be seen in the process i.e., the use of multiple wavelengths did not reduce the disinfection rate. In all cases, at least a summation effect of the wavelengths has been observed [305]. As mentioned earlier, for a synergistic effect to be concluded, the actual inactivation rate of the combination must be significantly greater than the sum of individual inactivation rates of the wavelengths. Fig. 5.14 plots *synergy* of inactivation values for each combination with error bars representing the propagated standard deviation of all samples considered. Note that this analysis was also conducted for SS mode of irradiation, however as mentioned earlier, given its similarity to SI mode of irradiation, the discussion has been given for the general "3–wavelength combination" and Table 5.6, 5.7 lists the LRV's for SI mode of irradiation.

Table 5.6: Synergy of Inactivation values (by LRV) (at 50% Dose).

UV Source Combination	Theoretical LRV	Actual LRV	*Synergy*
265 | 275	2.6 ± 0.3	2.7 ± 0.2	1.03 ± 0.11
265 | 310	1.5 ± 0.1	1.8 ± 0.3	1.2 ± 0.2
275 | 310	1.1 ± 0.3	1.8 ± 0.4	1.6 ± 0.5
265 | 275 | 310	2.6 ± 0.3	2.8 ± 0.2	1.06 ± 0.09
265 + 275	2.6 ± 0.3	2.8 ± 0.3	1.06 ± 0.13
310 + 265	1.5 ± 0.2	1.8 ± 0.2	1.17 ± 0.16
310 + 275	1.1 ± 0.3	1.3 ± 0.2	1.13 ± 0.19

Table 5.7: Synergy of Inactivation values (by LRV) (at 100% Dose).

UV Source Combination	Theoretical LRV	Actual LRV	*Synergy*
265 | 275	5.2 ± 0.3	5.3 ± 0.1	1.01 ± 0.02
265 | 310	2.8 ± 0.2	2.9 ± 0.1	1.05 ± 0.05
275 | 310	2.5 ± 0.2	3.0 ± 0.4	1.2 ± 0.2
265 | 275 | 310	5.2 ± 0.3	5.4 ± 0.3	1.03 ± 0.06
265 + 275	5.2 ± 0.3	5.2 ± 0.2	0.99 ± 0.04
310 + 265	2.8 ± 0.2	3.0 ± 0.2	1.05 ± 0.09
310 + 275	2.5 ± 0.2	2.6 ± 0.3	1.08 ± 0.13

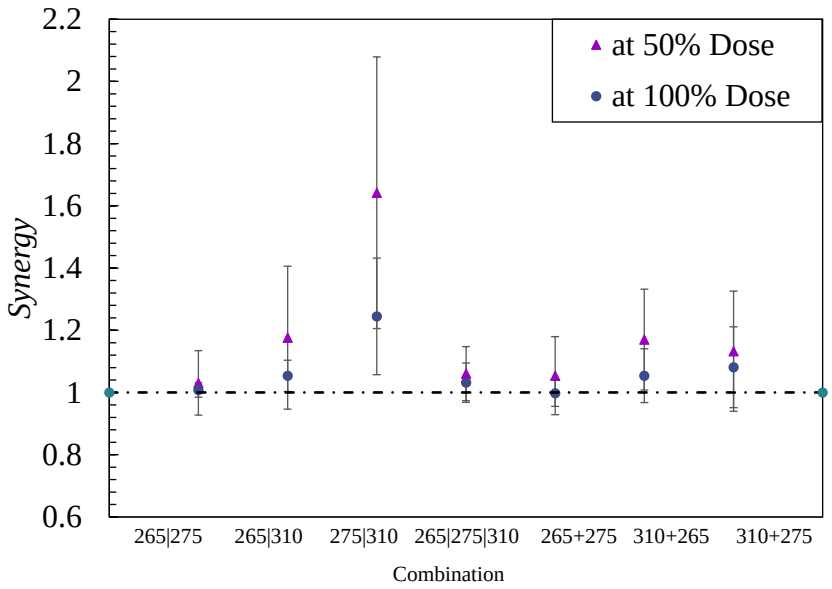

Figure 5.14: Synergy of inactivation for all combinations.

In all combinations studied, the *Synergy* values were close to or greater than 1. However, most of the propagated error bars in Fig. 5.14 can be seen to overlap with 1 and to conclude the existence of a synergistic effect, this value must be significantly greater than 1 [255, 257, 259, 282]. The following section uses statistical analysis to further evaluate the *synergy* of inactivation based on significance of the dataset obtained from experiments.

5.3.8.1. Dual Wavelength Combinations

To check for the statistical significance of the difference between theoretical and actual inactivation rates obtained in this study, *t*–Student analysis was the first technique employed. Using the LRV's and standard deviations from Table 5.6 and 5.7, the *CI* (95%) was calculated using Eq. 5.6. Further, a test was conducted to estimate if the sum of theoretical LRV and its *CI* was greater than the difference of the actual LRV and its *CI*. If there is no significant difference, between theoretical and actual LRV, that means there is no synergistic effect. Fig. 5.15 plots the comparison between theoretical LRV and actual LRV with error bars representing the calculated *CI*. Table 5.8 lists the observations for all combinations based on the argument discussed earlier.

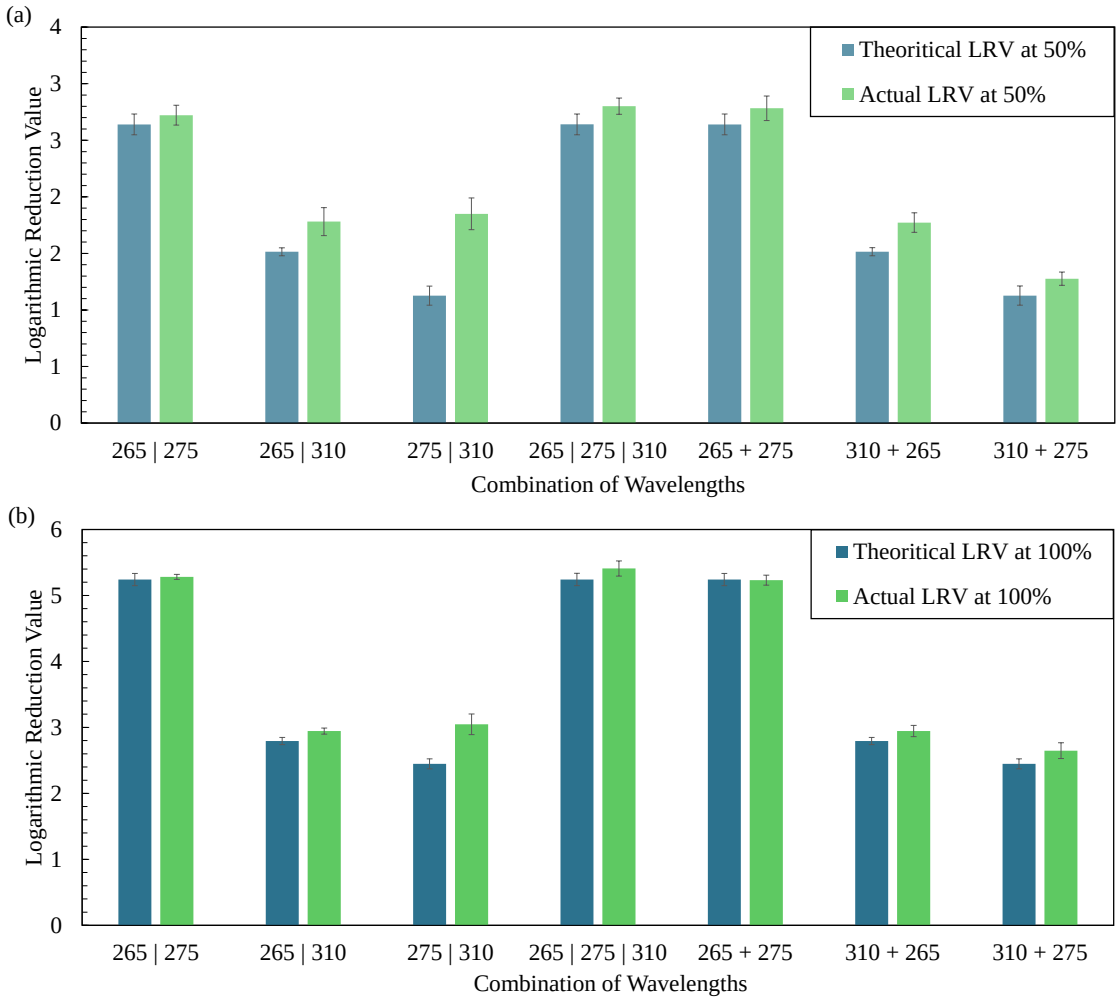

Figure 5.15: Comparison between theoretical and actual LRV for each combination at (a) 50% dose and (b) 100% dose with error bars representing 95% *CI* from *t*–Student analysis.

Table 5.8: *t*–Student analysis observations (based on LRV, at 95% *CI*).

UV Source	50%	100%
265 | 275	Not Significant	Not Significant
265 | 310	Significant	Significant
275 | 310	Significant	Significant
265 | 275 | 310	Not Significant	Not Significant
265 + 275	Not Significant	Not Significant
310 + 265	Significant	Significant
310 + 275	Significant	Significant

This analysis has also been conducted using kinetic constants (k_c in s^{-1}) obtained and the data can be found in Appendix 5.D. Given the closeness between the observation of

"significant" and "not significant" effect for the combinations, it was necessary to correlate results from codified ANOVA to substantiate any observations of synergistic effect. Codified ANOVA was performed for all the combinations, based on LRV, and the obtained *p*–values have been listed in Table 5.9. Detailed results from this analysis for all combinations can be found in Appendix 5.E.

Table 5.9: Significance *p*–values from codified ANOVA ($p < 0.05$).

UV Source	50%	100%
265|275	0.4107	0.0774
265|310	0.0614	**0.0000**
275|310	**0.0000**	**0.0000**
265|275|310	**0.0000**	**0.0000**
265+275	0.7871	0.4329
310+265	**0.0000**	**0.0041**
310+275	**0.0016**	**0.0004**
275 + 265	0.0771	0.7184
265 + 310	0.3113	**0.0000**
275 + 310	0.2189	**0.0063**
265 + 275 | 310	**0.0000**	**0.0000**
275 + 265 | 310	**0.0000**	**0.0000**
310 + 265 | 275	**0.0000**	**0.0000**

The **bold** numbers in Table 5.9 show the cases in which there is a significant difference between the sum of LRVs from individual wavelengths and the LRV in combination. It is worth noting that the 0.0000 value means that the theoretical and actual values are statistically different with a significant level above 99.99%, as the *p*–value is lower than 10^{-4}. From Table 5.8 and 5.9, it can be seen that irrespective of order of arrangement and mode of irradiation, the combinations of FX–1 265 nm and 275 nm devices showed no synergistic effect. In combinations of FX–1 310 nm with FX–1 265 nm, *t*–Student analysis showed "potential" synergy between the wavelengths, and this was confirmed with the codified ANOVA results.

In this combination, it was seen that SI mode of irradiation, at 50% dose each, showed no significant synergistic effect whereas at 100% dose each, there is a potential synergistic effect. Upon closer analysis of the codified ANOVA results, the *p*–value for 265 | 310

combination is just above the 95% *CI* chosen and it is possible that the experimental error is playing a role in this case. If the *CI* is chosen at a 94% interval, then potential synergistic effect can also be concluded between the two wavelengths. However, this has not been done to ensure consistency between all the analysis conducted. In the SE mode of irradiation, the exposure of FX–1 310 followed by FX–1 265 presented a significant synergistic effect, at both UV doses tested. Interestingly, the other order of exposure (265 + 310) also presents a significant synergistic effect at 100% UV dose. No explanation has been found for this behavior.

For combinations of FX–1 310 nm with FX–1 275 nm, both modes of irradiation (SE and SI), presented a significant synergistic effect. Similar to the FX–1 265/310 nm combination, when the FX–1 275 was irradiated first, followed by FX–1 310 at 100% UV dose each, there exists a significant synergistic effect. Comparing the two combinations i.e., 265/310 and 275/310 combinations, Fig. 5.14 and Table 5.9, it can be seen that the synergistic effect is more prominent in the 275/310 nm combinations. This could be because in this combination, both wavelengths contribute equally to the total UV dose as discussed in Section 5.3.6.

5.3.8.2. Three Wavelength Combinations

Four possible combinations of 3 wavelengths have been studied in this work in two modes – SI and SS. It was seen that the two modes presented similar inactivation rates (See Fig. 5.10 (c)). The *t*–Student analysis found that there was no significant difference between the sum of individual wavelength LRVs and the combination. However, codified ANOVA found that there exists a significant difference between the two variables with up to 99.99% confidence. In all the modes and UV doses of three wavelength combinations, it was seen that there existed a significant synergistic effect between the wavelengths.

To summarize, statistically, it was seen that the combination of 310 nm in SE/SI modes with 265/275 nm and three wavelength combinations (both SI and SS mode of irradiation) resulted in a synergistic effect on the disinfection of *E. coli* K12. However, the mechanism behind this effect must be further discussed to justify this conclusion.

5.3.9.3. Synergistic Damage Mechanism

Absorption spectra and photochemical properties are specific to a given molecule. A photon may be absorbed only when its energy corresponds to the energy required for an allowed transition between quantized energy states of the molecule. In the ultraviolet and visible wavelengths, the photon energies are in the range associated with transitions of molecular electrons into excited electronic states [106, 310]. The photobiological reactions of multicellular organisms depend upon what happens to individual living cells within their organ systems, which in turn is determined by individual intracellular photochemical reactions [101, 311]. Ultraviolet radiation may inactivate enzymes in numerous biological systems by producing alterations in proteins [288-293]. To elucidate a possible damage mechanism in combination, the emission spectrum of the UV LED devices has been studied.

The emission spectra of each device relative to its peak wavelength can be seen in Fig. 5.16 (a). The peak wavelengths from each device have been listed in Table 5.3. At first glance, all the wavelengths are within the range of 255 – 320 nm, thus resulting in a single mechanism of damage (UV-2) discussed in Section 5.3.1. Any synergy seen could be assumed as an analytical or experimental error. However, as the codified ANOVA showed a significant difference in combination (with up to 99.99% confidence in some cases), it is necessary to further understand if the emission spectrum is possibly behind the observed synergistic effect. To do this, the peak emission and width of the spectrum have been studied.

The overlap of spectra using their peak wavelengths helps to understand the width of the spectrum and understand its light emission pattern. This has been conducted in Fig. 2.14 (Chapter 2). The FWHM lines, for each LED, are dotted lines drawn in Fig. 5.16 (b). The 310 nm device has the highest spectral width (13.998 nm) compared to the other two devices in this study. It can also be seen that, for FX–1 310, the area under the curve after the FWHM points (i.e., 317 nm onwards) is significantly higher (contributes to about 35% in the overall spectrum) than the other two wavelengths. Table 5.10 lists the % of the calculated area under the curve before and after the width of the spectrum for each LED used in this study.

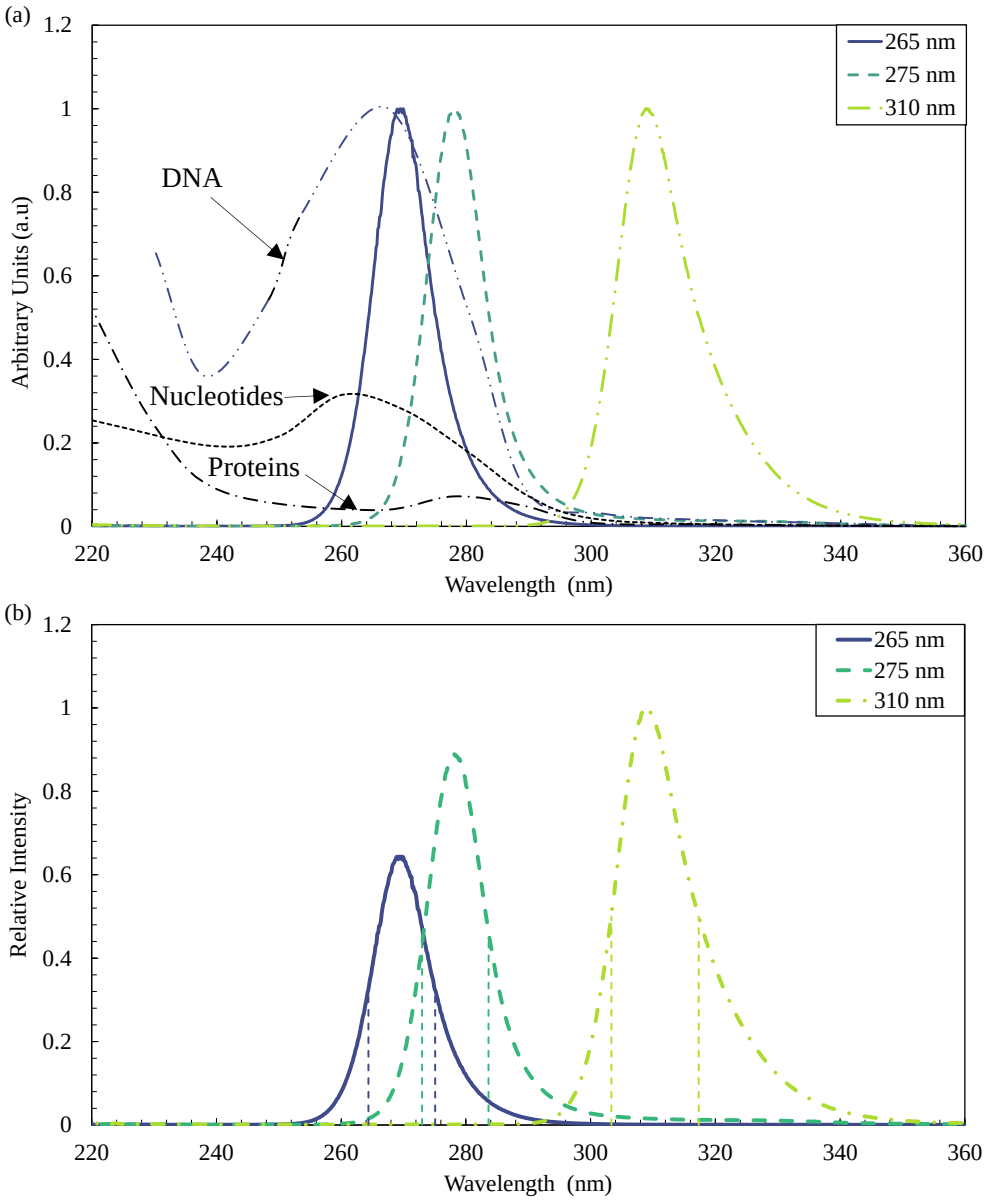

Figure 5.16: (a) Individual wavelength spectra of the light sources relative to their respective peaks alongside absorption spectra for DNA, proteins, and nucleotides extracted from [106, 289] and (b) Spectra relative to the measured peak at 309.518 nm.

Fig. 5.17 (a – d) combines the wavelengths for each combination tested. It is worth noting that the intensity emitted at 50% of 310 nm device is about 15% lesser than the intensity emitted at 100% by the 265 nm device. For the 265 and 275 nm LED combinations (see Fig. 5.17 (a)), the 275 nm spectrum overlaps 50% width of 265 nm, with negligible emission above 300 nm. Hence only one mechanism of inactivation is possible (UV-2) [289-294]. This explains why no synergistic effect was seen for SE and SI modes of irradiation. In both cases,

the value of synergy is the closest to 1 compared to the other combinations i.e., there is a summation effect as expected due to the Second Law of Photochemistry (see Fig. 5.14).

Table 5.10: Contribution of the different spectral ranges to the emission of the light sources.

Device Name	% Contribution below half maximum (From 200 nm)	% Contribution within the half maximum spectrum width	% Contribution above half maximum (until 400nm)
FX–1 265	12.8% (Below 264 nm)	67.4% (b/n 264 – 277 nm)	19.8% (After 277 nm)
FX–1 275	12.1% (Below 273 nm)	64.8% (b/n 273 – 283 nm)	23.1% (After 283 nm)
FX–1 310	10.8% (Below 303 nm)	63.2% (b/n 303 – 317 nm)	26.0% (After 317 nm)

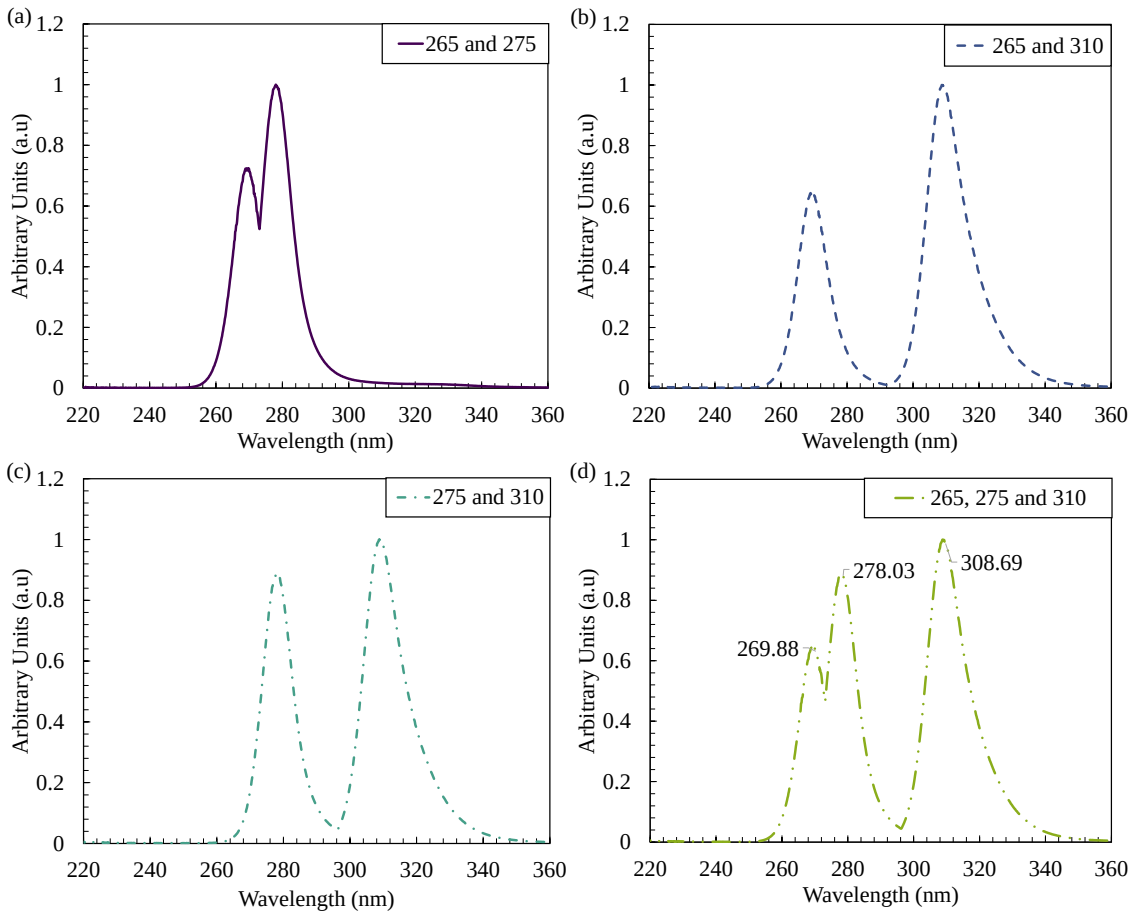

Figure 5.17: Combined emission spectrum relative to maximum intensity measured for (a) 265/275, (b) 265/310, (c) 275/310, and (d) 265/275/310 combinations.

In the case of 265/310 and 275/310 combinations, the 26% contribution of wavelengths above 317 nm means that there could be a second inactivation mechanism involved (UV-3)

along with UV-2 mode of inactivation [297-300]. In all the cases for both SE and SI modes of irradiation, significant synergy was observed (with a minimum of 94% confidence). The 310 nm LED spectrum contributes more photons when irradiated in combination with FX–1 265. The 26% photon contribution from the range of 320 – 400 nm corresponds to low doses that have been proven to induce many physiological alterations, mainly the well–known radio–induced growth inhibition as reported in the literature [295, 310, 311]. Therefore, two mechanisms of inactivation are in play for 310 nm – 265/275 nm combinations. This also justifies why for 310 nm combinations, in SE mode, the order of irradiation resulted in lower inactivation when 310 nm was irradiated after 265/275 nm device. Finally, it is also well known that LED spectra are a function of temperature of the device [127]. During the operation, there is a possibility of thermal drift towards increased wavelengths, which can in turn increase the 26% spectrum contribution (above 317 nm) discussed earlier, and thus resulting in the increased probability of damage by UV-3 mechanism. The temperatures of the device were monitored while just switched "ON" (25°C) and 2 min into operation (32°C). Although the device maintains the temperature constant on the substrate (as discussed in Section 2.3.2, Chapter 2), the temperature at the junction could rise for milli seconds. As the residence time in all the experiments was 0.7538 s, there is a possibility that thermal drifts impact the overall disinfection rate. Similarly, for combinations of 3 wavelengths, two damage mechanisms – UV-2 and UV-3, are in play during the process resulting in synergistic effects. In three wavelength combinations, the contribution of UV-2 is greater than the UV-3 mechanism, as the number of photons from 265 nm and 275 nm contributes to about 63% of the total dose received. This can be seen from the value of synergy of inactivation in Fig. 5.14, where, in comparison with the combination of 265/275 nm devices, the value is close to 1.

To summarize, the synergistic effect seen in this study is due to the action of two inactivation mechanisms. The FX–1 310 nm weakens the microorganism due to its spectral emission, making it much more susceptible and easier to damage with the other wavelengths. The order of irradiation in SE mode is crucial to obtain a synergistic effect. Whereas, in SI mode of irradiation, given that the FX–1 310 emits the highest intensity compared to the other wavelength, the same mode of damage is occurring within the microorganism as it passes through the reactor. One of the major differences between the current study and past researches is that in most cases, the 310 nm LED was a minor contributor and hence it had

an insignificant impact compared to the dominant wavelengths [271, 305]. In this study, 310 nm is high powered and equal to the number of LEDs used in the 265 nm device.

5.3.9. Electrical Energy Consumption

The importance of exploring the electrical energy consumption per unit order of inactivation (E_{EO}) lies in its ability to compare different processes (in this case individual wavelengths and combinations) on an equal basis [287, 312]. Since each wavelength and combination requires different amounts of energy to achieve a level of microbial reduction, the comparison between them can be misleading. This parameter takes into account both the energy consumption through the whole process and the degree of reduction achieved, allowing a more accurate comparison of the efficiency of each process [312, 313]. In this study, the electrical energy consumption per unit order of inactivation was calculated using Eq. 5.14. Table 5.11 lists the calculated E_{EO} values for all the combinations tested. Note that for each UV source, along with the device power consumption, the power required for the pump has also been considered in the analysis and for SE combinations, only the higher inactivation rate arrangement has been evaluated.

Table 5.11: Electrical energy consumption per unit order of inactivation.

UV Source	E_{EO} (kWh m^{-3}) 50% Intensity	E_{EO} (kWh m^{-3}) 100% Intensity
265 nm	0.44 ± 0.04	0.30 ± 0.03
275 nm	0.6 ± 0.2	0.4 ± 0.1
310 nm	1953 ± 190	1332 ± 275
265|275	0.32 ± 0.02	0.24 ± 0.02
265|310	0.5 ± 0.1	0.41 ± 0.02
275|310	0.5 ± 0.1	0.41 ± 0.04
265|275|310	0.37 ± 0.02	0.29 ± 0.01
265 + 275	0.31 ± 0.05	0.24 ± 0.02
310 + 265	0.5 ± 0.1	0.41 ± 0.06
310 + 275	0.7 ± 0.1	0.46 ± 0.06

In terms of individual wavelength mode of irradiation, the 265 nm UV LED device (FX–1 265) required lower electrical energy of 0.44 ± 0.04 kWh m^{-3} and 0.30 ± 0.03 kWh m^{-3}, at 50% and 100%, respectively, for the inactivation of *E. coli* K12. The lower electrical energy consumption from this device can be attributed to its higher inactivation efficacy. On the

other hand, 310 nm UV LED device (FX–1 310) has the highest energy consumption of 1953 ± 190 kWh m^{-3} and 1332 ± 275 kWh m^{-3}, at 50% and 100%, respectively. While the 310 nm LED does have the highest energy efficiency amongst the LEDs, the inactivation efficacy is extremely low in comparison and hence does not aid any decrease in electrical energy per unit order. Therefore, using the 310 nm device on its own is not an effective method for achieving the target disinfection. Fig. 5.18 plots the E_{EO} calculated for each UV source and combination.

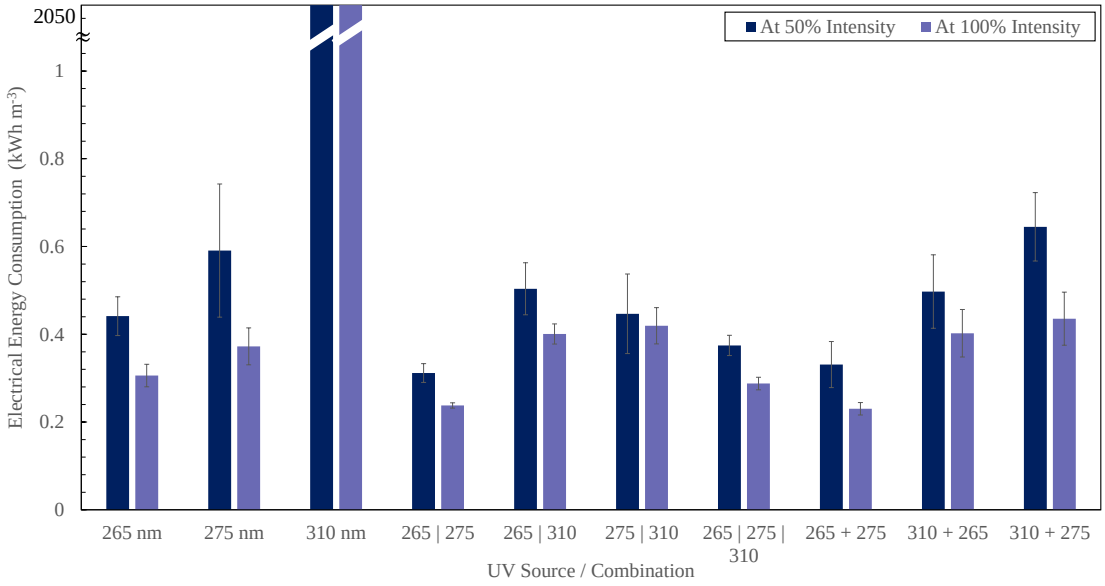

Figure 5.18: Electrical energy consumption per unit order at 50% (Dark blue bars) and 100% (Violet bars).

For combinations involving 265 nm and 275 nm LEDs, the E_{EO} shows similar values in both modes tested, at both intensities. This further justifies the results seen in Section 5.3.7, wherein the two modes of irradiation (SE and SI) resulted in similar inactivation rates. Given that the same amount of energy is being consumed i.e., the same number of photons are being delivered to the water matrix, and concurrent to the laws of photochemistry, it is fair to say that the inactivation rates should be similar [255]. The lowest E_{EO} was observed in this combination, in SE mode of irradiation of 0.31 ± 0.05 kWh m^{-3} at 50% intensity, whereas at 100% intensity, SI mode resulted in lowest E_{EO} of 0.24 ± 0.02 kWh m^{-3}. It can also be seen that the E_{EO} in combination is lower than the individual sum of the energy consumption individually. This means that the irradiation of these wavelengths is much more efficient than the wavelengths on their own. While no synergistic effect was seen in the combination of these two wavelengths, in terms of process efficiency this combination performs well.

For combinations involving 265 nm and 310 nm, the energy consumption in both SE and SI modes is similar at both intensities, being the energy consumption higher than the 265 nm LEDs acting alone. However, this combination resulted in a synergistic effect and hence counteracts the slight increase in energy consumption with a higher inactivation.

For combinations involving 275 nm and 310 nm, SI mode of irradiation the E_{EO} was calculated to be 0.5 ± 0.1 kWh m^{-3} and 0.41 ± 0.04 kWh m^{-3} at 50% and 100% intensities, respectively. The values of E_{EO} can be seen to be lower than the individual wavelengths acting alone, contrary to observations in 265 nm and 310 nm combinations. On the other hand, in SE mode of irradiation, the energy consumption is higher than the 275 nm LED device acting on its own and as mentioned before, the synergistic effect can compensate for the increase in energy consumption.

Finally, the combination of 3 wavelengths have a lower energy consumption than any of the three wavelengths acting on its own of 0.37 ± 0.02 kWh m^{-3} and 0.29 ± 0.02 kWh m^{-3}, at 50% and 100% intensity, respectively. All four combinations of 3 wavelengths showed significant synergistic effect and their electrical energy consumption per unit order of removal exhibited the lowest rates in comparison with other combinations that yielded synergy.

5.4. Conclusions

The development of UV LEDs in the past decade has led to significant research in water disinfection. The possible synergy between multiple wavelengths in the UV range has been widely debated. Some researchers have concluded the existence of synergy while others have discarded it. This study analyzed the use of three UV light sources with different wavelengths (265, 275 and 310 nm) on the inactivation of *E. coli* bacteria. A fixture to accommodate up to 8 high power light sources has been designed and used in the tests on two set–ups (recirculating batch reactor and single pass reactor). It was seen that the recirculating batch reactor set–up resulted in tailing of the bacterial inactivation curve. This behavior was investigated by varying and analyzing multiple parameters within the set–up to explain the curve obtained, however no conclusive explanation was found. On the other hand, individual disinfection experiments in a single pass, at a flow rate of 2 L min^{-1} and contact time of 0.753 s, confirmed the 265 nm light source to be most effective in the inactivation of *E. coli* (2.8 ± 0.2 log units' reduction), while the 310 nm led to the lowest disinfection (0.0003 ± 0.00008 log units' reduction). Due to the similar inactivation mechanism of wavelength in the 250 – 280 nm ranges, the observed log reduction for 265 nm and 275 nm (2.5 ± 0.3 log units' reduction) were similar within the experimental uncertainty. Also, resulting from a different inactivation mechanism, the 310 nm light source was ineffective in a single pass system due to short contact time. When a combination of the 265/275/310 was used, an average log reduction of 5.41 ± 0.32 was observed versus an average log–reduction of 5.3 ± 0.1 for combination of 265/275. Under combined irradiation experiments, the average log–reductions were similar to the sum of individual log–reductions of the respective wavelengths, for combinations of 265 nm and 275 nm wavelengths attempted. It was seen that the combination of three wavelengths, in any form, resulted in an enhanced disinfection rate. For combinations involving use of 310 nm, a possible synergistic effect was seen. To further evaluate synergistic effect of the wavelengths, a robust statistical analysis using 2 different techniques (*t*–Student and codified ANOVA) was conducted. It was concluded that combinations of 310 nm with 265 nm or 275 nm devices present a significant synergy at both intensities tested for two wavelength combinations. Moreover, all combinations of 3 wavelengths showed a significant synergistic effect. The observed synergistic effect has been correlated to the emission spectra of the respective LEDs to elucidate the possible mechanism of inactivation in combination. Finally, the electrical energy per order of inactivation has been calculated to evaluate if the

synergistic effect is energy efficient as well. Among individual wavelengths, 265 nm LED devices showed the lowest energy consumption per unit order of inactivation corresponding to 0.44 ± 0.05 kWh m^{-3} and 0.30 ± 0.03 kWh m^{-3}, at 50% and 100% UV dose, respectively. It was seen that the combination of 265 nm and 275 nm devices presented a highly energy efficient process. When the synergistic combinations were compared, it was seen that a three–wavelength combination (265/275/310) conferred a low energy consumption process in SI mode of irradiation corresponding to 0.37 ± 0.02 kWh m^{-3} and 0.29 ± 0.02 kWh m^{-3}, at 50% and 100% UV dose, respectively. In SE mode, the combination of 310 nm followed by 265 nm granted the lowest energy consumption with a value of 0.5 ± 0.1 kWh m^{-3} and 0.41 ± 0.05 kWh m^{-3}, at 50% and 100% UV dose from each device, respectively.

This chapter provided a perspective on the application of the designed LED sources for water disinfection using a model bacteria in a buffered water matrix. The following chapter uses the results from this chapter as a baseline and further applies the LED sources to the inactivation of real wastewater treatment plan effluents, evaluating if the observed synergistic effect is also achieved in the same combinations.

Appendix Chapter 5

5.A. FX–1 310 Disinfection

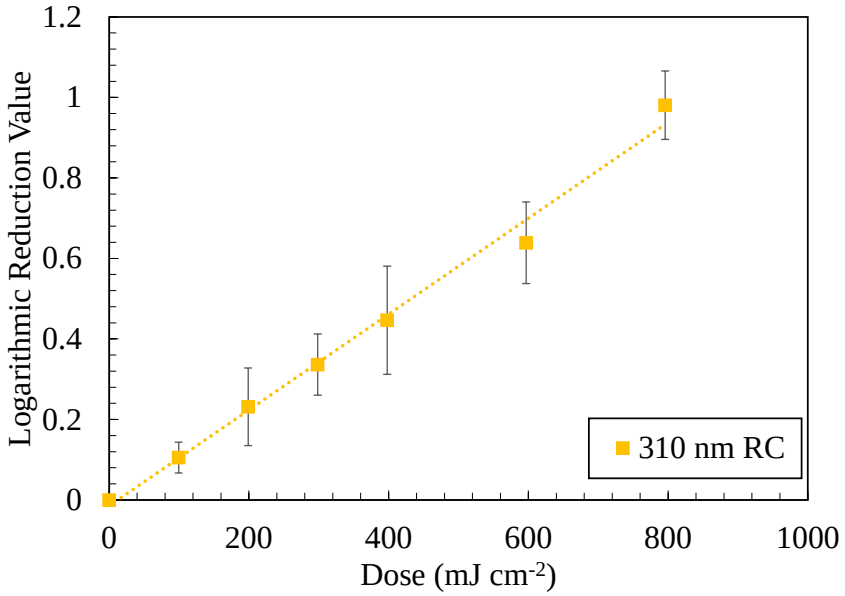

Figure 5.A.1: LRV *vs* UV Dose for 310 nm.

5.B. Inactivation Rate Constants

Table 5.B.1: Inactivation rate constants, k_c (s^{-1}).

UV Source/ Combination	50% intensity	100% intensity
265 nm	2.02 ± 0.15	3.5 ± 0.9
275 nm	1.5 ± 0.5	3.2 ± 0.3
310 nm	0.0005 ± 0.0008	0.0008 ± 0.0002
265|275	3.61 ± 0.32	7.0 ± 0.2
265|310	2.4 ± 0.5	3.9 ± 0.2
275|310	2.4 ± 0.5	4.1 ± 0.6
265|275|310	3.7 ± 0.3	7.2 ± 0.4
265 + 275	3.7 ± 0.4	6.9 ± 0.3
310 + 265	2.4 ± 0.3	3.9 ± 0.3
310 + 275	1.7 ± 0.2	3.5 ± 0.4

5.C. Synergy of Inactivation (in terms of kinetic constants)

Table 5.C.1: Synergy of inactivation at 50% Dose.

UV Source Combination	Theoretical k_c (s^{-1})	Actual k_c (s^{-1})	*Synergy*
265|275	3.5 ± 0.4	3.6 ± 0.3	1.03 ± 0.11
265|310	2.02 ± 0.15	2.4 ± 0.5	1.2 ± 0.2
275|310	1.5 ± 0.4	2.5 ± 0.5	1.6 ± 0.5
265|275|310	3.5 ± 0.4	3.7 ± 0.3	1.06 ± 0.09
265 + 275	3.5 ± 0.4	3.7 ± 0.4	1.06 ± 0.13
310 + 265	2.02 ± 0.15	2.4 ± 0.3	1.17 ± 0.16
310 + 275	1.5 ± 0.4	1.7 ± 0.2	1.13 ± 0.19

Table 5.C.2: Synergy of inactivation at 100% Dose.

UV Source Combination	Theoretical k_c (s^{-1})	Actual k_c (s^{-1})	*Synergy*
265|275	6.71 ± 0.95	7.01 ± 0.14	1.1 ± 0.1
265|310	3.5 ± 0.3	3.91 ± 0.17	1.15 ± 0.08
275|310	3.2 ± 0.3	4.04 ± 0.56	1.3 ± 0.2
265|275|310	6.7 ± 0.9	7.17 ± 0.42	1.07 ± 0.08
265 + 275	6.7 ± 0.9	6.94 ± 0.28	1.04 ± 0.06
310 + 265	3.5 ± 0.3	3.9 ± 0.3	1.09 ± 0.12
310 + 275	3.2 ± 0.3	3.5 ± 0.4	1.07 ± 0.15

5.D. *t*–Student Analysis (in terms of kinetic constants)

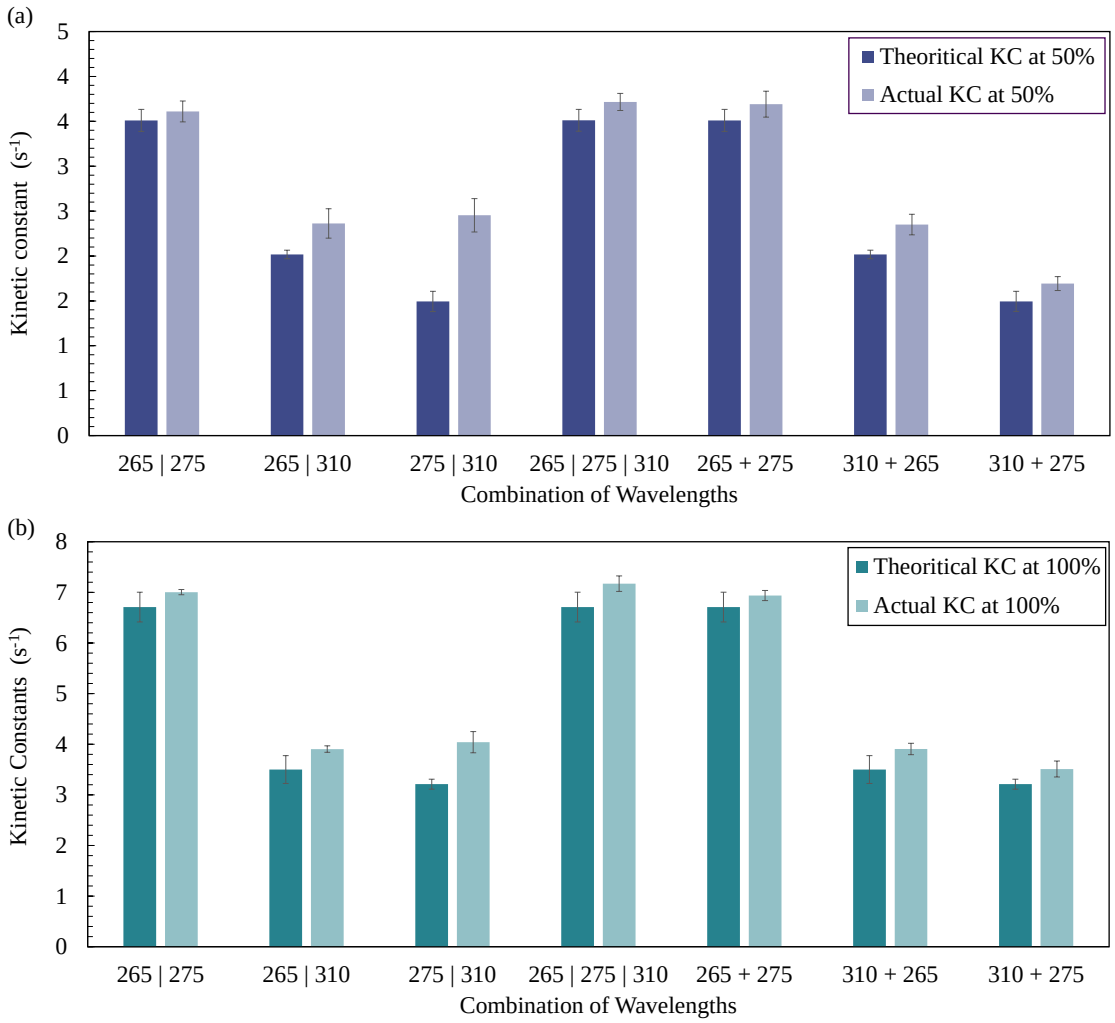

Figure 5.D.1: Comparison between theoretical and actual kinetic constants with error bars representing 95% *CI* for (a) 50% dose and (b) 100% dose.

5.E. Codified ANOVA Results

Note - **|** means simultaneous mode of operation, whereas **+** means sequential mode of operation in the order written. In dual wavelength combinations, standard errors are based on the total error with 68 degrees of freedom (DOF). While for three wavelength combinations, standard errors are based on the total error with 136 DOF.

- Abbreviations in Table – QS = Quadratic Sum, QA = Quadratic Average, STDEV = Standard Deviation
- Font Color Legend – **Significant** and **Not Significant**

5.E.1.Dual Wavelength Combinations

- FX–1 265 and FX–1 275 combinations
  - Simultaneous Irradiation (SI)

Estimated Effect for Y

	50% intensity		100% intensity	
Effect	Estimated	STDEV	Estimated	STDEV
Average	1.395	0.0277	2.646	0.0175
A: 265	1.527	0.0555	2.807	0.0351
B: 275	1.132	0.0555	2.462	0.0351
A **|** B	-0.046	0.0555	0.063	0.0351

Analysis of Variance

Source	DOF	50% intensity				100% intensity			
		QS	QA	F Value	*p*-Value	QS	QA	F Value	*p*-Value
A: 265	1	41.989	41.989	754.69	**0.0000**	139.818	139.818	6375.11	**0.0000**
B: 275	1	23.095	23.095	415.10	**0.0000**	107.554	107.554	4904.01	**0.0000**
A | B	1	0.038	0.038	0.69	**0.4107**	0.071	0.071	3.22	**0.0774**
Error	68	3.783	0.055			1.469	0.021		
Total	71	68.905				245.341			

Parameter	At 50% intensity	At 100% intensity
R^2	94.509%	99.401%
Standard Error of the residuals	0.2358	0.1480
Mean absolute error	0.1689	0.1129

- Sequential Irradiation (SE) – 265 followed by 275.

Estimated Effect for Y

	50% intensity		100% intensity	
Effect	Estimated	STDEV	Estimated	STDEV
Average	1.410	0.0303	2.631	0.0210
A: 265	1.556	0.0607	2.777	0.0420
B: 275	1.162	0.0607	2.432	0.0420
A + B	-0.016	0.0607	0.033	0.0420

Analysis of Variance

Source	DOF	50% intensity				100% intensity			
		QS	QA	F Value	*p*-Value	QS	QA	F Value	*p*-Value
A: 265	1	42.997	42.997	657.37	**0.0000**	138.866	138.866	4368.90	**0.0000**
B: 275	1	23.963	23.963	366.37	**0.0000**	106.500	106.500	3350.60	**0.0000**
A + B	1	0.004	0.004	0.07	**0.7871**	0.019	0.019	0.62	**0.4329**
Error	68	4.382	0.065			2.161	0.031		
Total	71	70.481				247.547			

Parameter	At 50% intensity	At 100% intensity
R^2	93.782%	99.162%
Standard Error of the residuals	0.2557	0.1782
Mean absolute error	0.1743	0.1384

- Sequential Irradiation (SE) – 275 followed by 265.

Estimated Effect for Y

	50% intensity		100% intensity	
Effect	Estimated	STDEV	Estimated	STDEV
Average	1.473	0.0306	2.608	0.0175
A: 275	1.683	0.0612	2.731	0.0351
B: 265	1.288	0.0612	2.386	0.0351
A + B	0.109	0.0612	-0.012	0.0351

Analysis of Variance

Source	DOF	50% intensity				100% intensity			
		QS	QA	F Value	*p*-Value	QS	QA	F Value	*p*-Value
A: 275	1	51.003	51.003	755.31	**0.0000**	134.315	134.31	6026.19	**0.0000**
B: 265	1	29.893	29.893	442.69	**0.0000**	102.519	102.51	4599.61	**0.0000**
A + B	1	0.217	0.217	3.22	**0.0771**	0.002	0.002	0.13	**0.7184**
Error	68	4.591	0.067			1.515	0.022		
Total	71	85.706				238.352			

Parameter	At 50% intensity	At 100% intensity
R^2	94.6424%	99.3641%
Standard Error of the residuals	0.2558	0.1492
Mean absolute error	0.1833	0.1149

- FX–1 310 and FX–1 265 combinations

- Simultaneous Irradiation (SI)

Estimated Effect for Y

	50% intensity		100% intensity	
Effect	Estimated	STDEV	Estimated	STDEV
Average	0.854	0.0241	1.451	0.0120
A: 265	1.665	0.0483	2.860	0.0241
B: 310	0.049	0.0483	0.073	0.0241
A | B	0.091	0.0483	0.115	0.0241

Analysis of Variance

Source	DOF	50% intensity				100% intensity			
		QS	QA	F Value	*p*-Value	QS	QA	F Value	*p*-Value
A: 265	1	49.918	49.918	1186.28	**0.0000**	147.240	147.240	14054.7	**0.0000**
B: 310	1	0.044	0.0441	1.05	**0.3095**	0.097	0.097	9.28	**0.0033**
A | B	1	0.152	0.152	3.62	**0.0614**	0.240	0.241	22.99	**0.0000**
Error	68	2.861	0.042			0.712	0.010		
Total	71	52.976				148.29			

Parameter	At 50% intensity	At 100% intensity
R^2	94.598%	99.519%
Standard Error of the residuals	0.2051	0.1023
Mean absolute error	0.1102	0.0679

- Sequential Irradiation (SE) – 310 followed by 265.

Estimated Effect for Y

	50% intensity		100% intensity	
Effect	Estimated	STDEV	Estimated	STDEV
Average	0.833	0.0151	1.443	0.0168
A: 265	1.623	0.0303	2.844	0.0336
B: 310	0.106	0.0303	0.057	0.0336
A + B	0.148	0.0303	0.100	0.0336

Analysis of Variance

Source	DOF	50% intensity				100% intensity			
		QS	QA	F Value	*p*-Value	QS	QA	F Value	*p*-Value
A: 265	1	47.416	47.416	2859.75	**0.0000**	145.638	145.638	7141.09	**0.0000**
B: 310	1	0.203	0.203	12.30	**0.0008**	0.060	0.060	2.96	**0.0899**
A + B	1	0.397	0.397	23.97	**0.0000**	0.180	0.180	8.84	**0.0041**
Error	68	1.127	0.016			1.386	0.020		
Total	71	49.145				147.266			

Parameter	At 50% intensity	At 100% intensity
R^2	97.705%	99.058%
Standard Error of the residuals	0.1287	0.1428
Mean absolute error	0.0772	0.0912

- Sequential Irradiation (SE) – 265 followed by 310.

Estimated Effect for Y

	50% intensity		100% intensity	
Effect	Estimated	STDEV	Estimated	STDEV
Average	0.750	0.0084	1.335	0.0114
A: 265	1.457	0.0168	2.628	0.0228
B: 310	-0.059	0.0168	-0.158	0.0228
A + B	-0.017	0.0168	-0.116	0.0228

Analysis of Variance.

Source	DOF	50% intensity				100% intensity			
		QS	QA	F Value	*p*-Value	QS	QA	F Value	*p*-Value
A: 265	1	38.225	38.225	7495.70	**0.0000**	124.343	124.343	13259.1	**0.0000**
B: 310	1	0.063	0.063	12.43	**0.0008**	0.450	0.450	48.08	**0.0000**
A + B	1	0.005	0.005	1.04	**0.3113**	0.242	0.242	25.87	**0.0000**
Error	68	0.346	0.005			0.637	0.009		
Total	71	38.640				125.674			

Parameter	At 50% intensity	At 100% intensity
R^2	99.102%	99.492%
Standard Error of the residuals	0.0741	0.0968
Mean absolute error	0.0483	0.0633

- FX–1 310 and FX–1 275 combinations

Simultaneous Irradiation (SI)

Estimated Effect for Y

	50% intensity		100% intensity	
Effect	Estimated	STDEV	Estimated	STDEV
Average	0.798	0.0278	1.421	0.0220
A: 275	1.553	0.0556	2.794	0.0441
B: 310	0.332	0.0556	0.353	0.0441
A | B	0.374	0.0556	0.399	0.0441

Analysis of Variance

Source	DOF	50% intensity				100% intensity			
		QS	QA	F Value	*p*-Value	QS	QA	F Value	*p*-Value
A: 275	1	43.430	43.430	779.43	**0.0000**	140.561	140.561	4008.79	**0.0000**
B: 310	1	1.985	1.985	35.63	**0.0000**	2.243	2.243	63.97	**0.0000**
A | B	1	2.525	2.525	45.32	**0.0000**	2.877	2.877	82.07	**0.0000**
Error	68	3.788	0.055			2.384	0.035		
Total	71	51.729				148.066			

Parameter	At 50% intensity	At 100% intensity
R^2	92.675%	98.389%
Standard Error of the residuals	0.2360	0.1872
Mean absolute error	0.1484	0.1140

Sequential Irradiation (SE) – 310 followed by 275.

Estimated Effect for Y

	50% intensity		100% intensity	
Effect	Estimated	STDEV	Estimated	STDEV
Average	0.550	0.0136	1.051	0.0162
A: 275	1.112	0.0272	2.116	0.0324
B: 310	0.102	0.0272	0.132	0.0324
A + B	0.089	0.0272	0.120	0.0324

Analysis of Variance

Source	DOF	50% intensity				100% intensity			
		QS	QA	F Value	*p*-Value	QS	QA	F Value	*p*-Value
A: 275	1	22.275	22.275	1669.45	**0.0000**	80.600	80.600	4243.77	**0.0000**
B: 310	1	0.187	0.187	14.07	**0.0004**	0.317	0.317	16.71	**0.0001**
A + B	1	0.144	0.144	10.80	**0.0016**	0.259	0.259	13.65	**0.0004**
Error	68	0.907	0.013			1.291	0.018		
Total	71	23.514				82.468			

Parameter	At 50% intensity	At 100% intensity
R^2	96.141%	98.433%
Standard Error of the residuals	0.1155	0.1378
Mean absolute error	0.0743	0.0859

- Sequential Irradiation (SE) – 275 followed by 310.

Estimated Effect for Y

	50% intensity		100% intensity	
Effect	Estimated	STDEV	Estimated	STDEV
Average	0.588	0.0178	1.283	0.0219
A: 275	1.129	0.0357	2.522	0.0438
B: 310	-0.091	0.0357	0.081	0.0438
A + B	-0.044	0.0357	0.123	0.0438

Analysis of Variance

Source	DOF	50% intensity				100% intensity			
		QS	QA	F Value	*p*-Value	QS	QA	F Value	*p*-Value
A: 275	1	22.967	22.967	999.68	**0.0000**	114.559	114.559	3314.80	**0.0000**
B: 310	1	0.150	0.150	6.53	**0.0128**	0.119	0.119	3.45	**0.0677**
A + B	1	0.035	0.035	1.54	**0.2189**	0.274	0.274	7.95	**0.0063**
Error	68	1.562	0.022			2.350	0.034		
Total	71	24.715				117.303			

Parameter	At 50% intensity	At 100% intensity
R^2	93.678%	97.996%
Standard Error of the residuals	0.1515	0.1859
Mean absolute error	0.0919	0.1147

5.E.2. Three Wavelength Combinations

- Simultaneous Irradiation

Estimated Effect for Y

	50% intensity		100% intensity	
Effect	Estimated	STDEV	Estimated	STDEV
Average	1.514	0.0203	2.785	0.0149
A: 265	0.167	0.0406	0.174	0.0298
B: 275	-0.115	0.0406	-0.107	0.0298
C: 310	1.589	0.0406	2.934	0.0298
AB: 265 | 275	-0.232	0.0406	-0.129	0.0298
AC: 265 | 310	-0.009	0.0406	0.022	0.0298
BC: 275 | 310	0.103	0.0406	0.086	0.0298
ABC: 265 | 275 | 310	1.165	0.0406	2.462	0.0298

- Analysis of Variance

Source	DOF	50% intensity				100% intensity			
		QS	QA	F Value	*p*-Value	QS	QA	F Value	*p*-Value
A: 265	1	1.007	1.007	16.92	**0.0001**	1.094	1.094	34.06	**0.0000**
B: 275	1	0.478	0.478	8.04	**0.0053**	0.415	0.415	12.95	**0.0004**
C: 310	1	90.929	90.929	1527.30	**0.0000**	309.9	309.9	9645.97	**0.0000**
AB	1	1.938	1.938	32.57	**0.0000**	0.607	0.607	18.92	**0.0000**
AC	1	0.003	0.003	0.05	**0.8293**	0.018	0.018	0.59	**0.4453**
BC	1	0.383	0.383	6.44	**0.0123**	0.267	0.267	8.32	**0.0046**
ABC	1	48.876	48.876	820.96	**0.0000**	218.38	218.38	6797.51	**0.0000**
Error	136	8.096	0.059			4.369	0.032		
Total	143	151.714				535.06			

Parameter	At 50% intensity	At 100% intensity
R^2	94.663%	99.183%
Standard Error of the residuals	0.2440	0.1792
Mean absolute error	0.1659	0.1207

- Sequential + Simultaneous Irradiation (SS)

Note – For SS mode of irradiation, the standard error values are based on the total error with 88 DOF.

SS – 265 followed by 275 | 310.

Estimated Effect for Y

	50% intensity		100% intensity	
Effect	Estimated	STDEV	Estimated	STDEV
Average	1.470	0.0226	2.687	0.0152
A: 265	0.156	0.0452	0.250	0.0304
B: 275	-0.208	0.0452	-0.263	0.0304
C: 310	1.519	0.0452	2.739	0.0304
AB: 265 + 275	-0.085	0.0452	-0.092	0.0304
AC: 265 + 310	-0.065	0.0452	0.098	0.0304
BC: 275 | 310	0.047	0.0452	-0.069	0.0304
ABC: 265 + 275 | 310	1.303	0.0452	2.500	0.0304

- Analysis of Variance

Source	DOF	50% intensity				100% intensity			
		QS	QA	F Value	*p*-Value	QS	QA	F Value	*p*-Value
A: 265	1	0.590	0.590	12.00	**0.0008**	2.258	2.258	67.50	**0.0000**
B: 275	1	1.041	1.041	21.17	**0.0000**	2.492	2.492	74.49	**0.0000**
C: 310	1	55.413	55.413	1126.04	**0.0000**	270.14	270.14	8072.70	**0.0000**
AB	1	0.175	0.175	3.56	**0.0624**	0.310	0.310	9.26	**0.0028**
AC	1	0.103	0.103	2.10	**0.1504**	0.352	0.352	10.54	**0.0015**
BC	1	0.053	0.053	1.09	**0.2997**	0.173	0.173	5.19	**0.0242**
ABC	1	40.750	40.750	828.09	**0.0000**	225.02	225.02	6724.22	**0.0000**
Error	88	4.330	0.049			4.551	0.033		
Total	95	102.459				505.30			

Parameter	At 50% intensity	At 100% intensity
R^2	95.773%	99.099%
Standard Error of the residuals	0.2218	0.1829
Mean absolute error	0.1296	0.1237

SS – 275 followed by 265 | 310.

Estimated Effect for Y

	50% intensity		100% intensity	
Effect	Estimated	STDEV	Estimated	STDEV
Average	1.472	0.0214	2.621	0.0121
A: 275	-0.120	0.0428	-0.068	0.0243
B: 265	-0.056	0.0428	0.110	0.0243
C: 310	1.522	0.0428	2.605	0.0243
AB: 265 + 275	0.107	0.0428	0.003	0.0243
AC: 275 + 310	-0.342	0.0428	-0.220	0.0243
BC: 265 | 310	0.198	0.0428	0.304	0.0243
ABC: 275 + 265 | 310	1.495	0.0428	2.596	0.0243

- Analysis of Variance

Source	DOF	50% intensity				100% intensity			
		QS	QA	F Value	*p*-Value	QS	QA	F Value	*p*-Value
A: 275	1	0.346	0.346	7.87	**0.0062**	0.170	0.170	7.96	**0.0055**
B: 265	1	0.077	0.077	1.76	**0.1880**	0.440	0.440	20.59	**0.0000**
C: 310	1	55.655	55.655	1262.41	**0.0000**	244.48	244.48	11435.4	**0.0000**
AB	1	0.276	0.276	6.28	**0.0141**	0.000	0.00	0.02	**0.8939**
AC	1	2.819	2.819	63.94	**0.0000**	1.746	1.746	81.68	**0.0000**
BC	1	0.947	0.947	21.50	**0.0000**	3.332	3.332	155.86	**0.0000**
ABC	1	53.704	53.704	1218.15	**0.0000**	242.64	242.64	11349.4	**0.0000**
Error	88	3.879	0.0440			2.9076	0.021		
Total	95	117.708				495.72			

Parameter	At 50% intensity	At 100% intensity
R^2	96.704%	99.413%
Standard Error of the residuals	0.2099	0.1462
Mean absolute error	0.1380	0.1046

SS – 310 followed by 265 | 275.

Estimated Effect for Y

	50% intensity		100% intensity	
Effect	Estimated	STDEV	Estimated	STDEV
Average	1.448	0.0193	2.690	0.0144
A: 265	0.057	0.0386	0.000	0.0288
B: 275	0.093	0.0386	-0.023	0.0288
C: 310	1.474	0.0386	2.744	0.0288
AB: 265 | 275	-0.118	0.0386	-0.030	0.0288
AC: 265 + 310	-0.164	0.0386	-0.151	0.0288
BC: 275 + 310	0.349	0.0386	0.170	0.0288
ABC: 310 + 265 | 275	1.270	0.0386	2.562	0.0288

- Analysis of Variance

Source	DOF	50% intensity				100% intensity			
		QS	QA	F Value	*p*-Value	QS	QA	F Value	*p*-Value
A: 265	1	0.080	0.080	2.24	**0.1380**	5.8E-7	5.8E-7	0.00	**0.9965**
B: 275	1	0.211	0.211	5.88	**0.0173**	0.019	0.019	0.65	**0.4200**
C: 310	1	52.206	52.206	1455.68	**0.0000**	271.09	271.09	9066.83	**0.0000**
AB	1	0.334	0.334	9.33	**0.0030**	0.032	0.032	1.09	**0.2973**
AC	1	0.650	0.650	18.14	**0.0001**	0.824	0.824	27.58	**0.0000**
BC	1	2.929	2.929	81.69	**0.0000**	1.044	1.044	34.94	**0.0000**
ABC	1	38.736	38.736	1080.09	**0.0000**	236.43	236.43	7907.66	**0.0000**
Error	88	3.156	0.035			4.0664	0.0299		
Total	95	98.305				513.52			

Parameter	At 50% intensity	At 100% intensity
R^2	96.789%	99.208%
Standard Error of the residuals	0.1893	0.1729
Mean absolute error	0.1185	0.1176

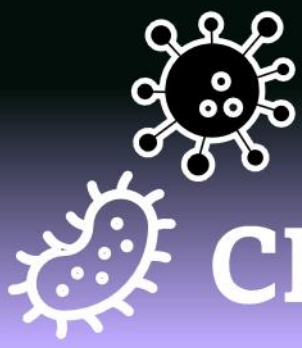

CHAPTER 6

WASTEWATER DISINFECTION

6.1. Introduction

Wastewater is any water that has been used and discarded by humans, typically as a result of domestic, commercial or industrial activities [78]. This discarded water may contain a wide range of impurities, including human and animal waste, food waste, and other harmful pollutants [79]. Wastewater can come from different sources like – *Domestic* – generated by households and includes waste from toilets, sinks, showers, etc.; *Industrial* – generated by industrial processes and contains a variety of pollutants such as metals, solvents etc.; and *Agricultural* – generated in farms and contains fertilizers, pesticides, and animal waste [314]. Wastewater is generally treated to remove impurities and pollutants before it is discharged into the environment either for reuse or to prevent harm to the environment. The treatment process depends on the characteristics of the wastewater and the regulations (local, national, and international) [314, 315].

Characterization of the wastewater plays a crucial role in selecting the treatment process and designing an effective treatment plant [316]. This step involves analyzing the physical, chemical, and biological properties of the matrix to determine its composition and quality. The process of characterization is done in several steps. Sampling is the first step in characterizing wastewater and involves collecting a representative sample at different times and locations to ensure that the sample takes the overall wastewater stream into account [315, 317]. Following sampling, physical analysis of the wastewater is done by parameters such as temperature, color, odor, turbidity, and pH. Chemical analysis is then conducted, measuring the concentration of various compounds in the water like nitrogen, phosphorous, and organic matter. These steps provide information on the composition and quality of wastewater [318].

The treatment of wastewater involves several stages, each of which is designed to remove specific types of contaminants from the water [315, 316]. The specific treatment process will depend on the characteristics. A general process is – pre–treatment followed by primary, secondary, and tertiary treatment [315]. In the pre–treatment stage, the larger solids and debris are removed using physical processes such as screening, grit removal, and sedimentation [314]. This helps protect the downstream processes from clogging and damage. Primary treatment involves the process of settling to remove suspended solids and reduce the organic load of the water. Secondary treatment involves the biological processes to further remove dissolved organic matter and nutrients from the water. The wastewater is

mixed with bacteria in aeration tanks wherein the bacteria consume organic matter and produce flocs that settle out of water in clarifiers. Tertiary treatment is an additional final stage of the process, in some cases, wherein there is a requirement to remove specific pollutants such as nitrogen or phosphorus or to disinfect the water for its safe reuse or disposal. This involves additional processes such as UV irradiation or chlorination [314-319].

It is well known that UV light has been used for disinfection since the start of the 20th century. However, interestingly, it was not until the 1980s and 1990s that UV disinfection rose above the ranks for use in wastewater treatment [33, 34, 108, 320]. In the early days, LP and MP mercury lamps were the most common type of UV lamps used for treatment. More recently, the use of UV LEDs has been the focus of research in wastewater treatment. In the field of wastewater, one of the earliest studies on wastewater treatment using multiple technologies was in 2003, by Caretti et al. [321]. The study investigated the use of UV light combined with peracetic acid for disinfection of wastewater. The study concluded that using both technologies together did not enhance the disinfection process. Since then, studies using multiple wavelengths or multiple technologies for disinfection of wastewater have progressed rapidly [321]. Kang et al. (2019) applied 222 nm KrCl lamp combined with a 254 nm LP mercury lamp on wastewater disinfection and found that synergistic bactericidal effect was produced by a series of chain reactions from inactivation of ROS enzymes leading to synergistic cell membrane damage [322]. Wastewater is a cause of serious concern for government and communities across the world and while there has been significant progress in research using other techniques, the number of studies on use of UV LEDs to treat wastewater, specifically multiple wavelengths has been seen to be limited [108, 322]. Wastewater disinfection is important for several reasons including, but not limited to, protecting public health and the environment [314]. Disinfection is a requirement for wastewater reuse purposes as per the RD1620/2007 and the updated regulation (EU) 2020/741 of the European parliament and of the council on minimum requirements for water reuse [323]. Multiple technologies have successfully disinfected wastewater and evaluated potential transformation products [324-326], however, studies on use of multiple wavelengths for effective disinfection of wastewater has been limited. UV light is known for its power to inactivate and kill bacteria, viruses, and parasites that could harm humans (Chapter 1, Section 1.4) and hence it is important that there a much more studies in this field.

Therefore, the following chapter studies the use of multiple wavelengths on the treatment of secondary effluent obtained from the WWTP at URJC facilities. The wastewater is primarily from the toilets and restaurant facilities at URJC. Similar to Chapter 5, the study explores the effect of each wavelength on disinfection of wastewater and further utilizes the sources for combined irradiation disinfection experiments. This chapter also analyses water quality parameters like pH, conductivity, and transmittance, and ensures that it is consistent throughout the course of experiments. It uses statistical analysis to check for the significance of the observed data to determine if there is a synergistic effect between the multiple wavelengths under study.

6.2. Methodology

Basic procedural (plating, set–up) and analytical steps (kinetic constants, synergy of inactivation, error propagation, statistical analysis, and electrical energy consumption) for evaluating germicidal effectiveness of the sources on wastewater matrixes is similar to the methodology employed in Chapter 5. The differences between the two studies have been discussed in the following sections.

6.2.1. Test Wastewater

The wastewater (WW) matrix used for this study was from the secondary effluent of the wastewater treatment plant (WWTP) at Universidad Rey Juan Carlos facilities (URJC, Mostoles, Spain). 2 L of secondary effluent have been extracted for each experiment and spiked to a known concentration with wild *E. coli* isolated from the plant. The WWTP at URJC undergoes three treatment processes.

Primary treatment of the wastewater is a physio–chemical process where the solids are eliminated by coagulation/flocculation, decantation, and flotation. The secondary treatment process involves the elimination of dissolved and colloidal organic matter in the wastewater by biological treatments in rotary biological contactors. Tertiary treatment involves filtration in sand filtration followed by UV disinfection and chlorination. For this study, the effluent has been extracted before UV disinfection process. Fig. 6.1 shows the WWTP at Centro de Apoyo Tecnológico URJC.

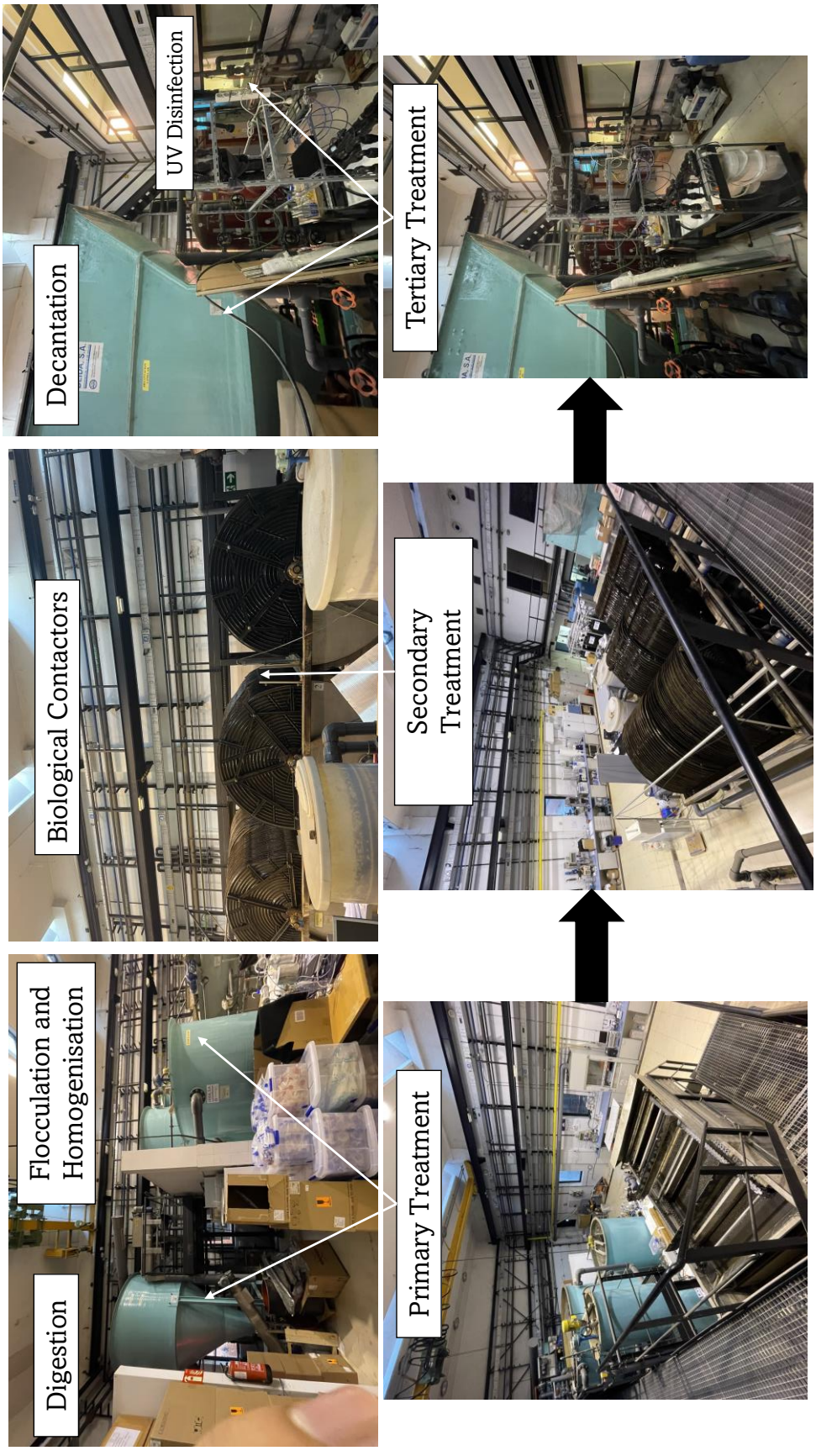

Figure 6.1: WWTP at URJC facilities, Spain.

6.2.2. Microorganism Propagation and Enumeration

Wild *E. coli* has been isolated from the influent of the WWTP. A sample was added to a MacConkey agar plate (selective agar for *E. coli*, Condalab [327]) and incubated inverted for 24 h at 37°C. Then, 4 – 8 colonies of the bacteria were obtained and spiked in 20 mL of culture media corresponding to Luria–Bertani (LB) broth (Scharlab, 020–384 [274]), for growth under stirring at 100 rpm for 24 h at 37°C in an incubator, until a concentration of 10^9 CFU/mL was obtained. 5 mL of the broth solution were then centrifuged (Orto Alresa, Minicen [276]) at 3500 rpm for 25 min. The cells were washed off the LB broth and resuspended in 0.9% NaCl solution prior to the dilution of 2 mL into 2 L of wastewater, to reach an initial concentration of 10^6 CFU/mL.

For enumeration, irradiated samples were serially diluted in 0.9% NaCl solution before plating in Tryptic Soy Agar (TSA) (Scharlab, [328]) plates. Drops of 10 µL were spread on TSA agar and incubated inverted at 37°C for 48 h. Samples were plated in triplicates. Plates yielding 10 to 100 colonies were included in the analysis (Representation can be found in Fig. 5.1, Chapter 5). The wastewater matrix used for this study was spiked with wild *E. coli* mainly because it was seen that the initial concentration of aerobic bacteria existing in the matrix, initially, was low (10^2 CFU/mL). Although the wastewater matrix is spiked with wild *E. coli*, the interest of this study was to track total aerobic microorganisms (Total Microbial Aerobic Count) present in the matrix. Therefore, total aerobic bacteria have been tracked in these experiments corresponding mainly to spiked wild *E. coli* [329].

6.2.3. UV Combinations

Like in Chapter 5, multiple combinations of the chosen light sources have been tested. Fig. 6.2 represents the different combinations attempted in this study. The selection of combinations is based on the observations in Chapter 5 i.e., certain combinations and arrangements showed significantly better germicidal effectiveness and some modes of irradiations behaved similarly. To this note, in this study, the effect of arrangements (Section 5.3.6, Chapter 5) and sequential + simultaneous mode of irradiation (Section 5.3.5.3, Chapter 5) have not been studied (Fig. 5.3 (d)).

To refresh the meaning of each combination, IW mode (Fig. 6.2 (a)) involves the use of only one device on the UV fixture. SE mode (Fig. 6.2 (b)) involves the irradiation of 2 wavelengths, at the same time but one after the other, on the water flowing through the

system. In SE mode of irradiation, note – the order of irradiation is as represented in Fig. 6.2 (b) (for instance – 310 nm followed by 265 nm).

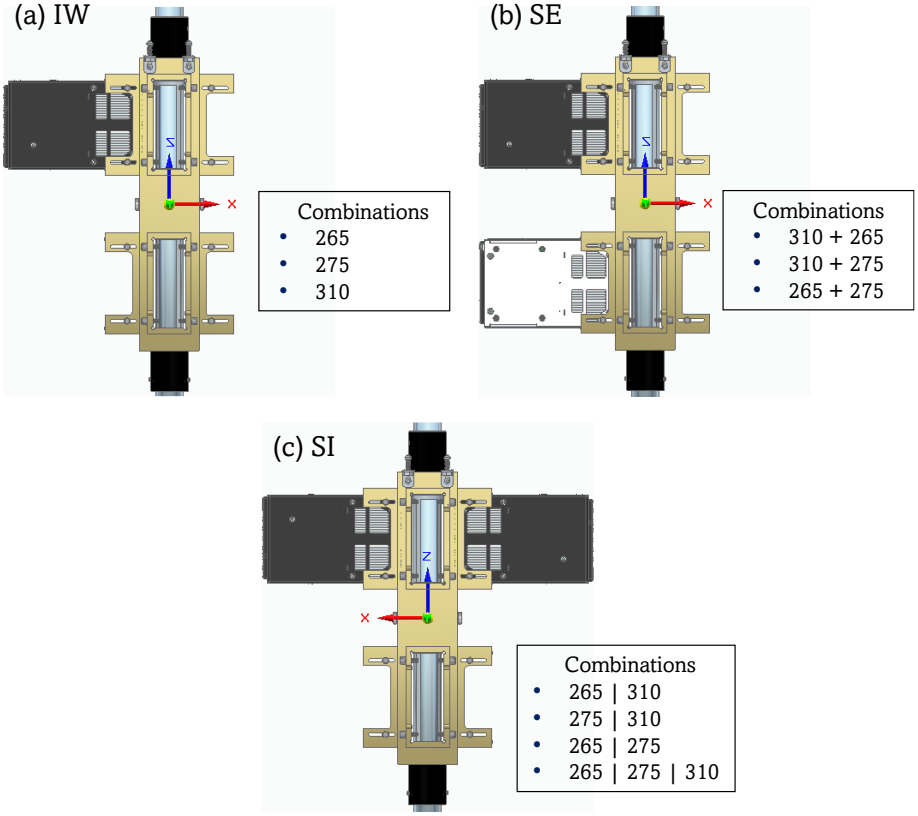

Figure 6.2: Possible combinations on UV fixture – (a) Individual wavelengths (IW), (b) Sequential Mode (SE), and (c) Simultaneous Mode (SI).

6.2.4. Water Quality Characterization

For wastewater, before conducting experiments, it is crucial to evaluate the quality of water being used. Water quality parameters include physical, chemical, and biological parameters such as temperature, turbidity, dissolved oxygen, biochemical oxygen demand (BOD), chemical oxygen demand (COD), nutrients (such as nitrogen and phosphorus) etc., [329, 330]. The measurement of such parameters provide valuable information about the quality of water and inputs regarding the effectiveness of the treatment process. Four water quality parameters have been selected and characterized for the water used in this study: pH, conductivity, UV transmittance, and TOC.

The pH of wastewater is a critical parameter that directly affects the efficiency of treatment process. The optimal pH range for most processes is typically between 6 and 9, and any deviations from this range could negatively impact the process [314]. For this reason, the

pH of input water was monitored during the course of experiments. The pH was measured using benchtop pH meter (pH 50 VioLab, Dostmann [331]). Conductivity is a measure of the ability of water to conduct electrical current and it is related to the total dissolved solids (TDS) content of the wastewater matrix. High conductivity can indicate the presence of dissolved salts like chlorides and sulfates, that can be harmful to the environment and human health [324]. Conductivity of the input wastewater was measured using a conductometer (712 conductometer, Metrohm [332]). Finally, transmission of UV light through the matrix is another parameter that can directly affect UV disinfection process. Measurement of the transmission is important as it provides information about the clarity or turbidity of the water [324]. Transmission of wastewater was measured using a UV–Vis–NIR Spectrophotometer (Cary 5000, Agilent [333])

Concentration of TOC is a measure of the level of organic molecules or contaminants in water. This is an analytical technique that helps understand whether the water is pure enough for further discharge or, in this case, for further studies. Total organic carbon is any organic matter or carbon–based contaminants in untreated water [329, 334]. This parameter is affected by multiple variables including, but not limited to, climate, transport, vegetation, human activity etc. TOC is used to monitor the overall levels of organic compounds present in the water matrix under study. A TOC analyzer measures total carbon (TC), inorganic carbon (IC), TOC, purgeable organic carbon (POC) and non-purgeable organic carbon (NPOC) [335, 336]. It is well known that the presence of organic matter can affect UV disinfection process and hence it is important to measure the TOC levels of the effluent under study. To ensure that the wastewater effluent has a low level of TOC, 20 mL of the effluent was filtered using a 0.20 µm nylon membrane (Millex – GN, Merck Millipore [337]) and placed in TOC–L (TOC analyzer, Shimadzu [338]) for measurement. All the analyses were repeated a minimum of 3 times per sample and monitored throughout the period of experimentation.

6.2.5. Statistical Analysis

The synergy of inactivation has been calculated using Eq. 5.5 (Chapter 5). The statistical analysis to test the significance of effect of multiple wavelengths has been conducted using *t*–Student analysis (Section 5.2.7.1, Chapter 5) and Codified ANOVA (Section 5.2.7.2, Chapter 5) for this study.

6.3. Results and Discussions

6.3.1. Water Quality

The pH of wastewater used in this study was found to be 7.5 ± 0.1 meaning that the water is neutral and within the optimal range required for disinfection process. Similarly, the conductivity of the water was measured to be 752 ± 4 μS cm^{-1}, which indicates a mid–range conductivity (200 – 1000 μS cm^{-1}) prominent in wastewaters from facilities [324]. Fig. 6.3 plots the measured transmittance of the wastewater between a wavelength range of 200 – 400 nm. It is important to note that the transmittance was measured between 200 – 1200 nm, however, it has been plotted considering that UV range of this measurement is the specific interest in this study. The transmittance, at the peak wavelength, was seen to be 99.37%, 99.95%, and 100%, for FX–1 265, 275, and 310 respectively.

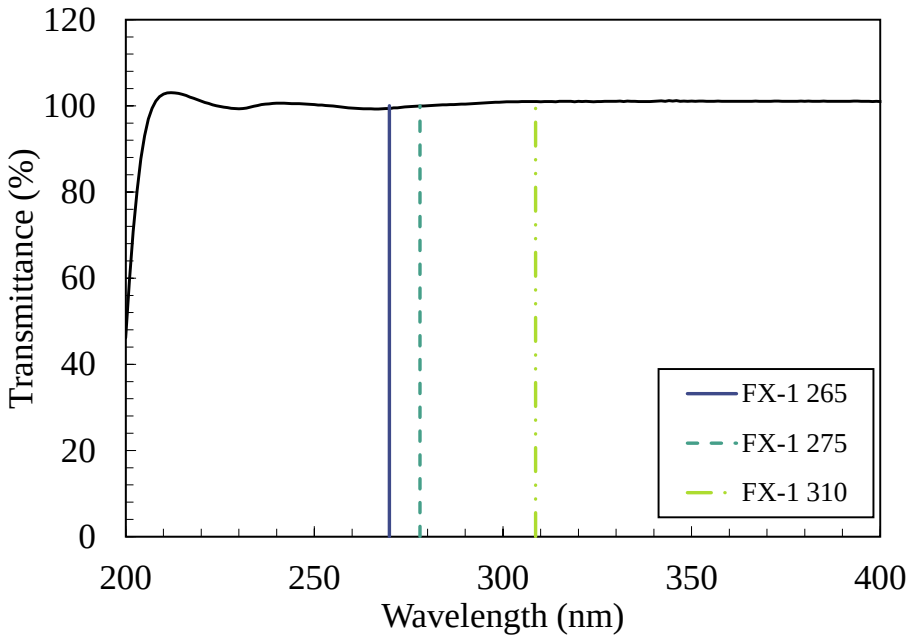

Figure 6.3: Transmittance of the wastewater between 200 – 400 nm.

Measurement of TOC helps in monitoring the level of organic matter within the wastewater matrix used. A constant TOC reading can indicate that the process is operating consistently over time. This can be important in ensuring the quality and safety of the effluent for release into environment [315, 339, 340]. A constant TOC reading also indicates the presence of a persistent organic contaminant and helps ensure that successive experiments are repeatable and reproducible [340]. For the period of time of the experiments in this study, the TOC in the matrix was measured to be 23.3 ± 3.3 mg L^{-1}. The TOC level was also monitored before

and after irradiation experiments and was seen that the readings were within the instrumental error of the equipment and there was no significant reduction in TOC readings (± 5%). In the literature, it has been noted that UV–C light can break down organic compounds in water and wastewater through photolysis [341]. However, the effectiveness of the UV–C light in reducing TOC levels may depend on various factors such as initial TOC concentrations, the type of organic compounds in the matrix, and the system designed [342, 343]. As the interest of this study was to investigate a possible synergistic effect on disinfection, no further analysis of these parameters have been conducted.

6.3.2. UV Inactivation by Individual Wavelengths in Wastewater

The effect of each wavelength on disinfection of wastewater has been presented in Fig. 6.4. Similar to the findings in Chapter 5, FX–1 265 showed the highest log–inactivation at low UV doses when compared to the other two wavelengths. At ~25 mJ cm^{-2}, the germicidal effectiveness of the devices tested follows the order of LRV (265) > LRV (275) > LRV (310).

Comparing the results in Chapter 5 to these results showed that wild *E. coli* may be more UV resistant compared to *E. coli* K12. While, in wastewater matrix the log–inactivation obtained at 100% intensity of FX–1 265 was 2.2 ± 0.2, the buffered matrix resulted in a log inactivation of 2.8 ± 0.2. It is worth noting here that, although the bacteria was spiked to the effluent, there exist other microorganisms that compete with the wild *E. coli* for the light and could affect the inactivation rate. Table 6.1 lists the LRVs for each other devices studied. Note that the FX–1 310 inactivation rates are based on calculated log–reductions per pass. Single pass experiments did not result in significant and dependable log inactivation. The data on recirculating inactivation experiment, until 1–log reduction, can be found in Appendix 6.A.

Table 6.1: LRV for individual wavelength disinfection of wastewater.

UV Source	Average LRV (50% Dose)	Average LRV (100% Dose)	R^2	k_d (cm^2 mJ^{-1})	k_d (cm^2 mJ^{-1}) (*E. coli* K12)
FX–1 265	1.2 ± 0.1	2.2 ± 0.2	0.9957	0.0815	0.1047
FX–1 275	1.1 ± 0.2	1.9 ± 0.1	0.9986	0.0508	0.0627
FX–1 310	0.0002 ± 2.52 × 10^{-5}	0.0003 ± 7.03 × 10^{-5}	0.9862	8 × 10^{-6}	2 × 10^{-5}

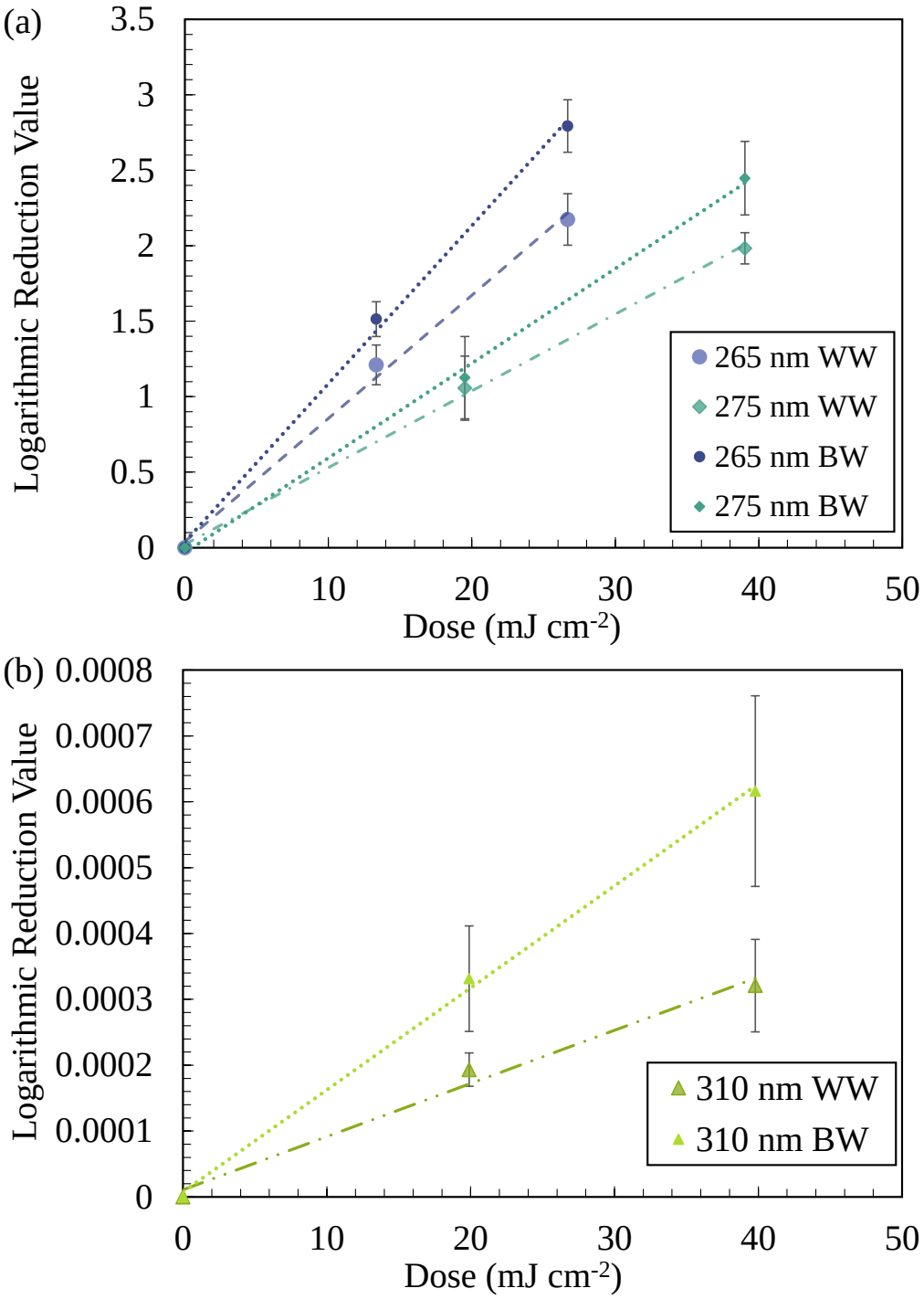

Figure 6.4: LRV *vs* UV dose for (a) FX–1 265, 275 and (b) FX–1 310, in comparison with buffered water spiked with model bacteria (*E. coli* K12, Chapter 5) (Legend – WW = Wastewater and BW = Buffered Water).

6.3.3. UV Inactivation by Combination of Wavelengths in Wastewater

Fig. 6.5 (a) plots the reduction in aerobic bacterial concentration against the UV dose received by the matrix. It must be noted that the order of exposure in the graph legend corresponds to the actual order of irradiation in the set–up i.e., 310 + 265 corresponds to exposure of FX–1 310 followed by FX–1 265. In the case of wastewater matrix, the other arrangement has not been investigated as it was seen in buffered water (Chapter 5) that the exposure of FX–1 265/275, first, followed by FX–1 310 resulted in a lower inactivation rate. In SE mode of irradiation, the order of inactivation was similar to as seen in the buffered water i.e., at ~60 mJ cm^{-2}, LRV (265 + 275) > LRV (310 + 265) > LRV (310 + 275). Table 6.2 lists the inactivation rates of each of the combinations discussed alongside a comparison between the k_d values (in cm^2 mJ^{-1}) of wild *E. coli* (Wastewater) and *E. coli* K12 (Buffered water, Chapter 5).

Table 6.2: LRV at different UV doses for each combination.

UV Combination	Average LRV (50% Dose)	Average LRV (100% Dose)	R^2	k_d (cm^2 mJ^{-1})	k_d (cm^2 mJ^{-1}) (*E. coli* K12)
265 + 275	2.3 ± 0.3	4.3 ± 0.2	0.9984	0.0650	0.0796
310 + 265	1.4 ± 0.2	2.4 ± 0.1	0.9903	0.0367	0.0443
310 + 275	1.20 ± 0.07	2.2 ± 0.3	0.9981	0.0284	0.0336
265 | 275	2.2 ± 0.2	4.1 ± 0.3	0.9990	0.0623	0.0804
275 | 310	1.3 ± 0.2	2.2 ± 0.2	0.9913	0.0277	0.0387
265 | 310	1.5 ± 0.1	2.5 ± 0.2	0.990	0.0380	0.0443
265 | 275 | 310	2.6 ± 0.4	4.4 ± 0.2	0.9873	0.0417	0.0513

In SI mode of irradiation (Fig. 6.5 (b)), the order of inactivation was as expected i.e., at ~60 mJ cm^{-2}, LRV (265 | 275) > LRV (265 | 275 | 310) >LRV (265 | 310) > LRV (275 | 310). Similar to the observations in Section 5.3.5.2 (Chapter 5). the combination of 3 wavelengths resulted in similar inactivation as that of 265 | 275 combination. The combination of 3 wavelengths required 60% more dose compared to the other combination.

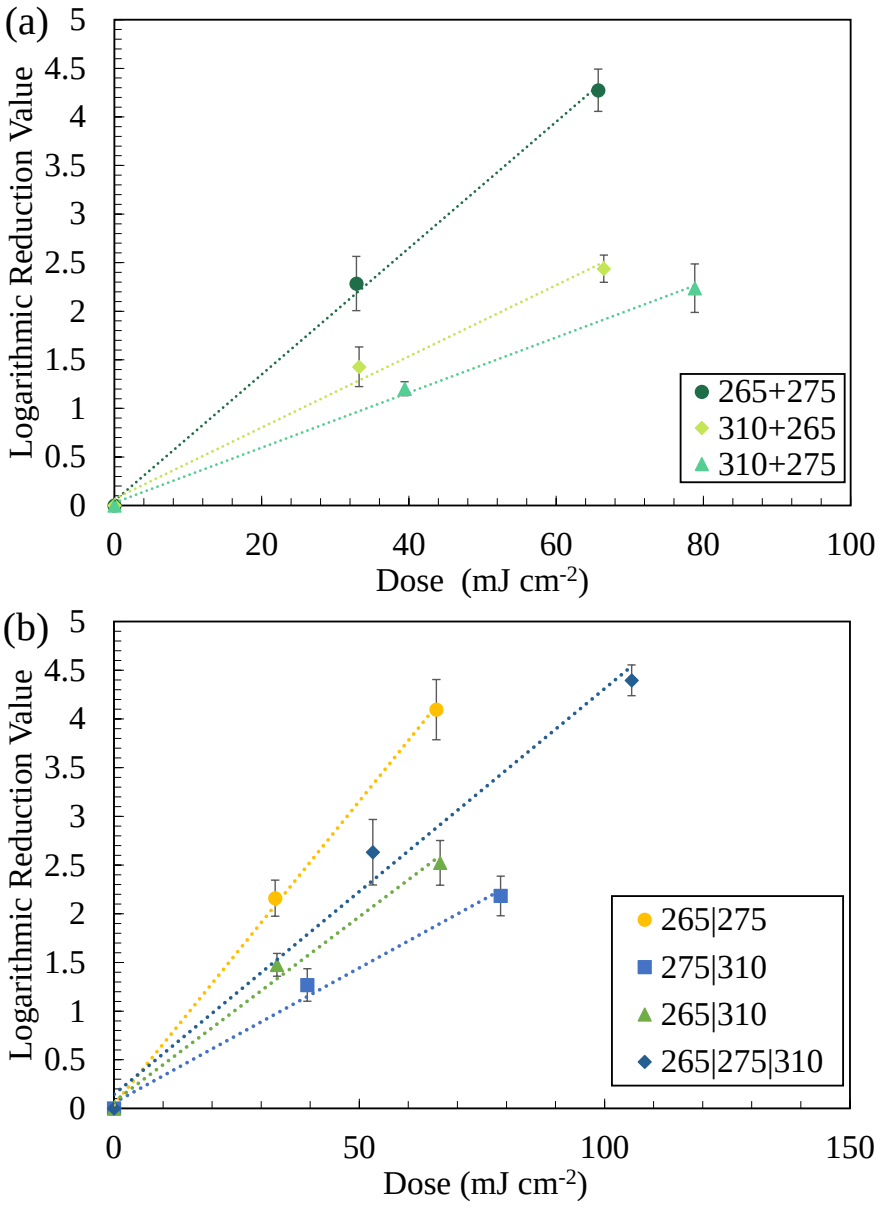

Figure 6.5: Inactivation rates in combination for (a) SE mode of irradiation and (b) SI mode of irradiation in wastewater matrix.

6.3.4. Synergy of Inactivation

Synergy of inactivation values have been calculated using the formula discussed in Section 5.2.6 (Chapter 5), and error has been propagated using Eq. 5.11 and Eq. 5.13. Table 6.3 and 6.4 lists the theoretical LRVs and actual LRVs for each combination tested, at 50% and 100% UV dose, respectively. The theoretical LRV has been calculated using the sum of individual wavelength LRVs in Table 6.1. This analysis has also been conducted in terms of kinetic constants and data can be found in Appendix 6.B.

Table 6.3: Synergy of inactivation values (by LRV) (at 50% Dose).

UV Source Combination	Theoretical LRV	Actual LRV	*Synergy*
265 + 275	2.3 ± 0.3	2.3 ± 0.3	1.01 ± 0.14
310 + 265	1.2 ± 0.1	1.4 ± 0.2	1.18 ± 0.18
310 + 275	1.1 ± 0.2	1.20 ± 0.07	1.14 ± 0.12
265 | 275	2.3 ± 0.3	2.2 ± 0.2	0.95 ± 0.09
265 | 310	1.2 ± 0.1	1.3 ± 0.2	1.2 ± 0.1
275 | 310	1.1 ± 0.2	1.5 ± 0.1	1.2 ± 0.2
265 |275 | 310	2.3 ± 0.3	2.6 ± 0.4	1.2 ± 0.2

Table 6.4: Synergy of inactivation values (by LRV) (at 100% Dose).

UV Source Combination	Theoretical LRV	Actual LRV	*Synergy*
265 + 275	4.2 ± 0.2	4.3 ± 0.2	1.03 ± 0.06
310 + 265	2.2 ± 0.2	2.4 ± 0.1	1.1 ± 0.1
310 + 275	1.98 ± 0.11	2.2 ± 0.3	1.13 ± 0.13
265 | 275	4.2 ± 0.2	4.1 ± 0.3	0.99 ± 0.08
265 | 310	2.2 ± 0.2	2.2 ± 0.2	1.16 ± 0.11
275 | 310	1.98 ± 0.11	2.5 ± 0.2	1.1 ± 0.1
265 | 275 | 310	4.2 ± 0.2	4.4 ± 0.2	1.06 ± 0.04

At both UV doses, it was found that the value of *Synergy* was greater than 1 except for the combination of 265 | 275, although the sum of error and the value was seen to be greater than 1. This pointed to the fact that no antagonism was seen when the wavelengths were irradiated in combination. In all cases, a minimum summation effect of individual wavelengths was observed. Fig. 6.6 plots the synergy of inactivation values for each combination with error bars representing the propagated standard deviation.

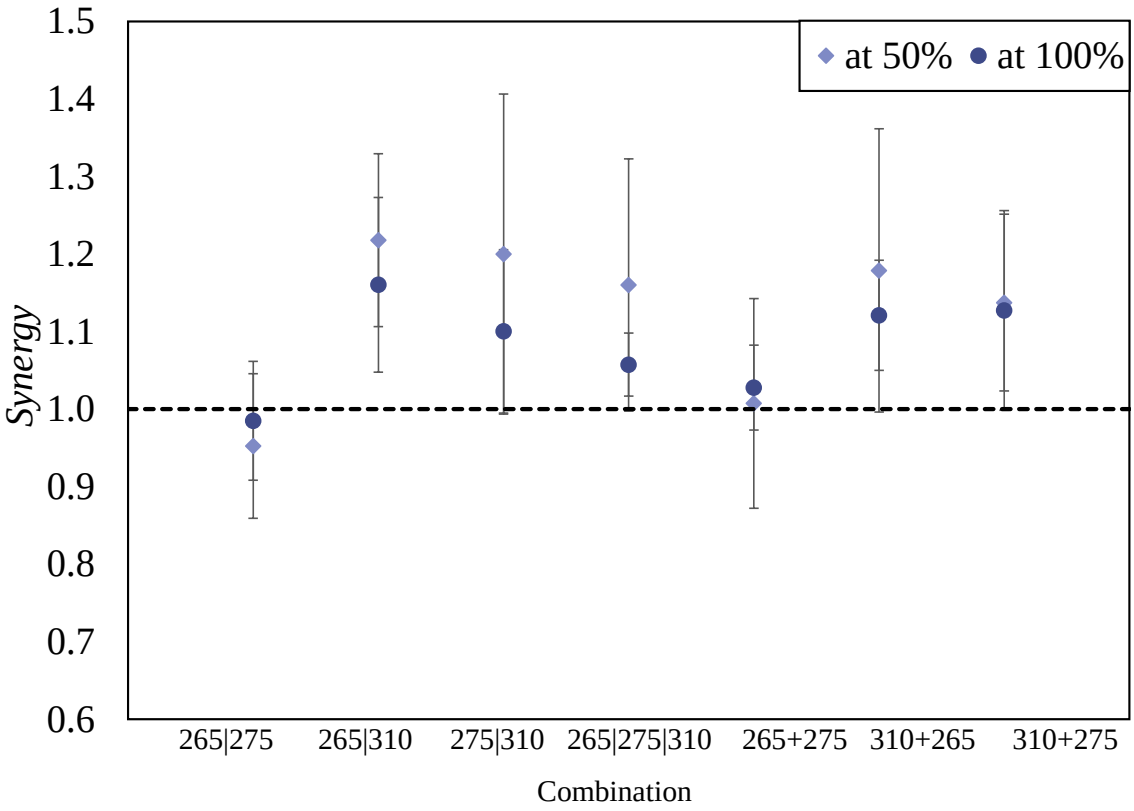

Figure 6.6: Synergy of inactivation in wastewater matrix.

To ascertain any synergistic effect between multiple wavelengths in this study, as in Chapter 5, *t*-Student analysis and codified ANOVA has been conducted on the data. Using the standard deviations obtained from the dataset, a 95% *CI* was calculated. Fig. 6.7 (a, b) plots the comparison between theoretical and actual LRVs obtained with error bars representing the 95% *CI* obtained. Akin to Chapter 5, the significance was determined using the argument that the maximum possible inactivation theoretically must be lower than the minimum possible inactivation in combination. If this is agreed, potential synergy can be seen. Table 6.5 lists the summary of test results.

Similar to the observations in Chapter 5, Section 5.3.8.1, the combination of FX–1 265 and FX–1 275 did not present any significant synergy when checked using *t*–Student analysis whereas the combination of FX–1 265/275 with FX–1 310 resulted in potential synergistic effect. Also, the combination of 3 wavelengths, in simultaneous mode of irradiation, resulted in a potential significant difference between theoretical and actual LRV.

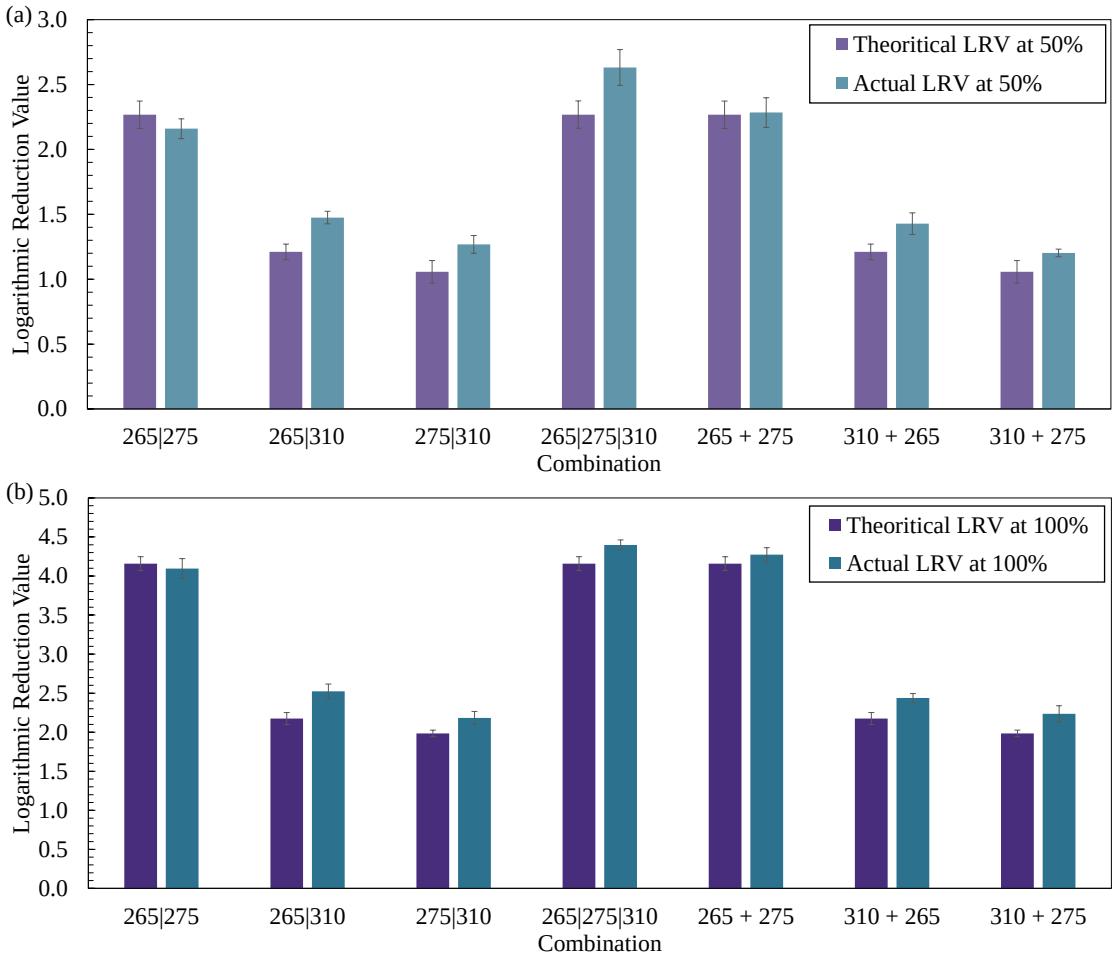

Figure 6.7: Comparison between theoretical and actual LRV at (a) 50% Dose and (b) 100% Dose using *t*–Student analysis in wastewater matrix.

Table 6.5: *t*–Student analysis observations for wastewater matrix.

UV Source	50%	100%
265 + 275	Not Significant	Not Significant
310 + 265	Significant	Significant
310 + 275	Significant	Significant
265 | 275	Not Significant	Not Significant
265 | 310	Significant	Significant
275 | 310	Significant	Significant
265 | 275 | 310	Significant	Significant

This analysis has also been conducted using kinetic constants and the data can be found in Appendix 6.C. To confirm the significance of each combination to confirm synergistic effect, a codified ANOVA has been conducted. *p*–values obtained from the codified ANOVA has been listed in Table 6.6 and a detailed result obtained can be found in Appendix 6.D.

Table 6.6: *p*–values from codified ANOVA at 95% *CI*.

UV Source	50%	100%
265 + 275	0.5718	0.2235
310 + 265	**0.0009**	**0.0000**
310 + 275	**0.0016**	**0.0004**
265 | 275	0.3237	0.3042
265 | 310	**0.0000**	**0.0000**
275 | 310	**0.0003**	**0.0012**
265 | 275 | 310	**0.0000**	**0.0000**

In almost all cases, compared to Chapter 5, a synergistic effect was observed. Dual wavelength combinations of 265 and 275 nm devices (SE and SI) showed no synergistic effect while those involving 310 nm with 265/275 nm devices (SE and SI) showed a synergistic effect. It is worth noting that, in the case of buffered water matrix, no significant synergistic effect was obtained at 95% significance for the 265 | 310 combination at 50% intensity, however in the wastewater matrix this combination showed significant synergistic effect with 99.99% confidence. The three–wavelength combination also showed synergistic effect with the results exhibiting a significant difference with a confidence of 99.99%.

The inactivation mechanism of wild *E. coli* is similar to that of *E. coli* K12 discussed in Chapter 5. Therefore, as mentioned earlier, due to two inactivation mechanisms (UV-2, UV-3) presented by the wavelengths chosen, the FX–1 310 seems to weaken the bacteria in the matrix thus making it more susceptible to damage with FX–1 265 or 275 or both wavelengths, when irradiated in combination. However, it is possible that the presence of other aerobic bacteria and chemical composition of the matrix may be contributing to this effect to a great extent, as seen by Chevremont et al. (2012) [265]. It is important to note that this is only a hypothesis and needs to be investigated further. To summarize, the analysis confirmed that a significant difference existed between the obtained LRVs in combination in comparison to the individual wavelength disinfection results, thus

establishing that a potential synergistic effect was occurring between the wavelengths in a wastewater matrix.

6.3.5. Electrical Energy Consumption

In any research involving pathogen inactivation, it is necessary to determine the electrical energy per unit order of inactivation of any UV source used [287]. In this study, plenty of UV sources and their combinations have been tested to understand their germicidal effectiveness in a wastewater matrix. Fig. 6.8 plots the E_{EO} for each UV source/ combination at the two intensities studied.

Identical to the observations in Chapter 5, it can be seen that the FX–1 265 nm device displays the lowest energy consumption per unit order of inactivation of 0.5 ± 0.03 kWh/m^3 and 0.39 ± 0.02 kWh/m^3, at 50% and 100% respectively. The 310 nm LEDs see a 1000–fold increase in energy consumption compared to the other UV sources and combinations tested mainly due to their low inactivation efficiency. Table 6.7 lists electrical energy values in kWh m^{-3} for all the combinations tested.

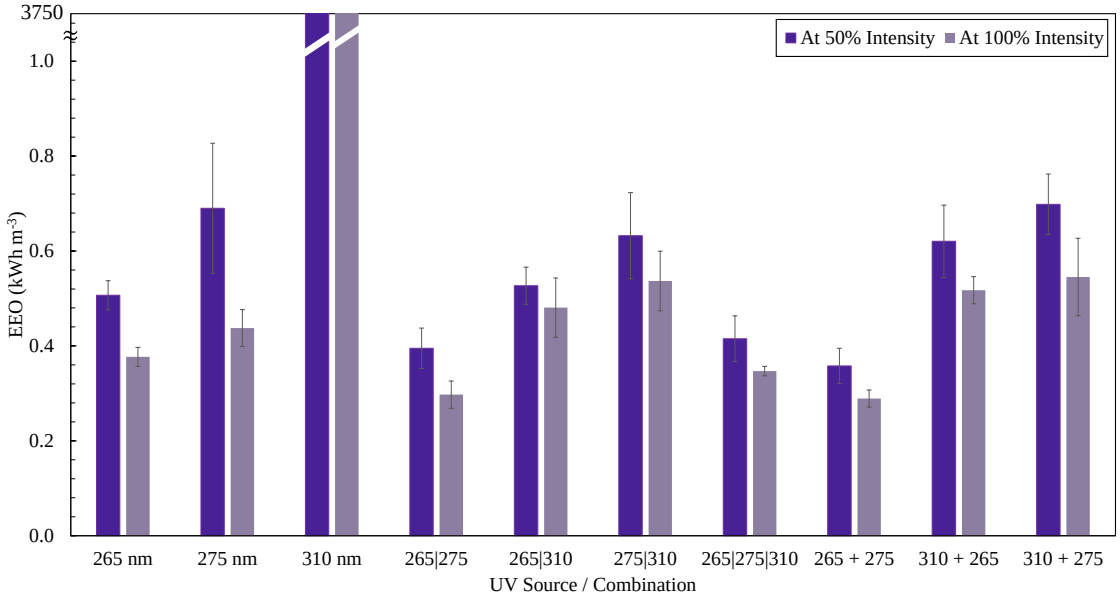

Figure 6.8: Electrical energy consumption per unit order at 50% (purple bars) and 100% (light violet bars) for wastewater matrix.

In the case of inactivation tests in wastewater matrix, the SE mode of irradiation of 265 nm and 275 nm devices were found to consume the lowest amount of electrical energy at both intensities corresponding to 0.38 ± 0.04 kWh m^{-3} and 0.29 ± 0.02 kWh m^{-3}, at 50% and 100%

intensity respectively. It can also be seen that in SE and SI modes of irradiation, the energy consumptions are similar and the E_{EO} in combination is lower than the individual sum of the energy consumption of the respective wavelengths. This means that the irradiation of two wavelengths is effective compared to the irradiation of wavelengths on their own. In all cases involving the combination of 310 nm, the process consumes much lower energy compared to individual wavelengths (acting on their own), mainly due to high energy consumption by the FX–1 310 devices, given its low inactivation rate. It must be noted that in buffered water matrix, the combination of 275 nm and 310 nm LEDs in SI mode resulted in lower energy consumption per unit order whereas in wastewater the combination of 265 nm and 310 nm LEDs can be seen to be a better option. However, in SE mode, the results are similar and consistent with the findings in Chapter 5.

Table 6.7: Electrical energy per unit order of inactivation (WW).

UV Source	E_{EO} (kWh m^{-3}) 50% Intensity	E_{EO} (kWh m^{-3}) 100% Intensity
265 nm	0.55 ± 0.03	0.39 ± 0.02
275 nm	0.64 ± 0.12	0.44 ± 0.03
310 nm	3347 ± 364	2558 ± 486
265 | 275	0.4 ± 0.1	0.30 ± 0.03
265 | 310	0.56 ± 0.04	0.47 ± 0.06
275 | 310	0.67 ± 0.09	0.56 ± 0.06
265 | 275 | 310	0.39 ± 0.05	0.36 ± 0.01
265 + 275	0.38 ± 0.04	0.30 ± 0.02
310 + 265	0.58 ± 0.08	0.49 ± 0.03
310 + 275	0.71 ± 0.06	0.55 ± 0.08

Comparing the two water matrixes from Chapter 5 and 6, the wastewater matrix was seen to require a higher energy consumption. This could be due to multiple reasons, while the buffered water is transparent, the wastewater matrix was yellow in color meaning that the number of photons passing through were lower in comparison to the buffered water in Chapter 5. It is true that the transmission of the UV wavelengths through this matrix is high (99.37%, 99.95%, and 100%, for FX–1 265, 275, and 310 respectively) but at the same time the residence time of microorganisms in front of the source is low (0.7426 s) and therefore to achieve the same amount of germicidal efficiency, more photons are required in the case of wastewater.

In the case of wastewater matrix, the microorganism under investigation was wild *E. coli*, that has been known to be more UV resistant compared to *E. coli* K12 [343] and also, in such a matrix, other aerobic bacteria (~10^2 CFU/mL) were seen and could be competing with the wild *E. coli* for the same light. The number of parameters affecting the process are significantly higher than that of a buffered water matrix [101]. Finally, between the synergistic combinations, at 50% intensity a three–wavelength combination of 265, 275, and 310 nm devices can be seen to be efficient whereas at 100% intensity, the combination of 265 nm and 310 nm in SI mode of irradiation can be seen to be optimum combination for effective disinfection of the wastewater effluent.

6.4. Conclusions

Advanced technology can enable the reuse of wastewater, while specialized equipment and processes can help transform it into energy. The use of UV LEDs has grown to prominence in the past decade dragging attention to check for optimal conditions for quick and effective disinfection of wastewater. The chapter investigated potential synergistic effect between the multiple wavelengths, selected in Chapter 2, for application on a secondary wastewater effluent. The study was conducted on a single pass flow reactor at a flow rate of 2 L min^{-1} and utilized the same procedural and analytical steps as discussed in Chapter 5 to enable comparison between the two water matrixes.

The investigation found that the microorganism and matrix used led to lower inactivation rates in comparison to the buffered water matrix and model bacterium studied earlier. Similar to the findings in Chapter 5, the individual disinfection experiments found that the 265 nm device was the most effective between the sources with an average log–reduction of 1.2 ± 0.1 at 50% intensity and 2.2 ± 0.2 at 100% intensity while the 310 nm device was the least effective ($0.0003 \pm 7.03 \times 10^{-5}$ log–reduction at 100% intensity). When a combination of the three wavelengths was used, an average log reduction of 4.4 ± 0.2 was observed and a significant synergistic effect was obtained when analyzed using statistical techniques. Under combined irradiation experiments, the log–reduction seen for combinations of 265 nm and 275 nm LEDs were equal to the sum of individual log reductions of the wavelengths. For combinations involving 310 nm LEDs with 265/275 nm LEDs, the log–reduction was seen to be greater than the sum of individual wavelength effects in both sequential and simultaneous mode of operation. Upon further analysis, using *t*–Student and codified ANOVA, it was concluded that the combinations presented a significant difference between the sum of individual wavelength effects and the actual log–reductions, in combination, indicating a synergistic effect of the wavelengths in terms of bacterial inactivation.

It was anticipated that the wastewater disinfection process would behave similar to the buffered matrix, and this was confirmed in this chapter. The findings were concurrent with that of Chapter 5. All combinations that showed a synergistic effect with *E. coli* K12 were synergistic in the wastewater matrix. The damage mechanism was concluded to be the same as *E. coli* K12 in Chapter 5 wherein the 310 nm LEDs seem to weaken the wild *E. coli* with high intensity photons, making it susceptible for faster damage under 265/275 nm LEDs.

This mechanism is based on the assumption that the wastewater matrix consisted mainly wild *E. coli*. Since only total aerobic bacteria have been tracked in this study for evaluation of synergistic effect of multiple wavelengths, it is possible that other pollutants, such as ionic species, suspended solids, and organic matter in the water matrix could have interfered. This could be next potential investigation using the sources used.

The study highlighted that multiple wavelengths centered in different mechanism ranges could be customized for achieving a synergistic effect in disinfection. It further pointed out that the use of 310 nm LEDs, in combination, is much more energy efficient than on its own. However, the wastewater matrix was yellow in color and hence questions still remain as if turbidity, organic matter and ionic strength could potentially affect or enhance the synergistic effect obtained in this chapter. Considering only the inactivation rate and consequent electrical energy consumption per unit order of inactivation, the combination of 3 wavelengths, simultaneously, was seen to be best combination in comparison to other combinations demonstrating synergistic effect of multiple wavelengths.

Appendix Chapter 6

6.A. FX–1 310 Disinfection

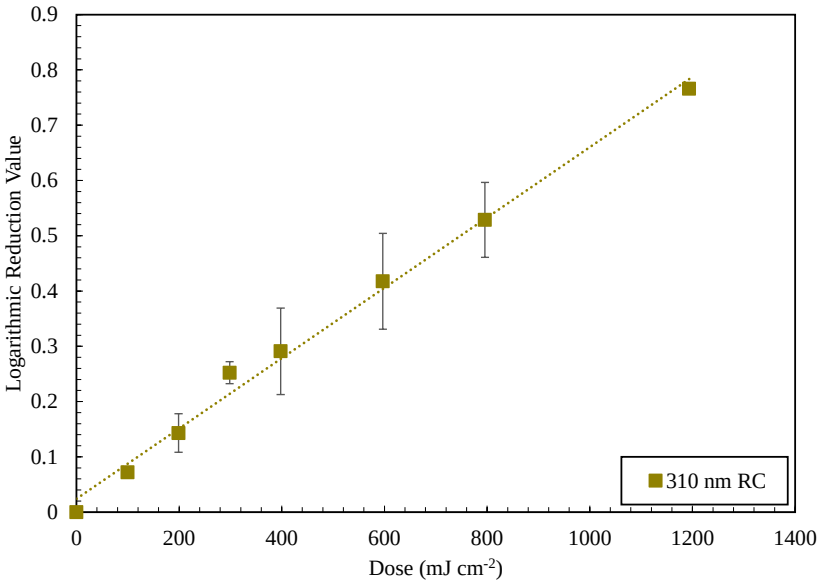

Figure 6.A.1: LRV *vs* UV dose for 310 nm recirculation until 1–log reduction.

6.B. Synergy of Inactivation (in terms of kinetic constants (k_c))

Table 6.B.1: At 50% Dose.

UV Source Combination	Theoretical k_c	Actual k_c	*Synergy*
265 | 275	2.95 ± 0.33	2.86 ± 0.25	1.0 ± 0.1
265 | 310	1.6 ± 0.2	1.96 ± 0.16	1.2 ± 0.1
275 | 310	1.34 ± 0.28	1.68 ± 0.22	1.26 ± 0.22
265 | 275 | 310	2.95 ± 0.33	3.49 ± 0.45	1.18 ± 0.17
265 + 275	2.95 ± 0.33	3.03 ± 0.37	1.03 ± 0.14
265 + 310	1.6 ± 0.2	1.89 ± 0.27	1.2 ± 0.2
275 + 310	1.34 ± 0.28	1.6 ± 0.1	1.2 ± 0.1

Table 6.B.2: At 100% Dose.

UV Source Combination	Theoretical k_c	Actual k_c	*Synergy*
265 | 275	5.5 ± 0.3	5.4 ± 0.4	0.98 ± 0.08
265 | 310	2.9 ± 0.2	3.35 ± 0.31	1.2 ± 0.1
275 | 310	2.6 ± 0.2	2.9 ± 0.3	1.1 ± 0.1
265 | 275 | 310	5.5 ± 0.3	5.8 ± 0.2	1.05 ± 0.04
265 + 275	5.5 ± 0.3	5.6 ± 0.3	1.03 ± 0.06
265 + 310	2.9 ± 0.2	3.2 ± 0.2	1.12 ± 0.07
275 + 310	2.6 ± 0.2	2.9 ± 0.3	1.13 ± 0.13

6.C. *t*–Student Analysis (in terms of kinetic constants)

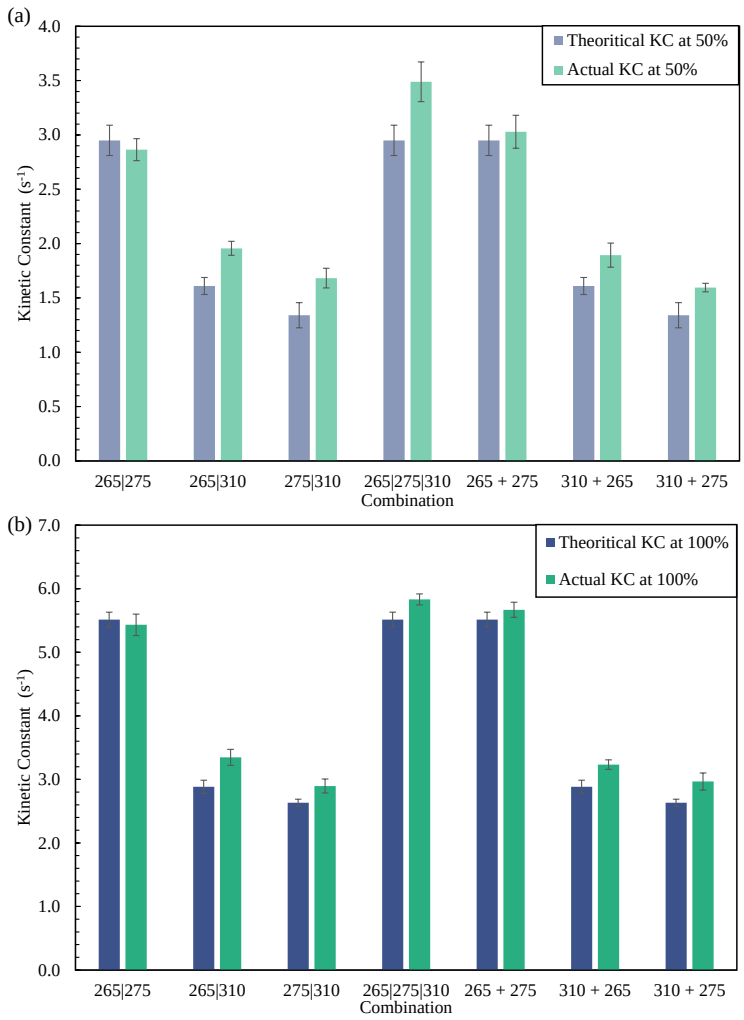

Figure 6.C.1: Comparison between theoretical and actual kinetic constants with error bars representing 95% *CI* for (a) 50% Dose and (b) 100% Dose.

6.D. Codified ANOVA Results

Note - **|** means simultaneous mode of operation whereas **+** means sequential mode of operation in the order written. In dual wavelength combinations, standard errors are based on the total error with 68 DOF. While for three wavelength combinations, standard errors are based on the total error with 136 DOF.

- Abbreviations in Table - QS = Quadratic Sum, QA = Quadratic Average, STDEV = Standard Deviation
- Font Color Legend – **Significant** and **Not Significant**

6.D.1.Dual Wavelength Combinations

- FX–1 265 and FX–1 275 combinations
- Simultaneous Irradiation (SI)

Estimated Effect for Y

	50% intensity		100% intensity	
Effect	Estimated	STDEV	Estimated	STDEV
Average	1.092	0.0186	2.064	0.0219
A: 265	1.186	0.0372	2.157	0.0439
B: 275	0.985	0.0372	1.950	0.0439
A **|** B	-0.037	0.0372	-0.045	0.0439

Analysis of Variance

Source	DOF	50% intensity				100% intensity			
		QS	QA	F Value	*p*-Value	QS	QA	F Value	*p*-Value
A: 265	1	25.329	25.329	1014.89	**0.0000**	83.783	83.783	2412.04	**0.0000**
B: 275	1	17.497	17.497	701.07	**0.0000**	68.485	68.485	1971.62	**0.0000**
A | B	1	0.024	0.024	0.99	**0.3237**	0.037	0.037	1.07	**0.3042**
Error	68	1.697	0.024			2.362	0.034		
Total	71	44.548				154.668			

Parameter	At 50% intensity	At 100% intensity
R^2	96.190%	98.472%
Standard Error of the residuals	0.1579	0.1863
Mean absolute error	0.1262	0.1180

- Sequential Irradiation (SE) – 265 followed by 275.

Estimated Effect for Y

	50% intensity		100% intensity	
Effect	Estimated	STDEV	Estimated	STDEV
Average	1.123	0.0222	2.108	0.0177
A: 265	1.248	0.0445	2.246	0.0355
B: 275	1.048	0.0445	2.039	0.0355
A + B	0.025	0.0445	0.043	0.0355

Analysis of Variance

Source	DOF	50% intensity				100% intensity			
		QS	QA	F Value	*p*-Value	QS	QA	F Value	*p*-Value
A: 265	1	28.061	28.061	784.47	**0.0000**	90.847	90.847	4001.36	**0.0000**
B: 275	1	19.779	19.779	552.95	**0.0000**	74.885	74.885	3298.31	**0.0000**
A + B	1	0.011	0.011	0.32	**0.5718**	0.034	0.034	1.51	**0.2235**
Error	68	2.432	0.035			1.543	0.022		
Total	71	50.285				167.31			

Parameter	At 50% intensity	At 100% intensity
R^2	95.162%	99.077%
Standard Error of the residuals	0.1891	0.1506
Mean absolute error	0.1454	0.1164

- FX–1 310 and FX–1 265 combinations

Simultaneous Irradiation (SI)

Estimated Effect for Y

	50% intensity		100% intensity	
Effect	Estimated	STDEV	Estimated	STDEV
Average	0.668	0.0108	1.175	0.0172
A: 265	1.348	0.0217	2.362	0.0344
B: 310	0.138	0.0217	0.172	0.0344
A **|** B	0.125	0.0217	0.159	0.0344

Analysis of Variance

Source	DOF	50% intensity				100% intensity			
		QS	QA	F Value	*p*-Value	QS	QA	F Value	*p*-Value
A: 265	1	32.754	32.754	3834.63	**0.0000**	100.495	100.495	4704.86	**0.0000**
B: 310	1	0.344	0.344	40.32	**0.0000**	0.536	0.536	25.12	**0.0000**
A | B	1	0.284	0.284	33.30	**0.0000**	0.460	0.460	21.55	**0.0000**
Error	68	0.580	0.008			1.452	0.021		
Total	71	33.964				102.945			

Parameter	At 50% intensity	At 100% intensity
R^2	98.289%	98.589%
Standard Error of the residuals	0.0924	0.1461
Mean absolute error	0.0603	0.0993

Sequential Irradiation (SE) – 310 followed by 265.

Estimated Effect for Y

	50% intensity		100% intensity	
Effect	Estimated	STDEV	Estimated	STDEV
Average	0.656	0.0146	1.154	0.0134
A: 265	1.325	0.0293	2.320	0.0268
B: 310	0.114	0.0293	0.129	0.0268
A **+** B	0.102	0.0293	0.117	0.0268

Analysis of Variance

Source	DOF	50% intensity				100% intensity			
		QS	QA	F Value	*p*-Value	QS	QA	F Value	*p*-Value
A: 265	1	31.619	31.619	2036.16	**0.0000**	96.892	96.892	7442.81	**0.0000**
B: 310	1	0.236	0.236	15.26	**0.0002**	0.303	0.303	23.34	**0.0000**
A + B	1	0.187	0.187	12.09	**0.0009**	0.247	0.247	18.98	**0.0000**
Error	68	1.055	0.015			0.885	0.013		
Total	71	33.099				98.328			

Parameter	At 50% intensity	At 100% intensity
R^2	96.809%	99.099%
Standard Error of the residuals	0.1246	0.1140
Mean absolute error	0.0854	0.0757

- FX–1 310 and FX–1 275 combinations
- Simultaneous Irradiation (SI)

Estimated Effect for Y

	50% intensity		100% intensity	
Effect	Estimated	STDEV	Estimated	STDEV
Average	0.566	0.0162	1.038	0.0138
A: 275	1.145	0.0324	2.089	0.0276
B: 310	0.135	0.0324	0.106	0.0276
A | B	0.122	0.0324	0.093	0.0276

Analysis of Variance

Source	DOF	50% intensity				100% intensity			
		QS	QA	F Value	*p*-Value	QS	QA	F Value	*p*-Value
A: 275	1	23.621	23.621	1242.57	**0.0000**	78.576	78.576	5700.32	**0.0000**
B: 310	1	0.329	0.329	17.32	**0.0001**	0.202	0.202	14.68	**0.0003**
A | B	1	0.270	0.270	14.23	**0.0003**	0.156	0.156	11.36	**0.0012**
Error	68	1.292	0.019			0.937	0.013		
Total	71	25.513				79.872			

Parameter	At 50% intensity	At 100% intensity
R^2	94.933%	98.826%
Standard Error of the residuals	0.1378	0.1174
Mean absolute error	0.0923	0.0730

- Sequential Irradiation (SE) – 310 followed by 275.

Estimated Effect for Y

	50% intensity		100% intensity	
Effect	Estimated	STDEV	Estimated	STDEV
Average	0.550	0.0136	1.051	0.0162
A: 275	1.112	0.0272	2.116	0.0324
B: 310	0.102	0.0272	0.132	0.0324
A **+** B	0.089	0.0272	0.120	0.0324

Analysis of Variance

Source	DOF	50% intensity				100% intensity			
		QS	QA	F Value	*p*-Value	QS	QA	F Value	*p*-Value
A: 275	1	22.275	22.275	1669.44	**0.0000**	80.600	80.600	4243.78	**0.0000**
B: 310	1	0.187	0.187	14.07	**0.0004**	0.317	0.317	16.71	**0.0001**
A + B	1	0.144	0.144	10.80	**0.0016**	0.259	0.259	13.65	**0.0004**
Error	68	0.907	0.013			1.291	0.018		
Total	71	23.514				82.468			

Parameter	At 50% intensity	At 100% intensity
R^2	96.141%	98.434%
Standard Error of the residuals	0.1155	0.1378
Mean absolute error	0.0743	0.0859

6.D.2. Three Wavelength Combination

- Simultaneous Irradiation

Estimated Effect for Y

	50% intensity		100% intensity	
Effect	Estimated	STDEV	Estimated	STDEV
Average	1.217	0.0148	2.170	0.0149
A: 265	0.119	0.0297	0.045	0.0299
B: 275	0.122	0.0297	0.111	0.0299
C: 310	1.331	0.0297	2.259	0.0299
AB: 265 | 275	-0.046	0.0297	-0.099	0.0299
AC: 265 | 310	0.012	0.0297	-0.064	0.0299
BC: 275 | 310	0.216	0.0297	0.208	0.0299
ABC: 265 | 275 | 310	1.070	0.0297	1.993	0.0299

- Analysis of Variance

Source	DOF	50% intensity				100% intensity			
		QS	QA	F Value	*p*-Value	QS	QA	F Value	*p*-Value
A: 265	1	0.513	0.513	16.11	**0.0001**	0.073	0.073	2.28	**0.1333**
B: 275	1	0.540	0.540	16.95	**0.0001**	0.450	0.450	13.96	**0.0003**
C: 310	1	63.793	63.793	2002.31	**0.0000**	183.73	183.73	5695.88	**0.0000**
AB	1	0.077	0.077	2.45	**0.1200**	0.359	0.359	11.15	**0.0011**
AC	1	0.006	0.006	0.19	**0.6647**	0.150	0.150	4.66	**0.0326**
BC	1	1.684	1.684	52.88	**0.0000**	1.571	1.571	48.70	**0.0000**
ABC	1	41.235	41.235	1294.27	**0.0000**	143.02	143.02	4433.74	**0.0000**
Error	136	4.332	0.031			4.386	0.032		
Total	143	112.185				333.74			

Parameter	At 50% intensity	At 100% intensity
R^2	96.137%	98.685%
Standard Error of the residuals	0.1784	0.1796
Mean absolute error	0.1238	0.1176

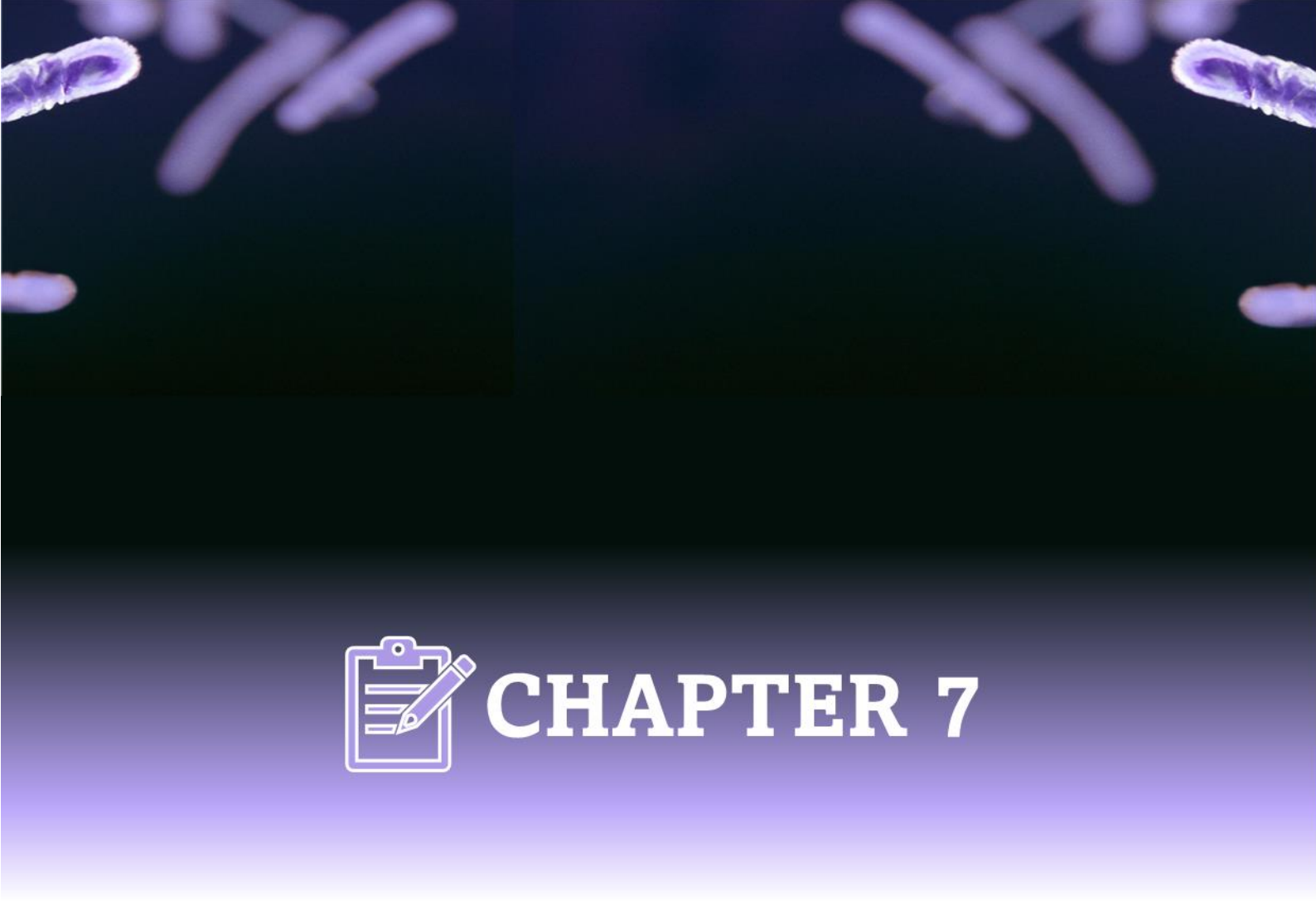

CHAPTER 7

CONCLUSIONS

Ultraviolet light has seen a long and fascinating story, starting from its discovery in the early 19th century to its many applications in industry, medicine, and science. The ability of this range of the light spectrum to cause chemical reactions and inactivate microorganisms has made it an essential tool in a range of fields. This thesis aimed to develop a comprehensive understanding of UV LED technology for disinfecting drinking water and wastewater matrixes, while also investigating the potential synergistic effect between multiple wavelengths. To achieve this, the study initially evaluated and selected UV–C LEDs from a pool of more than 600 products, by establishing a decision criterion. The selected LEDs were then integrated into a COBRA Clean FX–1 device and characterized. To validate the measurements conducted, multiple sensors operating in the same region were compared, and the effect of important parameters was quantified. Before the application of the LED sources into a water matrix, a ray tracing model was simulated on ZeMax Optic studio. This allowed for the understanding of the radiant intensity reaching the points of interest within the system and the quantification of the light received by water in a 4–wavelength germicidal system. The following conclusions highlight the key takeaways from each chapter of the thesis:

- ✓ **LED Characterization:** The selection of LEDs was made based on a decision criterion that took into account critical parameters affecting the light source's performance. This criterion created a ranking system that aided in the careful selection of LEDs. LED characterization was carried out, and it was determined that conducting a rollover test was crucial in creating an understanding of the safe current for each device. The lifetime tests of the selected LEDs revealed that the 285 nm LEDs, although emitting the highest radiant intensity, were not reliable and experienced a significant intensity drop after approximately 800 h of operation. The intensity drop with working distance followed an exponential trend, while the dose loss was gradual with an increase in the distance between the sensor and device. These findings demonstrate the importance of careful selection and testing of LEDs to ensure optimal performance and reliability in disinfection applications.
- ✓ **UV Sensors:** Validating the measurement sensor used in characterization was crucial for the reliability and accuracy of the data used in this research. The study demonstrated the necessity of the concept of “extended sources” to obtain dependable and precise results. The investigation revealed that certain sensors could exhibit varying behaviors at multiple wavelengths in the same region. Moreover, the orientation of the sensor with

respect to the UV LED was found to be critical in avoiding erroneous readings from the measurement. The results indicated that different sensors exhibited varying levels of accuracy and consistency in their measurements and emphasized the significance of meticulously selecting and calibrating optical sensors to ensure precise measurements of UV radiation emitted from UV LED lamps.

- ✓ **Radiation Modeling:** This study utilized an optical ray tracing method to predict the irradiation reaching the point of interest as the light propagates, through water, in a germicidal system comparing it with multiple techniques like DOM, radiometry, and actinometry. A close agreement was found between the techniques leading to confidence in the model built. The study further quantified the effect of quartz material on irradiation in the UV–C range of the light spectrum and observed a decrease of light intensity by 10.0 ± 0.5% for the 265 nm source. The method was then used in a 4–wavelength complex system and enabled a better understanding of the system designed and provided a valuable understanding of how the light source propagates through the system, how to optimize the light irradiation within the system designed, and the difference between air and water–based systems.
- ✓ **UV Disinfection:** This chapter involved the application of the UV LED sources for disinfection of a buffered water matrix spiked with *E. coli* K12 and investigating potential synergistic effects between the wavelengths. A single pass reactor set–up showed that, amongst the LEDs studied, the 265 nm light sources was most effective in inactivation. Statistical analysis using codified ANOVA confirmed significant synergy between the dual wavelength combinations of 310 nm with 265 nm or 275 nm devices and in three wavelength combinations. Comparing the combinations that presented a significant synergistic effect, the combination of 3 wavelengths (log–reduction of 2.8 ± 0.2 and 5.4 ± 0.3, at 50% and 100% UV dose, respectively), in simultaneous mode of operation, resulted in an energy efficient process (E_{EO}= 0.37 ± 0.02 kWh m^{-3} and 0.29 ± 0.02 kWh m^{-3}, at 50% and 100% UV dose, respectively) whereas, in sequential mode, the combination of 265 nm and 310 nm (log–reduction of 1.77 ± 0.24 and 2.95 ± 0.23 , at 50% and 100% UV dose respectively) was seen to be the most effective (E_{EO}= 0.47 ± 0.08 kWh m^{-3} and 0.41 ± 0.06 kWh m^{-3}, at 50% and 100% UV dose, respectively).
- ✓ **Wastewater Disinfection:** Synergistic effect obtained in a wastewater matrix demonstrated parallels to the buffered water matrix. Dual wavelength combinations of 310 nm with 265/275 nm, in sequential and simultaneous mode of operation, and three

wavelength combination (in simultaneous mode) resulted in a significant synergistic effect on the disinfection of total aerobic bacteria present in the secondary effluent of wastewater. At 50% intensity each, the three wavelength combination (log–reduction of 2.63 ± 0.34) was calculated to consume the lowest energy (E_{EO}= 0.40 ± 0.05 kWh m^{-3}) in comparison with the other synergistic combinations whereas at 100% intensity each, the combination of 265 nm with 310 nm device (log–reduction of 2.44 ± 0.14), in simultaneous mode of operation, was found to be optimum (E_{EO}= 0.47 ± 0.06 kWh m^{-3}).

As our understanding of UV light continues to grow, it is likely that we will discover more applications for this versatile form of radiation. The findings from this thesis can be useful for the design and implementation of efficient disinfection systems using UV LED technology. Overall, this work contributes to the growing body of research on UV–C LED technology and its potential for disinfection applications. It also highlights the need for further investigation of the potential synergistic effects between multiple wavelengths by carefully selecting the sources.

7.1. Future Work

- Evaluating if parameters like substrate temperature, and thermal resistance could be added to the decision criterion to further optimize the selection process and enable a better understanding of the light source.
- Investigating the varying behavior of the sensors with wavelength due to possible Brillouin scattering.
- Modeling of a multi–wavelength germicidal system using particle tracing for prediction and optimization of the system.
- Study on by–product formations in wastewater to evaluate if the use of multiple wavelengths can reduce such formations.
- Investigation of the use of multiple wavelength LEDs on the same substrate of a device to evaluate potential synergistic effects and establish control over each wavelength in the device.
- Evaluation of potential effects of turbidity, organic matter, and other pollutants on the synergistic effect between multiple wavelengths.

REFERENCES

1. Zubairy, M.S., 2016. A Very Brief History of Light. In: Al-Amri, M., El-Gomati, M., Zubairy, M. (eds) Optics in Our Time. Springer. Cham. https://doi.org/10.1007/978-3-319-31903-2_1
2. Lyons, J., 2009. The house of wisdom: how the Arabs transformed western civilization. Bloomsbury Press. New York. URL https://www.bloomsbury.com/us/house-of-wisdom-9781608190584/
3. McGuigan, K. G., Conroy, R. M., Mosler, H.J., Preez, M.D., Udomba-Jaswa, E., Fernandez- Ibañez, P., 2012. Solar water disinfection (SODIS): A review from bench-top to roof-top. Hazardous Materials. J 235–236, 29-46. https://doi.org/10.1016/j.jhazmat.2012.07.053
4. Weinberg, S., 2015. To explain the world: the discovery of modern science. HarperCollins. New York. URL https://www.harpercollins.com/products/to-explain-the-world-steven-weinberg (Accessed 13/02/23)
5. Kingslake, R., Thompson, . Brian, J. Optics. Encyclopaedia Britannica. URL https://www.britannica.com/science/optics. (Accessed 15/02/23)
6. Stark, G. Light. Encyclopaedia Britannica. URL https://www.britannica.com/science/light. (Accessed 12/02/23)
7. Joyce, B., 2004. Thomas Edisons inventive life. URL https://web.archive.org/web/20180401075142/http://invention.si.edu/thomas-edisons-inventive-life (Accessed 18/02/23)
8. Bromberg, L.B., 1991.The Laser in America, 1950-1970. The MIT Press. Cambridge. Bulletin of Science, Technology & Society. 13-2, 116–116. https://doi.org/10.1177/027046769301300242
9. Andrzej Grzybowski, A., Sak, J., Pawlikowski, J., 2016. A brief report on the history of phototherapy. Clinics in Dermatology. 34-5, 532-537. https://doi.org/10.1016/j.clindermatol.2016.05.002.
10. Boixeda, P.,Calvo, M., Bagazgoitia, L., 2008. Recent Advances in Laser Therapy and Other Technologies. Actas Dermo-Sifiliográficas (English Edition). 99-4, 262-268. https://doi.org/10.1016/S1578-2190(08)70249-X.
11. Barillaro, G., Pieri, F., Mastromatteo, U., 2001. A porous silicon LED based on a standard BCD technology. Optical Materials. 17-2, 91-94. https://doi.org/10.1016/S0925-3467(01)00026-X.
12. Livingston, W., 2004. Energy from Sun - Editor(s): Cutler J. Cleveland. Encyclopedia of Energy. Elsevier, 777-788. https://doi.org/10.1016/B0-12-176480-X/00049-8.
13. Zhu, X.,Gao, T., 2019. Chapter 10 – Spectrometry. Editor(s): Genxi Li, Nano-Inspired Biosensors for Protein Assay with Clinical Applications. Elsevier, 237-264. https://doi.org/10.1016/B978-0-12-815053-5.00010-6.
14. Collini, E., 2022. Fundamental aspects of quantum biology. Reference Module in Materials Science and Materials Engineering. Elsevier. https://doi.org/10.1016/B978-0-323-90800-9.00022-6.
15. Fromhold, A.T., 2003. Quantum Mechanics. Editor(s): Robert A. Meyers. Encyclopaedia of Physical Science and Technology (Third Edition). Academic Press, 359-408. https://doi.org/10.1016/B0-12-227410-5/00626-8.
16. Mieres-Perez, J., Sanchez-Garcia, E., 2020. Chapter Four - Quantum mechanics/molecular mechanics multiscale modeling of biomolecules. Editor(s): Williams, I.H., Williams, N.H. Advances in Physical Organic Chemistry. Academic Press. 54, 143-183. https://doi.org/10.1016/bs.apoc.2020.08.002.
17. Sandle, T., 2013. 4 - Gamma radiation. Editor(s): Sandle, T. Biomedicine, Sterility, Sterilisation and Sterility Assurance for Pharmaceuticals. Woodhead Publishing, 55-68. https://doi.org/10.1533/9781908818638.55

18. Parola, A.H., Markel, A., 1994. 9 - Electric and Magnetic Fields and Carcinogenesis. Editor(s): Carpenter, D.O., Ayrapetyan, S. Biological Effects of Electric and Magnetic Fields. Academic Press, 177-197. https://doi.org/10.1016/B978-0-12-160262-8.50014-1
19. Shama, G., 2014. Ultraviolet Light. Editor(s): Batt, C.A., Tortorello, M.L. Encyclopaedia of Food Microbiology (Second Edition). Academic Press, 665-671. https://doi.org/10.1016/B978-0-12-384730-0.00341-4
20. Marcus, R.T., 1998. Chapter 2 - The Measurement of Color. Editor(s): Nassau, K., Azimuth. North-Holland. 1, 31-96. https://doi.org/10.1016/S1387-6783(98)80005-6
21. Reichle, D.E., 2020. Chapter 3 - Energy relationships between organisms and their environment. Editor(s): Reichle, D.E. The Global Carbon Cycle and Climate Change. Elsevier, 15-41. https://doi.org/10.1016/B978-0-12-820244-9.00003-2
22. Wadge, G., 2005. REMOTE SENSING | Active Sensors. Editor(s): Selley, R.C., Robin, L., Cocks, M., Plimer, I.R. Encyclopaedia of Geology. Elsevier, 414-420. https://doi.org/10.1016/B0-12-369396-9/00112-X
23. Doviak, R.J., Zrnić, D.S., 1993. 2 - Electromagnetic Waves and Propagation. Editor(s): Doviak, R.J., Zrnić, D.S. Doppler Radar and Weather Observations (Second Edition). Academic Press, 10-29. https://doi.org/10.1016/B978-0-12-221422-6.50007-3
24. Levy, S.B., 2013. 46 – Sunscreens. Editor(s): Wolverton, S.E. Comprehensive Dermatologic Drug Therapy (Third Edition). W.B. Saunders, 551-561. https://doi.org/10.1016/B978-1-4377-2003-7.00046-7
25. Frercks, J.,Weber, H., Wiesenfeldt, G., 2009. Reception and discovery: the nature of Johann Wilhelm Ritter's invisible rays. Studies in History and Philosophy of Science Part A.40-2, 143-156. https://doi.org/10.1016/j.shpsa.2009.03.014
26. Davidson, M., 2014. Pioneers in Optics: Johann Wilhelm Ritter and Ernest Rutherford. Microscopy Today. 22-2, 48-51. doi:10.1017/S1551929514000029
27. Steigerwald, J., 2008. Figuring Nature: Ritter's Galvanic Inscriptions. Bulletin d'histoire et d'épistémologie des sciences de la vie. 15, 137-146. https://doi.org/10.3917/bhesv.152.0137
28. Downes, A., 1886. On the Action of Sunlight on Micro-Organisms, &c., with a Demonstration of the Influence of Diffused Light. Proceedings of the Royal Society of London. 40, 14–22. http://www.jstor.org/stable/114763
29. Downes, A., Blunt, T., 1877. The influence of light upon the development of bacteria. Nature, 16, 218. https://doi.org/10.1038/016218a0
30. Grzybowski, A., Pietrzak, K., 2012. From patient to discoverer—Niels Ryberg Finsen (1860–1904)—the founder of phototherapy in dermatology. Clinics in Dermatology. 30-4, 451-455. https://doi.org/10.1016/j.clindermatol.2011.11.019
31. Randle, H.W., 1997. Suntanning: Differences in Perceptions Throughout History. Mayo Clinic Proceedings. 72-5, 461-466. https://doi.org/10.4065/72.5.461
32. Wells, W.F.,Wells, M.W., 1936. Air-Borne Infection. Jama. 107-21,1698–1703. https://doi.org/10.1001/jama.1936.02770470016004
33. Reed, N.G., 2010. The history of ultraviolet germicidal irradiation for air disinfection. Public Health Rep. 125-1,15-27. https://doi.org/10.1177/003335491012500105
34. Thornton, G.M., Fleck, B.A., Fleck, N., Kroeker, E., Dandnayak, D., Zhong, L., 2022. The impact of heating, ventilation, and air conditioning design features on the transmission of viruses, including the 2019 novel coronavirus: A systematic review of ultraviolet radiation. PLoS ONE. 17-4 : e0266487. https://doi.org/10.1371/journal.pone.0266487
35. Drescher, A.C., Greene, D.M., Gadgil, A.J., 2001. Cryptosporidium inactivation by low-pressure UV in a water disinfection device. J Environ Health.64-3, 31-35. https://pubmed.ncbi.nlm.nih.gov/11605325/

36. Raeiszadeh, M., Adeli, B., 2020. A critical review on ultraviolet disinfection systems against COVID-19 outbreak: Applicability, validation, and safety considerations. ACS Photonics. 7-11, 2941–2951. https://doi.org/10.1021/acsphotonics.0c01245
37. D'Orazio, J., Jarrett, S., Amaro-Ortiz, A., Scott, T., 2013. UV Radiation and the Skin. International Journal of Molecular Sciences. 14-6, 12222-12248. https://doi.org/10.3390/ijms140612222
38. Patrolecco, L., Ademollo, N., Grenni, P., Tolomei, A., Barra Caracciolo, A., Capri, S., 2013. Simultaneous determination of human pharmaceuticals in water samples by solid phase extraction and HPLC with UV-fluorescence detection. Microchemical Journal, Devoted to the Application of Microtechniques in All Branches of Science. 107, 165–171. https://doi.org/10.1016/j.microc.2012.05.035
39. Sonnenschein, H., Hennrich, G., Resch-Genger, U., Schulz, B., 2000. Fluorescence and UV/Vis spectroscopic behaviour of novel biindolizines. Dyes and Pigments: An International Journal. 46-1, 23–27. https://doi.org/10.1016/s0143-7208(00)00032-2
40. Pandiscia, L., 2013. Fluorescence detection in the detection of counterfeit US currency - JASCO. JASCO Inc. URL https://jascoinc.com/applications/using-fluorescence-detection-detection-counterfeit-us-currency/ (Accessed 01/03/23)
41. Bardi, M. A. G., Machado, L. D. B., 2012. Accompanying of parameters of color, gloss and hardness on polymeric films coated with pigmented inks cured by different radiation doses of ultraviolet light. Radiation Physics and Chemistry. 81-9, 1332–1335. https://doi.org/10.1016/j.radphyschem.2011.11.068
42. Schwalm, R., 2007. Introduction to coatings technology. In UV Coatings. Elsevier,1–18. https://doi.org/10.1016/B978-044452979-4/50001-9.
43. Sokol, A. A., 2000. Ultraviolet (UV) cured coatings. Metal Finishing. 98-6, 246–253. https://doi.org/10.1016/s0026-0576(00)80418-3
44. ter Vrugt, J. W., Verwimp, J. K. P., 1980. High pressure mercury vapour lamps. IEE Proceedings A (Physical Science Measurement and Instrumentation Management and Education). 127-3, 173. https://doi.org/10.1049/ip-a-1.1980.0028
45. Lighting-gallery.net., 2023. High Pressure Lamps/Mercury Cadmium colour comparison. (n.d.). Lighting-gallery.net. URL: https://www.lighting-gallery.net/gallery/displayimage.php?album=1994&pos=20&pid=150822 (Accessed 13/04/23)
46. Rajkhowa, S., 2020. Heat, solar pasteurization, and ultraviolet radiation treatment for removal of waterborne pathogens. In Waterborne Pathogens. Elsevier, 69–187. https://doi.org/10.1016/B978-0-12-818783-8.00009-8
47. Choudhury, A. K. R., 2014. Characteristics of light sources. In Principles of Colour and Appearance Measurement. Elsevier, 1–52. https://doi.org/10.1533/9780857099242.1
48. Rhee, S.-W., Choi, H.-H., Park, H.-S., 2014. Characteristics of mercury emission from linear type of spent fluorescent lamp. Waste Management (New York, N.Y.). 34-6, 1066–1071. https://doi.org/10.1016/j.wasman.2013.07.029
49. Kim, Y.-J., Lee, J.-I., & Kang, D.-H., 2023. Inactivation of foodborne pathogenic bacteria in water and stainless-steel surfaces by vacuum-UV amalgam lamp and low-pressure mercury UV lamp irradiation. Innovative Food Science & Emerging Technologies: IFSET: The Official Scientific Journal of the European Federation of Food Science and Technology. 84-103297, 103297. https://doi.org/10.1016/j.ifset.2023.103297
50. Kadam, A. R., Nair, G. B., Dhoble, S. J., 2019. Insights into the extraction of mercury from fluorescent lamps: A review. Journal of Environmental Chemical Engineering. 7-4, 103279. https://doi.org/10.1016/j.jece.2019.103279

51. Mercury Vapor Lamps., 2023. Fda.gov. URL https://www.fda.gov/radiation-emitting-products/home-business-and-entertainment-products/mercury-vapor-lamps-mercury-vapor-light-bulbs. (Accessed 20/03/23)
52. Jang, M., Hong, S. M., Park, J. K., 2005. Characterization and recovery of mercury from spent fluorescent lamps. Waste Management (New York, N.Y.). 25-1, 5–14. https://doi.org/10.1016/j.wasman.2004.09.008
53. Clean and circular electronics: Commission ends use of mercury in lamps as mercury-free alternatives prevail. 2021. European Commission. News Article. URL https://environment.ec.europa.eu/news/clean-and-circular-electronics-commission-ends-use-mercury-lamps-mercury-free-alternatives-prevail-2021-12-16_en. (Accessed 15/03/23)
54. Recycling and Disposal of CFLs and Other Bulbs that Contain Mercury. 2021. United States Environmental Protection Agency. URL https://www.epa.gov/mercury/recycling-and-disposal-cfls-and-other-bulbs-contain-mercury. (Accessed 16/03/23)
55. The history of LED lighting: Then and now. 2015. Stouch Lighting, Inc. URL https://www.stouchlighting.com/blog/history_of_light_emitting_diode_led-lighting (Accessed 17/03/23)
56. Zhao, S., & Mi, Z., 2017. Al(Ga)N Nanowire Deep Ultraviolet Optoelectronics. In Semiconductors and Semimetals. Elsevier, 167–199. https://doi.org/10.1016/bs.semsem.2016.05.001
57. Succeeded in commercialization of the world's first "deep UV-LED." 2015. Press Release - NIKKISO CO., LTD. URL https://www.nikkiso.com/technology/r_d/duv-led.html (Accessed 17/03/23)
58. Shatalov, M., Jain, R., Saxena, T., Dobrinsky, A., Shur, M., 2017. Development of deep UV LEDs and current problems in material and device technology. Semiconductors and Semimetals. Elsevier, 45-83. https://doi.org/10.1016/bs.semsem.2016.08.002.
59. Wu, Y., Wang, P., Kioupakis, E., Mi, Z., 2021. Nanoscale AlGaN and BN: Molecular beam epitaxy, properties, and device applications. Ultrawide Bandgap Semiconductors. Elsevier, 153-189. https://doi.org/10.1016/bs.semsem.2021.04.005
60. Datasheet for UVA + UVC LED. 2023. Ivy Bridge Technology. URL https://www.uvledchip.com/uvac-led.html. (Accessed 15/03/23)
61. Lister, G. G., Waymouth, J. F., 2003. Light Sources. Encyclopaedia of Physical Science and Technology. Elsevier, 557-595. https://doi.org/10.1016/B0-12-227410-5/00378-1.
62. LED Lights Manufacturing Process: How LED Lighting is Made. 2020. EGLO Leuchten GmbH. URL https://www.eglo.com/uk/led-lights-manufacturing-process-how-led-lighting-is-made. (Accessed 15/03/23)
63. Manufacturing Process Of LED Chips. 2022. Eagle New Energy Technology Co., Ltd. URL https://enetcl.com/manufacturing-process-of-led-chips/ (Accessed 15/03/23)
64. Liu, S., Gan, Z., Luo, X., Wang, K., Song, X., Chen, Z., Yan, H., Liu, Z., Wang, P., Wei, W., 2008. Multi-physics multi-scale modeling issues in LED. In X. He, H. Xie, Y. Kang (Eds.). International Conference on Experimental Mechanics. SPIE. URL https://www.semanticscholar.org/paper/Multi-physics-multi-scale-modeling-issues-in-LED-Liu-Gan/f7608a6e955a7c5ae1d98a245315da24c3277113
65. Advantages of Stanley's UV-C LED. 2018. Stanley Electric Co., Ltd. URL https://www.stanley.co.jp/e/product/uvc_product/led_advantage/ (Accessed 15/03/23)
66. Senthil Kumar, P., Yaashikaa, P. R., 2019. Introduction—Water. Water in Textiles and Fashion. Elsevier, 1-20. https://doi.org/10.1016/B978-0-08-102633-5.00001-4.

67. Cheuvront, S. N., Kenefick, R. W., Montain, S. J., Sawka, M. N., 2020. Water. Present Knowledge in Nutrition. Elsevier, 503-514. https://doi.org/10.1016/B978-0-323-66162-1.00030-5.
68. Human Rights to water and sanitation. 2019. United Nations. URL https://www.unwater.org/water-facts/human-rights-water-and-sanitation. (Accessed 18/03/23)
69. Water Scarcity. 2019. United Nations. URL https://www.unwater.org/water-facts/water-scarcity (Accessed 15/03/23)
70. Water. 2019. World Health Organisation. URL https://www.afro.who.int/health-topics/water (Accessed 19/03/23)
71. Africa Population. 2023. Worldometer. URL https://www.worldometers.info/world-population/africa-population/ (Accessed 16/03/23)
72. Asia Population. 2023. Worldometer. URL https://www.worldometers.info/world-population/asia-population/ (Accessed 16/03/23)
73. Progress on drinking-water, sanitation and hygiene: 2017 update and SDG baselines. 2018. World Health Organization. URL https://www.who.int/publications/i/item/9789241512893 (Accessed 16/03/23)
74. Water Account, Australia, 2017-18. 2019. Australia: Australian Bureau of Statistics. Australian Government. URL https://www.abs.gov.au/statistics/environment/water/water-account-australia/2017-18 (Accessed 17/03/23)
75. Guerrant., 1988. Diarrhoeal Diseases. Bailliere Tindall. URL https://www.who.int/news-room/fact-sheets/detail/diarrhoeal-disease (Accessed 18/03/23)
76. Industrial Agricultural Pollution 101. 2022. Nrdc.org. URL https://www.nrdc.org/stories/industrial-agricultural-pollution-101 (Accessed 19/03/23)
77. Drinking water quality guidelines. 2022. World Health Organization (WHO). URL https://www.who.int/teams/environment-climate-change-and-health/water-sanitation-and-health/water-safety-and-quality/drinking-water-quality-guidelines (Accessed 20/03/23)
78. Water Quality and Wastewater. 2023. UN Water. URL https://www.unwater.org/water-facts/water-quality-and-wastewater (Accessed 12/04/23)
79. WASH in health care facilities: Global baseline report 2019. 2019. UNICEF. URL https://data.unicef.org/resources/wash-in-health-care-facilities/ (Accessed 12/04/23)
80. Drinking water data and reports. 2023. US Environmental Protection Agency. URL https://www.epa.gov/ground-water-and-drinking-water/drinking-water-data-and-reports (Accessed 12/04/23)
81. Acra, A., Karahagopian, Y., Raffoul, Z., Dajani, R., 1980. Disinfection of oral rehydration solutions by sunlight. Lancet. 316-8206, 1257–1258. https://doi.org/10.1016/s0140-6736(80)92530-1
82. Moreira, N. F. F., Narciso-da-Rocha, C., Polo-López, M. I., Pastrana-Martínez, L. M., Faria, J. L., Manaia, C. M., Fernández-Ibáñez, P., Nunes, O. C., Silva, A. M. T., 2018. Solar treatment (H2O2, TiO2-P25 and GO-TiO2 photocatalysis, photo-Fenton) of organic micropollutants, human pathogen indicators, antibiotic resistant bacteria and related genes in urban wastewater. Water Research. 135, 195–206. https://doi.org/10.1016/j.watres.2018.01.064
83. Berney, M., Weilenmann, H.-U., Simonetti, A., Egli, T., 2006. Efficacy of solar disinfection of Escherichia coli, Shigella flexneri, Salmonella Typhimurium and Vibrio

cholerae. Journal of Applied Microbiology. 101-4, 828–836. https://doi.org/10.1111/j.1365-2672.2006.02983.x
84. Mani, S. K., Kanjur, R., Bright Singh, I. S., Reed, R. H., 2006. Comparative effectiveness of solar disinfection using small-scale batch reactors with reflective, absorptive and transmissive rear surfaces. Water Research. 40-4, 721–727. https://doi.org/10.1016/j.watres.2005.11.039
85. McGuigan, K. G., Méndez-Hermida, F., Castro-Hermida, J. A., Ares-Mazás, E., Kehoe, S. C., Boyle, M., Sichel, C., Fernández-Ibáñez, P., Meyer, B. P., Ramalingham, S., Meyer, E. A., 2006. Batch solar disinfection inactivates oocysts of Cryptosporidium parvum and cysts of Giardia muris in drinking water. Journal of Applied Microbiology. 101-2, 453–463. https://doi.org/10.1111/j.1365-2672.2006.02935.x
86. McMichael, S., Fernández-Ibáñez, P., Byrne, J. A., 2021. A review of photoelectrocatalytic reactors for water and wastewater treatment. Water. 13-9, 1198. https://doi.org/10.3390/w13091198
87. Saravanan, A., Kumar, P. S., Jeevanantham, S., Karishma, S., Kiruthika, A. R., 2021. Photocatalytic disinfection of micro-organisms: Mechanisms and applications. Environmental Technology & Innovation. 24-101909, 101909. https://doi.org/10.1016/j.eti.2021.101909
88. Gamage McEvoy, J., Zhang, Z., 2014. Antimicrobial and photocatalytic disinfection mechanisms in silver-modified photocatalysts under dark and light conditions. Journal of Photochemistry and Photobiology C: Photochemistry Reviews. 19, 62–75. https://doi.org/10.1016/j.jphotochemrev.2014.01.001
89. Rahimi, R., Zargari, S., Yousefi, A., Yaghoubi Berijani, M., Ghaffarinejad, A., Morsali, A., 2015. Visible light photocatalytic disinfection of E. coli with TiO 2 –graphene nanocomposite sensitized with tetrakis(4-carboxyphenyl)porphyrin. Applied Surface Science. 355, 1098–1106. https://doi.org/10.1016/j.apsusc.2015.07.115
90. Yan, Y., Zhou, X., Lan, J., Li, Z., Zheng, T., Cao, W., Zhu, N., Liu, W., 2018. Efficient photocatalytic disinfection of Escherichia coli by N-doped TiO2 coated on coal fly ash cenospheres. Journal of Photochemistry and Photobiology. A, Chemistry. 367, 355–364. https://doi.org/10.1016/j.jphotochem.2018.08.045
91. Xiao, G., Zhang, X., Zhang, W., Zhang, S., Su, H., Tan, T., 2015. Visible-light-mediated synergistic photocatalytic antimicrobial effects and mechanism of Ag-nanoparticles@chitosan–TiO2 organic–inorganic composites for water disinfection. Applied Catalysis. B, Environmental. 170–171, 255–262. https://doi.org/10.1016/j.apcatb.2015.01.042
92. Wei, F., Li, J., Dong, C., Bi, Y., Han, X., 2020. Plasmonic Ag decorated graphitic carbon nitride sheets with enhanced visible-light response for photocatalytic water disinfection and organic pollutant removal. Chemosphere. 242-125201, 125201. https://doi.org/10.1016/j.chemosphere.2019.125201
93. Handwashing an effective tool to prevent COVID-19, other diseases. 2020. World Health Organisation. URL https://www.who.int/southeastasia/news/detail/15-10-2020-handwashing-an-effective-tool-to-prevent-covid-19-other-diseases (Accessed 20/03/23)
94. Water Conservation at EPA. 2020. US Environmental protection agency. URL https://www.epa.gov/greeningepa/water-conservation-epa (Accessed 20/03/23)
95. Summary of the safe drinking water act. 2018. US Environmental Protection Agency. URL https://www.epa.gov/laws-regulations/summary-safe-drinking-water-act (Accessed 20/03/23)

96. Summary of the Clean Water act. 2018. US Environmental Protection Agency. URL https://www.epa.gov/laws-regulations/summary-clean-water-act (Accessed 21/03/23)
97. International standards. 2023. United Nations. URL https://www.ohchr.org/en/special-procedures/sr-water-and-sanitation/international-standards (Accessed 21/03/23)
98. World Health Organization. 1971. International standards for drinking-water. World Health Organization. URL https://apps.who.int/iris/handle/10665/39989 (Accessed 22/03/23)
99. Directive (EU) 2020/2184 of the European Parliament and of the Council on 16 December 2020 on the quality of water intended for human consumption (recast). 2020. European Union. URL https://eur-lex.europa.eu/eli/dir/2020/2184/oj (Accessed 22/03/23)
100. Gray, N. F., 2014. Ultraviolet Disinfection. In Microbiology of Waterborne Diseases. Elsevier, 617–630. https://doi.org/10.1016/B978-0-12-415846-7.00034-2.
101. Kowalski, W., 2009. Ultraviolet germicidal irradiation handbook: UVGI for air and surface disinfection. Springer Berlin Heidelberg. https://link.springer.com/book/10.1007/978-3-642-01999-9
102. Chick, H., 1908. An investigation of the laws of disinfection. The Journal of Hygiene. 8-1, 92–158. https://doi.org/10.1017/s0022172400006987
103. Watson, H. E., 1908. A note on the variation of the rate of disinfection with change in the concentration of the disinfectant. The Journal of Hygiene. 8-4, 536–542. https://doi.org/10.1017/s0022172400015928
104. Hom, L. W., 1972. Kinetics of chlorine disinfection in an ecosystem. Journal of the Sanitary Engineering Division. 98-1, 183–194. https://doi.org/10.1061/jsedai.0001370
105. Shields, J. M., Hill, V. R., Arrowood, M. J., Beach, M. J., 2008. Inactivation of Cryptosporidium parvum under chlorinated recreational water conditions. Journal of Water and Health. 6-4, 513–520. https://doi.org/10.2166/wh.2008.068
106. Bolton J. R. Cotton C. A., 2008. Ultraviolet (UV) disinfection for Water Treatment, second edition. Awwa. URL https://engage.awwa.org/PersonifyEbusiness/Bookstore/Product-Details/productId/92298805
107. Ashok, A., & Khedikar, P. I. P., 2016. Overview of water disinfection by UV technology -A review. Water Research. https://doi.org/10.13140/RG.2.2.30976.25608
108. Song, K., Mohseni, M., Taghipour, F., 2016. Application of ultraviolet light-emitting diodes (UV-LEDs) for water disinfection: A review. Water Research. 94, 341–349. https://doi.org/10.1016/j.watres.2016.03.003
109. Chen, J., Loeb, S., Kim, J.-H., 2017. LED revolution: fundamentals and prospects for UV disinfection applications. Environmental Science: Water Research & Technology. 3-2, 188–202. https://doi.org/10.1039/c6ew00241b
110. Sánchez Pérez, J. A., Soriano-Molina, P., Rivas, G., García Sánchez, J. L., Casas López, J. L., Fernández Sevilla, J. M., 2017. Effect of temperature and photon absorption on the kinetics of micropollutant removal by solar photo-Fenton in raceway pond reactors. Chemical Engineering Journal (Lausanne, Switzerland: 1996). 310, 464–472. https://doi.org/10.1016/j.cej.2016.06.055
111. Qualls, R. G., Johnson, J. D., 1985. Modeling and efficiency of ultraviolet disinfection systems. Water Research. 19-8, 1039–1046. https://doi.org/10.1016/0043-1354(85)90374-4
112. Kim, S.-H., Shahbaz, H. M., Park, D., Chun, S., Lee, W., Oh, J.-W., Lee, D.-U., Park, J., 2017. A combined treatment of UV-assisted TiO2 photocatalysis and high hydrostatic

pressure to inactivate internalized murine norovirus. Innovative Food Science & Emerging Technologies: IFSET: The Official Scientific Journal of the European Federation of Food Science and Technology. 39, 188–196. https://doi.org/10.1016/j.ifset.2016.11.015
113. Greif, D., Galla, L., Ros, A., Anselmetti, D., 2008. Single cell analysis in full body quartz glass chips with native UV laser-induced fluorescence detection. Journal of Chromatography A. 1206-1, 83–88. https://doi.org/10.1016/j.chroma.2008.07.013
114. Lawal, O., Cosman, J., Pagan, J., 2018. UV-C LED devices and systems: Current and Future State, IUVA. 20-1, 22-28. URL https://uvledsource.org/wp-content/uploads/54-UVC-LED-Devices-and-Systems.pdf. (Accessed 01/03/23)
115. Kim, D.-K., Kang, D.-H., 2018. UVC LED irradiation effectively inactivates aerosolized viruses, bacteria, and fungi in a chamber-type air disinfection system. Applied and Environmental Microbiology. 84-17, AEM.00944-18. https://doi.org/10.1128/aem.00944-18
116. Bhardwaj, S. K., Singh, H., Deep, A., Khatri, M., Bhaumik, J., Kim, K.-H., Bhardwaj, N., 2021. UVC-based photoinactivation as an efficient tool to control the transmission of coronaviruses. The Science of the Total Environment. 792-148548, 148548. https://doi.org/10.1016/j.scitotenv.2021.148548
117. Lee, J.-H., Dinh, T.-V., Song, C.-S., Hong, K.-J., Kim, J.-C., 2021. A study on the effect of integrated ozone and UVC-LED approaches on the reduction of salmonella typhimurium bacteria in droplets. Asian Journal of Atmospheric Environment. 15-3, 65–74. https://doi.org/10.5572/ajae.2021.100
118. Lai, A. C. K., Nunayon, S. S., 2021. A new UVC-LED system for disinfection of pathogens generated by toilet flushing. Indoor Air. 31-2, 324–334. https://doi.org/10.1111/ina.12752
119. Winward, G. P., Avery, L. M., Frazer-Williams, R., Pidou, M., Jeffrey, P., Stephenson, T., Jefferson, B., 2008. A study of the microbial quality of grey water and an evaluation of treatment technologies for reuse. Ecological Engineering. 32-2, 187–197. https://doi.org/10.1016/j.ecoleng.2007.11.001
120. Winward, G. P., Avery, L. M., Stephenson, T., Jefferson, B., 2008. Ultraviolet (UV) disinfection of grey water: particle size effects. Environmental Technology. 29-2, 235–244. https://doi.org/10.1080/09593330802030069
121. SteriPen. 2020. Katadyn Products Inc. URL https://www.katadyngroup.com/int/en/brands/Steripen~b4908/overview (Accessed 01/04/23)
122. Klaran WR Series UVC LED Reactor. 2023. Crystal IS. URL https://cisuvc.com/products/klaran/uvc-led-systems/klaran-wr (Accessed 01/04/23)
123. PealAqua Deca. 2023. Aquisense Technologies. URL https://aquisense.com/products/water-treatment/pearl-aqua-deca/ (Accessed 02/04/23)
124. Koutchma, T., Popović, V., Green, A., 2019. Overview of ultraviolet (UV) LEDs technology for applications in food production. In Ultraviolet LED Technology for Food Applications. Elsevier, 1-23. https://doi.org/10.1016/B978-0-12-817794-5.00001-7.
125. Won, W.-S., Tran, L. G., Park, W.-T., Kim, K.-K., Shin, C. S., Kim, N., Kim, Y.-J., Yoon, Y.-J., 2018. UV-LEDs for the disinfection and bio-sensing applications. International Journal of Precision Engineering and Manufacturing. 19-12, 1901–1915. https://doi.org/10.1007/s12541-018-0218-5
126. Kebbi, Y., Muhammad, A. I., Sant'Ana, A. S., do Prado-Silva, L., Liu, D., Ding, T., 2020. Recent advances on the application of UV-LED technology for microbial inactivation:

Progress and mechanism. Comprehensive Reviews in Food Science and Food Safety. 19-6, 3501–3527. https://doi.org/10.1111/1541-4337.12645
127. Reynolds, K. J., de Kock, J. P., Tarassenko, L., Moyle, J. T. B., 1991. Temperature dependence of led and its theoretical effect on pulse oximetry. British Journal of Anaesthesia, 67-5, 638–643. https://doi.org/10.1093/bja/67.5.638
128. Yin, R., Shang, C., 2018. UV-LED 101: Fundamentals and applications of UV-LEDs in water treatment. URL https://www.semanticscholar.org/paper/1f6be49f8f8dd61dad46f0ba37beb7ffad8b6a01
129. Eppeldauer, G. P., Larason, T. C., Yoon, H. W., 2015. Standardization of UV LED measurements. In M. H. Kane, J. Jiao, N. Dietz, J.-J. Huang (Eds.), Fourteenth International Conference on Solid State Lighting and LED-based Illumination Systems. SPIE. https://doi.org/10.1117/12.2189714
130. Lyn, D.A., Chiu, K., Blatchley III, E.R., 1999. Numerical Modeling of Flow and Disinfection in UV Disinfection Channels. Journal of Environmental Engineering. 125. 10.1061/(ASCE)0733-9372(1999)125:1(17). https://doi.org/10.1061/(ASCE)0733-9372(1999)125:1(17)
131. Castro-Alférez, M., Polo-López, M. I., Marugán, J., Fernández-Ibáñez, P., 2017. Mechanistic modeling of UV and mild-heat synergistic effect on solar water disinfection. Chemical Engineering Journal (Lausanne, Switzerland: 1996). 316, 111–120. https://doi.org/10.1016/j.cej.2017.01.026
132. Pereira, A. R., Braga, D. F. O., Vassal, M., Gomes, I. B., Simões, M., 2023. Ultraviolet C irradiation: A promising approach for the disinfection of public spaces? The Science of the Total Environment. 879-163007, 163007. https://doi.org/10.1016/j.scitotenv.2023.163007
133. Keshavarzfathy, M., Taghipour, F., 2019. Computational modeling of ultraviolet light-emitting diode (UV-LED) reactor for water treatment. Water Research. 166-115022, 115022. https://doi.org/10.1016/j.watres.2019.115022
134. Koutchma, T., 2023. Evolvement of ultraviolet light (UV) technology for microbial and viral control in food applications. In Reference Module in Food Science. Elsevier. https://doi.org/10.1016/B978-0-12-822521-9.00085-X.
135. Koutchma, T., 2014. UV disinfection of air, water, and surfaces. Food Plant Safety. Elsevier, 15-30. https://doi.org/10.1016/B978-0-12-416620-2.00003-5.
136. Jasenak, B., 2018. Design consideration for creating an optimized UV LED system, IUVA News. 20-1, 10-13, URL https://uvsolutionsmag.com/stories/pdf/IUVA_2018_Quarter1_Jasenak-article_hyperlinks.pdf. (Accessed 14/03/23)
137. Guillard, C., 2000. Photocatalytic degradation of butanoic acid. Journal of Photochemistry and Photobiology. A, Chemistry. 135-1, 65–75. https://doi.org/10.1016/s1010-6030(00)00275-6
138. Park, S.-K., Jo, D.-M., Kang, M.-G., Khan, F., Hong, S. D., Kim, C. Y., Kim, Y.-M., Ryu, U.-C., 2021. Bactericidal effect of ultraviolet C light-emitting diodes: Optimization of efficacy toward foodborne pathogens in water. Journal of Photochemistry and Photobiology. B, Biology. 222-112277, 112277. https://doi.org/10.1016/j.jphotobiol.2021.112277
139. Brainard, G. C., Lewy, A. J., Menaker, M., Fredrickson, R. H., Miller, L. S., Weleber, R. G., Cassone, V., Hudson, D., 1988. Dose-response relationship between light irradiance and the suppression of plasma melatonin in human volunteers. Brain Research. 454-1/2, 212–218. https://doi.org/10.1016/0006-8993(88)90820-7

140. Becker, J., 2018. Irradiance or energy density: Understanding the difference between them and why both matter. Phoseon Technology White Paper. URL https://phoseon.com/wp-content/uploads/2019/03/Phoseon-White-Paper_April-2018_Power-vs-Irradiance.pdf. (Accessed 01/02/23)
141. Uppinakudru, A.P., 2020. The Impact of Irradiance and Energy Density in UV LED Curing Applications. ProPhotonix White Paper. URL https://www.prophotonix.com/resources/whitepapers/. (Accessed 10/02/23)
142. Paul Mills, P., Raymont, J., 2013. The UV LED paradigm shift. UV-LED by RadTech, 53-59. URL https://www.radtech.org/uvledbook/. (Accessed 02/02/23)
143. Nieland, S., Weizman, M., Mitrenga, D., Rotsch, P., Schaedel, M., Brodersen, O., Ortlepp, T., 2019. Discussion on reliability issues for UVB and UVC LED-based devices. M. Strassburg, J. K. Kim, M. R. Krames (Eds.). Light-Emitting Devices, Materials, and Applications. SPIE. https://doi.org/10.1117/12.2509418
144. Mitrenga, D., Brodersen, O., Schaedel, M., Ortlepp, T., Nieland, S., 2019. Enhanced heat dissipation for high-power UV LED devices using sintering. M. Strassburg, J. K. Kim, M. R. Krames (Eds.). Light-Emitting Devices, Materials, and Applications. SPIE. https://doi.org/10.1117/12.2509438
145. Piva, F., Fiorimonte, D., Trivellin, N., De Santi, C., Buffolo, M., Meneghesso, G., Zanoni, E., Meneghini, M., 2022. On the performance and reliability of state-of-the-art commercial UV-C LEDs for disinfection purposes. H. Morkoç, H. Fujioka, & U. T. Schwarz (Eds.). Gallium Nitride Materials and Devices XVII. SPIE. https://doi.org/10.1117/12.2625979
146. Heathcote, J., 2010. UV-LED Overview Part 1- Operation and Measurement. RadTech Report. 23-33. URL https://radtech.org/magazinearchives/Publications/RadTechReport/jul-aug-2010/UV-LED%20Basics%20Part%20I-Operation%20and%20Measurement.pdf.
147. Kheyrandish, A., Mohseni, M., Taghipour, F., 2018. Protocol for determining ultraviolet light emitting diode (UV-LED) fluence for microbial inactivation studies. Environmental Science & Technology. 52-13, 7390–7398. https://doi.org/10.1021/acs.est.7b05797
148. Kheyrandish, A., Taghipour, F., Mohseni, M., 2018. UV-LED radiation modeling and its applications in UV dose determination for water treatment. Journal of Photochemistry and Photobiology. A, Chemistry. 352, 113–121. https://doi.org/10.1016/j.jphotochem.2017.10.047
149. Imoberdorf, G., Mohseni, M., 2011. Modeling and experimental evaluation of vacuum-UV photoreactors for water treatment. Chemical Engineering Science. 66-6, 1159–1167. https://doi.org/10.1016/j.ces.2010.12.020
150. Anaya, M., Rand, B. P., Holmes, R. J., Credgington, D., Bolink, H. J., Friend, R. H., Wang, J., Greenham, N. C., Stranks, S. D., 2019. Best practices for measuring emerging light-emitting diode technologies. Nature Photonics. 13-12, 818–821. https://doi.org/10.1038/s41566-019-0543-y
151. Schreiber, P., Kudaev, S., Dannberg, P., Zeitner, U. D., 2005. Homogeneous LED-illumination using microlens arrays. R. Winston & R. J. Koshel (Eds.). Nonimaging Optics and Efficient Illumination Systems II. SPIE. https://doi.org/10.1117/12.618747
152. Cai, M., Yang, D., Mo, Y., Huang, J., Yin, L., Yang, L., Chen, X., Chen, W., Zhang, G., 2016. Determining the thermal stress limit of LED lamps using highly accelerated decay testing. Applied Thermal Engineering. 102, 1451–1461. https://doi.org/10.1016/j.applthermaleng.2016.04.012
153. Bickermann, M., 2016. Growth and properties of bulk AlN substrates. In III-Nitride Ultraviolet Emitters. Springer International Publishing, 27–46. https://doi.org/10.1007/978-3-319-24100-5_2.

154. Rass, J., Lobo-Ploch, N., 2016. Optical polarization and light extraction from UV LEDs. In III-Nitride Ultraviolet Emitters. Springer International Publishing, 137–170. https://doi.org/10.1007/978-3-319-24100-5_6.
155. Gutmann, E., Erfurth, F., Drewitz, A., Scheibe, A., Meinke, M. C., 2016. UV fluorescence detection and spectroscopy in chemistry and life sciences. III-Nitride Ultraviolet Emitters. Springer International Publishing, 351–386. https://doi.org/10.1007/978-3-319-24100-5_13.
156. Ha, H. N., Lino, C., Christie, M., Olivier, P., 2010. An interactive interface for lighting-by-example. Smart Graphics. Springer Berlin Heidelberg, 244–252. https://doi.org/10.1007/978-3-642-13544-6_23
157. Datasheet for ILT950UV, 2022. International Light Technologies. URL https://www.intl-lighttech.com/products/ilt950-spectroradiometer (Accessed 19/04/2022)
158. Input Optics, 2022. International Light Technologies. URL https://www.intl-lighttech.com/product-group/light-measurement-input-optics (Accessed 19/04/2022)
159. Valaskovic, G. A., Holton, M., Morrison, G. H., 1995. Parameter control, characterization, and optimization in the fabrication of optical fiber near-field probes. Applied Optics. 34-7), 1215–1228. https://doi.org/10.1364/AO.34.001215
160. Lin, C.-W., Hsu, K.-F., Hwang, J.-M., Lee, L.-L., Wu, T.-H., Yang, S.-Y., 2015b. Optical design of flexible LED panel lighting. 342. 145-150. https://doi.org/10.13140/2.1.2654.8002
161. Datasheet for PD300RM-8W, 2021. Ophir Optronics Solutions. URL https://www.ophiropt.com/laser--measurement/laser-power-energy-meters/products/LED-Measurement/Irradiance-and-Dosage-sensors/PD300RM-8W. (Accessed 28/12/2021)
162. Yoshida, E., Shizuma, K., Endo, S., Oka, T., 2002. Application of neural networks for the analysis of gamma-ray spectra measured with a Ge spectrometer. Nuclear Instruments & Methods in Physics Research. Section A, Accelerators, Spectrometers, Detectors and Associated Equipment. 484-1/3, 557–563. https://doi.org/10.1016/s0168-9002(01)01962-3
163. Sivaranjani, S., Velmurugan, S., Kathiresan, K., Karthik, M., Gunapriya, B., Gokul, C., Suresh, M., 2021. Visualization of virtual environment through labVIEW platform. Materials Today: Proceedings. 45, 2306–2312. https://doi.org/10.1016/j.matpr.2020.10.559
164. Mohiuddin, T., Nawrocki, M., Bitter, R., 2006. LabView: Advanced programming techniques, SECOND EDITION. CRC Press. https://doi.org/10.1201/9780849333255
165. Fan, J., Jing, Z., Cao, Y., Ibrahim, M. S., Li, M., Fan, X., Zhang, G., 2021. Prognostics of radiation power degradation lifetime for ultraviolet light-emitting diodes using stochastic data-driven models. Energy and AI. 4-100066, 100066. https://doi.org/10.1016/j.egyai.2021.100066
166. Datasheet for S120UV Power Head, 2021. ThorLabs. URL https://www.thorlabs.com/thorproduct.cfm?partnumber=S120VC (Accessed 28/12/2021)
167. Datasheet for S6060 SMD 265 nm, 2023. Bolb Inc. URL https://bolb.co/s6060-smd-265nm/ (Accessed 01/02/2023)
168. Datasheet for WD Series UVC LEDs, 2023. Crystal IS. URL https://klaran.com/images/Products/cis_klaran_wd_ds_031021.pdf. (Accessed 01/02/2023)

169. Datasheet for XBT-1313-UV ,2023. Luminus Devices. URL https://download.luminus.com/datasheets/Luminus_XBT-1313-UVC_Datasheet.pdf. (Accessed 01/02/2023)
170. Datasheet for XBT-3535-UV, 2023. Luminus Devices. URL https://download.luminus.com/datasheets/Luminus_XST-3535-UV_Datasheet.pdf. (Accessed 01/02/2023)
171. Datasheet for EOLS-310-697, 2023. EQ Photonics GmbH. URL https://www.eqphotonics.de/en/product/epigap-optronic-uv-led-eols-310-697/. (Accessed 01/02/2023)
172. UV LED Curing Systems, 2022. ProPhotonix IRL. URL https://www.prophotonix.com/led-and-laser-products/uv-led-curing-systems/ (Accessed 10/12/2022)
173. COBRA Clean FX–1, 2022. ProPhotonix IRL. URL https://www.prophotonix.com/led-and-laser-products/uvc-led-systems/uvc-led-system/ (Accessed 10/12/2022)
174. Möller, F., Blanco, A. M., Meyer, J., 2023. Characteristic leakage current of household devices and their impact on the tripping behaviour of residual current devices. Electric Power Systems Research. 214-108832, 108832. https://doi.org/10.1016/j.epsr.2022.108832
175. Huang, X., Wang, S., Zhu, S., Ye, Z., 2022. Spectroscopic characteristics and disinfection byproduct formation during UV-assisted photoelectrochemical degradation of humic acid. Journal of Cleaner Production. 375-134171, 134171. https://doi.org/10.1016/j.jclepro.2022.134171
176. Verrelst, J., Rivera Caicedo, J. P., Vicent, J., Morcillo Pallarés, P., Moreno, J., 2019. Approximating empirical surface reflectance data through emulation: Opportunities for synthetic scene generation. Remote Sensing. 11-2, 157. https://doi.org/10.3390/rs11020157
177. Choi, H. W., Dawson, M. D., 2005. Improved current spreading in 370nm AlGaN microring light emitting diodes. Applied Physics Letters. 86-5, 053504. https://doi.org/10.1063/1.1861130
178. Mukai, T., Yamada, M., Nakamura, S., 1999. Characteristics of InGaN-Based UV/Blue/Green/Amber/Red Light-Emitting Diodes. Japanese Journal of Applied Physics. 38-7R, 3976. https://doi.org/10.1143/jjap.38.3976
179. Raymont, J., 2002. Establishing and Maintaining a UV Process Window. RadTech Report, 14-25. URL https://radtech2020.com/wp-content/uploads/Papers/Measurement/ (Accessed 20/03/23)
180. Xiu, H., Zhang, Y., Fu, J., Ma, Z., Zhao, L., Feng, J., 2019. Degradation behavior of deep UV-LEDs studied by electro-optical methods and transmission electron microscopy. Current Applied Physics: The Official Journal of the Korean Physical Society. 19-1, 20–24. https://doi.org/10.1016/j.cap.2018.10.019
181. Meneghini, M., Trevisanello, L., Meneghesso, G., Zanoni, E., Rossi, F., Pavesi, M., Zehnder, U., Strauss, U., 2006. High-temperature failure of GaN LEDs related with passivation. Superlattices and Microstructures. 40-4/6, 405–411. https://doi.org/10.1016/j.spmi.2006.09.028
182. Muramoto, Y., Kimura, M., Nouda, S., 2014. Development and future of ultraviolet light-emitting diodes: UV-LED will replace the UV lamp. Semiconductor Science and Technology. 29-8, 084004. https://doi.org/10.1088/0268-1242/29/8/084004
183. Gong, Z., Gaevski, M., Adivarahan, V., Sun, W., Shatalov, M., Asif Khan, M., 2006. Optical power degradation mechanisms in AlGaN-based 280nm deep ultraviolet light-emitting diodes on sapphire. Applied Physics Letters. 88-12, 121106. https://doi.org/10.1063/1.2187429

184. Sandhu, A., 2007. The future of ultraviolet LEDs. Nature Photonics. 1-1, 38–38. https://doi.org/10.1038/nphoton.2006.36
185. Kheyrandish, A., Mohseni, M., Taghipour, F., 2017. Development of a method for the characterization and operation of UV-LED for water treatment. Water Research. 122, 570–579. https://doi.org/10.1016/j.watres.2017.06.015
186. Noori, A., Mahbub, P., Dvořák, M., Lucieer, A., Macka, M., 2018. Radiometric analysis of UV to near infrared LEDs for optical sensing and radiometric measurements in photochemical systems. Sensors and Actuators. B, Chemical. 262, 171–179. https://doi.org/10.1016/j.snb.2018.01.179
187. Borikar, D., Mohseni, M., Jasim, S., 2015. Evaluation and comparison of conventional and advanced oxidation processes for the removal of PPCPs and EDCs and their effect on THM-formation potentials. Ozone: Science & Engineering. 37-2, 154–169. https://doi.org/10.1080/01919512.2014.940028
188. L Leal-Junior, A., Avellar, L., Biazi, V., Soares, M.S., Frizera, A., et al., 2022. Multifunctional flexible optical waveguide sensor: on the bioinspiration for ultrasensitive sensors development. Opto-Electron Adv 5, 210098. https://doi.org/10.29026/oea.2022.210098
189. LED Products, 2021. UVphotonics. URL https://uvphotonics.de/products. (Accessed 28/12/2021)
190. INTERNATIONAL ATOMIC ENERGY AGENCY., 2016. Guidelines for development, validation and routine control of industrial radiation processes. In Guidelines for Development, Validation and Routine Control of Industrial Radiation Processes. IAEA. 4, 1–129. URL https://www.iaea.org/publications/8676/guidelines-for-development-validation-and-routine-control-of-industrial-radiation-processes
191. Ryer, A., 1997. Light measurement handbook. International Light. URL https://internationallight.com/ilt-light-measurement-handbook-tutorials (Accessed 20/03/23)
192. Diffey, B. L., 2002. Sources and measurement of ultraviolet radiation. Methods (San Diego, Calif.). 28-1, 4–13. https://doi.org/10.1016/s1046-2023(02)00204-9
193. Sholtes, K., Keliher, R., Linden, K. G., 2019. Standardization of a UV LED peak wavelength, emission spectrum, and irradiance measurement and comparison protocol. Environmental Science & Technology. 53-16, 9755–9763. https://doi.org/10.1021/acs.est.9b02567
194. Grum, F., Becherer, R. J., 1979. Optical radiation measurements. Volume 1 - Radiometry. New York. URL https://ui.adsabs.harvard.edu/abs/1979nyap.book.....G/abstract?
195. Pedrotti, F., Pedrotti, L., 2017. Introduction to Optics. Cambridge: Cambridge University Press. 3, 386-395. https://doi.org/10.1017/9781108552493.020.
196. Alves, L. C., Coelho, C. T., Corrêa, J. S. P. M., Menegotto, T., da Silva, T. F., de Souza, M. A., da Silva, E. M., de Lima, M. S., de Alvarenga, A. P. D., 2016. Characterisation of optical filters for broadband UVA radiometer. Journal of Physics. Conference Series. 733, 012062. https://doi.org/10.1088/1742-6596/733/1/012062
197. Blankenbach, K., 2016. Ambient Light. In Handbook of Visual Display Technology. Springer International Publishing, 3193–3226. https://doi.org/10.1007/978-3-319-14346-0_148.
198. Smith, W.J., 2008. Modern Optical Engineering: The Design of Optical Systems. New York: McGraw-Hill. 4. URL https://www.accessengineeringlibrary.com/content/book/9780071476874 (Accessed 12/04/23)

199. Michalsky, J. J., Harrison, L. C., Berkheiser, W. E., 1995. Cosine response characteristics of some radiometric and photometric sensors. Solar Energy (Phoenix, Ariz.). 54-6, 397–402. https://doi.org/10.1016/0038-092x(95)00017-l
200. Eppeldauer, George P., 2012. Standardization of Broadband UV Measurements for 365 nm LED Sources. Journal of Research of the National Institute of Standards and Technology. 117, 96–103. https://doi.org/10.6028/jres.117.004
201. Igoe, D. P., Parisi, A. V., Downs, N. J., Amar, A., Turner, J., 2018. Comparative signal to noise ratio as a determinant to select smartphone image sensor colour channels for analysis in the UVB. Sensors and Actuators. A, Physical. 272, 125–133. https://doi.org/10.1016/j.sna.2018.01.057
202. Datasheet for UV A/B Radiometer Dosimeter, 2021. Loctite. URL https://www.cureuv.com/products/loctite-uv-radiometer-uva-uvb-light-sources. (Accessed 28/12/2021)
203. Datasheet for UV-V Radiometer Dosimeter, 2021. Loctite. URL https://www.cureuv.com/products/loctite-uv-radiometer-visible-led-uvv-light-sources. (Accessed 28/12/2021)
204. Matsumura, K., Kagawa, Y., 2009. Spectral evaluation of local light scattering behavior in glass particle-dispersed epoxy matrix composite. Optical Materials. 31-6, 1027–1031. https://doi.org/10.1016/j.optmat.2008.11.010
205. Priya, S., Laha, R., Dantham, V. R., 2020. Wavelength-dependent angular shift and figure of merit of silver-based surface plasmon resonance biosensor. Sensors and Actuators. A, Physical. 315-112289, 112289. https://doi.org/10.1016/j.sna.2020.112289
206. Reshak, A. H., Shahimin, M. M., Murad, S. A. Z., Azizan, S., 2013. Simulation of Brillouin and Rayleigh scattering in distributed fibre optic for temperature and strain sensing application. Sensors and Actuators. A, Physical. 190, 191–196. https://doi.org/10.1016/j.sna.2012.11.034
207. Optical and electrical measurement of ultraviolet LEDs. 2023. Illuminating Engineering Society. New York, ANSI/IES LM-92-22. URL https://store.ies.org/product/lm-92-22-approved-method-optical-and-electrical-measurement-of-ultraviolet-leds/ (Accessed 10/04/23)
208. Zalewski, Edward F., 2010. RADIOMETRY AND PHOTOMETRY. Chap. 34 in Handbook of Optics: Volume II - Design, Fabrication, and Testing. Sources and Detectors. Radiometry and Photometry. New York: McGraw-Hill Professional. 3. URL https://www.accessengineeringlibrary.com/content/book/9780071498906/chapter/chapter34 (Accessed 01/04/23)
209. Datasheet for UVX-SE, 2022. Opsytec Dr Grobel. URL https://www.opsytec.com/products/uv-sensors/sensor-uvx-se (Accessed 18/04/2022)
210. Omar, A. F. B., Matjafri, M. Z. B., 2009. Turbidimeter design and analysis: a review on optical fiber sensors for the measurement of water turbidity. Sensors (Basel, Switzerland). 9-10, 8311–8335. https://doi.org/10.3390/s91008311
211. Wriedt, B., Ziegenbalg, D., 2020. Common pitfalls in chemical actinometry. Journal of Flow Chemistry. 10-1, 295–306. https://doi.org/10.1007/s41981-019-00072-7
212. Adick, H.-J., Schmidt, R., Brauer, H.-D., 1990. Chemical actinometry between 670 and 795 nm. Journal of Photochemistry and Photobiology. A, Chemistry. 54-1, 27–30. https://doi.org/10.1016/1010-6030(90)87004-u
213. Gardner, D. W. M., Shama, G., 1999. UV intensity measurement and modelling and disinfection performance prediction for irradiation of solid surfaces with UV light. Food and Bioproducts Processing. 77-3, 232–242. https://doi.org/10.1205/096030899532510

214. Chiu, K., Lyn, D.A., Savoye, P., Blatchley III, E.R.,1999. Integrated UV disinfection model based on particle tracking. J. Environ. Eng. 125-1, 7-16. American Society of Civil Engineers (ASCE). https://doi.org/10.1061/(ASCE)0733-9372(1999)125:1(7)
215. Wright, H. B., Lawryshyn, Y. A., 2000. An assessment of the bioassay concept for UV reactor validation. Proceedings of the Water Environment Federation. 2000-2, 378–400. https://doi.org/10.2175/193864700785372460
216. Ducoste, J. J., Liu, D., Linden, K., 2005. Alternative Approaches to Modeling Fluence Distribution and Microbial Inactivation in Ultraviolet Reactors: Lagrangian versus Eulerian. J. Environ. Eng. 131-10, 1393–1403. https://doi.org/10.1061/(asce)0733-9372(2005)131:10(1393)
217. Sozzi, D. A., Taghipour, F., 2006. UV reactor performance modeling by Eulerian and Lagrangian methods. Environmental Science & Technology. 40-5, 1609–1615. https://doi.org/10.1021/es051006x
218. Jacobm, S. M., Dranoff, J. S., 1970. Light intensity profiles in a perfectly mixed photoreactor. AIChE Journal. American Institute of Chemical Engineers. 16-3, 359–363. https://doi.org/10.1002/aic.690160309
219. Irazoqui, H. A., Cerdá, J., Cassano, A. E., 1973. Radiation profiles in an empty annular photoreactor with a source of finite spatial dimensions. AIChE Journal. American Institute of Chemical Engineers. 19-3, 460–467. https://doi.org/10.1002/aic.690190307
220. Blatchley, E. R., 1997. Numerical modelling of UV intensity: Application to collimated-beam reactors and continuous-flow systems. Water Research. 31-9, 2205–2218. https://doi.org/10.1016/s0043-1354(97)82238-5
221. Liu, D., Ducoste, J., Jin, S., Linden, K., 2004. Evaluation of alternative fluence rate distribution models. Journal of Water Supply Research and Technology—AQUA. 53-6, 391–408. https://doi.org/10.2166/aqua.2004.0031
222. Jenny, R. M., Simmons, O. D., III, Shatalov, M., Ducoste, J. J., 2014. Modeling a continuous flow ultraviolet Light Emitting Diode reactor using computational fluid dynamics. Chemical Engineering Science. 116, 524–535. https://doi.org/10.1016/j.ces.2014.05.020
223. Unluturk, S. K., Arastoopour, H., Koutchma, T., 2004. Modeling of UV dose distribution in a thin-film UV reactor for processing of apple cider. J. Food Eng. 65-1, 125–136. https://doi.org/10.1016/j.jfoodeng.2004.01.005
224. Keshavarzfathy, M., Taghipour, F., 2019. Computational modeling of ultraviolet light-emitting diode (UV-LED) reactor for water treatment. Water Research. 166-115022, 115022. https://doi.org/10.1016/j.watres.2019.115022
225. Spadoni, G., Bandini, E., Santarelli, F., 1978. Scattering effects in photosensitized reactions. Chemical Engineering Science. 33-4, 517–524. https://doi.org/10.1016/0009-2509(78)80012-8
226. Heinrich, J. M., Niizawa, I., Botta, F. A., Trombert, A. R., Irazoqui, H. A., 2012. Analysis and design of photobioreactors for microalgae production II: experimental validation of a radiation field simulator based on a Monte Carlo algorithm. Photochemistry and Photobiology. 88-4, 952–960. https://doi.org/10.1111/j.1751-1097.2012.01149.x
227. Cyr, I. H., Jones, C. E., Robinson, J., 2021. Detailed modelling of ultraviolet radiation (UV) from the interaction of multiple lamps in reactors, using radiative transfer techniques. https://doi.org/10.48550/ARXIV.2110.06275
228. Busciglio, A., Alfano, O. M., Scargiali, F., Brucato, A., 2016. A probabilistic approach to radiant field modeling in dense particulate systems. Chemical Engineering Science. 142, 79–88. https://doi.org/10.1016/j.ces.2015.11.025

229. Shah, J., Židonis, A., Aggidis, G., 2021. State of the art of UV water treatment technologies and hydraulic design optimisation using computational modelling. Journal of Water Process Engineering. 41-102099, 102099. https://doi.org/10.1016/j.jwpe.2021.102099
230. Keshavarzfathy, M., Taghipour, F., 2019b. Radiation modeling of ultraviolet light-emitting diode (UV-LED) for water treatment. Journal of Photochemistry and Photobiology. A, Chemistry. 377, 58–66. https://doi.org/10.1016/j.jphotochem.2019.03.030
231. Li, J., Zhang, X., Pan, Y., Zhuang, H., Yang, R., 2022. Comparison of Ray Tracing and Monte Carlo calculation algorithms for spine lesions treated with CyberKnife. Frontiers in Oncology. 12, 898175. https://doi.org/10.3389/fonc.2022.898175
232. Benacquista, R., Pourrouquet, P., Varotsou, A., Mangeret, R., Barillot, C., Santin, G., Evans, H., 2019. Comparison of Ray-Tracing and Reverse Monte-Carlo Methods: Application to GEO orbit. 2019 19th European Conference on Radiation and Its Effects on Components and Systems (RADECS). https://doi.org/10.1109/radecs47380.2019.9745642
233. Onigbajumo, A., Taghipour, A., Will, G., Chu Van, T., Couperthwaite, S., Steinberg, T., Rainey, T., 2022. Effects of process-thermal configuration on energy, exergy, and thermo-economic performance of solar driven supercritical water gasification. Energy Conversion and Management. 251-115002, 115002. https://doi.org/10.1016/j.enconman.2021.115002
234. Venkataraman, M. B., Asselineau, C.-A., Rahbari, A., Pye, J., 2019. Modelling of a 50 MWth on-sun reactor for SCWG of algae: Understanding the design constraints. SOLARPACES 2018: International Conference on Concentrating Solar Power and Chemical Energy Systems. https://doi.org/10.1063/1.5117697
235. Bergman, R. S., 2021. Germicidal UV sources and systems. Photochemistry and Photobiology. 97-3, 466–470. https://doi.org/10.1111/php.13387
236. Introduction to 3Delight, 2022. Illumination Research, URL https://www.3delight.com/documentation/display/3DFM9/Introduction (Accessed 05th October 2022)
237. POV-Ray documentation, 2022. Persistence of Vision Raytracer Pty. Ltd. URL http://www.povray.org/documentation/3.7.0/ (Accessed 05th October 2022)
238. Optical design program and user's manual, 2011. Radiant ZEMAX LLC. (Available on tool) URL https://www.zemax.com/blogs/eguides/designing-for-manufacturability (Accessed 05th October 2022)
239. Moreno, J., Casado, C., Marugán, J., 2019. Improved discrete ordinate method for accurate simulation radiation transport using solar and LED light sources. Chemical Engineering Science. 205, 151–164. https://doi.org/10.1016/j.ces.2019.04.034
240. Martin, C. A., Camera-Roda, G., Santarelli, F., 1999. Effective design of photocatalytic reactors: influence of radiative transfer on their performance. Catalysis Today. 48-1/4, 307–313. https://doi.org/10.1016/s0920-5861(98)00386-1
241. Cassano, A. E., Martin, C. A., Brandi, R. J., Alfano, O. M., 1995. Photoreactor analysis and design: Fundamentals and applications. Industrial & Engineering Chemistry Research. 34-7, 2155–2201. https://doi.org/10.1021/ie00046a001
242. Mueses, M. A., Machuca-Martinez, F., Hernández-Ramirez, A., Li Puma, G., 2015. Effective radiation field model to scattering – Absorption applied in heterogeneous photocatalytic reactors. Chemical Engineering Journal (Lausanne, Switzerland: 1996). 279, 442–451. https://doi.org/10.1016/j.cej.2015.05.056
243. Datasheet for COBRA Clean FX–1, 2022. ProPhotonix. URL https://www.prophotonix.com/led-and-laser-products/uvc-led-systems/uvc-led-system/ (Accessed 19/04/2022)
244. Hale, G. M., Querry, M. R., 1973. Optical Constants of Water in the 200-nm to 200-microm Wavelength Region. Applied Optics. 12-3, 555–563. https://doi.org/10.1364/AO.12.000555

245. Rabani, J., Mamane, H., Pousty, D., Bolton, J. R., 2021. Practical chemical actinometry-A review. Photochemistry and Photobiology. 97-5, 873–902. https://doi.org/10.1111/php.13429
246. Kuhn, H. J., Braslavsky, S. E., Schmidt, R., 2004. Chemical actinometry (IUPAC Technical Report). Pure and Applied Chemistry. 76-12, 2105–2146. https://doi.org/10.1351/pac200476122105
247. Kuhn, H., Braslavsky, S. Schmidt, R., 1989. Chemical actinometry. Pure and Applied Chemistry. 61-2, 187-210. https://doi.org/10.1351/pac198961020187
248. Hatchard, C. G., Parker, C. A., 1956. A new sensitive chemical actinometer - II. Potassium ferrioxalate as a standard chemical actinometer. Proceedings of the Royal Society of London. 235-1203, 518–536. https://doi.org/10.1098/rspa.1956.0102
249. ANSYS User and Theory Guide, 2012. ANSYS. Release 14.5. URL https://www.academia.edu/38091499/ANSYS_Fluent_Theory_Guide
250. Ciddor, P. E., 1996. Refractive index of air: new equations for the visible and near infrared. Applied Optics. 35-9, 1566–1573. https://doi.org/10.1364/AO.35.001566
251. Keiser, G., 2016. Fundamentals of light sources. In Graduate Texts in Physics. Springer Singapore, 91–118. https://doi.org/10.1007/978-981-10-0945-7_4
252. Bass, M., DeCusatis, C., Enoch, J. M., Lakshminarayanan, V., Li, G., MacDonald, C. A., Mahajan, V. N., Van Stryland, E. W., 2009. Handbook of optics, third edition volume II: Design, fabrication and testing, sources and detectors, radiometry and photometry (3rd ed.). McGraw-Hill Professional. URL https://www.accessengineeringlibrary.com/content/book/9780071498906
253. Li, X., Cai, M., Wang, L., Niu, F., Yang, D., Zhang, G., 2019. Evaluation survey of microbial disinfection methods in UV-LED water treatment systems. The Science of the Total Environment. 659, 1415–1427. https://doi.org/10.1016/j.scitotenv.2018.12.344
254. Pichel, N., Vivar, M., Fuentes, M., 2019. The problem of drinking water access: A review of disinfection technologies with an emphasis on solar treatment methods. Chemosphere. 218, 1014–1030. https://doi.org/10.1016/j.chemosphere.2018.11.205
255. Beck, S. E., Ryu, H., Boczek, L. A., Cashdollar, J. L., Jeanis, K. M., Rosenblum, J. S., Lawal, O. R., Linden, K. G., 2017. Evaluating UV-C LED disinfection performance and investigating potential dual-wavelength synergy. Water Research. 109, 207–216. https://doi.org/10.1016/j.watres.2016.11.024
256. Hull, N. M., Linden, K. G., 2018. Synergy of MS2 disinfection by sequential exposure to tailored UV wavelengths. Water Research. 143, 292–300. https://doi.org/10.1016/j.watres.2018.06.017
257. Nyangaresi, P. O., Qin, Y., Chen, G., Zhang, B., Lu, Y., Shen, L., 2019. Comparison of the performance of pulsed and continuous UVC-LED irradiation in the inactivation of bacteria. Water Research. 157, 218–227. https://doi.org/10.1016/j.watres.2019.03.080
258. Woo, H., Beck, S. E., Boczek, L. A., Carlson, K., Brinkman, N. E., Linden, K. G., Lawal, O. R., Hayes, S. L., Ryu, H., 2019. Efficacy of inactivation of human enteroviruses by dual-wavelength germicidal ultraviolet (UV-C) light emitting diodes (LEDs). Water. 11-6, 1–1131. https://doi.org/10.3390/w11061131
259. Green, A., Popović, V., Pierscianowski, J., Biancaniello, M., Warriner, K., Koutchma, T., 2018. Inactivation of Escherichia coli , Listeria and Salmonella by single and multiple wavelength ultraviolet-light emitting diodes. Innovative Food Science & Emerging Technologies: IFSET: The Official Scientific Journal of the European Federation of Food Science and Technology. 47, 353–361. https://doi.org/10.1016/j.ifset.2018.03.019

260. Li, G.-Q., Wang, W.-L., Huo, Z.-Y., Lu, Y., & Hu, H.-Y., 2017. Comparison of UV-LED and low pressure UV for water disinfection: Photoreactivation and dark repair of Escherichia coli. Water Research. 126, 134–143. https://doi.org/10.1016/j.watres.2017.09.030
261. Nakahashi, M., Mawatari, K., Hirata, A., Maetani, M., Shimohata, T., Uebanso, T., Hamada, Y., Akutagawa, M., Kinouchi, Y., Takahashi, A., 2014. Simultaneous irradiation with different wavelengths of ultraviolet light has synergistic bactericidal effect on Vibrio parahaemolyticus. Photochemistry and photobiology. 90-6, 1397–1403. https://doi.org/10.1111/php.12309
262. Matafonova, G., & Batoev, V., 2022. Dual-wavelength light radiation for synergistic water disinfection. The Science of the Total Environment. 806-3, 151233. https://doi.org/10.1016/j.scitotenv.2021.151233
263. Nyangaresi, P. O., Rathnayake, T., Beck, S. E., 2023. Evaluation of disinfection efficacy of single UV-C, and UV-A followed by UV-C LED irradiation on Escherichia coli, B. spizizenii and MS2 bacteriophage, in water. The Science of the Total Environment. 859-160256, 160256. https://doi.org/10.1016/j.scitotenv.2022.160256
264. Gao, Z.-C., Lin, Y.-L., Xu, B., Xia, Y., Hu, C.-Y., Cao, T.-C., Zou, X.-Y., Gao, N.-Y., 2019. Evaluating iopamidol degradation performance and potential dual-wavelength synergy by UV-LED irradiation and UV-LED/chlorine treatment. Chemical Engineering Journal. 360, 806–816. https://doi.org/10.1016/j.cej.2018.12.022A
265. Chevremont, A.-C., Farnet, A.-M., Sergent, M., Coulomb, B., Boudenne, J.-L., 2012. Multivariate optimization of fecal bioindicator inactivation by coupling UV-A and UV-C LEDs. Desalination. 285, 219–225. https://doi.org/10.1016/j.desal.2011.10.006
266. Würtele, M. A., Kolbe, T., Lipsz, M., Külberg, A., Weyers, M., Kneissl, M., Jekel, M., 2011. Application of GaN-based ultraviolet-C light emitting diodes--UV LEDs--for water disinfection. Water Research. 45-3, 1481–1489. https://doi.org/10.1016/j.watres.2010.11.015
267. Li, G.-Q., Huo, Z.-Y., Wu, Q.-Y., Lu, Y., Hu, H.-Y., 2018. Synergistic effect of combined UV-LED and chlorine treatment on Bacillus subtilis spore inactivation. The Science of the Total Environment. 639, 1233–1240. https://doi.org/10.1016/j.scitotenv.2018.05.240
268. Song, K., Taghipour, F., Mohseni, M., 2019. Microorganisms inactivation by wavelength combinations of ultraviolet light-emitting diodes (UV-LEDs). The Science of the Total Environment. 665, 1103–1110. https://doi.org/10.1016/j.scitotenv.2019.02.041
269. Kojima, M., Mawatari, K., Emoto, T., Nishisaka-Nonaka, R., Bui, T. K. N., Shimohata, T., Uebanso, T., Akutagawa, M., Kinouchi, Y., Wada, T., Okamoto, M., Ito, H., Tojo, K., Daidoji, T., Nakaya, T., Takahashi, A., 2020. Irradiation by a combination of different peak-wavelength ultraviolet-light emitting diodes enhances the inactivation of influenza A viruses. Microorganisms. 8-7, 1014. https://doi.org/10.3390/microorganisms8071014
270. Chevremont, A.-C., Farnet, A.-M., Coulomb, B., Boudenne, J.-L., 2012. Effect of coupled UV-A and UV-C LEDs on both microbiological and chemical pollution of urban wastewaters. The Science of the Total Environment. 426, 304–310. https://doi.org/10.1016/j.scitotenv.2012.03.043
271. Nyangaresi, P. O., Qin, Y., Chen, G., Zhang, B., Lu, Y., Shen, L., 2018. Effects of single and combined UV-LEDs on inactivation and subsequent reactivation of E. coli in water disinfection. Water Research. 147, 331–341. https://doi.org/10.1016/j.watres.2018.10.014

272. Datasheet for Milli-Q IQ 7003, 2023. Sigma Aldrich. URL https://www.sigmaaldrich.com/deepweb/assets/sigmaaldrich/product/documents/136/926/iq7003-dfs-scorecard-visual.pdf (Accessed 16/04/2023)
273. Datasheet for Sodium Chloride SO0227, 2023. Scharlab. URL https://www.scharlab.com/docs/tds/descargarpdf.php?path=SO0227_TDS_EN.pdf&idid=EN&ref=SO02270500 (Accessed 16/04/2023)
274. Datasheet for LB Broth, 2023. Scharlau. URL https://www.scharlabmagyarorszag.hu/katalogus/02-385_TDS_EN.pdf (Accessed 16/04/2023)
275. Datasheet for Orbital Shaker-Incubator, 2023. Biosan. URL https://biosan.lv/products/es-20/ (Accessed 16/04/2023)
276. Datasheet for Minicen centrifuge, 2023. Orto Alresa. URL https://ortoalresa.com/en/centrifugas/minicen/ (Accessed 16/04/2023)
277. Datasheet for LB Agar (Miller), 2023. Scharlau. URL https://www.scharlab.com/productos-producto-catalogo-productos-detalle-referencia.php?r=01-385-500 (Accessed 16/04/2023)
278. Datasheet for Automatic colony counter 4905002, 2023. Quimega S. L. URL https://www.medicalexpo.com/prod/jp-selecta/product-79782-1015769.html (Accessed 16/04/2023)
279. Datasheet for Flojet pump, 2023. RS Pro. URL https://my.rs-online.com/web/p/water-pumps/0266597 (Accessed 16/04/2023)
280. Ahmad, S. I., 2017. Reactive oxygen species in biology and human health. CRC Press. https://doi.org/10.1201/b20228
281. Casado, C., García-Gil, Á., van Grieken, R., Marugán, J., 2019. Critical role of the light spectrum on the simulation of solar photocatalytic reactors. Applied Catalysis. B, Environmental. 252, 1–9. https://doi.org/10.1016/j.apcatb.2019.04.004
282. Koivunen, J., Heinonen-Tanski, H., 2005. Inactivation of enteric microorganisms with chemical disinfectants, UV irradiation and combined chemical/UV treatments. Water Research. 39-8, 1519–1526. https://doi.org/10.1016/j.watres.2005.01.021
283. Student., 1908. The Probable Error of a Mean. Biometrika. 6-1, 1. https://doi.org/10.2307/2331554
284. Simkus, J., 2022. What is ANOVA (Analysis Of Variance). Simply Psychology. Web Article. URL www.simplypsychology.org/anova.html (Accessed 23/03/23)
285. Reichardt, C. S., 2019. Quasi-experimentation: A guide to design and analysis. Guilford Publications. URL https://www.guilford.com/books/Quasi-Experimentation/Charles-Reichardt/9781462540204
286. Error Propagation., 2020. Uncertainty Analysis for Engineers and Scientists, 181–232. https://doi.org/10.1017/9781108777513.006
287. Keen, O., Bolton, J., Litter, M., Bircher, K., Oppenländer, T., 2018. Standard reporting of Electrical Energy per Order (E EO) for UV/H2O2 reactors (IUPAC Technical Report). Pure and Applied Chemistry. 90-9, 1487–1499. https://doi.org/10.1515/pac-2017-0603
288. Ramsay, I. A., Niedziela, J. C., Ogden, I. D., 2000. The synergistic effect of excimer and low-pressure mercury lamps on the disinfection of flowing water. Journal of Food Protection. 63-11, 1529–1533. https://doi.org/10.4315/0362-028x-63.11.1529
289. Payne, G., Sancar, A., 1990. Absolute action spectrum of E-FADH2 and E-FADH2-MTHF forms of Escherichia coli DNA photolyase. Biochemistry. 29-33, 7715–7727. https://doi.org/10.1021/bi00485a021
290. Kelner, A., 1949. Effect of visible light on the recovery of Streptomyces griseus conidia from ultra-violet irradiation injury. Proceedings of the National Academy of Sciences of the United States of America. 35-2, 73–79. https://doi.org/10.1073/pnas.35.2.73

291. Kuball, H.-G., Höfer, T., Kiesewalter, S., 2017. Chiroptical Spectroscopy. General Theory. In Encyclopaedia of Spectroscopy and Spectrometry. Elsevier, 217–231. https://doi.org/10.1016/B978-0-12-409547-2.04980-5.
292. Rastogi, R. P., Richa, Kumar, A., Tyagi, M. B., Sinha, R. P., 2010. Molecular mechanisms of ultraviolet radiation-induced DNA damage and repair. Journal of Nucleic Acids. 2010, 592980. https://doi.org/10.4061/2010/592980
293. Cockell, C. S., Airo, A., 2002. Origins of Life and Evolution of the Biosphere: The Journal of the International Society for the Study of the Origin of Life. 32-3, 255–274. https://doi.org/10.1023/a:1016507810083
294. Hiraku, Y., Ito, K., Hirakawa, K., Kawanishi, S., 2007. Photosensitized DNA damage and its protection via a novel mechanism. Photochemistry and Photobiology. 83-1, 205–212. https://doi.org/10.1562/2006-03-09-IR-840
295. Eisenstark, A., Calcutt, M. J., Becker-Hapak, M., Ivanova, A., 1996. Role of Escherichia coli rpoS and associated genes in defense against oxidative damage. Free Radical Biology & Medicine. 21-7, 975–993. https://doi.org/10.1016/s0891-5849(96)00154-2
296. You, C., Dai, X., Yuan, B., Wang, J., Wang, J., Brooks, P. J., Niedernhofer, L. J., Wang, Y., 2012. A quantitative assay for assessing the effects of DNA lesions on transcription. Nature Chemical Biology. 8-10, 817–822. https://doi.org/10.1038/nchembio.1046
297. Wang, Y., Wang, Y., Wang, Y., Murray, C. K., Hamblin, M. R., Hooper, D. C., Dai, T., 2017. Antimicrobial blue light inactivation of pathogenic microbes: State of the art. Drug Resistance Updates: Reviews and Commentaries in Antimicrobial and Anticancer Chemotherapy. 33–35, 1–22. https://doi.org/10.1016/j.drup.2017.10.002
298. Biener, G., Masson-Meyers, D. S., Bumah, V. V., Hussey, G., Stoneman, M. R., Enwemeka, C. S., Raicu, V., 2017. Blue/violet laser inactivates methicillin-resistant Staphylococcus aureus by altering its transmembrane potential. Journal of Photochemistry and Photobiology. B, Biology. 170, 118–124. https://doi.org/10.1016/j.jphotobiol.2017.04.002
299. Kumar, A., Ghate, V., Kim, M.-J., Zhou, W., Khoo, G. H., Yuk, H.-G., 2015. Kinetics of bacterial inactivation by 405nm and 520nm light emitting diodes and the role of endogenous coproporphyrin on bacterial susceptibility. Journal of Photochemistry and Photobiology. B, Biology. 149, 37–44. https://doi.org/10.1016/j.jphotobiol.2015.05.005
300. Maclean, M., MacGregor, S. J., Anderson, J. G., Woolsey, G., 2008. High-intensity narrow-spectrum light inactivation and wavelength sensitivity of Staphylococcus aureus. FEMS Microbiology Letters. 285-2, 227–232. https://doi.org/10.1111/j.1574-6968.2008.01233.x
301. Tang, W. Z., Sillanpää, M., 2015. Bacteria sensitivity index of UV disinfection of bacteria with shoulder effect. Journal of Environmental Chemical Engineering. 3-4, 2588–2596. https://doi.org/10.1016/j.jece.2015.09.010
302. Kowalski, W., 2009. Mathematical modeling of UV disinfection. In Ultraviolet Germicidal Irradiation Handbook, Springer Berlin Heidelberg, 51-72. https://doi.org/10.1007/978-3-642-01999-9_3
303. Vermeulen, N., Keeler, W. J., Nandakumar, K., Leung, K. T., 2008. The bactericidal effect of ultraviolet and visible light on Escherichia coli. Biotechnology and Bioengineering. 99-3, 550–556. https://doi.org/10.1002/bit.21611
304. Lee, H., Jin, Y., Hong, S., 2018. Understanding possible underlying mechanism in declining germicidal efficiency of UV-LED reactor. Journal of Photochemistry and Photobiology. B, Biology. 185, 136–142. https://doi.org/10.1016/j.jphotobiol.2018.06.001
305. Oguma, K., Kita, R., Sakai, H., Murakami, M., Takizawa, S., 2013. Application of UV light emitting diodes to batch and flow-through water disinfection systems. Desalination. 328, 24–30. https://doi.org/10.1016/j.desal.2013.08.014

306. Mamane-Gravetz, H., Linden, K. G., 2005. Relationship between physiochemical properties, aggregation and u.v. inactivation of isolated indigenous spores in water. Journal of Applied Microbiology. 98-2, 351–363. https://doi.org/10.1111/j.1365-2672.2004.02455.x
307. Mattle, M. J., & Kohn, T., 2012. Inactivation and tailing during UV254 disinfection of viruses: contributions of viral aggregation, light shielding within viral aggregates, and recombination. Environmental Science & Technology. 46-18, 10022–10030. https://doi.org/10.1021/es302058v
308. Papciak, D., Domoń, A., Zdeb, M., Tchórzewska-Cieślak, B., Konkol, J., Sočo, E., 2022. Mechanism of biofilm formation on installation materials and its impact on the quality of tap water. Water. 14-15, 2401. https://doi.org/10.3390/w14152401
309. von Recklinghausen, M., 1914. Sterilization of water by ultra-Violet rays of the mercury-vapor quartz lamp. Transactions of the American Institute of Electrical Engineers. XXXIII-2, 1217–1242. https://doi.org/10.1109/t-aiee.1914.4765179
310. Favre, A., Hajnsdorf, E., Thiam, K., Caldeira de Araujo, A., 1985. Mutagenesis and growth delay induced in Escherichia coli by near-ultraviolet radiations. Biochimie. 67-3/4, 335–342. https://doi.org/10.1016/s0300-9084(85)80076-6
311. Eisenstark, A., 1987. Mutagenic and lethal effects of near-ultraviolet radiation (290-400 nm) on bacteria and phage. Environmental and Molecular Mutagenesis. 10-3, 317–337. https://doi.org/10.1002/em.2850100311
312. Bolton, J. R., Linden, K. G., 2003. Standardization of Methods for Fluence (UV Dose) Determination in Bench-Scale UV Experiments. Journal of Environmental Engineering. 129-3, 209–215. https://doi.org/10.1061/(asce)0733-9372(2003)129:3(209)
313. Daneshvar, N., Aleboyeh, A., & Khataee, A. R., 2005. The evaluation of electrical energy per order (E(Eo)) for photooxidative decolorization of four textile dye solutions by the kinetic model. Chemosphere. 59-6, 761–767. https://doi.org/10.1016/j.chemosphere.2004.11.012
314. Wastewater Contaminants Research, 2023. United States Environmental Protection Agency. URL https://www.epa.gov/water-research/wastewater-contaminants-research (Accessed 18/04/2023)
315. Urban Wastewater, 2023. Article. European Commission. URL https://environment.ec.europa.eu/topics/water/urban-wastewater_en (Accessed 18/04/2023)
316. Tran, N. H., Ngo, H. H., Urase, T., Gin, K. Y.-H., 2015. A critical review on characterization strategies of organic matter for wastewater and water treatment processes. Bioresource Technology. 193, 523–533. https://doi.org/10.1016/j.biortech.2015.06.091
317. Rodríguez-Chueca, J., Mesones, S., Marugán, J., 2019. Hybrid UV-C/microfiltration process in membrane photoreactor for wastewater disinfection. Environmental Science and Pollution Research International. 26-36, 36080–36087. https://doi.org/10.1007/s11356-018-3262-x
318. Philippe, K. K., Timmers, R., van Grieken, R., Marugan, J., 2016. Photocatalytic disinfection and removal of emerging pollutants from effluents of biological wastewater treatments, using a newly developed large-scale solar simulator. Industrial & Engineering Chemistry Research. 55-11, 2952–2958. https://doi.org/10.1021/acs.iecr.5b04927
319. Giannakis, S., López, M. I. P., Spuhler, D., Pérez, J. A. S., Ibáñez, P. F., Pulgarin, C., 2016. Solar disinfection is an augmentable, in situ-generated photo-Fenton reaction—Part 2: A review of the applications for drinking water and wastewater disinfection. Applied Catalysis. B, Environmental. 198, 431–446. https://doi.org/10.1016/j.apcatb.2016.06.007

320. Collivignarelli, M. C., Abbà, A., Miino, M. C., Caccamo, F. M., Torretta, V., Rada, E. C., Sorlini, S., 2020. Disinfection of wastewater by UV-based treatment for reuse in a circular economy perspective. Where are we at? International Journal of Environmental Research and Public Health. 18-1, 77. https://doi.org/10.3390/ijerph18010077
321. Caretti, C., Lubello, C., 2003. Wastewater disinfection with PAA and UV combined treatment: a pilot plant study. Water Research. 37-10, 2365–2371. https://doi.org/10.1016/S0043-1354(03)00025-3
322. Kang, J.-W., & Kang, D.-H., 2019. The synergistic bactericidal mechanism of simultaneous treatment with a 222-nanometer krypton-chlorine excilamp and a 254-nanometer low-pressure mercury lamp. Applied and Environmental Microbiology. 85-1. https://doi.org/10.1128/AEM.01952-18
323. BOE-A-2007-21092 Real Decreto 1620/2007., 2007, por el que se establece el régimen jurídico de la reutilización de las aguas depuradas. https://www.boe.es/eli/es/rd/2007/12/07/1620
324. Tchobanoglous, G., Burton, F., 1990. Wastewater engineering: Treatment, Disposal, Reuse. McGraw-Hill Inc.,US. URL https://www.iberlibro.com/9780070416901/Wastewater-Engineering-Treatment-Disposal-Reuse-0070416907/plp (Accessed 18/04/23)
325. Mecha, A. C., Onyango, M. S., Ochieng, A., Momba, M. N. B., 2017. Evaluation of synergy and bacterial regrowth in photocatalytic ozonation disinfection of municipal wastewater. The Science of the Total Environment. 601–602, 626–635. https://doi.org/10.1016/j.scitotenv.2017.05.204
326. Rodríguez-Chueca, J., Garcia-Cañibano, C., Sarro, M., Encinas, Á., Medana, C., Fabbri, D., Calza, P., Marugán, J., 2019. Evaluation of transformation products from chemical oxidation of micropollutants in wastewater by photoassisted generation of sulfate radicals. Chemosphere. 226, 509–519. https://doi.org/10.1016/j.chemosphere.2019.03.152
327. Datasheet for MacConkey Agar, 2023. Condalab. URL https://www.condalab.com/int/en/dehydrated-culture-media/60-15217-macconkey-agar-ep-usp-iso.html (Accessed 15/04/23)
328. Datasheet for Tryptic Soy Agar, 2023. Scharlab. URL https://www.scharlab.com/productos-producto-catalogo-productos-detalle-referencia.php?r=01-200-500 (Accessed 15/04/23)
329. Rodríguez-Chueca, J., Varella Della Giustina, S., Rocha, J., Fernandes, T., Pablos, C., Encinas, Á., Barceló, D., Rodríguez-Mozaz, S., Manaia, C. M., Marugán, J., 2019. Assessment of full-scale tertiary wastewater treatment by UV-C based-AOPs: Removal or persistence of antibiotics and antibiotic resistance genes? The Science of the Total Environment. 652, 1051–1061. https://doi.org/10.1016/j.scitotenv.2018.10.223
330. Jin, X., Li, Z., Xie, L., Zhao, Y., Wang, T., 2013. Synergistic effect of ultrasonic pre-treatment combined with UV irradiation for secondary effluent disinfection. Ultrasonics Sonochemistry. 20-6, 1384–1389. https://doi.org/10.1016/j.ultsonch.2013.03.010
331. Datasheet for pH 50 VioLab, 2023. VioLab. URL https://www.xsinstruments.com/phmeters/50101012/ph-50-violab-benchtop-phmeter-without-electrode.htm (Accessed 15/04/23)
332. Datasheet for 712 conductometer, 2023. Metrohm. URL https://www.metrohm.com/es_es/products/8/7121/87121003.html (Accessed 15/04/23)
333. Datasheet for Cary 5000 UV-Vis-NIR Spectrophotometer, 2023. Agilent. URL https://www.agilent.com/en/product/molecular-spectroscopy/uv-vis-uv-vis-nir-spectroscopy/uv-vis-uv-vis-nir-systems/cary-5000-uv-vis-nir (Accessed 15/04/23)

334. Sillanpää, M., Matilainen, A., Lahtinen, T., 2015. Characterization of NOM. In Natural Organic Matter in Water. Elsevier, 17–53. https://doi.org/10.1016/B978-0-12-801503-2.00002-1.
335. Miralles-Cuevas, S., De la Obra, I., Gualda-Alonso, E., Soriano-Molina, P., Casas López, J. L., & Sánchez Pérez, J. A., 2021. Simultaneous disinfection and organic microcontaminant removal by UVC-LED-driven advanced oxidation processes. Water. 13-11, 1507. https://doi.org/10.3390/w13111507
336. Park, Y., Sillanpää, M., Anderson, L., Gagnon, G. A., Matilainen, A., 2023. Characterization of natural organic matter. In Natural Organic Matter in Water. Elsevier, 43–92. https://doi.org/10.1016/B978-0-12-824274-2.00002-8
337. Datasheet for Millex-GN for Samplicity G2, 0.20 µm, nylon, 33 mm, non-sterile, 2023. Merck Millipore. URL https://www.merckmillipore.com/ES/es/product/Millex-GN-for-Samplicity-G2-0.20m-nylon-33mm-non-sterile. (Accessed 15/04/23)
338. Datasheet for TOC-L, 2023. Shimadze. URL https://www.shimadzu.com/an/products/total-organic-carbon-analysis/toc-analysis/toc-l-series/index.html. (Accessed 15/04/23)
339. Wallace, B., Purcell, M., & Furlong, J., 2002. Total organic carbon analysis as a precursor to disinfection byproducts in potable water: oxidation technique considerations. Journal of Environmental Monitoring: JEM. 4-1, 35–42. https://doi.org/10.1039/b106049j
340. Eaton, A. D., Franson, M. A. H., 2005. Standard methods for the examination of water & wastewater. Centennial ed. / Washington. American Public Health Association. 21. URL https://engage.awwa.org/PersonifyEbusiness/Bookstore/Product-Details/productId/162167531
341. Pelayo, D., Rivero, M. J., Santos, G., Gómez, P., Ortiz, I., 2023. Techno-economic evaluation of UV light technologies in water remediation. The Science of the Total Environment. 868-161376, 161376. https://doi.org/10.1016/j.scitotenv.2022.161376
342. Choi, J., Chung, J., 2019. Effect of dissolved oxygen on efficiency of TOC reduction by UV at 185 nm in an ultrapure water production system. Water Research. 154, 21–27. https://doi.org/10.1016/j.watres.2019.01.037
343. E. Coli, 2018. World Health Organisation. Article. URL https://www.who.int/news-room/fact-sheets/detail/e-coli. (Accessed 19/04/23)

List Of Figures

Figure 1.1: White light splitting as it passes through a prism (Source: [4]). **23**

Figure 1.2: Light spectrum as defined by Sir Isaac Newton (Representation drawn from [5]). **24**

Figure 1.3: Timeline of significant research on UV light (Source: [23-26]). **26**

Figure 1.4: (a) A high pressure mercury vapor lamp (Source: [44]) and (b) Mercury lamp emitting bright blue light (Source: [45]). **29**

Figure 1.5: Light generation mechanism in LEDs (Source: [59]). **32**

Figure 1.6: Stages in LED manufacturing (Source: [61]). **33**

Figure 1.7: (a) UV LED chip and (b) Schematic of layer stack of LEDs (Source: [65]). **34**

Figure 1.8: Water accessibility statistics by each continent as of 2017 (Source: [73,74]). **36**

Figure 1.9: Mechanism of inactivation (Source: [106]). **40**

Figure 1.10: Areas of interest. **42**

Figure 1.11: Objectives of this study. **46**

Figure 2.1: UV dose variation in a curing process (Source: [141]). **52**

Figure 2.2: (a) Top view of X–Y tester for radiometry, (b) Optical sensor equipment, and (c) COBRA FX–1 device. **55**

Figure 2.3: Device bypass for rollover test. **56**

Figure 2.4: (a) Balancing set–up and (b) Burn–In Cabinet. **57**

Figure 2.5: Representation of spectral Measurement set–up. **58**

Figure 2.6: Representation of the area covered by the sensor in each measurement. **59**

Figure 2.7: (a) Lifetime chamber, (b) Set–up for overall output measurement, and (c) Set–up for individual chain output measurement. **60**

Figure 2.8: Selected LEDs for further analysis. **63**

Figure 2.9: Optical options for COBRA FX–1 Series. **64**

Figure 2.10: Redesigned substrate for 265 nm light source. **65**

Figure 2.11: COBRA Clean FX–1 devices - (a) 265 nm, (b) 275 nm, (c) 285 nm, and (d) 310 nm [173]. **65**

Figure 2.12: Rollover test results for the devices (a) 265 nm, (b) 275 nm, (c) 285 nm, and (d) 310 nm. **67**

Figure 2.13: Measured Intensity with time – (a) At 440 mA set current and (b) at 420 mA set current. **68**

Figure 2.14: (a) Measured LED spectrum relative to their respective peaks and (b) Spectral width comparison. **69**

Figure 2.15: Relative intensity *vs* current measurements. **71**

Figure 2.16: Measured spectrum at each intensity and peak wavelength shift with current for – (a–b) FX–1 265, (c–d) FX–1 275, (e–f) FX–1 285, and (g–h) FX–1 310. **72**

Figure 2.17: 3D Uniformity Plot at 10 mm away from the sensor for – (a) FX–1 265, (b) FX–1 275, (c) FX–1 285, and (d) FX–1 310. **74**

Figure 2.18: (L) Longitudinal profile and (R) Lateral profiles for FX–1 devices. **75**

Figure 2.19: (a) Representation of effect of working distance, (b) Plot of measured intensity *vs* working distance, and (c) Plot of dose (at 1 cm s^{-1}) *vs* working distance. **77**

Figure 2.20: Lifetime data for – (a) FX–1 265 (after 9700 h), (b) FX–1 275 (after 3800 h), (c) FX–1 285 (after 3200 h), and (d) FX–1 310 (after 6200 h). **80**

Figure 2.21: (a) Individual chain output with time for FX–1 285 and (b) FX–1 285 LED degradation. **81**

Figure 2.B.1: Individual chain power output measurements (a) FX–1 265, (b) FX–1 275, (c) FX–1 310. **85**

Figure 3.1: (a) Typical configuration of radiometric measurement systems adapted from [194] and (b) Schematic representation of an extended light source. **90**

Figure 3.2: Peak wavelength of light sources studied (dotted line), wavelength range, and intensity calibration accuracy of the sensors used. Own elaboration based on manufacturers data [202, 203, 166, 161, 157]. **93**

Figure 3.3: Relative spectral intensity of each light source. **94**

Figure 3.4: (a) Light source mounted on the heatsink and (b) Angle of acceptance test set–up using the Ophir detector. **95**

Figure 3.5: Schematic representation of the set–up for analyzing the impact of temperature on measurements. **97**

Figure 3.6: Angle of Acceptance of sensors – (a) Loctite – UV A/B 1390323, UV V 1265282, (b) Ophir PD300RM-8W, (c) ThorLabs S120VC, (d) International Light Technologies - RAA4, (e) International Light Technologies - W Optic, and (f) **100**

Schematic representation of the cross-sectional views of the detectors (not to scale) [202, 203, 166, 161, 157, 158].
Figure 3.7: Change of acceptance angle of detectors with wavelength – (a) ThorLabs S120VC and (b) ILT W Optic Diffuser. **102**
Figure 3.8: Raw reference counts measured by a saturated and unsaturated sensor. **105**
Figure 3.9: Change in measured intensity with integration time– (a) 395 nm and (b) 265 nm. **107**
Figure 3.10: Effect of temperature on intensity measured by the sensor. **108**
Figure 3.11: Comparison between sensor measurements. **109**
Figure 3.A.1: Top view of the rotational stage used for the angle of acceptance experiments. **112**
Figure 3.A.2: Experimental set–up using the Ophir Detector at 0°. **112**
Figure 3.A.3: Experimental set–up using the Ophir Detector when the detector is at -90°. **113**
Figure 3.A.4: Experimental set–up using the Ophir Detector when the detector is at 90°. **113**
Figure 3.A.5: Test set–up for measurements using the Loctite detectors. **114**
Figure 3.A.6: Test set–up for intensity and integration time measurement experiments. **114**
Figure 3.B.1: Ambient light and dark signal measured on SpectrLite III **115**
Figure 4.1: UV Fixture – (a) Top View, (b) Isometric View, and (c) Representation of distance between center of the tube to source window. **123**
Figure 4.2: Top view of X–Y tester for half–quartz tube radiometry. **124**
Figure 4.3: (a) Side view of the designed model on ZeMax interface, (b) Top view of the designed model, and (c) Section view of simulated 265nm Optical Model. **128**
Figure 4.4: Schematic representation of the set–up used for actinometric experiments. **130**
Figure 4.5: (a) Isometric view of the meshed DOM model for 265 nm source, modeled in ANSYS Fluent and (b) Upper view of the 4–wavelength complex system. (CW from the left) FX–1 emitting window of 265 nm, 310 nm, 275 nm, and 285 nm, respectively. **132**
Figure 4.6: Ray tracing data *vs* experimental data (265 nm). **133**

Figure 4.7: (a) Plot of peak intensity *vs* working distance for 265 nm source and (b) Comparison between radiometry and ray tracing in the presence of a quartz tube in front of the light source. **135**

Figure 4.8: (a) Comparison between the average loss at multiple distances in radiometry, ray tracing, and transmission curve and (b) Plot of percentage loss of intensity for all wavelengths at multiple working distances. **138**

Figure 4.9: (a) Comparison between radiometry, ray tracing, and DOM, (b) Uniformity plot obtained from radiometry, (c) Uniformity plot obtained on ray tracing interface, and (d) Uniformity plot observed on DOM. **140**

Figure 4.10: (a) Plot of intensity with wavelength between the two techniques and (b) Isometric view of changed ray tracing model. **144**

Figure 4.11: Plot of change in peak intensity as light propagates through the quartz tube within the fixture at multiple working distances for the 265 nm source. **146**

Figure 4.12: (a) Ray tracing model for a complex system involving multiple devices operating at different wavelengths (CW from the left: FX–1 emitting window of 265 nm, 310 nm, 275 nm, and 285 nm, respectively) and (b) Depiction of points of interest in a complex system. **147**

Figure 4.A.1: Constituents of UV Fixture. **150**

Figure 4.A.2: FEA Analysis conducted on UV Fixture – (a) Forces applied – where A is the upward force exerted by the headplate, B is the downward gravitational force, C is the force applied by the device and D is the contact force between main body and headplate, and (b) Static structural analysis indicating low fracture possibility. **151**

Figure 4.A.3: Manufactured Fixture. **151**

Figure 4.B.1: Screen grab of ZeMax optic studio. **152**

Figure 4.C.1: Mesh sensitivity analysis for 265 nm source. **153**

Figure 4.C.2: Mesh sensitivity analysis for 275 nm source. **153**

Figure 4.C.3: Mesh sensitivity analysis for 310 nm source. **153**

Figure 4.D.1: Optical model comparison between datasheet and actual power simulations (a) 275 nm and (b) 310 nm. **154**

Figure 4.D.2: Plot of peak intensity *vs* working distance (a) 275 nm and (b) 310 nm. **155**

Figure 4.D.3: Plot of peak intensity *vs* working distance in the presence of quartz tube (a) 275 nm and (b) 310 nm. **156**

Figure 4.E.1: Fused quartz transmittance curve as obtained from the manufacturer (see white line for GE214 material type). **157**

Figure 4.F.1: Comparison between ZeMax, DOM, and radiometry (a) 275 nm and (b) 310 nm. **158**

Figure 4.G.1: Plots of E/L *vs* time for ferrioxalate actinometry – (a) 265 nm, (b) 275 nm, and (c) 310 nm. **160**

Figure 5.1: Representation of dilution, plating, and counting procedure. **166**

Figure 5.2: Schematic representation of – (a) recirculating batch reactor set–up and (b) single pass flow–through set–up. **168**

Figure 5.3: Possible combinations on UV fixture – (a) Individual wavelengths (IW), (b) Sequential Mode (SE), (c) Simultaneous Mode (SI), and (d) Sequential + Simultaneous Mode (SS). **169**

Figure 5.4: Representation of set–up change for study on the effect of flow rate. **170**

Figure 5.5: Disinfection rates in a recirculating batch reactor for (a) FX–1 265, 275, (b) FX–1 310, and (c) evaluation of first–order kinetics within the reactor. **178**

Figure 5.6: Observation of (a) unirradiated sample and (b) irradiated sample under the microscope for potential microbial aggregation. **180**

Figure 5.7: (a) Effect of cleaning the system in the presence/absence of magnetic stirrer and (b) difference between measured log inactivation at the tank and outlet of the pipe. **181**

Figure 5.8: Comparison between inactivation rates for two bacterial concentrations within a single pass reactor for FX–1 265 **182**

Figure 5.9: LRV *vs* dose for (a) FX–1 265 and 275, (b) FX–1 310. **184**

Figure 5.10: Plot of LRV against UV dose for (a) SE mode, (b) SI mode, and (c) SS Mode. **186**

Figure 5.11: Comparison between arrangements in SE mode for (a) 265/275, (b) 265/310, and (c) 275/310 combinations. **189**

Figure 5.12: Comparison between obtained LRV for each combination at (a) 50% Dose and (b) 100% Dose with error bars representing 95% *CI*. **190**

Figure 5.13: Inactivation rates at multiple flow rates as a function of (a) Input intensity and (b) Residence time. **192**

Figure 5.14: Synergy of inactivation for all combinations. **194**

Figure 5.15: Comparison between theoretical and actual LRV for each combination at (a) 50% dose and (b) 100% dose with error bars representing 95% *CI* from *t*–Student analysis. **195**

Figure 5.16: (a) Individual wavelength spectra of the light sources relative to their respective peaks alongside absorption spectra for DNA, proteins, and nucleotides extracted from [106,289] and (b) Spectra relative to the measured peak at 309.518 nm. **199**

Figure 5.17: Combined emission spectrum relative to maximum intensity measured for (a) 265/275, (b) 265/310, (c) 275/310, and (d) 265/275/310 combinations. **200**

Figure 5.18: Electrical energy consumption per unit order at 50% (Dark blue bars) and 100% (Violet bars). **203**

Figure 5.A.1: LRV vs UV Dose for 310 nm. **207**

Figure 5.D.1: Comparison between theoretical and actual kinetic constants with error bars representing 95% CI for (a) 50% dose and (b) 100% dose. **209**

Figure 6.1: WWTP at URJC facilities, Spain. **226**

Figure 6.2: Possible combinations on UV fixture – (a) Individual wavelengths (IW), (b) Sequential Mode (SE), and (c) Simultaneous Mode (SI). **228**

Figure 6.3: Transmittance of the wastewater between 200 – 400 nm. **230**

Figure 6.4: LRV *vs* UV dose for (a) FX–1 265, 275 and (b) FX–1 310, in comparison with model bacteria (E. coli K12, Chapter 5). **232**

Figure 6.5: Inactivation rates in combination for (a) SE mode of irradiation and (b) SI mode of irradiation in wastewater matrix. **234**

Figure 6.6: Synergy of inactivation in wastewater matrix. **236**

Figure 6.7: Comparison between theoretical and actual LRV at (a) 50% Dose and (b) 100% Dose using *t*–Student analysis in wastewater matrix. **237**

Figure 6.8: Electrical energy consumption per unit order at 50% (purple bars) and 100% (light violet bars) for wastewater matrix. **239**

Figure 6.A.1: LRV *vs* UV dose for 310 nm recirculation until 1–log reduction. **244**

Figure 6.C.1: Comparison between theoretical and actual kinetic constants with error bars representing 95% CI for (a) 50% Dose and (b) 100% Dose. **245**

List Of Tables

Table 1.1: Advantages of UV LEDs. **31**

Table 2.1: Decision criterion for choosing the light source. **54**

Table 2.2: LEDs evaluated. **61**

Table 2.3: Characteristics of selected LEDs. **63**

Table 2.4: Comparison between manufacturer currents and device–controlled tests. **66**

Table 2.5: Comparison between manufacturer mentioned peak and measured peak wavelength. **70**

Table 2.6: Measured Intensity (I in mW cm^{-2}) and dose (D in mJ cm^{-2}) at multiple working distances. **78**

Table 3.1: Sensor Specifications. **92**

Table 3.2: Summary of angular response of detectors. **99**

Table 3.B.1. Measured ambient light figures at the lab facility. **115**

Table 4.1: Material and optical properties of the quartz tube. **124**

Table 4.2: Refractive index and quantum yield input from literature studies [244,245]. **127**

Table 4.3: Recorded peak intensity at multiple working distances using radiometry and ray tracing. **136**

Table 4.4: Data on the loss of intensity in comparison with the transmission curve. **139**

Table 4.5: Recorded peak intensity at multiple working distances between simulation tools. **140**

Table 4.6: Data on comparison between actinometry measurements and ray tracing. **144**

Table 4.7: Comparison between measured intensity in air and water medium for 265 nm source. **145**

Table 4.8: Simulated intensity in water at different points within the tube. **148**

Table 4.C.1. Optimum mesh data. **152**

Table 4.D.1: Recorded peak intensity at multiple working distances using radiometry and ZeMax (without the effect of quartz tube). **156**

Table 4.D.2: Recorded peak intensity at multiple working distances using radiometry and ZeMax for effect of quartz. **157**

Table 4.F.1: Recorded peak intensity at multiple working distances using DOM and ZeMax (in air). **158**

Table 4.G.1: Actinometry data on incident irradiation. **159**

Table 5.1: Flow rates tested. **170**

Table 5.2: Codified ANOVA example for 265 + 275 and 265 | 275 | 310 combination. **174**

Table 5.3: Intensity and spectrum details at 100% intensity. **183**

Table 5.4: LRV for individual wavelength disinfection. **183**

Table 5.5: LRV of UV combinations. **187**

Table 5.6: Synergy of Inactivation values (by LRV) (at 50% Dose). **193**

Table 5.7: Synergy of Inactivation values (by LRV) (at 100% Dose). **193**

Table 5.8: *t*–Student analysis observations (based on LRV, at 95% CI). **195**

Table 5.9: Significance *p*–values from codified ANOVA ($p < 0.05$). **196**

Table 5.10: Contribution of the different spectral ranges to the emission of the light sources. **200**

Table 5.11: Electrical energy consumption per unit order of inactivation. **202**

Table 5.B.1: Inactivation rate constants, k_c (s^{-1}). **207**

Table 5.C.1: Synergy of inactivation at 50% Dose. **208**

Table 5.C.2: Synergy of inactivation at 100% Dose. **208**

Table 6.1: LRV for individual wavelength disinfection of wastewater. **231**

Table 6.2: LRV at different UV doses for each combination. **233**

Table 6.3: Synergy of inactivation values (by LRV) (at 50% Dose). **235**

Table 6.4: Synergy of Inactivation values (by LRV) (at 100% Dose) **235**

Table 6.5: *t*–Student analysis observations for wastewater matrix. **237**

Table 6.6: *p*–values from codified ANOVA at 95% *CI*. **238**

Table 6.7: Electrical energy per unit order of inactivation (WW). **240**

Table 6.B.1: At 50% Dose. **244**

Table 6.B.2: At 100% Dose. **245**

PUBLICATIONS

- A version of chapter 3 is a published article in "Measurement" Journal - Adithya Pai Uppinakudru, Ken Reynolds, Simon Stanley, Cristina Pablos, Javier Marugán, Critical assessment of optical sensor parameters for the measurement of ultraviolet LED lamps, Measurement, Volume 196, 2022, 111278, ISSN 0263-2241, https://doi.org/10.1016/j.measurement.2022.111278.
- A version of chapter 4 is under review in "Measurement".
- Paper based on chapters 5 and 6 are currently in preparation for submission.

RESEARCH CONGRESSES

- A. Pai Uppinakudru, Cintia Casado, Ken Reynolds, Simon Stanley, Cristina Pablos, Javier Marugán. A Synergistic effect of 3 wavelengths for inactivation of E. coli. 32nd Irish Environmental Researchers Colloquium, Belfast (UK), 20th – 22nd June 2022. Oral presentation.
- A. Pai Uppinakudru, Miguel Martín-Sómer, Ken Reynolds, Simon Stanley, Cristina Pablos, Javier Marugán. Prediction of radiant intensity using analytical and numerical simulation techniques. 32nd Irish Environmental Researchers Colloquium, Belfast (UK), 20th – 22nd June 2022. Poster presentation.
- A. Pai Uppinakudru, K. Reynolds, S. Stanley, C. Pablos, J. Marugán. Critical assessment of optical sensor parameters for the measurement of ultraviolet LED lamps. Measurement, Sensor Systems and Applications Conference 24th – 26th August 2022, Online and On Demand. Oral Presentation and Science Talk

PARTICIPANT CONFERENCES

- International Conference on Ultraviolet disinfection for Air and Surface, celebrated between 08-09 December 2020 (virtual conference).
- Fifth South Asian Cities Summit 2020, celebrated in Goa (India) between 04-06 March 2020.
- International Conference on UV LED Technologies & Applications (ICULTA 2021), organized jointly by the German consortium 'Advanced UV for Life' and the 'International Ultraviolet Association (IUVA).

OTHER PUBLICATIONS

- Adithya Pai Uppinakudru, The Impact of Irradiance and Energy Density in UV LED Curing Applications, ProPhotonix White Paper, 2020, https://www.prophotonix.com/resources/whitepapers/.
- ProPhotonix, Datasheet for COBRA Clean FX–1. https://www.prophotonix.com/led-and-laser-products/uvc-led-systems/uvc-led-system/ (Accessed 19/04/2022)

NOTES

NOTES

2023